

ISSN 1573-160X

Vol. 31, Iss. 2

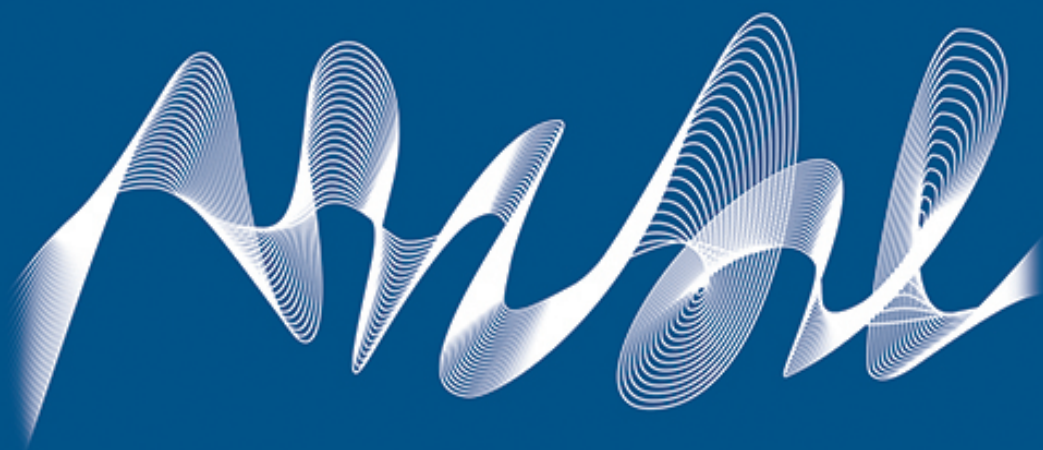
March – April

2024



Physical Oceanography

<http://physical-oceanography.ru/>



EDITORIAL BOARD

- Sergey K. Konovalov** – Editor-in-Chief, Director of FSBSI FRC MHI, corresponding member of RAS, Dr.Sci. (Geogr.), ORCID ID: 0000-0002-5200-8448, secretary@mhi-ras.ru (Sevastopol, Russia)
- Vladimir N. Belokopytov** – Deputy Editor-in-Chief, Head of Department of FSBSI FRC MHI, Dr.Sci. (Geogr.), ORCID ID: 0000-0003-4699-9588, (Sevastopol, Russia)
- Aleksandr I. Kubryakov** – Deputy Editor-in-Chief, Chief Scientist Researcher of FSBSI FRC MHI, Dr.Sci. (Phys.-Math.), ORCID ID: 0000-0003-1899-9230, ResearcherID: F-8959-2014, (Sevastopol, Russia)
- Igor K. Ivashchenko** – Executive Editor, Senior Scientist of FSBSI FRC MHI, Ph.D. (Econ.), (Sevastopol, Russia)
- Yuri V. Artamonov** – Head Scientist Researcher of FSBSI FRC MHI, Dr.Sci. (Geogr.), ResearcherID: AAC-6651-2020 (Sevastopol, Russia)
- Sergey V. Berdnikov** – Director of FRC SSC of RAS, Dr.Sci. (Geogr.), ORCID ID: 0000-0002-3095-5532 (Rostov-on-Don, Russia)
- Valery G. Bondur** – Scientific Supervisor of ISR "AEROCOSMOS", academician of RAS, Dr.Sci. (Techn.), ORCID ID: 0000-0002-2049-6176 (Moscow, Russia)
- Demuri I. Demetrasvili** – Head of the sector of mathematical modeling of geophysical processes of sea and atmosphere, the Nodia Institute of Geophysics of the Javakhishvili Tbilisi State University, Dr.Sci. (Phys.-Math.), ORCID ID: 0000-0002-4789-4852 (Tbilisi, Georgia)
- Sergey A. Dobrolyubov** – Dean of Faculty of Geography of MSU, academician of RAS, Dr.Sci. (Geogr.), prof., ResearcherID: A-9688-2012 (Moscow, Russia)
- Grigory I. Dolgikh** – Director of POI FEB of RAS, Dr.Sci. (Phys.-Math.), academician of RAS, prof., ORCID ID: 0000-0002-2806-3834 (Vladivostok, Russia)
- Vladimir A. Dulov** – Head of Laboratory of FSBSI FRC MHI, Dr.Sci. (Phys.-Math.), prof., ORCID ID: 0000-0002-0038-7255, (Sevastopol, Russia)
- Vladimir V. Efimov** – Head of Department of FSBSI FRC MHI, Dr.Sci. (Phys.-Math.), prof., ResearcherID: P-2063-2017, (Sevastopol, Russia)
- Vladimir V. Fomin** – Head of Department of FSBSI FRC MHI, Dr.Sci. (Phys.-Math.), ORCID ID: 0000-0002-9070-4460, (Sevastopol, Russia)
- Isaac Gertman** – Head of the Physical Oceanography Department of Israel Oceanographic & Limnological Research, Head of IOLR data center ISRAMAR, Ph.D. (Geogr.), ORCID ID: 0000-0002-6953-6722 (Haifa, Israel)
- Dmitry G. Gryazin** – Head of Department, Chief Metrologist of SRC of the "Concern CSRI Elektropribor" JSC, Dr.Sci. (Techn.), prof. of Mechatronics of ITMO University, Scopus AuthorID: 25638150600, (Saint Petersburg, Russia)
- Rashit A. Ibraev** – Chief Scientist Researcher of INM of RAS, corresponding member of RAS, Dr.Sci. (Phys.-Math.), ORCID ID: 0000-0002-9099-4541 (Moscow, Russia)
- Vasily V. Knysh** – Head Scientist Researcher of FSBSI FRC MHI, Dr.Sci. (Phys.-Math.), prof., ResearcherID: B-3603-2018 (Sevastopol, Russia)
- Gennady K. Korotaev** – Scientific Supervisor of FSBSI FRC MHI, corresponding member of RAS, Dr.Sci. (Phys.-Math.), prof., ResearcherID: K-3408-2017 (Sevastopol, Russia)
- Vladimir N. Kudryavtsev** – Executive Director of Satellite Oceanography Laboratory of RSHU, Dr.Sci. (Phys.-Math.), prof., ResearcherID: G-1502-2014 (Saint Petersburg, Russia)
- Michael E. G. Lee** – Head of Department of FSBSI FRC MHI, Dr.Sci. (Phys.-Math.), prof., ORCID ID: 0000-0002-2292-1877 (Sevastopol, Russia)
- Gennady G. Matishov** – Deputy President of RAS, Deputy academician-Secretary of the Department of Earth Sciences of Supervisor of RAS – Head of the Oceanology, Atmospheric Physics and Geography Section, Scientific Supervisor of SSC of RAS, Supervisor of MMBI KSC of RAS, academician of RAS, Dr.Sci. (Geogr.), prof., ORCID ID: 0000-0003-4430-5220 (Rostov-on-Don, Russia)
- Nikolay A. Rimski-Korsakov** – Deputy Director (Marine Engineering) of FSBSI P.P. Shirshov IO of RAS, Dr.Sci. (Techn.), ResearcherID: K-8378-2017 (Moscow, Russia)
- Angelo Rubino** – Professor of Ca' Foscari University, Ph.D. (Phys. Oceanogr.), ORCID ID: 0000-0003-3857-4811 (Venice, Italy)
- Anatoly S. Samodurov** – Head of Department of FSBSI FRC MHI, Dr.Sci. (Phys.-Math.), ResearcherID: V-8642-2017 (Sevastopol, Russia)
- Georgy I. Shapiro** – Head of Plymouth Ocean Forecasting Centre of the University of Plymouth, Dr.Sci. (Phys.-Math.), prof. in Phys. Oceanogr., (Plymouth, Great Britain)
- Naum B. Shapiro** – Head Scientist Researcher of FSBSI FRC MHI, Dr.Sci. (Phys.-Math.), ResearcherID: A-8585-2017 (Sevastopol, Russia)
- Mikhail V. Shokurov** – Head Scientist Researcher of FSBSI FRC MHI, Dr.Sci. (Phys.-Math.), ORCID ID: 0000-0003-1595-8281 (Sevastopol, Russia)
- Elena F. Vasechkina** – Deputy Director of FSBSI FRC MHI, Chief Research Associate of FSBSI FRC MHI, Dr.Sci. (Geogr.), ORCID ID: 0000-0001-7007-9496 (Sevastopol, Russia)
- Elizaveta V. Zabolotskikh** – Head Scientist Researcher of RSHU, Dr.Sci. (Phys.-Math.), Scopus Author ID: 6506482460 (Saint Petersburg, Russian)
- Vladimir B. Zalesny** – Head Scientific Researcher of INM of RAS, Dr.Sci. (Phys.-Math.), prof., ORCID ID: 0000-0003-3829-3374 (Moscow, Russia)
- Andrey G. Zatsepin** – Chief of Laboratory of FSBSI P.P. Shirshov IO of RAS, Chief Research Associate of FSBSI P.P. Shirshov IO of RAS, Dr.Sci. (Phys.-Math.), ORCID ID: 0000-0002-5527-5234 (Moscow, Russia)
- George Zodiatis** – Senior Researcher of Laboratory of Coastal and Marine Research of the Institute of Applied and Computational Mathematics, for Research and Technology Foundation – Hellas, Ph.D. (Oceanol.), ResearcherID: J-3032-2013 (Heraklion, Crete, Greece)

CONTENTS

Vol. 40, no. 2. 2024

March – April, 2024

THERMOHYDRODYNAMICS OF THE OCEAN AND THE ATMOSPHERE

- Demyshev S. G.** Finite-difference approximation of the potential vorticity equation for a stratified incompressible fluid and an example of its application for modeling the Black Sea circulation. Part I. Finite-difference equation of potential vorticity of ideal fluid 149
- Slepyshev A. A., Ankudinov N. O.** Generation of vertical fine structure by internal waves on a shear flow 161

ANALYSIS OF OBSERVATIONS AND METHODS OF CALCULATING HYDROPHYSICAL FIELDS IN THE OCEAN

- Lee M. E., Shybanov E. B.** New method for determining spectral absorption of light in the sea 178
- Rostov I. D., Dmitrieva E. V.** Interannual salinity changes in the upper 1000-meter layer of extratropical zone in the northwestern Pacific Ocean under conditions of the intensification of global hydrological cycle 194
- Zakharchuk E. A., Sukhachev V. N., Tikhonova N. A.** Wave nature and modulation of annual fluctuations in the level of the Baltic Sea 208

EXPERIMENTAL AND FIELD RESEARCH

- Kapustina M. V., Zimin A. V.** Influence of coastal upwelling on chlorophyll *a* distribution in the coastal zone of the southeastern Baltic Sea in summer periods, 2000–2019 231
- Kremenchutskii D. A.** Temporal variability of the Beryllium-7 (⁷Be) scavenging ratio in the Sevastopol region 246
- Kondratev S. I., Masevich A. V.** Vertical distribution of oxygen and hydrogen sulfide in the deep part of the Black Sea based on the 2017–2019 expedition data 258
- Zatsepin A. G., Elkin D. N.** Underwater ridge impact on the motion of anticyclonic eddies over a sloping bottom as a result of the topographic beta-effect: Laboratory experiment 271

SATELLITE HYDROPHYSICS

- Plotnikov E. V., Kozlov I. E., Zhuk E. V., Marchenko A. V.** Evaluation of sea ice drift in the Arctic marginal ice zone based on the *Sentinel-1A/B* satellite radar measurements 284

MATHEMATICAL MODELING OF MARINE SYSTEMS

- Dulov V. A., Yurovskaya M. V., Fomin V. V., Shokurov M. V., Yurovsky Yu. Yu., Barabanov V. S., Garmashov A. V.** Extreme Black Sea storm in November, 2023 295



All the materials of the journal are available under Creative Commons Attribution-NonCommercial 4.0 International (CC BY-NC 4.0)

Finite-Difference Approximation of the Potential Vorticity Equation for a Stratified Incompressible Fluid and an Example of its Application for Modeling the Black Sea Circulation

Part I. Finite-Difference Equation of Potential Vorticity of Ideal Fluid

S. G. Demyshev

Marine Hydrophysical Institute of RAS, Sevastopol, Russian Federation
✉ demyshev@gmail.com

Abstract

Purpose. The study is purposed at deriving the discrete equations of absolute and potential vorticity for a three-dimensional stratified incompressible fluid as an exact consequence of the finite-difference equations of sea dynamics in the field of a potential mass force in the adiabatic approximation provided that viscosity and diffusion are absent. The properties of two-dimensional projections of the absolute vorticity equation onto coordinate planes and the three-dimensional potential vorticity equation are analyzed.

Methods and results. In order to determine the discrete analogues of absolute and potential vorticity, an additional grid is introduced, where the finite-difference equations for the components both of absolute and potential vorticity are written down. Two-dimensional analogues of the three-dimensional equation of absolute vorticity on the planes (x, y) , (y, z) and (x, z) are obtained; they possess the feature of preserving vorticity, energy and enstrophy (square of vorticity). A discrete equation for potential vorticity of a stratified incompressible fluid is derived from the finite-difference system of three-dimensional equations of sea dynamics in the adiabatic approximation at the absence of viscosity and diffusion.

Conclusions. In the case of a linear equation of state, the discrete equations of absolute vorticity and potential vorticity which are the exact consequence of finite-difference formulation are obtained. The equation of potential vorticity is of a divergent form, and two-dimensional analogues of the absolute vorticity equation on the planes (x, y) , (y, z) and (x, z) have two quadratic invariants that provide preservation of the average wave number.

Keywords: discrete equation, dynamics of sea, kinetic energy, vortex, potential vorticity, Ertel invariant

Acknowledgments: The study was carried out with financial support of the Russian Science Foundation grant 23-27-00141.

For citation: Demyshev, S.G., 2024. Finite-Difference Approximation of the Potential Vorticity Equation for a Stratified Incompressible Fluid and an Example of its Application for Modeling the Black Sea Circulation. Part I. Finite-Difference Equation of Potential Vorticity of Ideal Fluid. *Physical Oceanography*, 31(2), pp. 149-160.

© 2024, S. G. Demyshev

© 2024, Physical Oceanography

Introduction

Currently, increasing attention is being paid to the study of vortex flows in seas and oceans based on the analysis of potential vorticity of a stratified fluid, which began with the works [1, 2]. A special role is played by the well-known Ertel's theorem [2], which establishes a connection between the displacements of isopycnal surfaces and the vorticity flow of an ideal fluid. Under the condition of mass force potentiality, incompressibility of fluid and absence of viscosity and diffusion, the water motion is isopycnic in nature, so that a particle of liquid located on the surface of constant density remains on it during movement. A detailed



presentation of historical and scientific chronology of potential vorticity (PV) research is given in [3, 4].

Transition to a discrete system of fluid dynamics equations raises the question of correspondence of the resulting difference solution to its continuous analogue and, in particular, satisfaction of PV conservation law in a finite-difference problem. The importance of this approach is that the Ertel potential vorticity equation describes the balance between nonlinear forces in the equations of motion and the density advection equation. Therefore, small errors associated with the inconsistency of discrete equation for potential vorticity with the original finite-difference formulation can lead to incorrect conclusions. In addition, the derivation of equation for PV in a relatively general form (without a quasi-static approximation) provides subsequent studies of any of its simplified versions.

Schemes that ensure satisfaction of a number of conservation laws for one-dimensional shallow water equation are considered in [5]. A new finite-difference scheme has been obtained, where the laws of energy, mass, center of mass, and momentum conservation are observed. Difference analogues, which have a set of linear and quadratic invariants, were studied for two-dimensional equations of flow dynamics. In [6], invariant discretization schemes are constructed for one-dimensional and two-dimensional shallow water equations with periodic boundary conditions. It is indicated that for maintaining invariance a redistribution of grid points is required, i.e., during the process of integrating model equations the grid cannot remain fixed. The resulting schemes conserve mass and momentum, but are not energy efficient.

The works ^{1, 2} are devoted to the development of a new numerical method for spatio-temporal solution for two-dimensional Navier–Stokes equations in the incompressibility approximation. It consists in constructing difference schemes that satisfy conservation laws in an integral formulation, not in a differential form. Therefore, discretization of model equations is carried out on the basis of the balance between energy and mass flows at the boundaries of discrete regions for local and integral variables ¹.

The work ² considers an improved version of flow approximation at the boundaries of regions, which provides a systematic and rigorous derivation of conditions for modeling differential equations while maintaining mass and momentum. For two- and three-dimensional Navier–Stokes equations in the incompressibility approximation, their discretization is studied in the formulation of energy – momentum – angular momentum conservation [7]. It is demonstrated that energy is conserved at skew-symmetric linearization of the Navier–Stokes equations, and momentum and angular momentum are conserved at Newtonian linearization. Based on numerical calculations, it is concluded that linearization with two Newton steps at each time step ensures preservation of all three parameters over large time intervals.

¹ Scott, J.R. and Chang, S.-C., 1993. *A New Flux Conserving Newton's Method Scheme for the Two-Dimensional, Steady Navier-Stokes Equations*. NASA Technical Memorandum; 106160. NASA, 50 p. Available at: <https://ntrs.nasa.gov/api/citations/19930019437/downloads/19930019437.pdf> [Accessed: 29 March 2024].

² Scott, J.R., 1994. *A New Flux-Conserving Numerical Scheme for the Steady, Incompressible Navier-Stokes Equations*. NASA Technical Memorandum; 106520. NASA, 49 p. Available at: <https://ntrs.nasa.gov/api/citations/19940024968/downloads/19940024968.pdf> [Accessed: 29 March 2024].

In [8], a generalization of the Arakawa–Lamb scheme [9] with high-order discretization, but accurate to time approximation, was obtained. It was revealed that the properties of symmetry and the laws of energy and enstrophy conservation are satisfied for periodic problems using high-order summation-by-parts operators.

Significant progress in this direction is due to the results of work [10]. It provides a discrete construction of the Nambu and Poisson brackets, which preserves their antisymmetry property. In turn, this makes it possible to construct numerical models of incompressible fluid flows in two and three dimensions satisfying basic conservation laws. The schemes conserve energy and potential vorticity, as well as potential enstrophy [11], which is considered particularly important since it prevents spurious energy flow into high-wavenumber motions. Based on time-discrete analogues of Nambu brackets, a difference scheme that has two discrete quadratic invariants (energy and potential enstrophy) in time and space is obtained. This demonstrates the possibility of generalizing the Arakawa–Lamb scheme to a time-discrete model without loss of invariants [12].

The present work lies in the field of the abovementioned studies and focuses on derivation of potential vorticity discrete equation for an incompressible stratified ideal fluid as an exact consequence of model difference equations without a quasi-static approximation.

Potential vorticity equation of a stratified incompressible fluid in differential formulation

We are to consider a system of differential equations for a stratified incompressible fluid in a field of potential forces under the conditions of adiabaticity and the absence of diffusion, viscosity and external sources. Then, in the Boussinesq approximation in the Cartesian coordinate system, the fluid motion in the region Ω with boundary $\partial\Omega$ in the Gromeka–Lamb form is described by the following system of equations:

$$\frac{\partial \vec{U}}{\partial t} + \vec{\xi}_x \vec{U} = -\frac{1}{\rho_0} \nabla(P + E) + \vec{g} \frac{\rho}{\rho_0}, \quad (1)$$

$$\nabla \vec{U} = 0, \quad (2)$$

$$\frac{\partial T}{\partial t} + \text{div}(T\vec{U}) = 0, \quad (3)$$

$$\frac{dS}{dt} + \text{div}(S\vec{U}) = 0, \quad (4)$$

$$\rho = f(T, S). \quad (5)$$

The following notations were introduced: $\vec{U} = (u, v, w)$ are the components of flow velocity vector along the axes (x, y, z) directed to the east, north, and vertically downward, respectively; $\vec{g} = (0, 0, g)$ is gravitational acceleration; (T, S, P, ρ) are seawater temperature, salinity, pressure, and density; $\rho_0 = 1 \text{ g/cm}^3$ (further we assume pressure and density normalized to ρ_0); $\vec{f} = (0, 0, f^z)$ is the Coriolis parameter, where $f^z = 2\omega \sin\varphi$; ω is angular velocity of the Earth's rotation; φ is latitude. Relationship (5) is the equation of state, which in this work is assumed to be linear. In terms of satisfying the conservation laws in a discrete problem, such an assumption is a fundamental simplification, which will be discussed in more detail later.

An absolute vorticity and kinetic energy of motion are introduced into equation (1):

$$\vec{\xi} = (\xi^x, \xi^y, \xi^z),$$

$$\xi^x = \frac{\partial w}{\partial y} - \frac{\partial v}{\partial z}, \xi^y = \frac{\partial u}{\partial z} - \frac{\partial w}{\partial x}, \xi^z = \frac{\partial v}{\partial x} - \frac{\partial u}{\partial y} + f^z, \quad (6)$$

$$E = \rho_0 \frac{u^2 + v^2 + w^2}{2}. \quad (7)$$

$$\text{At } z = 0 \quad w = -\zeta_r, \text{ at } z = H(x, y) \quad w = 0. \quad (8)$$

At the side walls the impermeability conditions are as follows:

$$\text{for meridional } u = 0, \text{ for zonal boundary sections } v = 0. \quad (9)$$

For temperature and salinity, the conditions of the absence of flows are set.

Initial conditions:

$$\text{at } t = t_0 \quad (T, S) = (T^0, S^0), u = u^0, v = v^0, w = w^0. \quad (10)$$

Applying the rot operation to equation (1), for $\vec{\xi}$ we obtain

$$\frac{\partial \vec{\xi}}{\partial t} + \nabla \times (\vec{\xi} \times \vec{U}) = \nabla \times (\vec{g} \rho). \quad (11)$$

Equation (11) explicitly describes the transformation of an important hydrodynamic characteristic – an absolute vorticity. Correct approximation of the properties of this equation is of fundamental importance. For example, if the right side of this equation (barotropic motion) is equal to zero, the Helmholtz theorem conditions are satisfied and vortex filaments and vortex tubes³ are preserved in the liquid. To fulfill these properties, the finite-difference approximation of the system of equations (1)–(6) in case of constant density must result in a discrete equation of the absolute vorticity with a zero right-hand side. Otherwise, computational features arise in the difference problem.

Due to absolute vorticity (6) definition, we have

$$\nabla \vec{\xi} = 0. \quad (12)$$

Then equation (11) can be rewritten as follows:

$$\frac{\partial \vec{\xi}}{\partial t} + \vec{U}(\nabla \vec{\xi}) - \vec{\xi}(\nabla \vec{U}) = \nabla \times (\vec{g} \rho). \quad (13)$$

If two-dimensional motion in (x, y) , (x, z) , (y, z) planes is considered, then for each projection the following conservation laws can be specified. In (x, z) plane, for example, equations (2) and (13) are rewritten as

$$\frac{\partial u}{\partial x} + \frac{\partial w}{\partial z} = 0, \quad \frac{\partial \xi^y}{\partial t} + u \frac{\partial \xi^y}{\partial x} + v \frac{\partial \xi^y}{\partial z} = 0.$$

Then the conservation laws (ψ^y is stream function):

$$\frac{\partial}{\partial t} \int_{\Omega} \xi^y d\Omega = \frac{\partial}{\partial t} \int_{\Omega} (\xi^y)^2 d\Omega = \frac{\partial}{\partial t} \int_{\Omega} (\nabla \psi^y)^2 d\Omega = 0$$

and the antisymmetry property are satisfied: $J(\psi^y, \xi^y) = -J(\xi^y, \psi^y)$.

If two quadratic conservation laws are satisfied, it can be demonstrated⁴ [12] that the average wavenumber does not depend on time. This property means that

³ Kochin, N.E., Kibel, I.A. and Roze, N.V., 1964. *Theoretical Hydromechanics*. New York: Interscience Publishers, 577 p.

⁴ Dymnikov, V.P., 1984. [*Computational Methods in Geophysical Fluid Dynamics*]. Moscow: Department of Computational Mathematics of the USSR Academy of Sciences, 148 p. (in Russian).

a systematic energy transfer to high-wavenumber motions cannot exist. If this property is not met in the numerical model, a false (computational) energy cascade to minimally resolved (two-step) waves on the grid may occur. The group velocity of two-step waves is zero, so energy accumulates on these scales.

The vorticity equation in the form (13) allows to obtain the potential vorticity equation for a stratified incompressible fluid.

The equations (3)–(5) imply the density advection equation

$$\frac{\partial \rho}{\partial t} + \text{div}(\rho \vec{U}) = 0. \quad (14)$$

Due to equality (12), we have

$$\nabla [\vec{U}(\nabla \vec{\xi})] - \nabla [\vec{\xi}(\nabla \vec{U})] - \nabla [\nabla \times (\vec{g} \rho)] = 0. \quad (15)$$

From the density advection equation (14) we obtain three equations for density gradients. To do this, we differentiate equation (14) sequentially with respect to x , y , z . We multiply the resulting equations by ξ^x, ξ^y, ξ^z , equation (13) – by the corresponding derivatives of ρ . After simple transformations, considering relations (14) and (15), we obtain the equation for PV [2]:

$$\frac{\partial \omega}{\partial t} + (\vec{U} \nabla) \omega = 0, \quad \omega = \vec{\xi} \nabla \rho, \quad (16)$$

where ω is potential vorticity of a stratified incompressible fluid. Equations (2) and (16) imply an important integral conservation law for a three-dimensional motion of a baroclinic fluid

$$\frac{\partial}{\partial t} \int_{\Omega} \omega \, d\Omega = 0. \quad (17)$$

Equality (17) means that potential vorticity ω is conserved in each particle as it moves. Let us note that equation (16) characterizes the main feature of a stratified incompressible fluid under the following conditions: potential mass force (gravity force) and incompressibility of seawater, absence of viscosity and density diffusion in motion equations [4]. The result obtained by G. Ertel has two remarkable features. If we consider any Lagrangian invariant (for example, ϑ) instead of density, then $\omega = \vec{\xi} \nabla \vartheta$ will also be an invariant [4]. The second feature is that for an incompressible fluid, due to the form of equation (16), an invariant is any Ψ operator differentiable with respect to ω . Let us multiply (16) by $\frac{d\Psi}{d\omega} = \Psi'$. Then we get

$$\frac{d\Psi(\omega)}{dt} = 0, \quad \frac{\partial}{\partial t} \int_{\Omega} \Psi(\omega) \, d\Omega = 0, \quad \int_{\Omega} \Psi(\omega) \, d\Omega = \text{const.}$$

Discrete equation of absolute vorticity and conservation laws

We approximate a basin with an uneven bottom by boxes; their centers correspond to integer values of indices i, j, k ($i = i_1, \dots, i_N$, $j = j_1, \dots, j_M$, $k = 1, \dots, K_{i,j}$), edges – to $i+1/2, j+1/2, k+1/2$. Horizontal dimensions of the boxes (h_x, h_y) are constant; uneven approximation ($h_z^k = z_{k+1/2} - z_{k-1/2}$, $h_z^{k+1/2} = z_{k+1} - z_k$) is applied vertically [13, 14].

Difference operators have the following form (for j, k – similarly):

$$\bar{\phi}_{i,j,k}^x = \frac{\phi_{i+1/2,j,k} + \phi_{i-1/2,j,k}}{2}, \delta_x \phi_{i,j,k} = \frac{\phi_{i+1/2,j,k} - \phi_{i-1/2,j,k}}{h_x}, \nabla_{x,y}^2 \phi_{i,j,k} = \delta_x^2 \phi_{i,j,k} + \delta_y^2 \phi_{i,j,k},$$

$$\{\phi\}^{\Omega_k} = \frac{1}{\Omega_k} \sum_{i,j} \phi_{i,j,k} h_x h_y, \quad \{\phi\}^V = \frac{1}{V} \sum_{i,j} \sum_{k=1}^{K_{i,j}} \phi_{i,j,k} h_z^k h_x h_y, \quad V = \sum_{i,j} \sum_{k=1}^{K_{i,j}} h_z^k h_x h_y. \quad (18)$$

Temperature, salinity, and horizontal velocity components are calculated at z_k horizons, vertical velocity is calculated at $z_{k+1/2}$ horizons. The distribution of variables is given in Fig. 1.

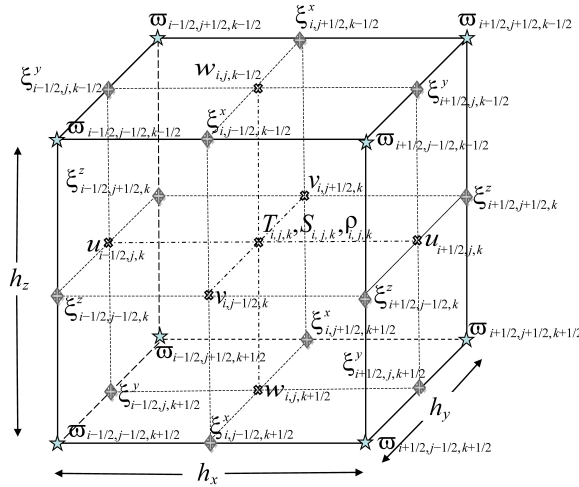


Fig. 1. Distribution of variables in box (i, j, k) . PV (ω) is determined at the box vertices indicated by an asterisk, and the components of absolute vorticity $\xi_{i,j+1/2,k}^x, \xi_{i+1/2,j,k+1/2}^y, \xi_{i+1/2,j+1/2,k}^z$ are determined at its edges

According to notations (6), (7) and (18), we write out the finite-difference equations of model (1)–(5) (differential in time) [9, 14]:

$$\frac{du_{i+1/2,j,k}}{dt} - [v, \xi^z]_{i+1/2,j,k} + [w, \xi^y]_{i+1/2,j,k} = -\delta_x (E_{i+1/2,j,k} + P_{i+1/2,j,k}), \quad (19.1)$$

$$\frac{dv_{i,j+1/2,k}}{dt} + [u, \xi^z]_{i,j+1/2,k} - [w, \xi^x]_{i,j+1/2,k} = -\delta_y (E_{i,j+1/2,k} + P_{i,j+1/2,k}), \quad (19.2)$$

$$\frac{dw_{i,j,k+1/2}}{dt} - [u, \xi^y]_{i,j,k+1/2} + [v, \xi^x]_{i,j,k+1/2} = -\delta_z (E_{i,j,k+1/2} + P_{i,j,k+1/2}) + g\rho_{i,j,k+1/2}, \quad (19.3)$$

$$\delta_x u_{i,j,k} + \delta_y v_{i,j,k} + \delta_z w_{i,j,k} = 0, \quad (20)$$

$$\frac{dT_{i,j,k}}{dt} + \delta_x (u_{i,j,k} T_{i,j,k}) + \delta_y (v_{i,j,k} T_{i,j,k}) + \delta_z (w_{i,j,k} T_{i,j,k}) = 0, \quad (21)$$

$$\frac{dS_{i,j,k}}{dt} + \delta_x (u_{i,j,k} S_{i,j,k}) + \delta_y (v_{i,j,k} S_{i,j,k}) + \delta_z (w_{i,j,k} S_{i,j,k}) = 0, \quad (22)$$

$$\rho_{i,j,k} = \alpha T_{i,j,k} + \beta S_{i,j,k}. \quad (23)$$

In accordance with difference operators (18), the vorticity components (Fig. 1) have the following form:

$$\xi_{i,j+1/2,k+1/2}^x = \delta_y (w_{i,j+1/2,k+1/2}) - \delta_z (v_{i,j+1/2,k+1/2}),$$

$$\begin{aligned}\xi_{i+1/2,j,k+1/2}^y &= \delta_z(u_{i+1/2,j,k+1/2}) - \delta_x(w_{i+1/2,j,k+1/2}), \\ \xi_{i+1/2,j+1/2,k}^z &= \delta_x(v_{i+1/2,j+1/2,k}) - \delta_y(u_{i+1/2,j+1/2,k}) + f_{j+1/2}^z.\end{aligned}\quad (24)$$

From approximation (24) it follows that at points $i + 1/2, j + 1/2, k + 1/2$ (analogous to (12)) the following is fulfilled:

$$\delta_x \xi^x + \delta_y \xi^y + \delta_z \xi^z = 0. \quad (25)$$

We assume that the terms in square brackets on the left side of equations (19.1)–(19.3) are written down in the form

$$\begin{aligned}[v, \xi^z]_{i+1/2,j,k} &= \frac{1}{3} \left\{ \overline{v_{i+1/2,j,k}^{xy} \xi_{i+1/2,j,k}^z}^y + \frac{\overline{v_{i+1,j,k} \xi_{i+1/2,j,k}^z}^y + \overline{v_{i,j,k} \xi_{i-1/2,j,k}^z}^y}{2} \right\}, \\ [w, \xi^y]_{i+1/2,j,k} &= \frac{1}{3} \left\{ \overline{w_{i+1/2,j,k}^{xz} \xi_{i+1/2,j,k}^y}^z + \frac{\overline{w_{i+1,j,k} \xi_{i+1/2,j,k}^y}^z + \overline{w_{i,j,k} \xi_{i-1/2,j,k}^y}^z}{2} \right\}, \\ [u, \xi^z]_{i,j+1/2,k} &= \frac{1}{3} \left\{ \overline{u_{i,j+1/2,k}^{xy} \xi_{i,j+1/2,k}^z}^x + \frac{\overline{u_{i,j+1,k} \xi_{i,j+1/2,k}^z}^x + \overline{u_{i,j,k} \xi_{i,j-1/2,k}^z}^x}{2} \right\}, \\ [w, \xi^x]_{i,j+1/2,k} &= \frac{1}{3} \left\{ \overline{w_{i,j+1/2,k}^{yz} \xi_{i,j+1/2,k}^x}^z + \frac{\overline{w_{i,j+1,k} \xi_{i,j+1/2,k}^x}^z + \overline{w_{i,j,k} \xi_{i,j-1/2,k}^x}^z}{2} \right\}, \\ [u, \xi^y]_{i,j,k+1/2} &= \frac{1}{3} \left\{ \overline{u_{i,j,k+1/2}^{xz} \xi_{i,j,k+1/2}^y}^x + \frac{\overline{u_{i,j,k+1} \xi_{i,j,k+1/2}^y}^x + \overline{u_{i,j,k} \xi_{i,j,k-1/2}^y}^x}{2} \right\}, \\ [v, \xi^x]_{i,j,k+1/2} &= \frac{1}{3} \left\{ \overline{v_{i,j,k+1/2}^{yz} \xi_{i,j,k+1/2}^x}^y + \frac{\overline{v_{i,j,k+1} \xi_{i+1/2,j,k}^x}^z + \overline{v_{i,j,k} \xi_{i-1/2,j,k}^x}^z}{2} \right\}.\end{aligned}\quad (26)$$

Finite-difference representation (26) ensures, in the case of two-dimensional divergence-free motion in (x, y) , (x, z) , (y, z) planes, the fulfillment of two quadratic conservation laws: kinetic energy and enstrophy (vorticity square), as well as antisymmetry property [9, 14].

Taking into account expression (24) and relations (26), we write down the equations for the components of the absolute vorticity – for ξ^x at $i, j + 1/2, k + 1/2$ point, for ξ^y at $i + 1/2, j + 1/2, k$ point, and for ξ^z at $i + 1/2, j + 1/2, k$ point (analogue of equation (13)):

$$\frac{d\xi^x}{dt} + \delta_y([v, \xi^x]) + \delta_z([w, \xi^x]) - \delta_y([u, \xi^y]) - \delta_z([u, \xi^z]) = g\delta_y \bar{\rho}^z, \quad (27.1)$$

$$\frac{d\xi^y}{dt} + \delta_x([u, \xi^y]) + \delta_z([w, \xi^y]) - \delta_x([v, \xi^x]) - \delta_z([v, \xi^z]) = -g\delta_x \bar{\rho}^z, \quad (27.2)$$

$$\frac{d\xi^z}{dt} + \delta_x([u, \xi^z]) + \delta_y([v, \xi^z]) - \delta_x([w, \xi^x]) - \delta_y([w, \xi^y]) = 0. \quad (27.3)$$

We are to analyze the system of equations (27.1)–(27.3) in terms of fulfillment of conservation laws.

Let us consider, for example, two-dimensional divergence-free motion in (x, z) plane. In this case, continuity equation (20) is transformed to the form

$$\delta_x u_{i,j,k} + \delta_z w_{i,j,k} = 0 \quad (28)$$

and provides the introduction of the flow function: $u_{i+1/2,k} = \delta_z \Psi_{i+1/2,k}^y$, $w_{i,k+1/2} = \delta_x \Psi_{i,k+1/2}^y$.

From the continuity equation (28), it follows that

$$\xi_{i+1/2,k+1/2}^y = \delta_z^2 \Psi_{i+1/2,k+1/2}^y + \delta_x^2 \Psi_{i+1/2,k+1/2}^y.$$

The vorticity equation is simplified and transformed [9] to the form

$$\frac{d\xi_{i+1/2,k+1/2}^y}{dt} + \frac{1}{3} \sum_{s=1}^3 J_s(\Psi_{i+1/2,k+1/2}^y, \xi_{i+1/2,k+1/2}^y) = 0, \quad (29)$$

where $J_1 = \delta_x (\overline{\Psi_{i+1/2,k+1/2}^y})^x \delta_y (\overline{\xi_{i+1/2,k+1/2}^y})^y - \delta_y (\overline{\Psi_{i+1/2,k+1/2}^y})^y \delta_x (\overline{\xi_{i+1/2,k+1/2}^y})^x$,

$$J_2 = \delta_x \left(\overline{\Psi_{i+1/2,k+1/2}^y} \delta_y (\overline{\xi_{i+1/2,k+1/2}^y})^x \right) - \delta_y \left(\overline{\Psi_{i+1/2,k+1/2}^y} \delta_x (\overline{\xi_{i+1/2,k+1/2}^y})^x \right), \quad (30)$$

$$J_3 = \delta_y \left(\overline{\xi_{i+1/2,k+1/2}^y} \delta_x (\overline{\Psi_{i+1/2,k+1/2}^y})^x \right) - \delta_x \left(\overline{\xi_{i+1/2,k+1/2}^y} \delta_y (\overline{\Psi_{i+1/2,k+1/2}^y})^x \right).$$

Expression (30) means that equation (29) has two quadratic invariants:

$$\frac{d}{dt} \sum_{i,k} \xi_{i+1/2,k+1/2}^y h_x h_z^k = 0, \quad \frac{d}{dt} \sum_{i,k} \left(\frac{(\delta_x \Psi_{i+1/2,k+1/2}^y)^2 + (\delta_z \Psi_{i+1/2,k+1/2}^y)^2}{2} \right) h_x h_z^k = 0, \quad (31)$$

$$\frac{d}{dt} \sum_{i,k} (\xi_{i+1/2,k+1/2}^y)^2 h_x h_z^k = 0.$$

Approximation of nonlinear terms in equation (29) provides the antisymmetry property:

$$J(\Psi_{i+1/2,k+1/2}^y, \xi_{i+1/2,k+1/2}^y) = -J(\xi_{i+1/2,k+1/2}^y, \Psi_{i+1/2,k+1/2}^y). \quad (32)$$

A similar situation occurs for the motion in (y, z) and (x, y) planes:

$$\frac{d}{dt} \sum_{j,k} \xi_{j+1/2,k+1/2}^x h_y h_z^k = \frac{d}{dt} \sum_{j,k} \left(\frac{(\delta_y \Psi_{j+1/2,k+1/2}^x)^2 + (\delta_z \Psi_{j+1/2,k+1/2}^x)^2}{2} \right) h_y h_z^k = \quad (33)$$

$$= \frac{d}{dt} \sum_{j,k} (\xi_{j+1/2,k+1/2}^x)^2 h_y h_z^k = 0,$$

$$J(\Psi_{j+1/2,k+1/2}^x, \xi_{j+1/2,k+1/2}^x) = -J(\xi_{j+1/2,k+1/2}^x, \Psi_{j+1/2,k+1/2}^x),$$

$$\frac{d}{dt} \sum_{i,j} \xi_{i+1/2,j+1/2}^z h_x h_y = \frac{d}{dt} \sum_{i,j} \left(\frac{(\delta_x \Psi_{i+1/2,j+1/2}^z)^2 + (\delta_y \Psi_{i+1/2,j+1/2}^z)^2}{2} \right) h_x h_y = \quad (34)$$

$$= \frac{d}{dt} \sum_{i,j} (\xi_{i+1/2,j+1/2}^z)^2 h_x h_y = 0,$$

$$J(\Psi_{i+1/2,j+1/2}^z, \xi_{i+1/2,j+1/2}^z) = -J(\xi_{i+1/2,j+1/2}^z, \Psi_{i+1/2,j+1/2}^z).$$

Along with the feature of total energy conservation [5], relations (31)–(34) ensure the presence of two quadratic discrete invariants in the system of equations (1)–(5) with boundary (8)–(9) and initial (10) conditions.

Discrete equation of potential vorticity of a stratified incompressible fluid

We consider the properties of system (27.1)–(27.3) in the case of three-dimensional motion. We write this system in the following form:

$$\frac{d\overline{\xi_{i+1/2, j+1/2, k+1/2}^x}}{dt} + \overline{\Upsilon_{i+1/2, j+1/2, k+1/2}^x} = g\delta_y(\overline{\rho_{i+1/2, j+1/2, k+1/2}^{xz}}), \quad (35.1)$$

$$\frac{d\overline{\xi_{i+1/2, j+1/2, k+1/2}^y}}{dt} + \overline{\Upsilon_{i+1/2, j+1/2, k+1/2}^y} = -g\delta_x(\overline{\rho_{i+1/2, j+1/2, k+1/2}^{yz}}), \quad (35.2)$$

$$\frac{d\overline{\xi_{i+1/2, j+1/2, k+1/2}^z}}{dt} + \overline{\Upsilon_{i+1/2, j+1/2, k+1/2}^z} = 0, \quad (35.3)$$

where

$$\begin{aligned} \Upsilon_{i, j+1/2, k+1/2}^x &= \delta_y([v, \xi^x])_{i, j+1/2, k} + \delta_z([w, \xi^x])_{i, j+1/2, k} - \\ &- \delta_y([u, \xi^y])_{i, j+1/2, k} - \delta_z([u, \xi^z])_{i, j+1/2, k}, \\ \Upsilon_{i+1/2, j, k+1/2}^y &= \delta_x([u, \xi^y])_{i+1/2, j, k+1/2} + \delta_z([w, \xi^y])_{i+1/2, j, k+1/2} - \\ &- \delta_x([v, \xi^x])_{i+1/2, j, k+1/2} - \delta_z([v, \xi^z])_{i+1/2, j, k+1/2}, \\ \Upsilon_{i+1/2, j+1/2, k}^z &= \delta_x([u, \xi^z])_{i+1/2, j+1/2, k} + \delta_y([v, \xi^z])_{i+1/2, j+1/2, k} - \\ &- \delta_x([w, \xi^x])_{i+1/2, j+1/2, k} - \delta_y([w, \xi^y])_{i+1/2, j+1/2, k}. \end{aligned} \quad (36)$$

It is easy to verify that according to relation (25), equations (27.1)–(27.3) at point $i + 1/2, j + 1/2, k + 1/2$ and definition (36) we obtain

$$\delta_x(\Upsilon_{i+1/2, j+1/2, k+1/2}^x) + \delta_y(\Upsilon_{i+1/2, j+1/2, k+1/2}^y) + \delta_z(\Upsilon_{i+1/2, j+1/2, k+1/2}^z) = 0. \quad (37)$$

Note that equality (37) is satisfied because density linearly depends on temperature and salinity. We assume that from equations (21)–(23) follows a discrete equation for density, which has the following form:

$$\frac{d\rho_{i, j, k}}{dt} + \delta_x(u_{i, j, k}\rho_{i, j, k}) + \delta_y(v_{i, j, k}\rho_{i, j, k}) + \delta_z(w_{i, j, k}\rho_{i, j, k}) = 0. \quad (38)$$

We write equation (38) at the points $(i, j + 1/2, k + 1/2)$, $(i + 1/2, j, k + 1/2)$, $(i + 1/2, j + 1/2, k)$, respectively:

$$\frac{d\overline{\rho_{i, j+1/2, k+1/2}}}{dt} + \delta_x(\overline{u_{i, j+1/2, k+1/2}\rho_{i, j+1/2, k+1/2}}) + \delta_y(\overline{v_{i, j+1/2, k+1/2}\rho_{i, j+1/2, k+1/2}}) + \quad (39.1)$$

$$+ \delta_z(\overline{w_{i, j+1/2, k+1/2}\rho_{i, j+1/2, k+1/2}}) = 0,$$

$$\frac{d\overline{\rho_{i+1/2, j, k+1/2}}}{dt} + \delta_x(\overline{u_{i+1/2, j, k+1/2}\rho_{i+1/2, j, k+1/2}}) + \delta_y(\overline{v_{i+1/2, j, k+1/2}\rho_{i+1/2, j, k+1/2}}) + \quad (39.2)$$

$$+ \delta_z(\overline{w_{i+1/2, j, k+1/2}\rho_{i+1/2, j, k+1/2}}) = 0,$$

$$\frac{d\overline{\rho_{i+1/2, j+1/2, k}}}{dt} + \delta_x(\overline{u_{i+1/2, j+1/2, k}\rho_{i+1/2, j+1/2, k}}) + \delta_y(\overline{v_{i+1/2, j+1/2, k}\rho_{i+1/2, j+1/2, k}}) + \quad (39.3)$$

$$+ \delta_z(\overline{w_{i+1/2, j+1/2, k}\rho_{i+1/2, j+1/2, k}}) = 0.$$

We differentiate equation (39.1) in the finite-difference sense with respect to x , (39.2) with respect to y and (39.3) – to z . As a result, we get

$$\frac{d\delta_x(\bar{\rho}_{i+1/2,j+1/2,k+1/2}^{-yz})}{dt} + \delta_x(R_{i+1/2,j+1/2,k+1/2}^x) = 0, \quad (40.1)$$

$$\frac{d\delta_y(\bar{\rho}_{i+1/2,j+1/2,k+1/2}^{-xz})}{dt} + \delta_y(R_{i+1/2,j+1/2,k+1/2}^y) = 0, \quad (40.2)$$

$$\frac{d\delta_z(\bar{\rho}_{i+1/2,j+1/2,k+1/2}^{-xy})}{dt} + \delta_z(R_{i+1/2,j+1/2,k+1/2}^z) = 0, \quad (40.3)$$

where the notations $R_{i,j+1/2,k+1/2}^x, R_{i+1/2,j,k+1/2}^y, R_{i+1/2,j+1/2,k}^z$ are obvious.

Let us mention the properties of the introduced functions in equations (39.1)–(39.3) and (40.1)–(40.3). They have the following form:

$$\begin{aligned} \overline{\bar{\rho}_{i,j+1/2,k+1/2}^{-yz}}^x &= \overline{\bar{\rho}_{i+1/2,j,k+1/2}^{-xz}}^y = \overline{\bar{\rho}_{i+1/2,j+1/2,k}^{-xy}}^z = \overline{\bar{\rho}_{i+1/2,j+1/2,k+1/2}^{-xyz}}, \\ \overline{R_{i,j+1/2,k+1/2}^x}^x &= \overline{R_{i+1/2,j,k+1/2}^y}^y = \overline{R_{i+1/2,j+1/2,k}^z}^z = \overline{\delta_x(u_{i+1/2,j+1/2,k+1/2} \bar{\rho}_{i+1/2,j+1/2,k+1/2})}^{-xyz} + \\ &+ \overline{\delta_y(v_{i+1/2,j+1/2,k+1/2} \bar{\rho}_{i+1/2,j+1/2,k+1/2})}^{-xyz} + \overline{\delta_z(w_{i+1/2,j+1/2,k+1/2} \bar{\rho}_{i+1/2,j+1/2,k+1/2})}^{-xyz}. \end{aligned} \quad (41)$$

We assume that the difference analogue of PV is defined at point $i + 1/2, j + 1/2, k + 1/2$ and is written down as follows: $\varpi_{i+1/2,j+1/2,k+1/2} =$

$$\begin{aligned} &= \overline{\xi_{i+1/2,j+1/2,k+1/2}^x}^x \delta_x(\bar{\rho}_{i+1/2,j+1/2,k+1/2}^{-yz}) + \overline{\xi_{i+1/2,j+1/2,k+1/2}^y}^y \delta_y(\bar{\rho}_{i+1/2,j+1/2,k+1/2}^{-xz}) + \\ &+ \overline{\xi_{i+1/2,j+1/2,k+1/2}^z}^z \delta_z(\bar{\rho}_{i+1/2,j+1/2,k+1/2}^{-xy}). \end{aligned} \quad (42)$$

Determination of potential vorticity of a three-dimensional stratified fluid (42) at the box vertices is determined by the fulfillment of discrete equation (25).

To obtain a difference analogue of Ertel's theorem (15), we multiply equations (35.1)–(35.3) by $\delta_x(\bar{\rho}_{i+1/2,j+1/2,k+1/2}^{-yz})$, $\delta_y(\bar{\rho}_{i+1/2,j+1/2,k+1/2}^{-xz})$, $\delta_z(\bar{\rho}_{i+1/2,j+1/2,k+1/2}^{-xy})$, and the system (40.1)–(40.3) – by $\overline{\xi_{i+1/2,j+1/2,k+1/2}^x}^x, \overline{\xi_{i+1/2,j+1/2,k+1/2}^y}^y, \overline{\xi_{i+1/2,j+1/2,k+1/2}^z}^z$, respectively. As a result, at point $i + 1/2, j + 1/2, k + 1/2$ we get

$$\frac{d\omega}{dt} + \overline{\Upsilon^x}^x \delta_x(\bar{\rho}^{-yz}) + \overline{\Upsilon^y}^y \delta_y(\bar{\rho}^{-xz}) + \overline{\Upsilon^z}^z \delta_z(\bar{\rho}^{-xy}) + \overline{\xi^x}^x \delta_x R^x + \overline{\xi^y}^y \delta_y R^y + \overline{\xi^z}^z \delta_z R^z = 0.$$

Since ξ^x, ξ^y, ξ^z satisfy relation (25), $\Upsilon^x, \Upsilon^y, \Upsilon^z$ – relation (37), with regard to equalities (41), at point $i + 1/2, j + 1/2, k + 1/2$ we obtain finite-difference equation of potential vorticity (differential in time) of a stratified incompressible fluid in a divergent form:

$$\frac{d\omega}{dt} + \delta_x(\Upsilon^x \bar{\rho}^{-yz} + \xi^x R^x) + \delta_y(\Upsilon^y \bar{\rho}^{-xz} + \xi^y R^y) + \delta_z(\Upsilon^z \bar{\rho}^{-xy} + \xi^z R^z) = 0. \quad (43)$$

Note that formally there is no difficulty in obtaining equation (43) with temporal discretization. Due to additional indexing, difference equations become cumbersome and therefore difficult to read.

Strictly speaking, the form of nonlinear terms in equation (43) does not correspond to their differential analogue (15). The integral over domain from $\frac{d\omega}{dt}$ is equal to zero when the following relations are satisfied at the boundaries:

$$\begin{aligned} Y_{i,j+1/2,k+1/2}^x &= 0, \quad R_{i,j+1/2,k+1/2}^x = 0 \quad \text{at} \quad i = i_1, \quad i = i_N, \\ Y_{i+1/2,j,k+1/2}^y &= 0, \quad R_{i+1/2,j,k+1/2}^y = 0 \quad \text{at} \quad j = j_1, \quad j = j_M, \\ Y_{i+1/2,j+1/2,k}^z &= 0, \quad R_{i+1/2,j+1/2,k}^z = 0 \quad \text{at} \quad k = 1/2, \quad k = K_{i,j} + 1/2, \end{aligned} \quad (44)$$

From relations (44) it follows that additional boundary conditions, which are absent in the original formulation, are required.

Conclusion

A finite-difference analogue of absolute vorticity is written out for the system of equations of an ideal fluid without a quasi-static approximation. Projections of this equation onto two-dimensional subspaces (x, y) , (y, z) , (x, z) preserve energy, vorticity, enstrophy and have the antisymmetry property. To obtain the well-known Arakawa–Lamb scheme for the shallow water equations, it is necessary to write out an original difference system of equations for horizontal velocities that differs from (26).

The original result is the obtained discrete equation for potential vorticity of a stratified incompressible fluid as an exact consequence of the original finite-difference system of equations which have a divergent form. In this case, density satisfied the linear equation of state, the approximation of which in this case ensures both total energy conservation and the divergent form of equation for PV. If a nonlinear density dependence on temperature and salinity is applied, a special density approximation at the box edges is required to preserve total energy. In this case, an additional term occurs in the discrete potential vorticity equation; it has no analogue in the differential problem. Another problem arises from the form of advective terms in the PV equation, which are fundamentally different from their differential counterparts. In order for the potential vorticity to be conserved, we require additional boundary conditions under which the PV discrete analogue is an invariant.

REFERENCES

1. Rossby, C.-G., 1940. Planetary Flow Patterns in the Atmosphere. *Quarterly Journal of the Royal Meteorological Society*, 66(S1), pp. 68–87. <https://doi.org/10.1002/j.1477-870X.1940.tb00130.x>
2. Ertel, H., 1942. Ein Neuer Hydrodynamischer Wirbelsatz. *Meteorologische Zeitschrift*, 59(9), pp. 277–281. <https://doi.org/10.1127/0941-2948/2004/0013-0451> (in German).
3. Hoskins, B.J., McIntyre, M.E. and Robertson, A.W., 1985. On the Use and Significance of Isentropic Potential Vorticity Maps. *Quarterly Journal of the Royal Meteorological Society*, 111(470), pp. 877–946. <https://doi.org/10.1002/qj.49711147002>
4. Zhmur, V.V., Novoselova, E.V. and Belonenko, T.V., 2021. Potential Vorticity in the Ocean: Ertel and Rossby Approaches with Estimates for the Lofoten Vortex. *Izvestiya, Atmospheric and Oceanic Physics*, 57(6), pp. 632–641. <https://doi.org/10.1134/S0001433821050157>
5. Kapsov, E.I., 2019. Numerical Implementation of an Invariant Scheme for One-Dimensional Shallow Water Equations in Lagrangian Coordinates. *Keldysh Institute Preprints*, (108), pp. 1–28. <https://doi.org/10.20948/prepr-2019-108> (in Russian).
6. Bihlo, A. and Popovych, R.O., 2012. Invariant Discretization Schemes for the Shallow-Water Equations. *SIAM Journal on Scientific Computing*, 34(6), pp. B810–B839. <https://doi.org/10.1137/120861187>

7. Charnyi, S., Heister, T., Olshanskii, M.A. and Rebholz, L.G., 2019. Efficient Discretizations for the EMAC Formulation of the Incompressible Navier–Stokes Equations. *Applied Numerical Mathematics*, 141, pp. 220-233. <https://doi.org/10.1016/j.apnum.2018.11.013>
8. Sorgentone, C., La Cognata, C. and Nordström, J., 2015. A New High Order Energy and Enstrophy Conserving Arakawa-Like Jacobian Differential Operator. *Journal of Computational Physics*, 301, pp. 167-177. <https://doi.org/10.1016/j.jcp.2015.08.028>
9. Arakawa, A. and Lamb, V.R., 1981. A Potential Enstrophy and Energy Conserving Scheme for the Shallow Water Equations. *Monthly Weather Review*, 109(1), pp. 18-36. [https://doi.org/10.1175/1520-0493\(1981\)109<0018:APEAEC>2.0.CO;2](https://doi.org/10.1175/1520-0493(1981)109<0018:APEAEC>2.0.CO;2)
10. Salmon, R., 2005. A General Method for Conserving Quantities Related to Potential Vorticity in Numerical Models. *Nonlinearity*, 18(5), pp. R1-R16. <https://doi.org/10.1088/0951-7715/18/5/R01>
11. Sugibuchi, Y., Matsuo, T. and Sato, S., 2018. Constructing Invariant-Preserving Numerical Schemes Based on Poisson and Nambu Brackets. *JSIAM Letters*, 10, pp. 53-56. <https://doi.org/10.14495/jsiaml.10.53>
12. Arakawa, A., 1966. Computational Design for Long-Term Numerical Integration of the Equations of Fluid Motion: Two-Dimensional Incompressible Flow. Part I. *Journal of Computational Physics*, 1(1), pp. 119-143. [https://doi.org/10.1016/0021-9991\(66\)90015-5](https://doi.org/10.1016/0021-9991(66)90015-5)
13. Demyshev, S.G., 2004. Energy of the Black Sea Climatic Circulation. Part I: Discrete Equations of the Rate of Change of Kinetic and Potential Energy. *Meteorologiya i Gidrologiya*, (9), pp. 65-80 (in Russian).
14. Demyshev, S.G., 2005. Numerical Experiments Aimed at the Comparison of Two Finite-Difference Schemes for the Equations of Motion in a Discrete Model of Hydrodynamics of the Black Sea. *Physical Oceanography*, 15(5), pp. 299-310. <https://doi.org/10.1007/s11110-006-0004-2>
15. Demyshev, S.G., 2023. Nonlinear Invariants of a Discrete System of the Sea Dynamics Equations in a Quasi-Static Approximation. *Physical Oceanography*, 30(5), pp. 523-548.

Submitted 09.06.2023; approved after review 25.07.2023;
accepted for publication 18.01.2024.

About the author:


Sergey G. Demyshev, Head of Wave Theory Department, Chief Research Associate, Marine Hydrophysical Institute of RAS (2 Kapitanskaya Str., Sevastopol, 299011, Russian Federation), DSc (Phys.-Math.), **Scopus Author ID: 6603919865**, **ResearcherID: C-1729-2016**, **ORCID ID: 0000-0002-5405-2282**, demyshev@gmail.com

The author has read and approved the final manuscript.

The author declares that he has no conflict of interest.

Generation of Vertical Fine Structure by Internal Waves on a Shear Flow

A. A. Slepyshev , N. O. Ankudinov

Marine Hydrophysical Institute of RAS, Sevastopol, Russian Federation
 *slep55@mail.ru*

Abstract

Purpose. The work is purposed at studying the wave mechanism of fine structure generation, as well as determining the vertical wave fluxes of mass.

Methods and Results. In contrast to the previously used mechanism of forming a fine structure by internal waves due to breaking, a new approach based on determining the vertical wave fluxes of mass in the field of an inertia-gravity internal wave without breaking is proposed. The inertia-gravity internal waves on the Black Sea northwestern shelf are considered on a flow with a vertical velocity shift. The flow is assumed to be geostrophically balanced with the vertical velocity shifts compensated by a horizontal density gradient. The *f*-plane approximation is used. Thus, the classical scheme for describing a wave field by the hydrodynamic equations is applicable with regard to the nonlinear effects. A weakly nonlinear approach is used. In the linear approximation, the eigenfunction and the dispersion relation are found by solving numerically the boundary value problem which determines the vertical structure of a mode in the presence of an average flow. In this case, the wave frequency is of a complex character since the coefficients in the differential equation of the specified boundary value problem are complex. Depending on the wave period and the mode number, either weak attenuation of a wave or its weak amplification is possible. The eigenfunction of internal waves is also complex. Therefore, the vertical wave fluxes of mass and the vertical component of the Stokes drift velocity are nonzero and lead to the generation of vertical fine structure which is irreversible.

Conclusions. In the presence of a two-dimensional shear flow, taking into account the horizontal inhomogeneity of the average density field enhances the effect of generation of a vertical fine structure by the inertia-gravity internal waves. The vertical wave fluxes of mass also increase. The indicated fluxes and generated fine structure for the waves of different frequencies are close and the effect is enhanced in the presence of the waves of different frequencies.

Keywords: internal waves, fine structure, Stokes drift

Acknowledgments: The study was carried out within the framework of the theme of state assignment FNNN-2021-0004.

For citation: Slepyshev, A.A. and Ankudinov, N.O., 2024. Generation of Vertical Fine Structure by Internal Waves on a Shear Flow. *Physical Oceanography*, 31(2), pp. 161-177.

© 2024, A. A. Slepyshev, N. O. Ankudinov

© 2024, Physical Oceanography

Introduction

Fine structure of a liquid medium is a very interesting object studied both theoretically and experimentally under laboratory conditions. Structures amenable to detailed experimental study and theoretical analysis [1, 2] arise when solids move in a liquid. No less interesting structures [3] appear when a liquid drop falls onto a liquid. Such structures can explain the processes in the sea surface layer during precipitation.

The fine structure of hydrophysical fields was discovered almost half a century ago owing to the creation of high-resolution sounding equipment. Indeed, no one had



imagined before its discovery that temperature and salinity vertical profiles on small spatial scales were very variable. This variability was initially thought ¹ [4] to be due to small-scale turbulence, also not fully understood object. But then it turned out that not only turbulence was responsible for the fine structure generation as the kinematic effect of internal waves also gave a fine structure in measurements [5, 6]. However, this was not a long-lived structure since the kinematic effect disappeared after the wave train passage.

Double diffusion provided a mechanism for vertical stratification of temperature and salinity profiles in the ocean ² [7–10]. The formation of convective cells in the form of salt fingers [11–14] is possible if temperature and salinity decrease with depth. They differ markedly from the surrounding liquid layers in terms of characteristic gradients, i.e. a structure appears with alternating thin stratified layers and quasi-homogeneous ones. This is actually the fine structure. Such conditions are very typical for the World Ocean and approximately 70% of its column is subject to such stratification ². Double diffusion takes place when temperature and salinity increase with depth [15, 16]. Geothermal heat sources at the bottom contribute to this process. Double diffusion can lead to the formation of step structures which have been repeatedly observed in field experiments [17, 18]. Intrusive layering with mutual penetration of waters with different T, S-characteristics [19–21] is possible in the area of fronts. Intrusions are possible due to internal wave breaking at the shelf edge in the continental slope area [22].

It should be noted that such conditions are not always realized and this phenomenon is more exotic than widespread in inland seas far from fronts. The fine structure still exists and can be explained by other mechanisms which, of course, also work in the open ocean. The internal waves breaking and hydrodynamic instability of flows is the mechanism that has been proposed to explain the fine structure formation [23–26]. However, it turned out that internal waves do not necessarily have to break in order to generate a fine structure. The wave field is intermittent, and internal waves often propagate as wave trains [27]. Due to nonlinearity, trains of internal waves produce small corrections to the flow density and velocity [28] with a horizontal scale equal to the train envelope scale, and the vertical scale is determined by relation c_g / N , where c_g is group velocity of train and N is Brunt–Väisälä frequency. However, these corrections are proportional to the square of the current wave amplitude and disappear after the wave train passage.

The waves attenuate and form boundary layers in the vicinity of the boundaries [29, 30] in a dissipative medium when viscosity and diffusion are taken into account. A beam of three-dimensional internal waves is reflected from the layer where wave and buoyancy frequencies coincide and the reflection occurs with energy losses [31] which can amount to several percentage points. Internal

¹ Gibson, C.H., 1980. Fossil Temperature, Salinity, and Vorticity Turbulence in the Ocean. In: J. C. J. Nihoul, ed., 1980. *Marine Turbulence*. Amsterdam: Elsevier Publishing Co., pp. 221-257. [https://doi.org/10.1016/S0422-9894\(08\)71223-6](https://doi.org/10.1016/S0422-9894(08)71223-6)

² Fedorov, K.N., 1978. *The Thermohaline Finestructure of the Ocean*. Oxford; New York: Pergamon Press, 170 p.

boundary layers are formed at discontinuities in the buoyancy frequency or its derivatives in the beam of internal waves with a reflected beam also present [31]. Boundary layers have split density and velocity scales. These boundary flows generate fine structure of the periodic flow.

Internal waves attenuate [32, 33] when turbulent viscosity and diffusion are taken into account. Vertical wave fluxes of heat, salt and momentum are nonzero and lead to the formation of an already irreversible fine structure [34–38]. However, not only consideration of turbulent viscosity and diffusion leads to the vertical fine structure generation. When taking into account the Earth rotation and inhomogeneous average flows, vertical wave fluxes of heat, salt and mass are nonzero even when turbulent viscosity and diffusion are not taken into account and result in formation of a vertical fine structure [39]. Vertical wave momentum fluxes are also nonzero [40–44]. However, the horizontal average density gradient which is always present in a geostrophically balanced flow was not considered in [39]. It was assumed that the horizontal scale of wave is much smaller than the scale of the average density field inhomogeneity. We take into account the horizontal gradient of average density and perform a comparison with the results for a homogeneous case in the present work. In [39], the boundary value problem for the vertical velocity amplitude is solved by the perturbation method with the introduction of small parameter $\varepsilon = V_0 / (H \cdot \omega)$, where V_0 is characteristic flow velocity, H is depth and ω is wave frequency. However, this parameter is not always small and in this work the boundary value problem for the amplitude of internal wave vertical velocity is solved numerically using the implicit Adams scheme of the third order accuracy [40, 42].

Problem statement

Free internal waves are considered in the Boussinesq approximation with regard to the Earth rotation and the average two-dimensional vertically inhomogeneous flow in a horizontal infinite basin of constant depth [34–44]. The f -plane approximation is used. Horizontal gradients of average density are found from geostrophic relations³ and expressed through vertical shifts of flow velocity components, as in [45]. The system of hydrodynamic equations for wave disturbances in the Boussinesq approximation is as follows:

$$\frac{D\mathbf{u}}{Dt} + 2[\boldsymbol{\Omega}_\perp \times \mathbf{u}] + u_3 \frac{d\mathbf{U}^0}{dx_3} = -\frac{1}{\rho_0} \nabla P + \mathbf{g} \frac{\rho}{\rho_0}, \quad (1)$$

$$\frac{D\rho}{Dt} + (\mathbf{u} \nabla) \rho_0 = 0, \quad (2)$$

$$\text{div} \mathbf{u} = 0, \quad (3)$$

³ Kamenkovich, V.M., 1977. *Fundamentals of Ocean Dynamics*. Amsterdam; New York: Elsevier Scientific Pub. Co., 249 p.

where $\mathbf{u}(u_1, u_2, u_3)$ is vector of flow velocity wave disturbances; ρ , P are density and pressure wave disturbances; ρ_0 is unperturbed average density; x_3 axis is directed opposite to the gravitational acceleration vector \mathbf{g} ; $\mathbf{\Omega}_\perp$ is vector of projection of the Earth rotation angular velocity onto the axis x_3 ; $\mathbf{U}^0(U_1^0(x_3), U_2^0(x_3), 0)$ is vector of average flow velocity; operator $\frac{D}{Dt}$ has form $\frac{D}{Dt} = \frac{\partial}{\partial t} + (\mathbf{u} + \mathbf{U}^0)\nabla$.

From the “thermal wind” relations ³ [45], the components of average density horizontal gradient are expressed through vertical shifts in the flow velocity as follows:

$$\frac{\partial \rho_0}{\partial x_1} = -\frac{\bar{\rho}_0 f}{g} \frac{dU_2^0}{dx_3}, \quad (4)$$

$$\frac{\partial \rho_0}{\partial x_2} = \frac{\bar{\rho}_0 f}{g} \frac{dU_1^0}{dx_3}, \quad (5)$$

where $f = 2(\mathbf{\Omega}_\perp \mathbf{e}_3) = 2\Omega_E \sin \varphi$ is Coriolis parameter, \mathbf{e}_3 is unit vector of x_3 axis, Ω_E is angular velocity of the Earth rotation, φ is latitude.

After substituting relations (4), (5) into equation (2), the latter becomes as follows:

$$\frac{D\rho}{Dt} - u_1 \frac{\bar{\rho}_0 f}{g} \frac{dU_2^0}{dx_3} + u_2 \frac{\bar{\rho}_0 f}{g} \frac{dU_1^0}{dx_3} + u_3 \frac{\partial \rho_0}{\partial x_3} = 0. \quad (6)$$

The boundary condition on the sea surface is the “rigid lid” condition which filters internal waves from surface ones and on the bottom – the impermeability condition ⁴:

$$u_3 = 0 \quad \text{at } x_3 = 0, \quad (7)$$

$$u_3 = 0 \quad \text{at } x_3 = -H, \quad (8)$$

where H is sea depth.

Linear approximation. We look for solutions to equations (1), (3), (6) in a linear approximation under the condition of horizontal homogeneity of Brunt–Väisälä frequency on the wave scale in the following form [34–45]:

$$u_i = u_{i0}(x_3)Ae^{i\theta} + \text{c.c.}, \quad i = 1, 2, 3, \quad (9)$$

$$P = P_1(x_3)Ae^{i\theta} + \text{c.c.}, \quad \rho = \rho_1(x_3)Ae^{i\theta} + \text{c.c.}, \quad (10)$$

⁴ Miropolsky, Yu.Z., 1981. *Dynamics of Internal Gravitational Waves in the Ocean*. Leningrad: Gidrometeoizdat, 302 p. (in Russian).

where c.c. are complex-conjugate terms; A is amplitude multiplier; $\theta = kx_1 - \omega t$ is wave phase, k is horizontal wavenumber, ω is wave frequency. We assume that the wave propagates along x_1 axis.

Expressions for amplitude functions u_{10} , u_{20} , ρ_1 , P_1 through u_{30} follow from system (1), (3), (6):

$$u_{10} = \frac{i}{k} \frac{du_{30}}{dx_3}, \quad \Omega = \omega - k \cdot U_1^0, \quad (11)$$

$$\frac{P_1}{\bar{\rho}_0} = \frac{i}{k} \left[\frac{\Omega}{k} \frac{du_{30}}{dx_3} + \frac{dU_1^0}{dx_3} u_{30} + \frac{f}{\Omega} \left(i \frac{dU_2^0}{dx_3} u_{30} - \frac{f}{k} \frac{d}{dx_3} u_{30} \right) \right],$$

$$u_{20} = \frac{1}{\Omega} \left(\frac{f}{k} \frac{du_{30}}{dx_3} - i u_{30} \frac{dU_2^0}{dx_3} \right). \quad (12)$$

$$\rho_1 = \frac{i}{\Omega} \left[\frac{i}{k} \frac{\bar{\rho}_0 f}{g} \frac{dU_2^0}{dx_3} \frac{du_{30}}{dx_3} - u_{30} \frac{d\rho_0}{dx_3} - \frac{\bar{\rho}_0 f}{g\Omega} \frac{dU_1^0}{dx_3} \left(\frac{f}{k} \frac{du_{30}}{dx_3} - i u_{30} \frac{dU_2^0}{dx_3} \right) \right], \quad (13)$$

where $\Omega = \omega - k \cdot U_0$ is frequency with Doppler shift.

The amplitude function of the vertical velocity component u_{30} satisfies the equation

$$\frac{d^2 u_{30}}{dx_3^2} + k \left[\frac{2if \frac{dU_2^0}{dx_3}}{\Omega^2 - f^2} - \frac{2f^2 \frac{dU_1^0}{dx_3}}{\Omega(\Omega^2 - f^2)} \right] \frac{du_{30}}{dx_3} +$$

$$+ k u_{30} \left[\frac{k(N^2 - \Omega^2) + \Omega \frac{d^2 U_1^0}{dx_3^2} + if \frac{d^2 U_2^0}{dx_3^2}}{\Omega^2 - f^2} + \frac{2ifk \frac{dU_1^0}{dx_3} \frac{dU_2^0}{dx_3}}{\Omega(\Omega^2 - f^2)} \right] = 0, \quad (14)$$

where $N^2 = -\frac{g}{\bar{\rho}_0} \frac{d\rho_0}{dx_3}$ is squared Brunt–Väisälä frequency.

Boundary conditions for u_{30} are as follows:

$$u_{30}(0) = u_{30}(-H) = 0. \quad (15)$$

Equation (14) has complex coefficients, therefore, generally speaking, its solution is a complex function and boundary value problem (14)–(15) must also have complex values of natural frequencies ω at a fixed wave number [34–43]. Indeed, subsequent calculations reveal that the wave frequency has a small imaginary part. Boundary value problem (14)–(15) was solved analytically in [46, 47] without taking into account the Earth rotation at $f = 0$ on a flow with a constant vertical velocity

PHYSICAL OCEANOGRAPHY VOL. 31 ISS. 2 (2024) 165

gradient at constant Brunt–Väisälä frequency. A solution is obtained in the form of imaginary order modified Bessel functions. The dispersion equation was solved using both asymptotic and numerical methods. It is shown that the flow leads to a noticeable anisotropy of the dispersion curves; in particular, frequency isolines in the plane of horizontal wave numbers can open up. Equation (14) has real coefficients at $f = 0$, so the wave frequency and the eigenfunction of internal waves are real when the Richardson number is larger than $1/4$ [46, 47].

Nonlinear effects. The flow velocities in the Euler \mathbf{u} and Lagrange \mathbf{u}_L representations are related by relation ⁵ [36, 43] up to second-order terms in wave steepness

$$\mathbf{u}_L = \mathbf{u} + \left(\int_0^t \mathbf{u}_L d\tau \nabla \right) \mathbf{u}. \quad (16)$$

Solving this equation by iteration method up to terms quadratic in the wave amplitude, we obtain an expression for the average Lagrangian velocity after averaging over the wave period

$$\overline{\mathbf{u}_L} = \mathbf{U} + \overline{\left(\int_0^t \mathbf{u} d\tau \nabla \right) \mathbf{u}}, \quad (17)$$

where vector $\mathbf{U}(U_0, V_0)$ is average flow velocity; \mathbf{u} is field of wave Euler velocities; the overbar means averaging over the wave period. The second term in (17) is the Stokes drift velocity which is determined by the following formula [34, 36, 38, 39, 41–43, 48]:

$$\mathbf{u}_S = \overline{\left(\int_0^t \mathbf{u} d\tau \nabla \right) \mathbf{u}}. \quad (18)$$

Vertical component of the Stokes drift velocity is nonzero for the complex frequency [39, 42]:

$$u_{3S} = iA_1 A_1^* \left(\frac{1}{\omega} - \frac{1}{\omega^*} \right) \frac{d}{dx_3} (u_{30} u_{30}^*), \quad (19)$$

where $A_1 = A \exp(\delta\omega \cdot t)$, $\delta\omega = \text{Im}(\omega)$ is wave frequency imaginary part. Two horizontal components of the Stokes drift velocity are determined by the following formulas:

$$u_{1S} = \frac{A_1 A_1^*}{k} \left[\frac{1}{\omega} \frac{d}{dx_3} \left(u_{30} \frac{du_{30}^*}{dx_3} \right) + \text{c.c.} \right], \quad (20)$$

⁵ Dvoryaninov, G.S., 1982. *Effects of Waves in the Boundary Layers of the Atmosphere and Ocean*. Kiev: Naukova Dumka, 176 p. (in Russian).

$$u_{2s} = A_1 A_1^* \left[\frac{1}{\omega \Omega^* k} \frac{du_{30}}{dx_3} \left(i f \frac{du_{30}^*}{dx_3} - k \frac{dU_2^0}{dx_3} u_{30}^* \right) + \text{c.c.} \right] -$$

$$- A_1 A_1^* \left\{ \frac{u_{30}^*}{\omega^* \Omega^2} \left[\Omega \left(\frac{du_{30}}{dx_3} \frac{dU_2^0}{dx_3} + \frac{i f}{k} \frac{d^2 u_{30}}{dx_3^2} + u_{30} \frac{d^2 U_2^0}{dx_3^2} \right) + k \frac{dU_1^0}{dx_3} \left(u_{30} \frac{dU_2^0}{dx_3} + \frac{i f}{k} \frac{du_{30}}{dx_3} \right) \right] \right\} + \text{c.c.} \quad (21)$$

We find the vertical wave mass flux taking into account formulas (10), (13) [37, 39]:

$$\overline{\rho u_3} = |A_1|^2 \left\{ \frac{i}{\Omega} \left[\frac{i}{k} \frac{\bar{\rho}_0 f}{g} \frac{dU_2^0}{dx_3} \frac{du_{30}}{dx_3} - u_{30} \frac{d\rho_0}{dx_3} - \frac{\bar{\rho}_0 f}{g \Omega} \frac{dU_1^0}{dx_3} \left(\frac{f}{k} \frac{du_{30}}{dx_3} - i u_{30} \frac{dU_2^0}{dx_3} \right) \right] u_{30}^* + \text{c.c.} \right\}. \quad (22)$$

The equation for a correction to average wave density $\bar{\rho}$ that does not oscillate on a time scale, accurate to terms quadratic in the wave amplitude, has the form:

$$\frac{\partial \bar{\rho}}{\partial t} + U_1^0 \frac{\partial \bar{\rho}}{\partial x_1} + U_2^0 \frac{\partial \bar{\rho}}{\partial x_2} + \frac{\partial \overline{\rho u_1}}{\partial x_1} + \frac{\partial \overline{\rho u_2}}{\partial x_2} + \frac{\partial \overline{\rho u_3}}{\partial x_3} + u_{1s} \frac{\partial \rho_0}{\partial x_1} + u_{2s} \frac{\partial \rho_0}{\partial x_2} + u_{3s} \frac{\partial \rho_0}{\partial x_3} = 0. \quad (23)$$

Considering relations (4), (5), equation (23) is transformed to the form:

$$\frac{\partial \bar{\rho}}{\partial t} + U_1^0 \frac{\partial \bar{\rho}}{\partial x_1} + U_2^0 \frac{\partial \bar{\rho}}{\partial x_2} + \frac{\partial \overline{\rho u_1}}{\partial x_1} + \frac{\partial \overline{\rho u_2}}{\partial x_2} + \frac{\partial \overline{\rho u_3}}{\partial x_3} - u_{1s} \frac{\bar{\rho}_0 f}{g} \frac{dU_2^0}{dx_3} + u_{2s} \frac{\bar{\rho}_0 f}{g} \frac{dU_1^0}{dx_3} + u_{3s} \frac{\partial \rho_0}{\partial x_3} = 0. \quad (24)$$

In the horizontally homogeneous case equation (24) takes the form:

$$\frac{\partial \bar{\rho}}{\partial t} + \frac{\partial \overline{\rho u_3}}{\partial x_3} - u_{1s} \frac{\bar{\rho}_0 f}{g} \frac{dU_2^0}{dx_3} + u_{2s} \frac{\bar{\rho}_0 f}{g} \frac{dU_1^0}{dx_3} + u_{3s} \frac{\partial \rho_0}{\partial x_3} = 0. \quad (25)$$

Integrating equation (25) over time, we obtain:

$$\Delta \bar{\rho} = - \int_0^t \left(\frac{\partial \overline{\rho u_3}}{\partial x_3} - u_{1s} \frac{\bar{\rho}_0 f}{g} \frac{dU_2^0}{dx_3} + u_{2s} \frac{\bar{\rho}_0 f}{g} \frac{dU_1^0}{dx_3} + u_{3s} \frac{\partial \rho_0}{\partial x_3} \right) dt'. \quad (26)$$

Substituting $\overline{\rho u_3}$ from formula (22) and three components of the Stokes drift velocity from formulas (19)–(21) into expression (26), after integration we obtain:

$$\Delta \bar{\rho} = \left[\frac{\partial \overline{\rho u_3}}{\partial x_3} - u_{1s} \frac{\bar{\rho}_0 f}{g} \frac{dU_2^0}{dx_3} + u_{2s} \frac{\bar{\rho}_0 f}{g} \frac{dU_1^0}{dx_3} + u_{3s} \frac{\partial \rho_0}{\partial x_3} \right] \cdot \frac{1}{2\delta\omega} (1 - e^{2\delta\omega t}), \quad (27)$$

where

$$\overline{\rho u_3}^0 = |A|^2 \left\{ \frac{i}{\Omega} \left[\frac{i}{k} \frac{\bar{\rho}_0 f}{g} \frac{dU_2^0}{dx_3} \frac{du_{30}}{dx_3} - u_{30} \frac{d\rho_0}{dx_3} - \frac{\bar{\rho}_0 f}{g \Omega} \frac{dU_1^0}{dx_3} \left(\frac{f}{k} \frac{du_{30}}{dx_3} - i u_{30} \frac{dU_2^0}{dx_3} \right) \right] u_{30}^* + \text{c.c.} \right\},$$

$$u_{1s}^0 = \frac{|A|^2}{k} \left[\frac{1}{\omega} \frac{d}{dx_3} \left(u_{30} \frac{du_{30}^*}{dx_3} \right) + \text{c.c.} \right], \quad u_{3s}^0 = i |A|^2 \left(\frac{1}{\omega} - \frac{1}{\omega^*} \right) \frac{d}{dx_3} (u_{30} u_{30}^*),$$

$$u_{2s}^0 = |A|^2 \left[\frac{1}{\omega \Omega^* k} \frac{du_{30}}{dx_3} \left(if \frac{du_{30}^*}{dx_3} - k \frac{dU_2^0}{dx_3} u_{30}^* \right) + \text{c.c.} \right] -$$

$$- |A|^2 \left\{ \frac{u_{30}^*}{\omega^* \Omega^2} \left[\Omega \left(\frac{du_{30}}{dx_3} \frac{dU_2^0}{dx_3} + if \frac{d^2 u_{30}}{dx_3^2} + u_{30} \frac{d^2 U_2^0}{dx_3^2} \right) + k \frac{dU_1^0}{dx_3} \left(u_{30} \frac{dU_2^0}{dx_3} + if \frac{du_{30}}{dx_3} \right) \right] + \text{c.c.} \right\}.$$

Correction to density $\Delta \bar{\rho}$ determined by formula (27) is a vertical fine structure generated by an internal wave and irreversible [37, 39]. The specified correction is retained after the wave train passage.

Calculation results

We calculate the vertical fine structure generated by the internal wave using the data from the third stage of the 44th cruise of R/V *Mikhail Lomonosov* at the Black Sea northwestern shelf⁶ [34, 35, 39–43].

Fig. 1 shows the time course of temperature isolines obtained by four gradient-distributed temperature sensors.

The instruments were hung from the board of the vessel and located at the following depths: 5–15 m – the first instrument; 15–25 m – the second instrument; 25–35 m – the third instrument; 35–60 m – the fourth instrument (indicated in Fig. 1 by Roman numerals I – IV, respectively).

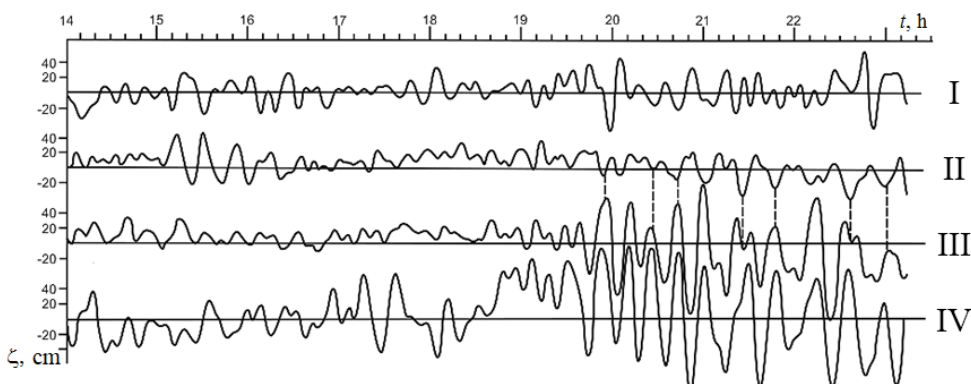


Fig. 1. Dependence of vertical displacements of temperature isolines on time

Figure 1 shows clearly a powerful wave train of 15-minute second-mode internal waves. The maximum amplitude at elevations is 0.5 m.

Figure 2, *a* shows Brunt–Väisälä frequency dependence on the vertical coordinate, and Fig. 2, *b* – dependence on two components of flow velocity.

⁶ Pantelev, N.A., 1985. *Report on the Work on the 44th Voyage (3rd Stage) of the NIS Mikhail Lomonosov August 7 – September 15, 1985*. Sevastopol: MHI Academy of Sciences of the Ukrainian SSR. Vol. 1, 135 p. (in Russian).

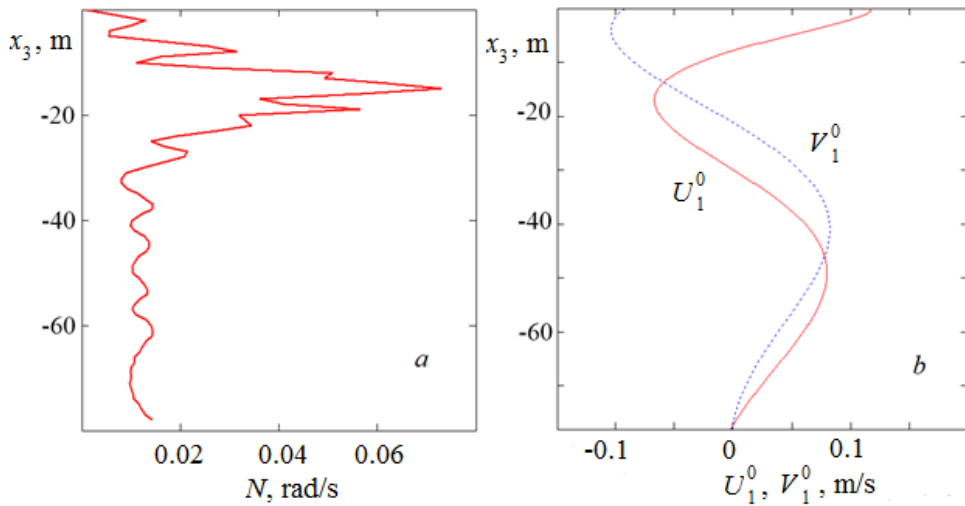


Fig. 2. Dependence of Brunt–Väisälä frequency (*a*) and flow velocity components (*b*) on the vertical coordinate

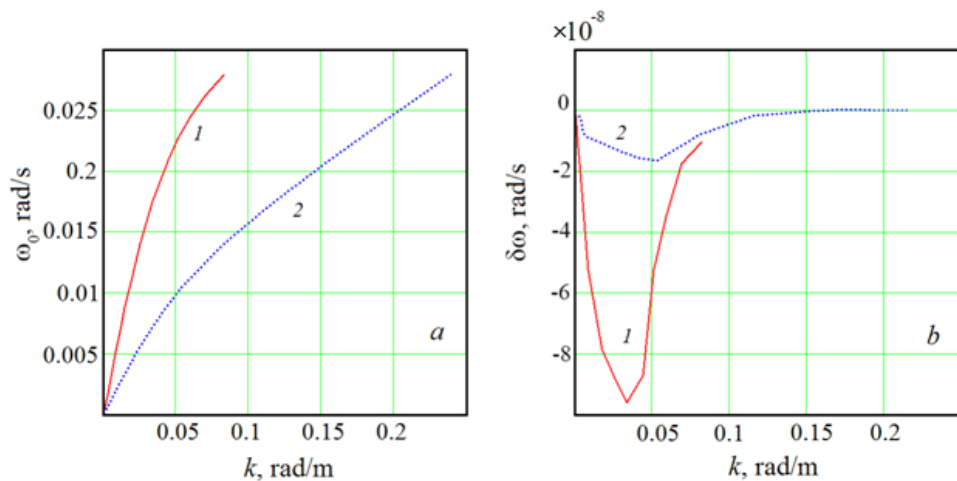


Fig. 3. Dispersion curves (*a*) and graphs of the frequency imaginary part (*b*) of the first (*1*) and second (*2*) modes

The boundary value problem (14), (15) is solved numerically using the implicit Adams scheme of the third order accuracy [34–43]. The shooting method is applied to determine the wave number and frequency imaginary part at a fixed wave period for a given mode of internal waves. The resulting solution is complex, as well as the wave frequency with a small imaginary part. Figure 3, *a* shows the dependence of frequency real part $\omega_0 = \text{Re}(\omega)$ on the wave number for the first two modes. Figure 3, *b* reveals the dependence of the frequency imaginary part on the wave number. The imaginary part of first-mode frequency $\delta\omega = \text{Im}(\omega)$ is negative, i.e. the wave is slightly attenuated.

For the second mode, the imaginary part of the frequency is negative when frequency ω_0 is less than 12 cph; if the frequency is higher, its imaginary part is positive, i.e., weak attenuation in the low-frequency region is replaced by weak amplification in the high-frequency region. The first-mode damping decrement is greater in absolute value than the second-mode damping decrement for a fixed wave number. For 15-minute internal waves of the second mode, the attenuation decrement is equal to $\delta\omega = -1,4 \cdot 10^{-8}$ rad/s, the wavelength is 197 m.

We calculate the vertical component of the Stokes drift velocity using formula (19). Normalizing factor A_1 is found by the known maximum amplitude of 0.5 m vertical displacements. The dependence of the Stokes drift velocity vertical component on the vertical coordinate for the first two modes is demonstrated in Fig. 4, *a*, the wave frequency was 4 cph.

Fig. 4, *b* shows the average density vertical profile.

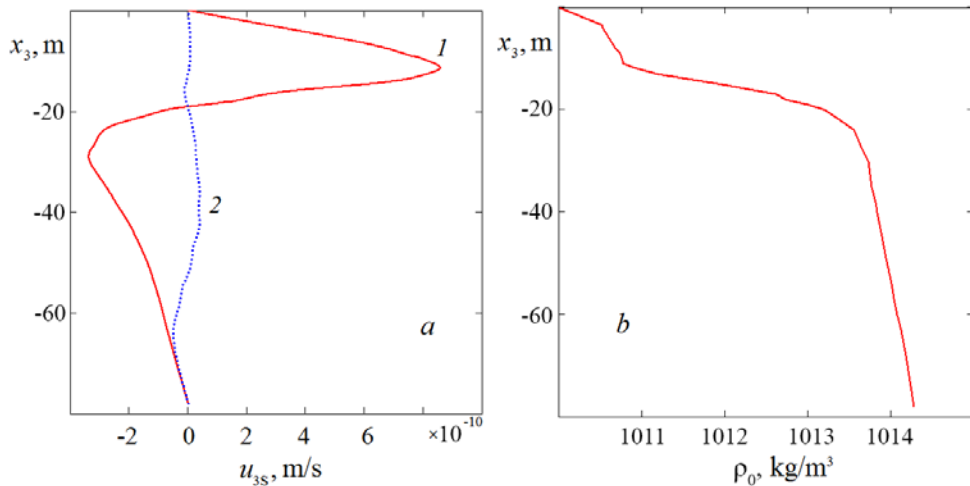


Fig. 4. Dependence of vertical component of the Stokes drift velocity on the vertical coordinate of internal waves of the first (1) and second (2) modes (*a*); average density profile (*b*)

Fig. 5 shows the profiles of vertical mass flow determined by formula (22) and non-oscillating correction to density (formula (27)) at $t = 9$ h for the first two modes of internal waves with 4 cycle/h frequency at the same maximum amplitude of 0.5 m.

The vertical wave mass flux of the first mode predominates significantly in the upper 40-meter layer, while the wave fluxes of the first and second modes are comparable in absolute value at greater depths. The intensity of the generated vertical fine structure of the density field for the first mode is greater than for the second one at the same maximum wave amplitude.

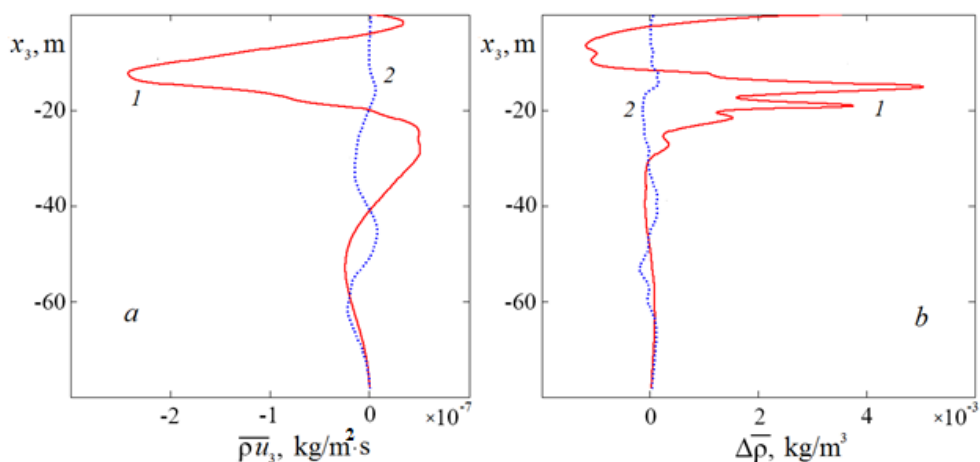


Fig. 5. Profiles of the vertical wave mass flux (*a*) and fine structure of density field (*b*) for the first (1) and second (2) modes of internal waves

Further we compare the wave fluxes and the generated fine structure of inertia-gravity internal waves of different frequencies. To do this, we consider the second mode with frequencies of 4, 1 and 12 cph at the same maximum wave amplitude of 0.5 m.

Figure 6, *a* shows vertical wave mass fluxes for waves of the indicated frequencies, and Fig. 6, *b* – profiles of the generated fine structure of the density field.

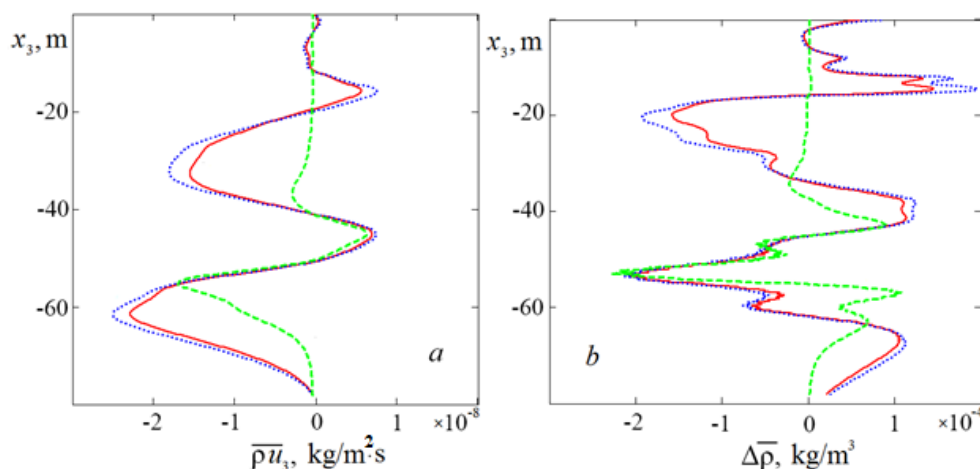


Fig. 6. Profiles of the vertical wave mass flux (*a*) and fine structure of density field (*b*) of the second mode for 15-minute internal waves (red curve), one-hour internal waves (blue curve) and 5-minute internal waves (green curve)

The vertical wave mass fluxes of the second mode of 15-minute, one-hour and 5-minute internal waves are co-directed and decrease in absolute value with the wave period decreasing. Fine-structure corrections to density for waves with 15-minute

and one-hour periods are close and only enhance the effect when summed up. The mentioned corrections do not introduce inversions into the vertical density distribution. A similar calculation was carried out for the first mode of internal waves. Fig. 7 shows the graphs of the vertical wave mass flux and generated fine density structure of the first-mode internal waves for 4, 1, and 12 cph frequencies.

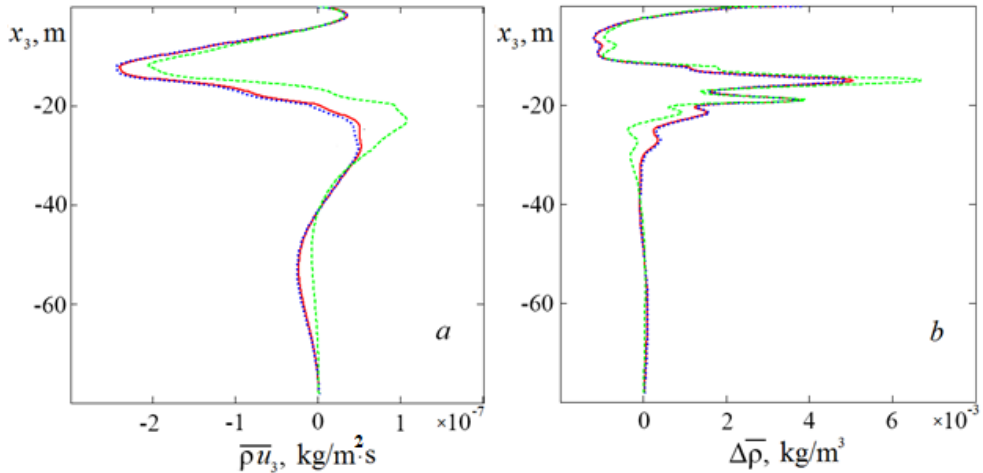


Fig. 7. Profiles of the vertical wave flux of mass (*a*) and fine structure of density field (*b*) of the first mode for 15-minute internal waves (red curve), one-hour internal waves (blue curve) and 5-minute internal waves (green curve)

In the first mode, the vertical wave mass fluxes and fine-structure corrections are almost the same for waves with 1 and 4 cph frequencies. They differ most noticeably in the pycnocline for waves with 12 cph frequency.

It is of interest to study the impact of horizontal inhomogeneity of the average density field on vertical wave mass fluxes and generated fine structure. In the horizontally homogeneous case, the terms containing horizontal gradients of the average density $\frac{\partial \rho_0}{\partial x}$ and $\frac{\partial \rho_0}{\partial y}$ are neglected in equation (4). Fig. 8 shows

the dependence of the vertical wave mass fluxes and generated fine structure on the vertical coordinate for the second-mode internal waves with 4 cph frequency in the horizontally homogeneous and inhomogeneous cases with the same maximum wave amplitude of 0.5 m.

Thus, the amplitude of fine-structure oscillations and vertical wave mass fluxes in the horizontally inhomogeneous case are higher than in the homogeneous one.

Similar calculations were also performed for the first mode of internal waves. Fig. 9 shows the profiles of the vertical mass flux and generated fine structure for the first mode of internal waves with 4 cph frequency in the horizontally inhomogeneous and homogeneous cases.

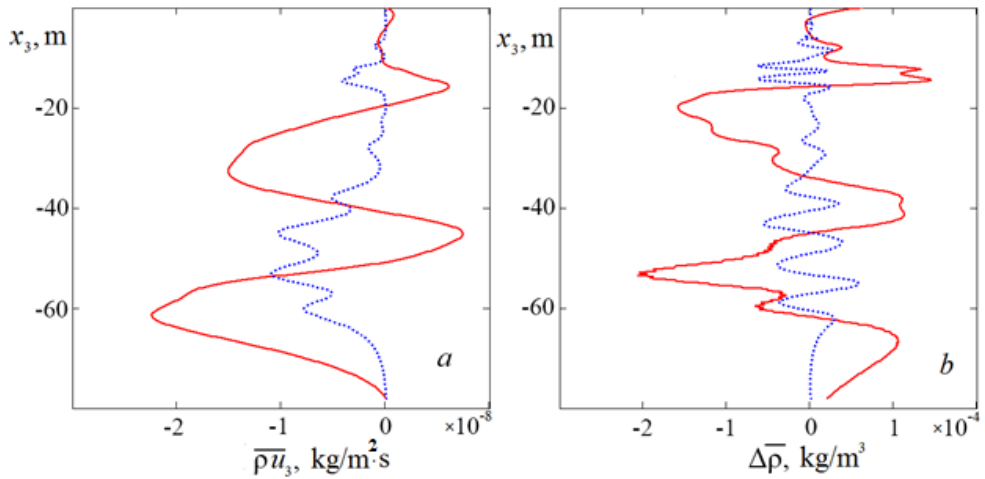


Fig. 8. Vertical distribution of the wave fluxes of mass (a) and generated fine structure (b) for the internal wave of the second mode in the horizontally inhomogeneous (red curve) and homogeneous (blue curve) cases

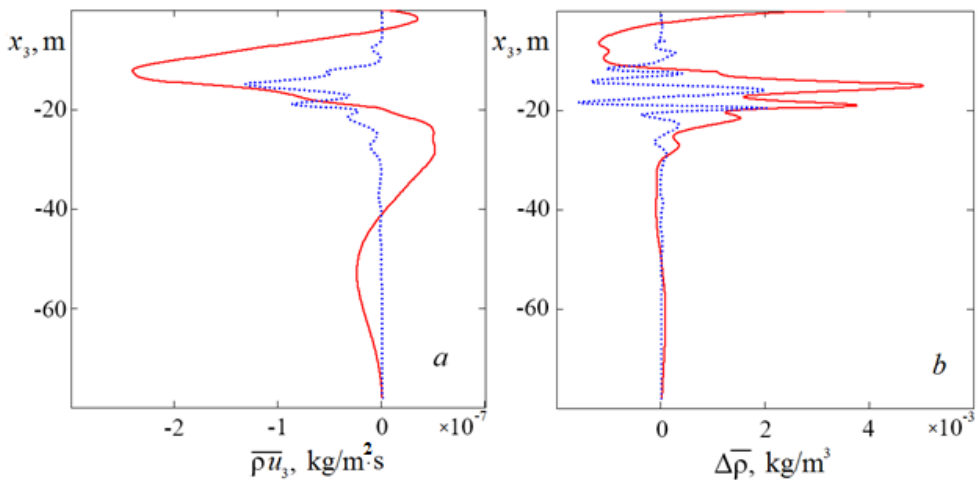


Fig. 9. Dependence on the vertical coordinate of the wave mass flux (a) and generated fine structure (b) for the internal wave of the second mode in the horizontally inhomogeneous (red curve) and homogeneous (blue curve) cases upon the vertical coordinate

Similarly, the first mode vertical wave mass fluxes and fine-structure correction to the density are higher in the case that is horizontally inhomogeneous in average density.

Conclusion

The paper presents a mechanism for generating vertical fine structure due to vertical wave mass fluxes. These fluxes are nonzero for the inertia-gravity internal waves in the presence of a flow in which the velocity component normal to the direction of wave propagation depends on the vertical coordinate. Unlike

previous works, we do not assume horizontal homogeneity of average density field. In contrast, the flow is assumed to be geostrophically balanced, i.e. vertical velocity shifts are balanced by the horizontal gradient of the average density field. This gradient is found from the “thermal wind” relations. It is shown that consideration of horizontal inhomogeneity of average density field increases both vertical wave mass fluxes and generated fine structure, the amplitude of fine-structure oscillations. The wave mass fluxes and fine-structure corrections to density are very close for waves of 1 and 4 cph frequencies, i.e. the overall effect only intensifies for waves of different frequencies.

REFERENCES

1. Chashechkin, Yu.D., 2022. Discrete and Continuous Symmetries of Stratified Flows past a Sphere. *Symmetry*, 14(6), 1278. <https://doi.org/10.3390/sym14061278>
2. Chashechkin, Yu.D., 2021. Foundations of Engineering Mathematics Applied for Fluid Flows. *Axioms*, 10(4), 286. <https://doi.org/10.3390/axioms10040286>
3. Chashechkin, Yu.D. and Ilinykh, A.Yu., 2023. Fine Structure of the Substance Distribution Pattern of a Free-Falling Drop on the Surface and in the Thickness of the Target Fluid in the Impact Mode of Merging. *Physical-Chemical Kinetics in Gas Dynamics*, 24(2), pp. 79-106. <https://doi.org/10.33257/PhChGD.24.2.1043> (in Russian).
4. Gargett, A.E., 1976. An Investigation of the Occurrences of Oceanic Turbulence with Respect to Finestructure. *Journal of Physical Oceanography*, 6(2), pp. 139-156. [https://doi.org/10.1175/1520-0485\(1976\)006<0139:AIOTOO>2.0.CO;2](https://doi.org/10.1175/1520-0485(1976)006<0139:AIOTOO>2.0.CO;2)
5. Bell, T.H.Jr., 1974. Internal Wave-Turbulence Interpretation of Ocean Fine Structure. *Geophysical Research Letters*, 1(6), pp. 253-255. <https://doi.org/10.1029/GL001i006p00253>
6. Bagimov, I.S., Bulgakov, P.G., Korotaev, G.K., Pantelev, N.A. and Timchenko, A.N., 1978. Experimental Studies of the Temperature Field in the Seasonal Thermocline. In: MHI, 1978. *Marine Hydrophysical Research*. Sevastopol: MHI. Iss. 3, pp. 75-90 (in Russian).
7. Turner, J.S., 1981. *Buoyancy Effects in Fluids*. Cambridge Monographs on Mechanics. Cambridge, Great Britain: Cambridge University Press, 367 p. <https://doi.org/10.1017/CBO9780511608827>
8. Schmitt, R.W., 1981. Form of the Temperature-Salinity Relationship in the Central Water: Evidence for Double-Diffusive Mixing. *Journal of Physical Oceanography*, 11(7), pp. 1015-1026. [https://doi.org/10.1175/1520-0485\(1981\)011<1015:FOTTSR>2.0.CO;2](https://doi.org/10.1175/1520-0485(1981)011<1015:FOTTSR>2.0.CO;2)
9. Rudels, B., Björk, G., Muench, R.D. and Schauer, U., 1999. Double-Diffusive Layering in the Eurasian Basin of the Arctic Ocean. *Journal of Marine Systems*, 21(1-4), pp. 3-27. [https://doi.org/10.1016/S0924-7963\(99\)00003-2](https://doi.org/10.1016/S0924-7963(99)00003-2)
10. Zhurbas, V.M. and Lips, U.K., 1987. Discrimination of the Main Types of Thermohaline Fine Structure in the Ocean. *Oceanology*, 27(4), pp. 416-420.
11. Williams, A.J.3rd, 1974. Salt Fingers Observed in the Mediterranean Outflow. *Science*, 185(4155), pp. 941-943. <https://doi.org/10.1126/science.185.4155.941>
12. Pereskokov, A.I. and Fedorov, K.N., 1989. [Oxygenation of Ocean Thermocline Waters by Salt-Finger Convection]. *Transactions (Doklady) of the USSR Academy of Sciences. Earth Science Sections*, 309(1), pp. 241-244 (in Russian).
13. Pogrebnoi, A.E. and Pantelev, N.A., 2000. Convection of Salt Fingers in the C–SALT Region. *Physical Oceanography*, 10(3), pp. 215-232. <https://doi.org/10.1007/BF02509220>
14. Zhurbas, V.M., Kuzmina, N.P. and Kul'sha, O.E., 1987. Step-Like Stratification of the Ocean Thermocline Resulting from Transformations Associated with Thermohaline Salt Finger Intrusions (Numerical Experiment). *Oceanology*, 27(3), pp. 277-281.

15. Falina, A.S. and Volkov, I.I., 2003. On the Fine Structure and Thermohalinic Stability of the Abyssal Water in the Black Sea. *Oceanology*, 43(4), pp. 485-492.
16. Falina, A.S. and Volkov, I.I., 2005. Influence of Double Diffusion on the General Hydrological Structure of the Deep Waters in the Black Sea. *Oceanology*, 45(1), pp. 16-25.
17. Zhurbas, V.M. and Ozmidov, R.V., 1983. On the Internal Structure of the Fine Stepped Structure of the Main Ocean Thermocline. *Oceanology*, 23(6), pp. 938-943.
18. Rudels, B., Kuzmina, N., Schauer, U., Stipa, T. and Zhurbas, V., 2009. Double-Diffusive Convection and Interleaving in the Arctic Ocean – Distribution and Importance. *Geophysica*, 45(1-2), pp. 199-213.
19. Panteleev, N.A. and Okhotnikov, I.N., 2003. Intrusive Stratification of the Gulf-Stream Frontal Zone According to the Results of Investigations Performed during Cruise 43 of the R/V Akademik Vernadskii. *Physical Oceanography*, 13(2), pp. 104-115. <https://doi.org/10.1023/A:1023748413882>
20. Golovin, P.N., Antipov, N.N. and Klepikov, A.V., 2016. Intrusive Layering of the Antarctic Slope Front. *Oceanology*, 56(4), pp. 470-482. <https://doi.org/10.1134/S0001437016030085>
21. Kuzmina, N., Rudels, B., Zhurbas, V. and Stipa, T., 2011. On the Structure and Dynamical Features of Intrusive Layering in the Eurasian Basin in the Arctic Ocean. *Journal of Geophysical Research: Oceans*, 116(C8), C00D11. <https://doi.org/10.1029/2010JC006920>
22. Samodurov, A.S., 1993. Intrusion Layering and Vertical Diffusion in the Ocean Owing to Tidal Mixing at a Sloping Bottom. *Physical Oceanography*, 4(3), pp. 213-219. <https://doi.org/10.1007/BF02197319>
23. Samodurov, A.S., Lubitsky, A.A. and Panteleev, N.A., 1995. Contribution of Breaking Internal Waves to Structure Formation, Energy Dissipation, and Vertical Diffusion in the Ocean. *Physical Oceanography*, 6(3), pp. 177-190. <https://doi.org/10.1007/BF02197516>
24. Zatsepin, A.G., Golenko, N.N., Korzh, A.O., Kremenetskii, V.V., Paka, V.T., Poyarkov, S.G. and Stunzhas, P.A., 2007. Influence of the Dynamics of Currents on the Hydrophysical Structure of the Waters and the Vertical Exchange in the Active Layer of the Black Sea. *Oceanology*, 47(3), pp. 301-312. <https://doi.org/10.1134/S0001437007030022>
25. Podymov, O.I., Zatsepin, A.G. and Ostrovsky, A.G., 2017. Vertical Turbulent Exchange in the Black Sea Pycnocline and Its Relation to Water Dynamics. *Oceanology*, 57(4), pp. 492-504. <https://doi.org/10.1134/S0001437017040142>
26. Navrotsky, V.V., Izergin, V.L. and Lozovatsky, V.V., 2007. Internal Waves and Formation of Hydrophysical Fields Fine Structure in the Shelf Zone. *Far Eastern Seas of Russia*. Moscow: Nauka. Vol. 1, pp. 507-527 (in Russian).
27. Ivanov, V.A., Shul'ga, T.Ya., Bagaev, A.V., Medvedeva, A.V., Plastun, T.V., Verzhnevskaya, L.V. and Svishcheva, I.A., 2019. Internal Waves on the Black Sea Shelf near the Heracles Peninsula: Modeling and Observation. *Physical Oceanography*, 26(4), pp. 288-304. <https://doi.org/10.22449/1573-160X-2019-4-288-304>
28. Leonov, A.I., Miropolsky, Yu.Z. and Tamsalu, R.E., 1977. Calculation of the Fine Structure of the Density and Velocity Fields as Exemplified by the Baltic Sea. *Oceanology*, 17(3), pp. 389-393.
29. Kistovich, A.V. and Chashechkin, Yu.D., 2007. Regular and Singular Components of Periodic Flows in the Fluid Interior. *Journal of Applied Mathematics and Mechanics*, 71(5), pp. 762-771. <https://doi.org/10.1016/j.jappmathmech.2007.11.009>
30. Chashechkin, Yu.D. and Ochirov, A.A., 2022. Periodic Waves and Ligaments on the Surface of a Viscous Exponentially Stratified Fluid in a Uniform Gravity Field. *Axioms*, 11(8), 402. <https://doi.org/10.3390/axioms11080402>
31. Kistovich, Y.V. and Chashechkin, Y.D., 1998. Linear Theory of the Propagation of Internal Wave Beams in an Arbitrarily Stratified Liquid. *Journal of Applied Mechanics and Technical Physics*, 39(5), pp. 729-737. <https://doi.org/10.1007/bf02468043>

32. LeBlond, P.H. and Mysak, L.A., 1978. *Waves in the Ocean*. Amsterdam; New York: Elsevier Scientific Publishing Company, 602 p.
33. LeBlond, P.H., 1966. On the Damping of Internal Gravity Waves in a Continuously Stratified Ocean. *Journal of Fluid Mechanics*, 25(1), pp. 121-142. <https://doi.org/10.1017/S0022112066000089>
34. Slepyshev, A.A., 2016. Vertical Momentum Transfer by Internal Waves When Eddy Viscosity and Diffusion Are Taken into Account. *Izvestiya, Atmospheric and Oceanic Physics*, 52(3), pp. 301-308. <https://doi.org/10.1134/S0001433816030117>
35. Slepyshev, A.A., 2022. Vertical Momentum Transfer Induced by Internal Inertial-Gravity Waves in Flow with Account of Turbulent Viscosity and Diffusion. *Fluid Dynamics*, 57(2), pp. 183-192. <https://doi.org/10.1134/S0015462822020094>
36. Slepyshev, A.A. and Nosova, A.V., 2022. Vertical Transfer of Momentum by Internal Waves in the Western Part of the Mediterranean Sea. *Physical Oceanography*, 29(4), pp. 334-346.
37. Slepyshev, A.A. and Nosova, A.V., 2020. Generation of Vertical Fine Structure by the Internal Waves with the Regard for Turbulent Viscosity and Diffusion. *Physical Oceanography*, 27(1), pp. 3-17. <https://doi.org/10.22449/1573-160X-2020-1-3-17>
38. Slepyshev, A.A., 2022. Vertical Momentum Transfer by Internal Waves in a Shear Flow Taking into Account Turbulent Viscosity and Diffusion. *Izvestiya, Atmospheric and Oceanic Physics*, 58(5), pp. 433-439. <https://doi.org/10.1134/S0001433822050115>
39. Slepyshev, A.A. and Vorotnikov, D.I., 2019. Generation of Vertical Fine Structure by Internal Waves in a Shear Flow. *Open Journal of Fluid Dynamics*, 9(2), pp. 140-157. <https://doi.org/10.4236/ojfd.2019.92010>
40. Ankudinov, N.O. and Slepyshev, A.A., 2021. Vertical Momentum Transfer Induced by Internal Waves in a Two-Dimensional Flow. *Fluid Dynamics*, 56(3), pp. 343-352. <https://doi.org/10.1134/S0015462821030022>
41. Slepyshev, A.A. and Vorotnikov, D.I., 2017. Vertical Transport of Momentum by the Inertial-Gravity Internal Waves in a Baroclinic Current. *Physical Oceanography*, (4), pp. 3-15. <https://doi.org/10.22449/1573-160X-2017-4-3-15>
42. Slepyshev, A.A., 2021. Vertical Transfer of Momentum by Inertia-Gravity Internal Waves on a Two-Dimensional Shear Flow. *Physical Oceanography*, 28(4), pp. 363-375. <https://doi.org/10.22449/1573-160X-2021-4-363-375>
43. Vorotnikov, D.I. and Slepyshev, A.A., 2018. Vertical Momentum Fluxes Induced by Weakly Nonlinear Internal Waves on the Shelf. *Fluid Dynamics*, 53(1), pp. 21-33. <https://doi.org/10.1134/S0015462818010160>
44. Slepyshev, A.A. and Laktionova, N.V., 2019. Vertical Transport of Momentum by Internal Waves in a Shear Current. *Izvestiya, Atmospheric and Oceanic Physics*, 55(6), pp. 662-668. <https://doi.org/10.1134/S0001433819060148>
45. Jones, W.L., 1967. Propagation of Internal Gravity Waves in Fluids with Shear Flow and Rotation. *Journal of Fluid Mechanics*, 30(3), pp. 439-448. <https://doi.org/10.1017/S0022112067001521>
46. Bulatov, V.V. and Vladimirov, Yu.V., 2020. Dynamics of Internal Gravity Waves in the Ocean with Shear Flows. *Russian Journal of Earth Sciences*, 20(4), ES4004. <https://doi.org/10.2205/2020ES000732>
47. Bulatov, V.V. and Vladimirov, I.Yu., 2022. Internal Gravity Waves Generated by an Oscillating Disturbance Source in a Stratified Medium in the Presence of Two-Dimensional Shear Flows. *Fluid Dynamics*, 57(4), pp. 477-485. <https://doi.org/10.1134/s0015462822040012>
48. Longuet-Higgins, M.S., 1969. On the Transport of Mass by Time Varying Ocean Current. *Deep Sea Research and Oceanographic Abstracts*, 16(5), pp. 431-447. [https://doi.org/10.1016/0011-7471\(69\)90031-X](https://doi.org/10.1016/0011-7471(69)90031-X)

Submitted 05.09.2023; approved after review 25.12.2023;
accepted for publication 18.01.2024.

About the authors:

Aleksandr A. Slepyshev, Leading Research Associate, Marine Hydrophysical Institute of RAS (2 Kapitanskaya Str., Sevastopol, 299011, Russian Federation), DSc (Phys.-Math.), **ResearcherID: V-6948-2017**, **ORCID ID: 0000-0002-9259-7558**, slep55@mail.ru

Nikita O. Ankudinov, Leading Engineer-Researcher, Marine Hydrophysical Institute of RAS (2 Kapitanskaya Str., Sevastopol, 299011, Russian Federation), ankudinff@gmail.ru

Contribution of the co-authors:

Aleksandr A. Slepyshev – problem statement, theoretical part of the work: mathematical formulation of the model, derivation of all formulas

Nikita O. Ankudinov – numerical calculations using the proposed model, graphical presentation of the results

The authors have read and approved the final manuscript.

The authors declare that they have no conflict of interest.

Original article

New Method for Determining Spectral Absorption of Light in the Sea

M. E. Lee ✉, E. B. Shybanov

Marine Hydrophysical Institute of RAS, Sevastopol, Russian Federation
✉ michael.lee.mhi@gmail.com

Abstract

Purpose. The study is purposed at presenting and analyzing a new method for determining light absorption in the sea which for the first time made it possible to redirect almost all the scattered rays from the studied light beam to the photodetector along the path of its propagation in a weakly absorbing medium, as well as at showing that application of a new method providing such an efficient collection of the scattered rays, permits not only to avoid significant errors from a strong influence of scattering upon the results of determining light absorption, but also to give up the necessity in correcting the data by theoretical modeling.

Methods and Results. It is known that sea water is a weakly absorbing light-scattering medium where light propagation is accompanied by its attenuation that is many times stronger due to scattering than due to absorption. Therefore, the determination of light absorption by sea water at a receiving device requires collection of not only the light that has traveled a certain distance in the absorption medium, but also all the light scattered along this path. Previously, a method was proposed for measuring the light absorption in a cylindrical mirror cuvette with a light source at the input and a collector with a photodetector at the output (reflective-tube absorption meter). Somewhat later, a similar method based on the phenomenon of total internal reflection was applied. Since these methods do not provide a complete collection of scattered rays, the data are to be corrected by theoretical modeling. The authors propose a new method for determining spectral absorption of light in a quartz cone cuvette with an external mirror cone. It is shown that the cone cuvette permits to collect most of the scattered rays in the beam passing through the water medium by means of more efficient redirection of these rays from the place of light scattering to the receiver. The rest of the scattered rays that have left the cuvette reach the receiver in the air space between the cuvette and the cone mirror due to multiple reflections from it. As a result, the new method makes it possible to redirect almost all of the scattered light to the receiver and thus to minimize the errors in determining light absorption in a weakly absorbing medium. To quantify the advantages of the new method, the authors have calculated geometric parameters of the scattered light propagation for a quartz cone cuvette in air and for the same cuvette placed inside the external cone mirror.

Conclusions. The combination of a quartz cone cuvette and an external mirror cone in the new method made it possible to collect all the rays scattered in a weakly absorbing medium in the receiver. Thus, it permitted not only to exclude their strong influence upon determining light absorption in the sea, but also to give up correcting the data by theoretical modeling.

Keywords: light absorption, scattering medium, total internal reflection, quartz cone cuvette, cone mirror, scattering angle, ray path

Acknowledgments: The work was carried out within the framework of state assignment FNNN-2024-0012.

For citation: Lee, M.E. and Shybanov, E.B., 2024. New Method for Determining Spectral Absorption of Light in the Sea. *Physical Oceanography*, 31(2), pp. 178-193.

© 2024, M. E. Lee, E. B. Shybanov

© 2024, Physical Oceanography



Introduction

Sea water absorption is one of the most important hydro-optical characteristics that determine propagation of light radiation in the sea. The absorption coefficient spectrum contains information about mineral and organic suspended matter, phytoplankton cells and dissolved organic matter in sea water. Light absorption and scattering by these impurities form an underwater light field of the open waters of most seas and oceans and, thus, affect the solar radiation spectrum penetrating into the depths and rising from the sea. Such spectral changes provide information about the ocean color that with the help of space color scanners can be used for systematic monitoring of global spatiotemporal changes in the surface vital layer throughout the World Ocean [1]. In all models of light radiation transfer in the marine environment, the inherent optical properties, which include absorption and scattering, are either necessary input parameters or, in the case of inverse problems, output data of calculations. In this regard, measurements of the absorption value are of great practical importance, especially for verification of satellite scanners of sea color closely related to the environmental monitoring of its condition.

The currently applied natural methods for determining the spectral coefficient of light absorption make it impossible to obtain reliable data due to insufficient measurement accuracy. For example, in the blue region of the spectrum, where the main absorption bands of phytoplankton pigments and dissolved organic substances are located, the amount of light absorption in highly transparent sea water is so insignificant that it can hardly be recorded by modern photometers.

An even more significant difficulty in light absorption measurement in the sea is due to the fact that sea water is a weakly absorbing light-scattering medium where light propagation is accompanied by many times stronger attenuation from scattering than from absorption. Consequently, when measuring light absorption by sea water, it is necessary to collect at the receiving device not only the light that has traveled a certain distance in the medium after absorption, but also all the light scattered along this path. This feature leads to mutually contradictory requirements when developing methods for measuring light absorption in the sea. On the one hand, to ensure the method sensitivity, it is necessary to measure weakened due to absorption light along as much of its path as possible in a medium longer than the measuring base length. On the other hand, the larger length of the base makes it very difficult to redirect all the light scattered along this path towards the collector to be collected in the light receiving device.

For relatively transparent sea water, the difficulties of collecting scattered rays increase many times as scattering predominates over absorption in the sea. For this reason, the existing methods for determining light absorption do not provide reliable data suitable for use in modeling and in problems of retrieving impurities based on sea color. Based on the range of sea radiance factor variability in the spectral interval, where pure water absorption can be neglected and also using the data on the characteristic values of the asymmetry parameter of scattering indicatrices [2], it can be estimated that the ratio between light attenuation from scattering and its attenuation from absorption can reach values of 20 and higher with intensive blossom of coccolithophores.

It should be borne in mind that in this case we are talking specifically about relatively pure waters and not about ideally pure waters or especially pure ocean

waters prepared in the laboratory because direct light absorption determination methods are not applicable to them due to impossibility of collecting all scattered light from measuring bases up to 10 meters long on the receiving device. To determine the spectral absorption of light for such ideally pure waters is possible only indirectly with the help of a method based on the use of characteristics of the natural underwater light field in the purest waters of certain World Ocean areas [3, 4].

To determine spectral absorption characteristics of pure water, the integrating cavity absorption meter (ICAM) method [5] has been proposed. It involved using two integrating cavities located one inside another: an internal one, filled with water, and an external one, creating isotropic radiance in the internal cavity, independent of any scattering effects. A rigorous theoretical justification of the ICAM method, working equations for taking into account the influence of scattering particles on the determination of spectral absorption of especially pure water and methods of absolute calibration are considered in [6]. Due to isotropic radiation and very high diffuse reflectivity of integrating cavities, ICAM enables us to measure very low optical absorption values, practically independent of scattering effects in a sample.

A method [7] was proposed to determine spectral absorption of light in very turbid sea water. It involved placing of the studied suspension of algal cultures not inside the integrating sphere, but outside it at different distances from the entrance to take into account scattering by cells. The use of this method is justified only in rare environmental situations, when in certain water area conditions of rapid growth of microalgae are realized and extremely high concentrations of phytoplankton are observed in sea water. It is shown that true absorption spectra, practically independent of the influence of scattering, are determined based on light attenuation measurements at different distances from the integrating sphere.

Light absorption spectra determinations under the conditions of sea expeditions can be carried out in a vessel laboratory using a portable spectrophotometer with an integrating sphere filled with sea water [8]. In this spectrophotometer, the sea water sampled in the studied water areas from different horizons is poured without preliminary preparation into a spherical quartz flask, lined over the entire outer surface with a diffusely reflective material – fluorilon (*Fluorilon 99-WTM*). In this method, the sea water-filled integrating sphere cannot provide spherical symmetry due to radiance by the collimated beam and the presence of a specular reflection component associated with the quartz shell. Nevertheless, a thorough analysis carried out in [9] showed that with appropriate calibration of the spectrophotometer against a standard aqueous solution, it is possible to obtain quite satisfactory data on the light absorption spectra of sea water.

Method for determining light absorption in a reflective-tube absorption meter

Currently, a reflective-tube absorption meter has become widespread in hydrooptics [10, 11]. Having ideal specular reflection, such an absorption meter could redirect all light scattered into the front hemisphere to the receiving collector and thereby provide a qualitative determination of its absorption in the sea. In fact, to prevent direct contact with aggressive sea water, a mirror coating on the outer wall of a thin glass tube with a reflectivity of < 95% was used. This was not enough to

achieve the minimum acceptable error in determining light absorption in weakly absorbing aquatic media. Due to the low specular reflection factor of such a tube absorption meter, the rays scattered towards the walls were lost because of losses during multiple reflections. As a result, only part of the forward-scattered light reached the collector, and with an elongated path through the medium. The influence of these scattered rays that did not reach the receiving device had to be taken into account through theoretical modeling with subsequent correction of the values [12]. Such correction allowed to obtain data with an acceptable error for turbid lake water, but for sea water only estimates were obtained.

In the 90s of the past century, a measurement scheme with a cylindrical quartz cuvette without a mirror coating was proposed. To redirect the rays scattered inside the cuvette to the collector, the phenomenon of total internal reflection from the quartz-air interface was used [13, 14]. An ideally smooth, well-polished cylindrical surface of a quartz cuvette reflects all photons incident on it at an angle greater than the critical one $\arcsin(1/n_w) \approx 48.5^\circ$ (where n_w is the refractive index of sea water), since the photons will experience total internal reflection. Therefore, all photons scattered in the angular range of $0-41.5^\circ$ will reach the receiving collector without loss, either directly without touching the wall or through several reflections. Due to the fact that the scattering indicatrix of natural sea waters has a strong peak in the forward direction [15, 16], in this case it is possible to redirect most of the forward scattered rays and thus preserve them in the beam passing through the aquatic medium. However, using this method, it is not possible to avoid the loss of some rays scattered at large angles, since they exit the cuvette into the air and do not reach the receiving collector. The elimination of these scattered rays from the main light beam is the main source of errors in the method for determining light absorption in a cylindrical quartz cuvette [11]. Thus, the disadvantages of this method, which is widely used in commercial devices [17], include the loss of scattered rays at angles in the $41.5-90^\circ$ range.

Another disadvantage of the method analyzed is lengthening of the path of scattered rays from the source to the collector, propagating in a zigzag pattern inside the cuvette. Due to these downsides, as when using a method based on the operation of reflective-tube absorption meter, it is necessary to resort to the obtained data correction through theoretical modeling [18, 19]. The results showed that the relative absorption error is always positive and increases linearly with increasing scattering to absorption ratio. The error increases with decreasing the cylindrical surface reflectivity of the cuvette.

Aspects of a new approach to determining light absorption properties in the sea

In the present paper, it is proposed to minimize errors by using a new method for determining spectral absorption of light, allowing to redirect almost all the light scattered in a weakly absorbing aquatic medium to the collector. To achieve the best results, it is necessary to redirect all scattered rays in the range of $0-180^\circ$ to the receiving collector. Taking into account the fact that only 1–2% of photons are scattered in the opposite direction in sea water, it is quite acceptable to limit to

intercepting rays scattered into the front hemisphere in the range of $0-90^\circ$. To solve this problem, we propose to determine light absorption in a **quartz cone cuvette** placed coaxially inside an external mirror cone (Fig. 1).

As shown in Fig. 1, instead of the currently commonly used cylindrical cuvette, the cone cuvette is made of quartz glass in the form of a thin-walled cone, which ends in a cylindrical part only in a short section in front of the receiving collector. This shape permits to redirect photons scattered in the aquatic environment and experiencing total internal reflection at the quartz-air interface to the collector more and more efficiently.

The rays scattered at large angles enter the air space between the cone cuvette and the mirror cone. These rays are not lost, as in currently used methods, but are collected by an outer mirror cone in a beam of light directed at the collector. Thus, determining light absorption in a cone cuvette combined with a cone mirror reflector allows to eliminate the above-mentioned disadvantages of existing methods, since almost all rays scattered into the front hemisphere are redirected to the receiving collector.

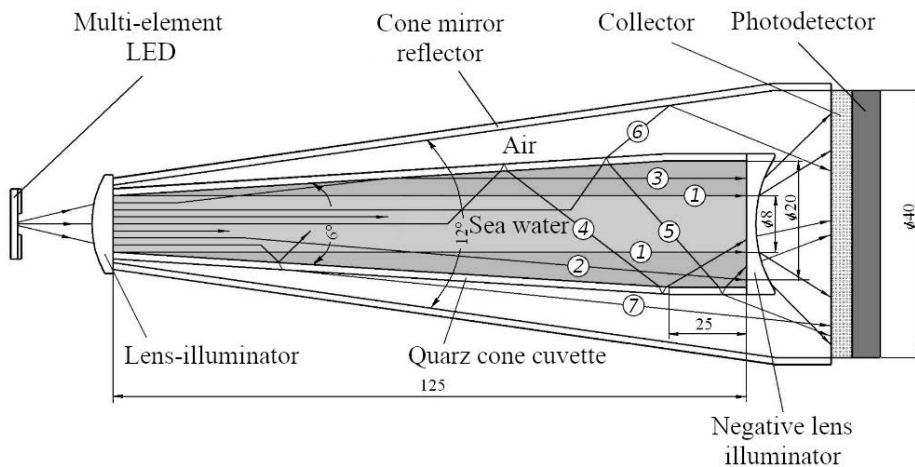


Fig. 1. Diagram of a new method to determine light absorption in sea water with the examples of ray paths from a source to a collector. The rays ending in water indicate the absorbed part of light in a beam: 1 – the rays which passed through the whole cuvette without attenuation; 2, 3 – the scattered rays at small angles which reached the collector without touching its wall and also redirected after their reflection from the cuvette wall; 4 – the scattered rays which experienced total internal reflection and reached the collector by means of the repeated additional reflections from one part of the cuvette wall to the opposite one; 5, 6 – the scattered rays partially reflected by the wall inward and exited after refraction into the air space between the cuvette and the mirror cone; 7 – the scattered rays which left the cuvette and reached the collector without touching the mirror cone reflector

Restrictive geometric parameter of the new approach is the length of the measuring base, which cannot exceed 0.1–0.15 m due to the cone shape of the cuvette and the mirror reflector. The main factor limiting the length of the measuring base is the cone cuvette angle. Note that a cylindrical cuvette is the limiting case of a cone cuvette with the 0° angle. Therefore, it is necessary to calculate the optimal angle of the cone cuvette satisfying many conflicting factors, such as measuring base length, diameter of the collimated light beam, diameter of

the collector, etc. As a result, the following were chosen as the optimal geometric parameters for determining light absorption in the sea using the new approach:

- measuring base length – 0.125 m;
- diameter of the collimated light beam – 0.008 m;
- angle of quartz cuvette cone – 6° ;
- angle of external mirror reflector cone – 12° ;
- diameter of receiving collector – 0.04 m.

A powerful multi-element LED with a collimator can be used as a light source, providing determination of light absorption in different parts of the spectrum in the range of 390–630 nm. The multi-element LED has an important advantage over traditionally used incandescent lamps due to its much higher light output. A comparative analysis shows that LEDs are tens and hundreds of times more powerful in terms of luminous flux in the selected spectral range than incandescent lamps. The spectral ranges of LEDs are relatively narrow (10–20 nm), so their radiation can be considered quasi-monochromatic. Multi-element multi-colored LEDs also allow for fast electronic scanning across the spectrum, as opposed to mechanical switching of a set of narrow-band interference filters.

A plate made of milk glass is most often used as a receiving collector. Its optical characteristics and geometric parameters are selected to ensure uniform redistribution of the incident light throughout its entire thickness. Rays fall onto the receiving collector from a variety of directions, unevenly illuminating the surface, and their intensity varies significantly. Therefore, the main function of the collector is to generate uniform total radiation at the output. In reality, it is not possible to achieve complete uniformity of the radiation coming out of the collector, therefore, for better matching, it is necessary to use light radiation receivers with a large photosensitive area comparable to the collector size.

The path of rays in a cone cuvette is characterized by the fact that for a light flux directly passing through an aquatic medium, everything happens in the same way as in a cylindrical cuvette. However, in a quartz cone cuvette, significantly more photons scattered at small angles reach the collector without contacting the walls. Due to this, the cuvette wall influence on determining light absorption in the sea is reduced, since in natural waters scattering occurs mainly in small angles and almost all of them are redirected to the collector without interacting with the walls.

Calculations of the ray path in a quartz cone cuvette

In the described method for determining light absorption in the sea, it is very important to take into account the variety of features of reflection, refraction and absorption of scattered rays when interacting with the walls of a quartz cuvette and an external cone mirror reflector to minimize errors in their impact on the final result. For that, the corresponding calculations of geometric parameters of scattered light propagation were carried out, first separately for a quartz cone cuvette in the air, and then for the same cuvette placed inside an external cone mirror reflector.

Figure 2 shows a block diagram of the algorithm for calculating the effective reflection coefficient and geometric parameters of the path of rays scattered by a weakly absorbing aquatic medium in a quartz cone cuvette in the air.

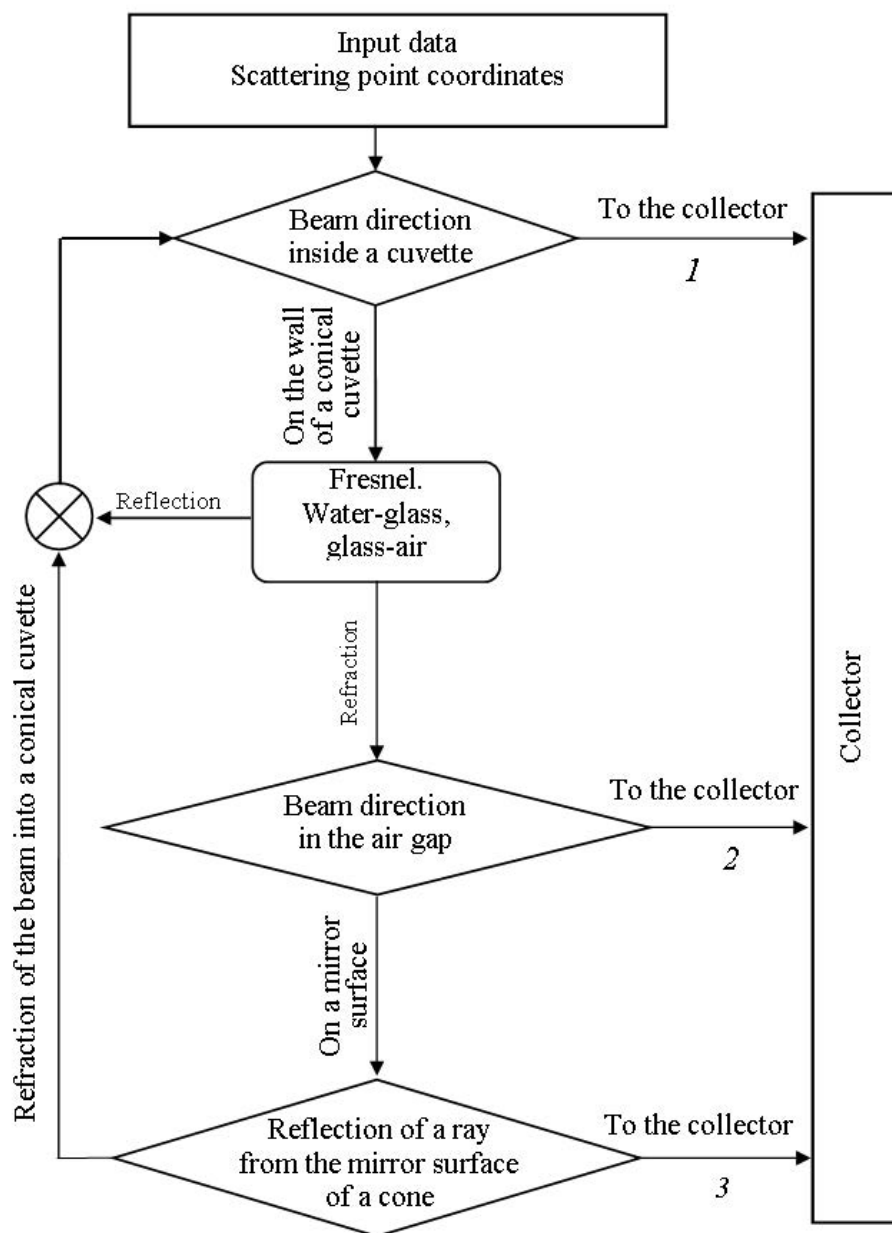


Fig. 2. Block diagram for calculating the ray paths in a cone cuvette with a mirror cone

The input parameters are the position of the initial point of light scattering in the medium, as well as the azimuthal and zenith angle. The ray can reach the collector in three ways: 1 – through a cone cuvette immediately or after several reflections from the walls; 2 – along the air gap between the cone cuvette and the mirror coating after refraction at the glass-air interface; 3 – along the air gap after reflection from the mirror coating. Thus, a ray can travel part of its path through

the air, reducing its absorption probability. However, this applies to those rays that are scattered at angles $> 44.5^\circ$. For such angles in the standard diagram, the path length increases significantly, which raises additional questions when calculating absorption.

To avoid multiple duplication of low-intensity rays, it was assumed that light reflected in the direction of a quartz cone cuvette penetrates the medium with a transmittance equal to unity. The relative error of this simplification is estimated at 5%. Further calculation of the Fresnel coefficients for such rays was carried out according to a simplified scheme, namely: a ray of greater intensity was selected from the reflected and refracted ray. The corresponding Fresnel coefficient was set to unity. For a given scattering angle, integration over two spatial coordinates and azimuth was carried out. Light losses in this scheme can only be associated with the ray reflection in the direction of the light source and with the absorption of light during specular reflection from the external cone mirror reflector.

For a narrow beam, initial geometric conditions are determined by the distance from the illuminator and the angle between the cone axis and the scattering direction. When calculating the path of wide beam rays, it is necessary to specify the distance from the cone axis to the scattering point, as well as the azimuthal angle.

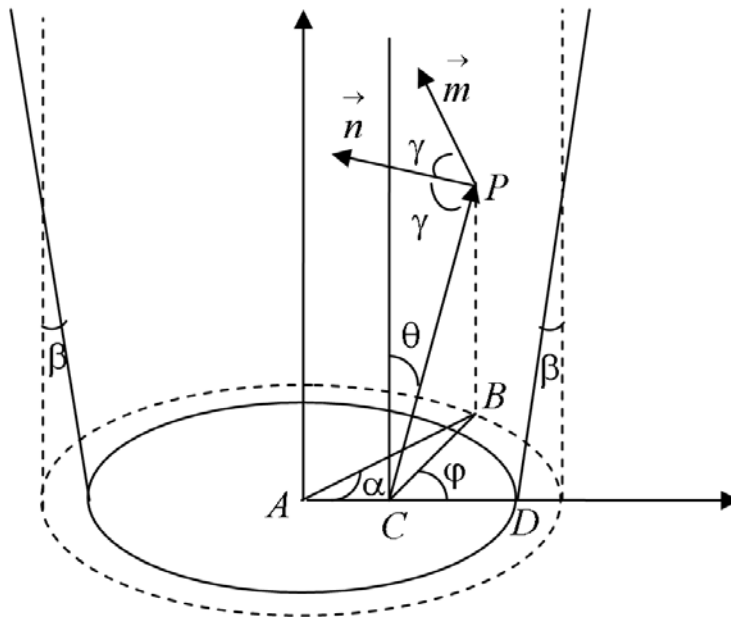


Fig. 3. Diagram of a scattered ray propagation in a cone cuvette used for calculating path length, reflection angles and their number

Let us consider the reflection geometry inside a quartz cone cuvette. Figure 3 shows a diagram of the scattered ray propagation in a cone cuvette with an opening angle of 2β . The cone axis is directed upward. The horizontal section of the cone forms a circle with r_1 radius and a center at point A. The cone is filled with sea water illuminated from below by a parallel beam. Let the direct light be scattered at point C

in a certain direction determined by zenith angle θ and azimuthal angle φ . The scattered ray intersects with the surface of the cone at height z at point P where the ray is reflected back into the medium. A horizontal section of a cone drawn through point P forms a circle with radius $r(z) = r_1 + z \cdot \operatorname{tg} \beta$, where $z = |BP|$. The circle projection is shown by a dashed line in Fig. 3.

Let us denote by x the $|AC|$ distance from the cone center. From the equations for ABC and BCP triangles, the BC segment length is determined

$$|BC| = \sqrt{(r_1 + x \cdot \operatorname{tg} \beta / \operatorname{tg} \theta)^2 - x^2 \sin^2 \varphi} - x \cdot \cos \varphi \quad (1)$$

and its corresponding height $z = |BC| / \operatorname{tg} \theta$. The path length of a light ray $|CP|$ to the reflection point is calculated using the Pythagorean Theorem.

The intersection of a ray with a cone is possible if the inequality is satisfied

$$(x \cdot \cos \varphi \cdot \operatorname{tg} \theta - r_1 \cdot \operatorname{tg} \beta)^2 \geq (x^2 - r_1^2)(\operatorname{tg}^2 \theta - \operatorname{tg}^2 \beta). \quad (2)$$

Condition (2) will be checked for cases where point C is outside the cone. Azimuth α relative to the center for the reflection point P satisfies the equation

$$\cos \alpha = \frac{|AC|}{r(z)} \cdot \sin^2 \varphi + \cos \varphi \sqrt{1 - \frac{|AC|^2}{r^2(z)} \sin^2 \varphi}. \quad (3)$$

The unit vector in the scattering direction has Cartesian coordinates

$$\vec{e}_s = (\sin \theta \cos \varphi, \sin \theta \sin \varphi, \cos \theta), \quad (4)$$

and the normal to the surface \vec{n} at the reflection point is

$$\vec{n} = (-\cos \beta \cos \alpha, -\cos \beta \sin \alpha, \sin \beta). \quad (5)$$

Cosine of reflection angle γ_r calculated through the scalar product

$$\cos \gamma_r = -(\vec{e}_s \cdot \vec{n}), \quad (6)$$

is used in determining Fresnel coefficients. The direction of reflected ray \vec{e}_r is given by the expression as follows

$$\vec{e}_r = \vec{e}_s - 2(\vec{e}_s \cdot \vec{n}) \vec{n} = \vec{e}_s + 2 \cos \gamma_r \cdot \vec{n}. \quad (7)$$

According to Snell's law $m_1 \sin \gamma_s = m_2 \sin \gamma_t$, the direction of the refracted ray \vec{e}_t is found from the following expression

$$\vec{e}_t = \frac{m_1}{m_2} \vec{e}_s + \left(\cos \gamma_t - \frac{m_1}{m_2} \cos \gamma_r \right) \vec{n}, \quad (8)$$

where m_1 is the refractive index of the medium under study; m_2 is the refractive index of the medium outside the cone.

Vector \vec{e}_r specifies the new direction of ray propagation at the next height z . Iterations are carried out until the ray leaves the cone. In this case, the number of reflections is summed up, the total path length and reflection losses are determined for any scattering angles. Integration is carried out over azimuthal angle φ , the full cross-section of the light beam and the entire length of the cone.

To demonstrate the advantages of using a cone cuvette compared to absorption measurement methods using a cylindrical cuvette [10–14], calculations using a simplified algorithm were carried out. In this case, refracted rays are not taken into account and calculations are reduced to determining the ray intersection point with the cone boundaries, as well as calculating the reflected ray direction (formulas (1) – (7)). Since the Fresnel reflection coefficient sharply decreases, starting from the angle of total internal reflection θ_f , the actual gain in saved energy is estimated through the integral of the indicatrix from the angle $90 - \theta_f$ to $90 - \theta_f + \beta$. Calculations show that the main advantage of measuring light absorption method using a cone cuvette is the reduction in the number of reflections and the reduction in path length variation depending on the scattering angle. The calculations were carried out for the following parameters: cone length $z_{\max} = 100$ mm, opening angle $2\beta = 6^\circ$, light beam circle radius equals to the minimum cone radius $r_0 = 4$ mm. The simplest case of a central ray does not require integration over two variables. The calculations for a cylindrical cuvette (a special case of a cone with a zero opening angle) with radii of 4 and 9.25 mm were also carried out.

Results and discussion

The calculations of the path of scattered rays made it possible to determine that when they propagate in a cone cuvette, half the number of reflections from the cuvette walls occurs than in a cylindrical cuvette (Fig. 4).

Reduction in the number of reflections results in the new approach permitting to weaken the effect of lengthening the path of scattered rays on the spectral absorption of light by straightening the zigzag propagation of light in the cuvette (Fig. 5).

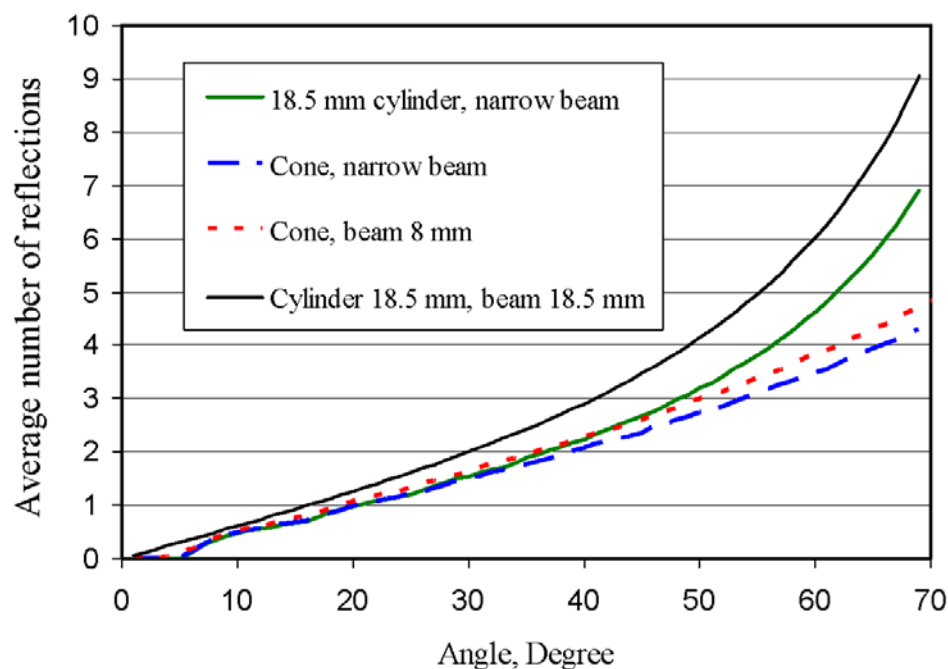


Fig. 4. Average number of reflections experienced by a beam as a function of the scattering angle

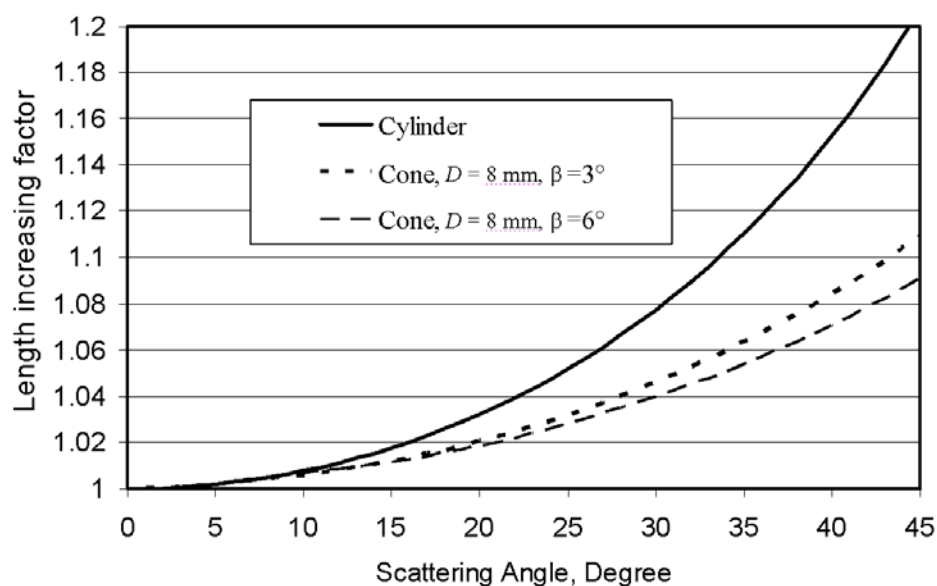


Fig. 5. Coefficient of a path length increase depending on the scattering angle for the cuvettes in the form of a cylinder and cones with the angles 6° and 12°

In a quartz cone cuvette, the region of angles where total internal reflection of scattered rays takes place becomes wider by half the cone angle, i.e., at $\beta = 3^\circ$ in

the range of 0–44.5°. According to the estimates, the proportion of scattered rays redirected to the receiving collector will increase by almost 1% for scattering indicatrices characteristic of sea water.

If the processes of reflection, refraction and transmission of light in a thin layer of quartz are neglected, then it can be argued that near the receiving collector such redirection occurs mainly as a result of a single reflection from the cuvette wall. The rays arriving at the collector after double reflection from one part of the wall to the opposite have lower intensity due to strong anisotropy of the scattering indicatrix. From the cuvette entrance to the collector, scattered rays will propagate along a zigzag path from one part of the wall to the opposite by repeated reflection along its entire length. The redirection of scattered rays as a result of single and double reflections in a cylindrical and cone cuvette occurs approximately in the same way, while for multiple reflections there is a significant difference. In a cylindrical cuvette, the propagation of scattered rays as a result of multiple reflection occurs along a uniform zigzag path with the same step. For large scattering angles, the zigzag path becomes so rapid that all rays that reached the cylindrical cuvette interface and did not experience total internal reflection eventually exit the cuvette into the air and are irretrievably lost. In a cone cuvette, the propagation of scattered rays as a result of multiple reflections from the walls occurs along an expanding zigzag path with a gradually increasing step. Accordingly, the scattered rays experience fewer reflections and therefore fewer photons are lost during interactions with the walls of the cone cuvette, as the calculation data in Fig. 6 show.

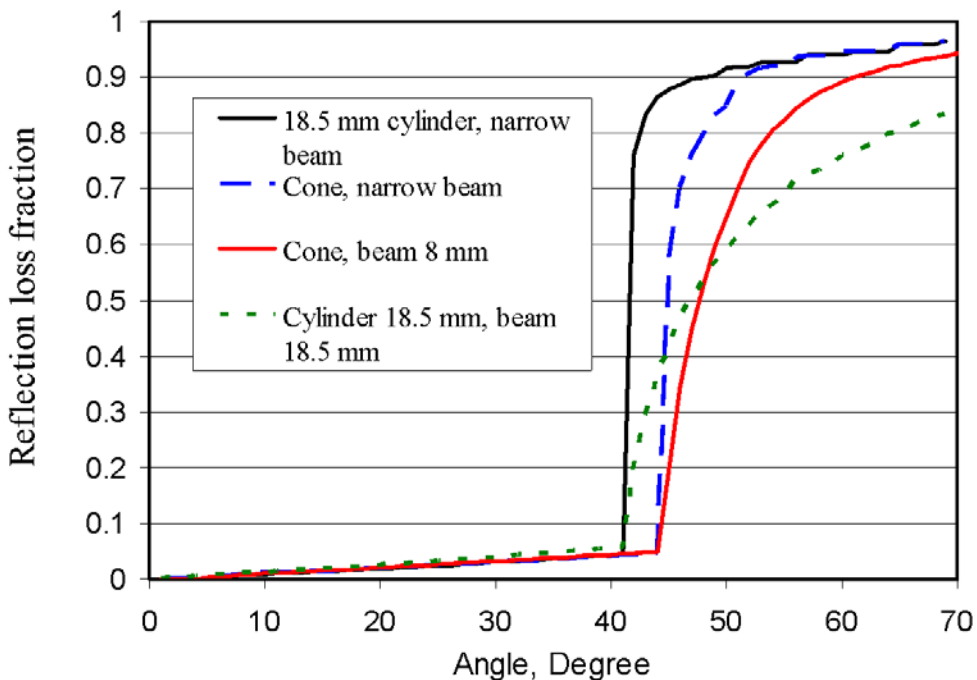


Fig. 6. Proportion of light losses in different forms of a quartz cuvette and a light beam. Calculations were carried out for the case of total internal reflection from the water – air interface, provided that another 2% of light energy is lost during reflection

According to the figure, we can see that a fraction of the energy leaving the measuring system has a characteristic step-like appearance in a device with a central narrow beam. This is explained by a sharp decrease in the Fresnel reflection coefficient after passing through the angle of total internal reflection. A strong dependence of the reflection angle on the azimuth appears in a device with a wide beam. Thus, for example, with zenith and azimuthal scattering angles equal to 90° and when the scattering point approaches the cuvette surface, the scattered light will propagate in a direction close to the tangent to the surface, which leads to specular reflection of light. Therefore, light loss as a result of ray refraction on the cuvette walls and exiting the measurement area increases more slowly. Apparently, the authors of [19] did not take into account the azimuthal dependence of the reflection angle, as evidenced by a comparison of Fig. 6 with the results of the calculations given in this study.

Consequently, a cone cuvette allows to collect more scattered rays on the receiving collector compared to a cylindrical one due to more efficient redirection of these rays from the place of light scattering in the medium to the collector. When calculating with the help of Petzold ¹ indicatrices for scattered rays in the range of angles $0-44.5^\circ$, this fraction varies within the range of 88–95% with an average value of 93%.

The remaining rays with scattering angles in the range of $44.5-90^\circ$ at the outer quartz–air interface are divided into two streams. In accordance with Fresnel’s law, part of the scattered rays enters the space between the cuvette and the mirror cone and another, reflected from the wall, returns back to the medium. As noted above, in currently used methods (reflective-tube absorption meter), these rays are irretrievably lost and their losses have to be taken into account by introducing a correction using theoretical modeling. Although the total share of these rays is relatively small and amounts to 5–12% of the total light scattering, failure to take them into account can lead in some cases to large errors in determining absorption of light in the sea. Therefore, it is important that the scattered rays leaving the cuvette, as well as the rays propagating inside the cuvette, reach the collector as far as possible without loss. Scattered rays emerging from the aquatic media propagate in the air space between the quartz cone cuvette and the cone mirror reflector. The redirection of these rays to the collector occurs either because the light from the quartz cuvette enters the air at a greater angle than in water, or because of its repeated reflection from the external mirror cone.

Conclusion

When light propagates in the sea, its scattering processes significantly prevail over absorption in high transparency waters in the spectral window, which ensures

¹ Petzold, T.J., 1972. *Volume Scattering Functions for Selected Ocean Waters: Final Report*. Warminster, Pennsylvania: Naval Air Development Center, 82 p. doi:10.21236/ad0753474

maximum light penetration into the thickness. This indicates that sea water is a weakly absorbing light-scattering medium, where the determination of light absorption depends mainly on how effectively the receiving device collects not only the light that has traveled a certain distance in the medium after absorption, but also all the light scattered along this path. A solution to this problem has been proposed by using a new approach for determining spectral absorption of light in a quartz cone cuvette placed coaxially inside an external mirror cuvette. Calculations of the ray path geometry show that a cone cuvette permits to collect up to 90% of the scattered rays on the receiving collector due to their more efficient redirection from the light scattering place in the medium to the collector. Another ~ 8% of the rays scattered at large angles can be collected at the receiving collector due to redirection through the air by an external mirror cone reflector. The combination of a quartz cone cuvette and an external mirror cone in a new approach made it possible to collect almost all the rays scattered in a weakly absorbing medium in the receiver (while in a cylindrical medium – only 75–85%) and thereby not only eliminate their strong influence on the light absorption determination in the sea, but also to abandon the need to correct data through theoretical modeling.

REFERENCES

1. Gordon, H.R. and Morel, A.Y., 1983. *Remote Assessment of Ocean Color for Interpretation of Satellite Visible Imagery. A Review*. Coastal and Estuarine Studies. Coastal, vol. 4. New York: Springer, 114 p. <https://doi.org/10.1007/978-1-4684-6280-7>
2. Levin, I.M. and Kopelevich, O.V., 2007. Correlations between the Inherent Hydrooptical Characteristics in the Spectral Range Close to 550 nm. *Oceanology*, 47(3), pp. 344-349. <https://doi.org/10.1134/S000143700703006X>
3. Smith, R.C. and Baker, K.S., 1981. Optical Properties of the Clearest Natural Waters (200–800 nm). *Applied Optics*, 20(2), pp. 177-184. <https://doi.org/10.1364/AO.20.000177>
4. Lee, Z., Wei, J., Voss, K., Lewis, M., Bricaud, A. and Huot, Y., 2015. Hyperspectral Absorption Coefficient of “Pure” Seawater in the Range of 350–550 nm Inverted from Remote Sensing Reflectance. *Applied Optics*, 54(3), pp. 546-558. <https://doi.org/10.1364/AO.54.000546>
5. Pope, R.M. and Fry, E.S., 1997. Absorption Spectrum (380–700 nm) of Pure Water. II. Integrating Cavity Measurements. *Applied Optics*, 36(33), pp. 8710-8723. <https://doi.org/10.1364/AO.36.008710>
6. Fry, E.S., Kattavar, G.W. and Pope, R.M., 1992. Integrating Cavity Absorption Meter. *Applied Optics*, 31(12), pp. 2055-2065. <https://doi.org/10.1364/AO.31.002055>
7. Merzlyak, M.N. and Naqvi, K.R., 2000. On Recording the True Absorption Spectrum and the Scattering Spectrum of a Turbid Sample: Application to Cell Suspensions of the Cyanobacterium *Anabaena Variabilis*. *Journal of Photochemistry and Photobiology B: Biology*, 58(2-3), pp. 123-129. [https://doi.org/10.1016/S1011-1344\(00\)00114-7](https://doi.org/10.1016/S1011-1344(00)00114-7)
8. Pogosyan, S.I., Durgaryan, A.M., Konyukhov, I.V., Chivkunova, O.B. and Merzlyak, M.N., 2009. Absorption Spectroscopy of Microalgae, Cyanobacteria, and Dissolved Organic Matter:

- Measurements in an Integrating Sphere Cavity. *Oceanology*, 49(6), pp. 866-871. <https://doi.org/10.1134/S0001437009060125>
9. Glukhovets, D.I., Sheberstov, S.V., Kopelevich, O.V., Zaitseva, A.F. and Poghosyan, S.I., 2018. Measuring the Sea Water Absorption Factor Using Integrating Sphere. *Light & Engineering*, 26(1), pp. 120-126. <https://doi.org/10.33383/2016-079>
 10. Clarke, G.L. and James, H.R., 1939. Laboratory Analysis of the Selective Absorption of Light by Sea Water. *Journal of the Optical Society of America*, 29(2), pp. 43-55. <https://doi.org/10.1364/JOSA.29.000043>
 11. Zaneveld, J.R.V. and Bartz, R., 1984. Beam Attenuation and Absorption Meters. In: M. A. Blizard, ed., 1984. *Proceedings SPIE*. SPIE. Vol. 0489: Ocean Optics VII, pp. 318-324. <https://doi.org/10.1117/12.943318>
 12. Zaneveld, J.R.V., Kitchen, J.C. and Moore, C.C., 1994. Scattering Error Correction of Reflecting-Tube Absorption Meters. In: J. S. Jaffe, ed., 1994. *Proceedings SPIE*. SPIE. Vol. 2258: Ocean Optics XII, pp. 44-55. <https://doi.org/10.1117/12.190095>
 13. Zaneveld, J.R.V., Bartz, R. and Kitchen, J.C., 1990. Reflective-Tube Absorption Meter. In: R. W. Spinrad, ed., 1990. *Proceedings SPIE*. SPIE. Vol. 1302: Ocean Optics X, pp. 124-136. <https://doi.org/10.1117/12.21439>
 14. Zaneveld, J.R.V., Kitchen, J.C., Bricaud, A. and Moore, C.C., 1992. Analysis of in-Situ Spectral Absorption Meter Data. In: G. D. Gilbert, ed., 1992. *Proceedings SPIE*. SPIE. Vol. 1750: Ocean Optics XI, pp. 187-200. <https://doi.org/10.1117/12.140649>
 15. Jonasz, M. and Fournier, G.R., 2007. *Light Scattering by Particles in Water. Theoretical and Experimental Foundations*. Amsterdam: Academic Press, 704 p. <https://doi.org/10.1016/B978-0-12-388751-1.X5000-5>
 16. Mankovsky, V.I. and Mankovskaya, E.V., 2020. Spatial Variability of Water Optical Characteristics in the Southern Mediterranean Sea in Spring (May, 1998). *Physical Oceanography*, 27(1), pp. 48-59. <https://doi.org/10.22449/1573-160X-2020-1-48-59>
 17. Moore, C.C., Bruce, E.J., Pegau, W.S. and Weidemann, A.D., 1997. WET Labs AC-9: Field Calibration Protocol, Deployment Techniques, Data Processing, and Design Improvements. In: S. G. Ackleson and R. J. Frouin, eds., 1997. *Proceedings SPIE*. SPIE. Vol. 2963: Ocean Optics XIII, pp. 725-730. <https://doi.org/10.1117/12.266391>
 18. Röttgers, R., McKee, D. and Woźniak, S.B., 2013. Evaluation of Scatter Corrections for AC-9 Absorption Measurements in Coastal Water. *Methods in Oceanography*, 7, pp. 21-39. <https://doi.org/10.1016/j.mio.2013.11.001>
 19. McKee, D., Piskozub, J., Röttgers, R. and Reynolds, R.A., 2013. Evaluation and Improvement of an Iterative Scattering Correction Scheme for in Situ Absorption and Attenuation Measurements. *Journal of Atmospheric and Oceanic Technology*, 30(7), pp. 1527-1541. <https://doi.org/10.1175/JTECH-D-12-00150.1>

Submitted 05.06.2023; approved after review 26.12.2023;
accepted for publication 18.01.2024.

About the authors:

Mikhail E. Lee, Chief Researcher, Marine Hydrophysical Institute of RAS (2 Kapitanskaya Str., Sevastopol, 299011, Russian Federation), DSc (Phys.-Maths), Professor, **ORCID ID: 0000-0002-2292-1877**, **ResearchID (WOS): R-4344-2018**, **Scopus Author ID: 56142710400**, michael.lee.mhi@gmail.com

Evgeniy B. Shybanov, Leading Researcher, Marine Hydrophysical Institute of RAS (2 Kapitanskaya Str., Sevastopol, 299011, Russian Federation), DSc (Phys.-Maths), **ORCID ID: 0000-0001-7943-305X**, **ResearcherID: ABB-9097-2021**, **Scopus Author ID: 6507075380**, shybanov@mail.ru

Contribution of the co-authors:

Mikhail E. Lee – basic concept, text writing, analysis of results

Evgeniy B. Shybanov – algorithm and calculation program, analysis of results, description of the calculation method, proposals for improving the design of the device

The authors have read and approved the final manuscript.

The authors declare that they have no conflict of interest.

Interannual Salinity Changes in the Upper 1000-Meter Layer of Extratropical Zone in the Northwestern Pacific Ocean under Conditions of the Intensification of Global Hydrological Cycle

I. D. Rostov ✉, E. V. Dmitrieva

V. I. Il'ichev Pacific Oceanological Institute, Far Eastern Branch of Russian Academy of Sciences, Vladivostok, Russian Federation

✉ rostov@poi.dvo.ru

Abstract

Purpose. The study is purposed at determining trends and regional features of interannual changes in salinity and salt content in the upper 1000-m layer of extratropical zone in the northwestern Pacific Ocean and at analyzing their possible cause-and-effect relations with large-scale and regional processes in the ocean and atmosphere over the last two decades of the current period of global warming.

Methods and Results. The study is based on NOAA climate data sets on salinity and current velocity in the nodes of the $0.3 \times 1^\circ$ regular grid at 31 levels for 2000–2022 derived from the oceanographic observation system GODAS (NCEP Global Ocean Data Assimilation System), as well as the series both of climate indices from the NOAA websites and routine salinity observations performed at the Rosgidromet coastal hydrometeorological stations. Besides, average monthly ERA5 reanalysis data on precipitation (Reanalysis Data ERA5 monthly 2d Surface) and evaporation from the underlying surface (WHOI OAF flux version3 monthly evap oaf flux) obtained from the NOAA Oceanographic Data Access ERDDAP server were applied. The process of analyzing involved the methods of cluster, correlation and regression analysis, as well as the apparatus of empirical orthogonal functions. The conducted research made it possible to identify and characterize the regional spatial and temporal features of the accelerated changes in salinity and salt content in the upper 1000-m water column of the studied area under conditions of the current warming phase accompanied by the intensification of global and local hydrological cycles. The quantitative characteristics of the noted trends and their statistical significance were assessed.

Conclusions. On the whole, a tendency towards a gradual decrease in average salinity near the sea surface and water desalination in the upper 1000-m layer accompanied by an increase of water heat content in this layer by 3% is observed over the water area under study.

Keywords: northwestern part of the Pacific Ocean, extratropical zone, climate changes, hydrological cycle, salinity, salt content, trends, regional features, climate indices, correlations

Acknowledgments: The study was carried out within the framework of the Comprehensive Interdepartmental Program "Ecological Safety of Kamchatka: Study and Monitoring of Hazardous Natural Phenomena and Human Impacts" (Registration number of NIOKTR 122012700198-9). The authors are grateful to the developers for the opportunity to use the climatic data posted on the NOAA and Rosgidromet websites.

For citation: Rostov, I.D. and Dmitrieva, E.V., 2024. Interannual Salinity Changes in the Upper 1000-Meter Layer of Extratropical Zone in the Northwestern Pacific Ocean under Conditions of the Intensification of Global Hydrological Cycle. *Physical Oceanography*, 31(2), pp. 194-207.

© 2024, I. D. Rostov, E. V. Dmitrieva

© 2024, Physical Oceanography

Introduction

Under conditions of accelerating global warming of the atmosphere and ocean [1–3], modern climate changes include intensification of the global water cycle (hydrologic cycle), significant interannual fluctuations in salinity and exacerbation



of spatial contrasts of ocean surface (OSS) and its water column salinity changes from regional to global scale [1, 2, 4, 5–8, 9]. At the same time, the OSS is one of the important components determining ocean circulation and the main indicator of the hydrologic cycle [6]. Large-scale humidification and warming of the atmosphere (as a reaction to an increase in the amount of greenhouse gases and water vapor in the atmosphere) enhance the combined effect of a wide range of processes – components of the water-salt balance – on the formation of OSS anomalies and three-dimensional spatial structures of the salinity field [6, 10]. The intensification of these processes is accompanied by salinity increase in areas with evaporation predominance over precipitation and desalination – in areas with precipitation predominance [1, 3, 11, 12].

Thus, the surface waters of subtropical ocean regions became saltier ($\sim +3\%$) and of tropical and high-latitude regions – fresher ($\sim -7\%$) in 1970–2005, which corresponds to an overall increase in freshwater inflow [4, 6] and leads to accelerated halosteric changes in ocean level [8]. As noted before [2, 11], the salinity field reflects a large-scale long-term balance among different components of the surface freshwater flow and the horizontal advection and mixing processes in the ocean. Corresponding response to changes in the hydrologic cycle is characterized by significant spatial and temporal heterogeneity and can be seen in the form of trends in salinity and salt content both on the surface and in the water column of oceans and seas [2, 3, 13]. Globally, the trends of a general salinity increase in the upper ocean layer, which was the greatest one in the maximum salinity area at the 100 m depth, and of decreasing salinity in the 600–1000-m layer of the intermediate minimum salinity were observed in 1970–2005 [3, 6, 14]. The upper 1500-m layer in the Pacific Ocean basin was generally desalinated [3]. At the same time, regional features and three-dimensional spatial structures of salinity and salt content variability of different ocean water column layers under conditions of the current phase of global warming and corresponding changes in the hydrologic cycle remain underestimated and require further analysis.

The present paper aims at determining trends and regional features of interannual changes in salinity and salt content in the upper 1000-m layer of extratropical zone in the northwestern Pacific Ocean and at analyzing their possible cause-and-effect relations with large-scale and regional processes in the ocean and atmosphere in the early 21st century.

Data and methods

Data on salinity and current velocity of the GODAS oceanographic observation assimilation system in grid nodes $0.3^\circ \times 1^\circ$ (<https://www.esrl.noaa.gov/psd/data/gridded/data.godas.html>) for 2000–2022 and data of regular salinity observations at Rosgidromet coastal hydrometeorological stations (HMSs) and posts off the Kamchatka eastern coast (<http://portal.esimo.ru/portal/>) were used. The average monthly data concerning precipitation (P) of the ERA5 reanalysis on a grid of $0.25^\circ \times 0.25^\circ$ (http://apdrc.soest.hawaii.edu/erddap/griddap/hawaii_soest_d124_2b_b9_c935.html) and evaporation (E) from the underlying surface of WHOI OAFlux version3 on a grid of $1^\circ \times 1^\circ$ (http://apdrc.soest.hawaii.edu/erddap/griddap/hawaii_soest_6b5a_df06_3eeb.html?page=1) were also used. The E–P difference value in one-degree grid nodes was calculated based on these data.

The reanalysis data of pressure, wind fields and a series of climate (circulation) indices (CI) [15]: NP, NPGO, PDO, SOI, PTW, IPO, WP, NINO. WEST and WPWP for the same period were also taken. The listed data were obtained from NOAA webpages <https://psl.noaa.gov/data/gridded/index.html> and <https://psl.noaa.gov/data/climateindices/list/>. In addition, the composite Kuroshio Extension (KE) index [16] was calculated synthesizing different indicators of low-frequency dynamics of waters in the area of the current continuation (extension) (31–36°N, 140–165°E) closely related to the wind regime characteristics of the northwestern Pacific Ocean.

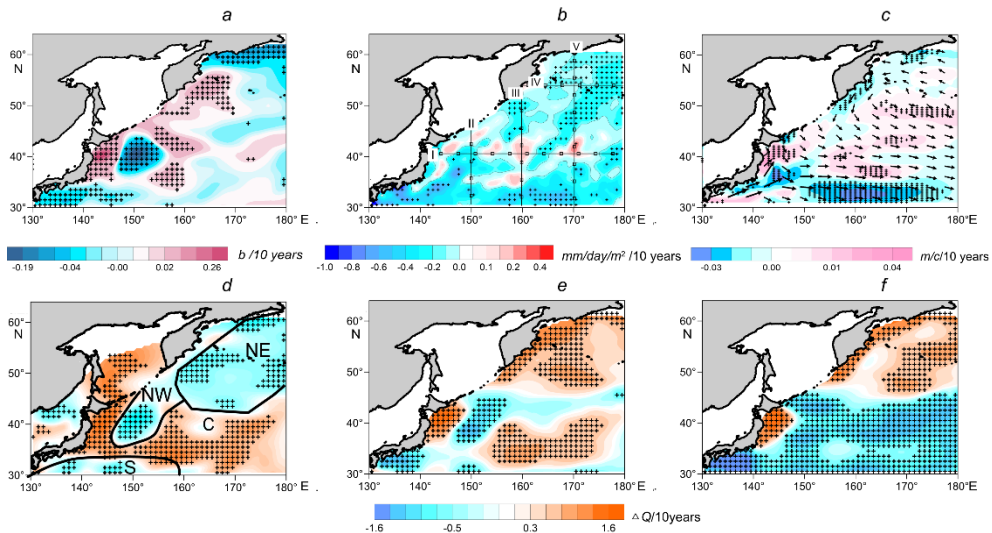


Fig. 1. Trends in mean annual salinity at the 5 m level (a), trends in mean annual evaporation-precipitation differences (b), currents (arrows) and current velocity trends (highlighted in color) at the 5 m level based on the GODAS data (c), trends in the normalized salt content values in the 5–200 m (d), 200–460 m (e) and 460–950 m layers (f) in 2000–2022. Here and in other figures, crosses indicate the areas where the estimates are statistically significant (95%). Fig. 1, b shows the section locations (I, II, III, IV and V) and Fig. 1, d shows the selected regions (NE, NW, C and S)

The calculation of statistical parameters and decomposition of anomalous fields of different characteristics into the EOF principal components (PCs) were carried out with unified methods [15]. Additionally, the values of salinity (Q_s) and their anomalies (ΔQ_s) in different depths from the surface down to 1000 meters were calculated based on GODAS data for salinity at 31 levels (uppermost depth of 5 meters) according to the equation provided in [13, p. 3520].

According to the analysis of interannual variability in the salt content of the upper 5–200-m layer, four distinct regions located in different parts of the water area were identified using cluster analysis techniques for three major components of the empirical orthogonal function (EOF): northeastern (NE), northwestern (NW), central (C) and southern (S) (Fig. 1, d). Subsequently, the long-term trend in salt content at 31 different levels and in three distinct layers: upper (5–200 m), intermediate (200–460 m) and deep (460–950 m) was determined by averaging the data from the grid within each of these four areas.

Features of interannual spatial and temporal variability of salinity field characteristics

Location of the selected regions (Fig. 1, *d*) is consistent with the position of the structural zones, frontal boundaries and the scheme of main near-surface currents [17, 18] and differs from the zoning of the field of thermal characteristics [19]. The localization of the northeastern region (NE), in which the subarctic water structure is located, corresponds to the location of the Western Subarctic Gyre. The East Kamchatka, Kuril (Oyashio) Currents and the sources of the Subarctic Current can be observed within the boundaries of the northwestern region (NW). The central region (C) position corresponds to the area of mixing of subarctic and subtropical waters in which many isolated mesoscale features and oceanographic structures are formed. The Kuroshio Extension zone is located in the southern region (S) [17, 18].

On average for the region during the period under study, a tendency for a gradual decrease in the average salinity at the surface level of 5 m from a maximum value of 33.82 in 2004 to a minimum of 33.75 in 2018 was observed in the interannual course. According to the data of the Japan Meteorological Agency (<https://ds.data.jma.go.jp/tcc/tcc/products/elnino/ensoevents.html>), the La Niña phase was expressed in the tropical zone of the Pacific Ocean during autumn 2017 – spring 2018, which was accompanied by an increase in water and air temperatures in the western sector of this zone, the development of ascending convective movements in the atmosphere, its humidification and OSS decrease [1]. Significant trends in the average annual salinity of both signs (up to ± 0.2 – 0.3 over 10 years) at the subsurface level were observed in all selected areas, but mainly in the northern and southwestern parts of the water area under consideration (Fig. 1, *a*). According to observation data at three coastal HMSs located off the Kamchatka southeastern coast (Ossora, Nikolskoye and Petropavlovsk-Kamchatsky), positive trends in interannual changes in salinity have been observed since 1999. Individual areas with maximum positive and negative salinity trends (Fig. 1, *a*) remained well defined throughout the entire water area both in the warm and cold periods of the year.

As noted above, the formation of large-scale spatial and temporal features of the salinity field occurs under changing weather conditions, evaporation, precipitation and other components of the water-salt balance under the influence of advection and vertical mixing processes.

Statistically significant trends in the increase in average annual precipitation were observed in the first decades of the current century (trend 0.3 – 0.5 mm/day/m² over 10 years), mainly in the northern part of the water area, north of 40 – 45°N , with a maximum value in the cold season (trend 0.5 – 1.0 mm/day/m² over 10 years). Moreover, negative trends in precipitation were expressed in the warm period (from -0.3 to -0.9 mm/day/m² over 10 years) in the southwestern part of the water area, south of 40°N . Almost no significant trends in precipitation of both signs were observed in the warm period of the year. It should be noted that similar estimates of precipitation according to <https://psl.noaa.gov/data/gridded/data.cmap.html> on a $2.5^{\circ} \times 2.5^{\circ}$ grid differ somewhat from the above estimates as they are significantly less pronounced by positive trends.

In the interannual course, statistically significant positive trends in average annual evaporation values are expressed within the boundaries of the northeastern

and northwestern regions, negative ones – mainly in the central and southern regions. The spatial distribution of trends in the evaporation-precipitation difference (E–P) demonstrates the predominant nature of precipitation over most of the water area (Fig. 1, *b*) corresponding to global trends in the hydrologic cycle in the middle and high latitudes of the Northern Hemisphere [6, 14], but poorly consistent with the salinity trend distribution (Fig. 1, *a*). As noted earlier [11], in contrast to long-term changes in the characteristics of salinity and humidification of the ocean surface on a global scale [3], trends in spatial changes in the E–P difference in the middle and high latitudes may not coincide with the corresponding regional trends in changes in salinity, since ocean dynamics and local factors can also play a controlling role in changes in the salinity field on the surface and in the ocean water column ensuring its regional balance [14]. One of these factors includes the influence of the processes of ice cover formation and destruction, usually expressed in the seasonal salinity course. At the same time, the analysis did not show any statistically significant linear trends in the long-term distributions of ice cover in the Bering Sea. Its sharp decrease was observed only in recent years after the harsh winter of 2011–2012 [20]. The role of spatial and temporal variability of individual components of the water-salt balance, as well as ocean dynamics (Fig. 1, *c*), in the formation of salinity field anomalies will be considered below based on the correlation and regression analysis methods.

Patterns of spatial features of interannual changes in salt content trends (Q_s) of the upper, intermediate and deep layers differ significantly from each other (Fig. 1, *d–f*). If in the upper layer the trends of water desalination are expressed only within the boundaries of the northeastern, northwestern and southern regions and salinization trends – in the central region, then this pattern is completely rearranged with increasing depth. Within the intermediate and deep layers of the northwestern Bering Sea and the adjacent waters, extensive areas of increasing salt content are formed and in the deep layer mostly located south of 45°N areas of accelerated water desalination caused by an increase in the fresher water inflow in this latitudinal band are observed [6]. At the same time, in the western part of the Pacific Ocean tropical zone, conditions of precipitation exceeding evaporation prevailed along with trends in increasing the heat and water vapor transfer to temperate latitudes [1, 21, 22], and in the western part of the subtropical gyre, in the Kuroshio region and the northern part of the Philippine Sea, rapid desalination of the upper 800-meter layer in the main halocline region was noted starting from the mid-1990s [23], which can be seen in Fig. 1, *a, d–f* in the region of Kuroshio and Kuroshio Extension [17, 18]. The noted trends in the decrease in deep layer salinity and salt content under conditions of intensification of the global hydrological cycle are consistent with the results of other researchers [3, 6, 14]. The spatial distribution patterns of salinity trends in the upper and intermediate layers in the warm and cold periods of the year do not show any noticeable differences.

An interesting feature of the distribution of salinity trends at the surface and the salt content of the entire water column is the localization of the area of their statistically significant positive values in the area located to the southeast of Hokkaido and adjacent to the Sangar Strait (Fig. 1, *a, d–f*). As noted before [19], this area with positive trends in heat and salt content was formed as a result of increased water exchange with adjacent areas of the eastern part of the Sea of Japan

(Fig. 1, *c*). Another feature is the area with the maximum negative trends of these values located to the east, with the center in the region of 40–45°N, 150°E, in the zone of convergence of desalinated waters of the Kuril and Subarctic Currents [18]. These features of the distribution of negative trends in salinity and salt content can be observed within the entire 1000-m layer and can be associated with the the wind field [14] effect and the intensification of mesoscale “Kuril” anticyclonic eddies [24] containing cold and desalinated water from the Sea of Okhotsk [19, 25]. The maximum values for the standard deviation of interannual fluctuations in salt content in the 5–200 m layer for the entire region are clearly expressed in the two mentioned regions. The main features of the spatial structure of the trends in the salt content of the upper and intermediate layers (Fig. 1, *d*, *e*) are in good agreement with the distribution scheme of the coefficients of the first EOF1 mode of decomposition of Q_s anomalies, which makes it possible to use the principal component (PC1) of this method of parameterizing Q_s fluctuations of these layers to establish correlations with different climate parameters.

Interannual variability of vertical salinity structure of the upper 1000-m layer

According to GODAS data, average profiles of the vertical distribution of salinity for each year and an average profile for the entire 2000–2022 period were obtained within the selected water areas. An analysis of the vertical distribution of trends in average annual salinity at different levels and the principal component PC1 of the EOF for a set of profiles was also carried out (Fig. 2). Analysis of the results obtained revealed a more complex picture compared to that observed in the variability of these characteristics averaged over the entire ocean basin [1, 3, 6, 9, 14] and subject to strong seasonal fluctuations [11].

Smoothed as a result of spatial averaging, the features of the vertical structure of salinity in the area of subarctic water distribution (NE and NW regions) are characterized by a monotonous increase in salinity with depth in the entire upper 1000-meter layer (Fig. 2, *a*, *d*). Maximum and minimum salinity layers with cores at depths of ~ 200 m and ~ 600–800 m, respectively, are observed in the zone of mixing of subarctic and subtropical waters and the Kuroshio Extension (C and S regions), below the upper halocline (Fig. 2, *g*, *j*). These layers are identified as subtropical and intermediate waters of the North Pacific Ocean with salinities of ~ 34.4–34.8 and 34.0–34.3 [26]. The PC1(z) curves (Fig. 2, *b*, *e*, *h*, *k*) characterize the amplitude structure of salinity fluctuations at different levels and approximately correspond to the vertical distribution of the range of its changes in the interannual variation (up to 0.11–0.20) and the vertical distribution of salinity trends $b(z)$. The correlation coefficient (R) of PC1(z) and $b(z)$ fluctuations is ± 0.9 . In general, the principal component PC1(S) in the studied regions accounts for from 53% (S region) to 82–90% (other regions) of the total salinity dispersion at different levels. Features of the vertical structure of salinity trends are formed as a result of the interaction of a wide range of different-scale processes on the ocean surface, advection and vertical mixing. However, in contrast to the characteristics of the vertical amplitude structure of temperature fluctuations in the studied region [19], the maximum values on the PC1(S) curves are observed not only in the upper part of the active layer (Fig. 2, *b*, *e*), but also in the underlying layers of the water column (Fig. 2, *h*, *k*).

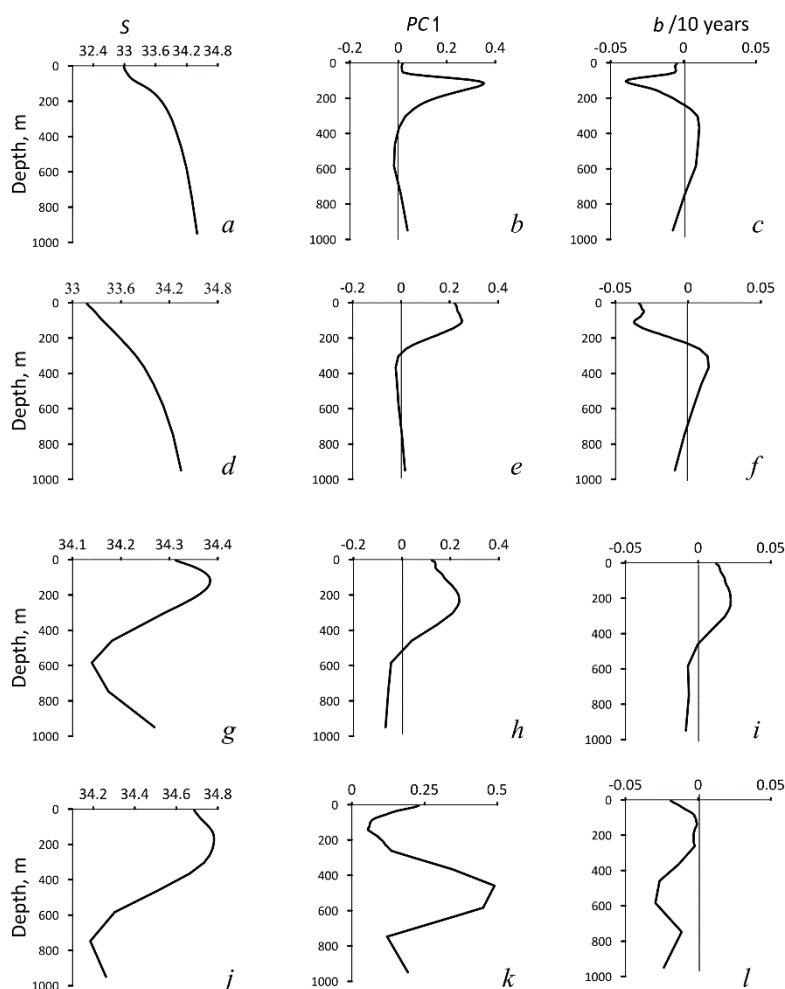


Fig. 2. Generalized curves of vertical distribution of salinity (*a, d, g, j*), principal component PC1 of the EOF of salinity anomalies (*b, e, h, k*) and salinity trend (*b*) at different levels (*c, f, i, l*) for 2000–2022. From top to bottom: the NE, NW, C, S regions according to Fig. 1, *d*

Analysis of interannual trends of statistically significant changes in the vertical structure of salinity showed that maximum freshening had occurred in the upper halocline (-0.04 over 10 years) in the NE and NW regions (Fig. 2, *c, f*) and in the minimum salinity layer (-0.03 for 10 years) in the S region (Fig. 2, *l*). The highest salinity (0.02 over 10 years) was observed in the upper layer of maximum salinity, in the central region (Fig. 2, *i*). These trends are also evident in corresponding changes in estimates of salinity trends in different layers of the studied areas (Table 1; Fig. 1, *d–f*).

Table 1 shows that desalination of the upper and lower layers and salinization of the intermediate layers, which was accompanied by a decrease in the salt content of the entire 1000-meter water column, generally occurred within the entire water area under study for the first decades of the 21st century. As noted earlier [19], an increase by statistically significant 3% was observed in the heat content of this layer water column.

Table 1

Estimates of the linear trend of salt content (Q_s , $\text{kg} \cdot \text{m}^{-2}/10$ years) in different layers of water column in the identified areas and the entire water area in the 2000–2022 period

Region	Layer boundaries, m			
	5–200	200–460	460–950	5–950
NE	–3.59	1.90	1.30	–0.13
NW	–5.89	2.36	–0.27	–1.26
C	3.71	3.50	–3.03	1.39
S	–0.91	–2.32	–9.76	–4.33
Average over the entire water area	–1.67	1.36	–2.94	–1.08

Note. Statistically significant (95%) estimates are highlighted in bold here and in Table 2.

Spatial features of the vertical structure of the water column with different values of desalination and salinization trends are expressed on zonal and meridional sections crossing the water area (Fig. 3).

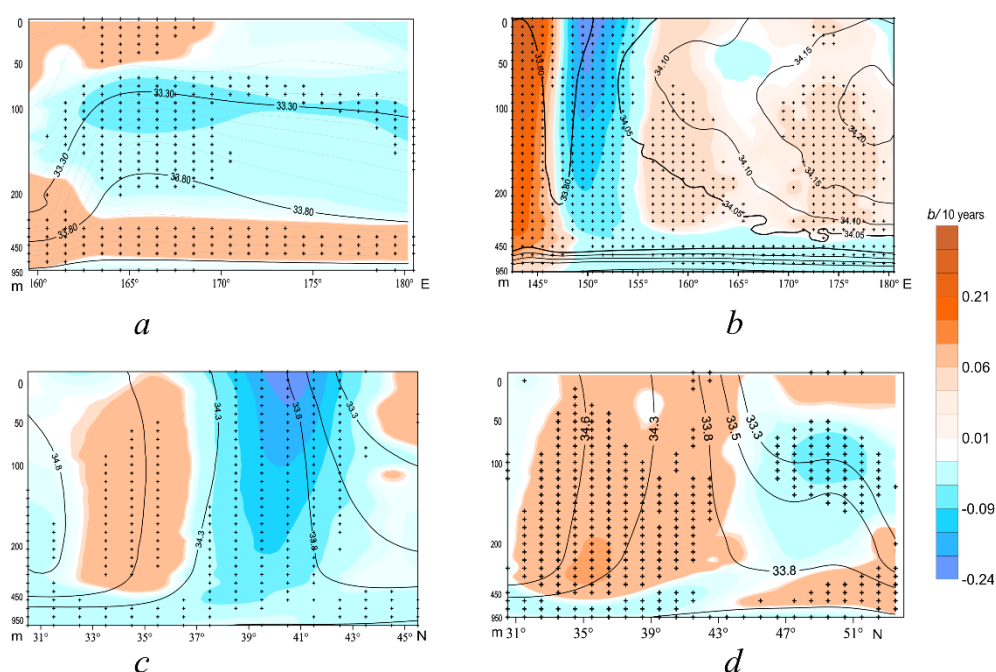


Fig. 3. Combined vertical distribution of salinity (solid lines) and salinity trends (highlighted in color) in zonal sections IV at 53°N (*a*) and I along 40°N (*b*) and at the meridional sections II along 150°E (*c*) and III along 160°E (*d*) in 2000–2022. Section locations are shown in Fig. 1, *b*

The aforementioned features of stratification – layers (water masses) of high and low salinity associated with their sources of origin – are distinguished in all isohaline field sections. The area of maximum statistically significant negative salinity trends can be observed in northern zonal section IV (Fig. 3, *a*) in the 100–400 m layer, in the zone of the greatest horizontal salinity gradients on the western boundary of the North Pacific Gyre and the East Kamchatka Current [11, 18]. Significant positive salinity gradients are expressed in the underlying water column of the entire section

and in the near-surface layer of the western part of this section, which corresponds to Fig. 1. The vertical structure of the salinity field and its trends is completely rearranged in zonal section I (Fig. 1, *b*). One desalination zone with the greatest negative trends in salinity is located in the southern part of the selected NW region (148°–155°E) – the convergence zone of desalinated waters of the Kuril and Subarctic Currents – and covers the entire water column of the upper 1000-meter layer. As noted above, to the west of this zone an area with maximum positive trends in salinity and heat content is pronounced, which is formed as a result of increased water exchange with adjacent areas of the eastern part of the Sea of Japan through the Sangar Strait. Another desalination zone can be observed in the deep layer of 460–1000 m throughout the entire length of section I east of 148°E.

A desalination zone with the greatest negative salinity trends between 37–42°N is also well defined in meridional section II (Fig. 3, *c*) located in the western part of the studied water area. However, the volume of the water column (with the exception of the deep layer of desalinated subarctic waters), in which statistically significant negative salinity trends are observed, gradually decreases, and the volume of the water column with positive trends increases in sections III (Fig. 3, *d*) and V located east of section II.

Correlations of interannual changes in salinity field characteristics with large-scale and regional processes in the ocean and atmosphere

A mutual correlation and regression analysis of interannual variations in time series of salt content and time coefficients (PC1) of the first EOF mode of decomposition of Q_s anomalies in the upper and intermediate water column layers with fluctuations in climate indices and other indicators characterizing both the dynamics of the climate system of the atmosphere and ocean and humidification regime in the study area was carried out. Correlation connections in changes in the average annual values of salt content Q_s in 5–200 and 200–460 m layers (over the entire region) with different climate variables are most pronounced with the following parameters: NPGO indices (with a time lag of 1 year), KE, WPWP, the second EOF PC2 mode of fluctuations in evaporation-precipitation (E–P) values and the first mode of fluctuations in geopotential anomalies of the isobaric surface $AT_{500} - PC1(\Delta H_{500})$ (Table 2).

The interannual variability of these parameters (except for KE) showed significant trends of different signs during the period under consideration. Maps of the spatial distribution of regression coefficients (Fig. 4) provide a visual representation of the nature of spatial features and the closeness of correlations of changes in salt content and the most important climate parameters in different areas reflecting both regional processes and inter-basin interaction, as well as the remote impact of atmospheric and ocean circulation. These features are in good agreement with the distribution patterns of salt content trends in the upper and intermediate layers (Fig. 1, *d*, *e*).

The identified relationships characterize the impact of interannual changes in the humidification regime on the ocean surface, advection and vertical mixing, and corresponding regression coefficients are statistically significant over most of the studied water area. These connections are complex and ambiguous and their

nature in the upper (Fig. 4, *a – c*) and intermediate (Fig. 4, *d, e*) layers changes significantly with depth. The NPGO index reflects changes in the intensity of the large-scale North Pacific Gyre, is influenced by variability in the position and severity of the atmospheric action centers and the surface wind field associated with sea level pressure fluctuations in the northern Pacific Ocean and has a remote and delayed effect on the Kuroshio-Oyashio current system and thermal conditions of adjacent areas of the marginal seas of the western Pacific Ocean with some phase delay [27].

Table 2

Correlation coefficients of average annual salt content values (Qs) in the 5–200 m and 200–460 m layers with climate indices for different regions for 2000–2022					
Regions	Parameter				
	NPGO	KE	WPWP	PC2(E–P)	PC1(ΔH_{500})
<i>5–200 m layer</i>					
NE	0.4	0.2	–0.4	0.6	–0.3
NW	0.7	–0.4	0.6	0.7	–0.6
C	–0.7	0.3	0.6	–0.7	0.6
S	0.4	0.2	–0.3	0.3	–0.5
Entire water area	0.7	0.0	–0.5	0.8	–0.6
<i>200–460 m layer</i>					
NE	–0.2	0.6	0.5	–0.2	0.4
NW	–0.1	0.1	0.0	–0.2	0.0
C	–0.4	0.6	0.5	–0.5	0.4
S	0.0	0.3	–0.1	0.1	–0.1
Entire water area	–0.3	0.7	0.4	–0.3	0.3

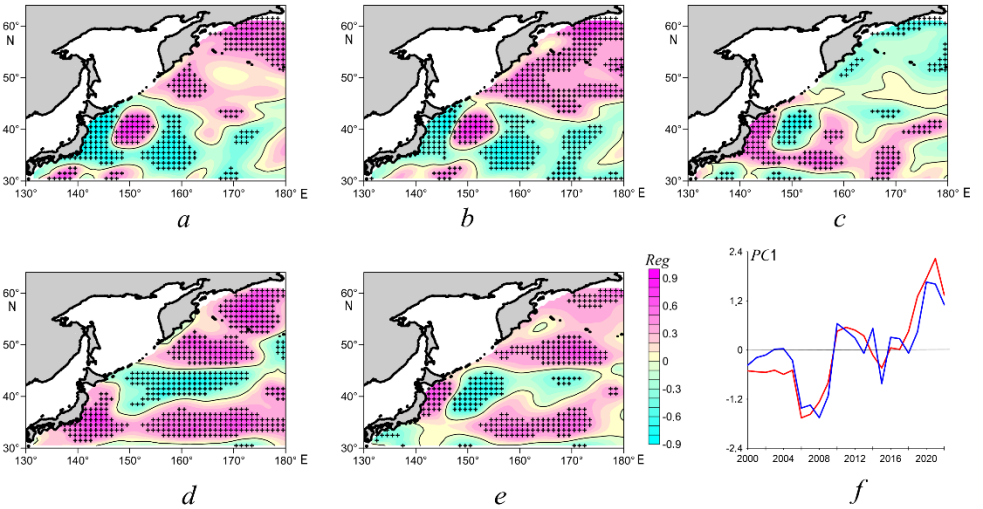


Fig. 4. Linear regression coefficients (Reg) of fluctuations Qs of the average annual salt content anomalies in the 5–200 m layer with NPGO (*a*), PC2(E–P) of evaporation–precipitation difference (*b*) and PC1(ΔH_{500}) (*c*) in 2000–2022. The same is for fluctuations Qs of the 200–600 m layer with KE (*d*) and WPWP (*e*); interannual changes in PC1(Qs) of the intermediate 200–460 m layer (red curve) and the fitting curve of the multiple regression equation with different climate indices (blue curve) (*f*)

The KE index characterizes low-frequency variability of the Kuroshio Extension region – simultaneous changes in its latitudinal position, eastward water transport, level of kinetic energy of eddies and strength of the southern recirculation gyre [16]. The WPWP index characterizes the thermal state of a warm tropical basin located in the western part of the Pacific Ocean equatorial zone [28]. Synchronous connections in interannual fluctuations of these indices are statistically significant ($R = 0.5$). The PC2(E–P) index characterizes current changes in fresh water flow on the sea surface or humidification regime, and PC1(ΔH_{500}) index shows trends in changes in the pressure field of the isobaric surface geopotential of 500 hPa in the middle troposphere. Fluctuations in these parameters are characterized by negative correlations ($R = -0.6$) in the warm season.

Variations in the main EOF modes of geopotential anomalies (ΔH_{500}) in the region are closely related to fluctuations in ocean surface temperature, wind field, different climate indices and changes in atmospheric circulation in the region [19]. Thus, their fluctuation connectivity is characterized by correlation coefficient $R = -0.8$ with multidirectional trends in interannual changes in PC1(ΔH_{500}) and NPGO. At the same time, the Aleutian Low weakening and strengthening of anticyclonic conditions are accompanied by the NPGO weakening, which can be seen in the current field (Fig. 1, *c*) and in the distribution of corresponding regression coefficients (Fig. 4, *a*).

Note that the value of the explained variance (R^2) of the multiple regression of PC1(Qs) variability of the upper 5–200 m layer and NPGO, PC2(E–P) and PC1(ΔH_{500}) climate variables for 2000–2022 was 58%, i.e., these variables describe satisfactorily the observed Qs changes. For the 200–460 m layer, the R^2 value of multiple regression of these climate indices (Table 2), as well as additional climate indices (NINO.WEST, IPO), was 89% (Fig. 4, *f*). The IPO, WPWP and NINO.WEST indices are commonly used to describe and parameterize the multi-scale variability of thermal conditions in the tropical Pacific Ocean [28, 29].

Conclusion

The performed studies made it possible to identify and characterize regional spatial and temporal features of previously discovered accelerated changes in salinity and salt content in the water column of the upper 1000 m of the studied area under the conditions of the current warming phase accompanied by the intensification of global and local hydrological cycles. Quantitative characteristics of the noted trends and their statistical significance were estimated.

This period was characterized by trends in decreasing precipitation and evaporation from the ocean surface in the southern part of the studied water area with a simultaneous increase in these humidity balance indicators in the north (primarily precipitation – up to 1.0 mm/day/m² over 10 years during the cold year period). In general, statistically significant negative trends in the evaporation-precipitation difference were observed throughout the region. In addition, significant changes in different indicators of atmospheric and ocean circulation accompanied by increased water exchange in the extratropical zone of the ocean with adjacent areas were observed at this time, which led to the formation of vast volumes of water columns subject to both desalination and salinization with subsequent transformation of water masses.

Extensive areas of statistically significant S trends of two signs (up to ± 0.2 – 0.3 over 10 years) were identified in the interannual variation of the average annual salinity at a near-surface level of 5 m in the northern and southwestern parts of the water area under consideration. In general, the water area shows a tendency for a gradual decrease in average salinity values at the surface from a maximum of 33.82 in 2004 to a minimum of 33.75 in 2018.

Variability of the upper 200-m layer salt content Qs demonstrates a tendency towards freshening in the water distribution area of the subarctic structure north of 40–45°N with a trend from -3.6 to -5.9 $\text{kg}\cdot\text{m}^{-2}/10$ years and in the Kuroshio Extension strip in the southwestern part of the studied water area (~ -0.9 $\text{kg}\cdot\text{m}^{-2}/10$ years). An increasing salt content zone at a rate of ~ 3.7 $\text{kg}\cdot\text{m}^{-2}/10$ years is located in the transition zone between these areas. On average, the upper layer waters are desalinated by ~ -1.7 $\text{kg}\cdot\text{m}^{-2}/10$ years throughout the entire water area.

The spatial structure of salt content trends is completely rearranged with increasing depth within the intermediate (200–460 m) and deep (460–950 m) layers. On average, salinization of the intermediate layer waters (1.9 $\text{kg}\cdot\text{m}^{-2}/10$ years) and desalination of the deep layer (-0.3 $\text{kg}\cdot\text{m}^{-2}/10$ years) are observed throughout the entire water area. Moreover, the average salt content of water in the upper 1000-m layer throughout the studied area decreased at a rate of -1.1 $\text{kg}\cdot\text{m}^{-2}/10$ years in 2000–2022. According to the authors' earlier estimates, these changes were accompanied by an increase in the heat content of this layer waters by 3%.

In the region as a whole, correlations of changes in the average annual values of salt content Qs in the upper and intermediate 5–200 and 200–460 m layers are most pronounced with the following climate indices and variables: NPGO (with a time lag of 1 year), KE, WPWP, the second EOF mode of fluctuation of evaporation-precipitation (E-P) values and AT₅₀₀ isobaric surface geopotential anomalies.

REFERENCES

1. Intergovernmental Panel on Climate Change (IPCC), 2023. *Climate Change 2021 – The Physical Science Basis: Working Group I Contribution to the Sixth Assessment Report of the Intergovernmental Panel on Climate Change*. Cambridge, United Kingdom: Cambridge University Press, 2391 p. <https://doi.org/10.1017/9781009157896>
2. Durack, P.J. and Wijffels, S.E., 2010. Fifty-Year Trends in Global Ocean Salinities and Their Relationship to Broad-Scale Warming. *Journal of Climate*, 23(16), pp. 4342–4362. <https://doi.org/10.1175/2010JCLI3377.1>
3. Skliris, N., Marsh, R., Josey, S.A., Good, S.A., Liu, C. and Allan, R.P., 2014. Salinity Changes in the World Ocean since 1950 in Relation to Changing Surface Freshwater Fluxes. *Climate Dynamics*, 43(3–4), pp. 709–736. <https://doi.org/10.1007/s00382-014-2131-7>
4. Cheng, L., Trenberth, K.E., Gruber, N., Abraham, J.P., Fasullo, J.T., Li, G., Mann, M.E., Zhao, X. and Zhu, J., 2020. Improved Estimates of Changes in Upper Ocean Salinity and the Hydrological Cycle. *Journal of Climate*, 33(23), pp. 10357–10381. <https://doi.org/10.1175/JCLI-D-20-0366.1>
5. Durack, P.J., Wijffels, S.E. and Matear, R.J., 2012. Ocean Salinities Reveal Strong Global Water Cycle Intensification during 1950 to 2000. *Science*, 336(6080), pp. 455–458. <https://doi.org/10.1126/science.1212222>
6. Helm, K.P., Bindoff, N.L. and Church, J.A., 2010. Changes in the Global Hydrological-Cycle Inferred from Ocean Salinity. *Geophysical Research Letters*, 37(18), L18701. <https://doi.org/10.1029/2010GL044222>

7. Hosoda, S., Suga, T., Shikama, N. and Mizuno, K., 2009. Global Surface Layer Salinity Change Detected by Argo and Its Implication for Hydrological Cycle Intensification. *Journal of Oceanography*, 65(4), pp. 579-586. <https://doi.org/10.1007/s10872-009-0049-1>
8. Malinin, V.N., 2012. *The Ocean Level: Present and Future*. Saint Petersburg: RSHU Publishers, 260 p. (in Russian).
9. Aretxabaleta, A.L., Smith, K.W. and Kalra, T.S., 2017. Regime Changes in Global Sea Surface Salinity Trend. *Journal of Marine Science and Engineering*, 5(4), 57. <https://doi.org/10.3390/jmse5040057>
10. Zika, J.D., Skliris, N., Nurser, A.J.G., Josey, S.A., Mudryk, L., Laliberté, F. and Marsh, R., 2015. Maintenance and Broadening of the Ocean's Salinity Distribution by the Water Cycle. *Journal of Climate*, 28(24), pp. 9550-9560. <https://doi.org/10.1175/JCLI-D-15-0273.1>
11. Liu, Y., Cheng, L., Pan, Y., Abraham, J., Zhang, B., Zhu, J. and Song, J., 2022. Climatological Seasonal Variation of the Upper Ocean Salinity. *International Journal of Climatology*, 42(6), pp. 3477-3498. <https://doi.org/10.1002/joc.7428>
12. Yu, L., Josey, S.A., Bingham, F.M. and Lee, T., 2020. Intensification of the Global Water Cycle and Evidence from Ocean Salinity: A Synthesis Review. *Annals of the New York Academy of Sciences*, 1472(1), pp. 76-94. <https://doi.org/10.1111/nyas.14354>
13. Corbett, C.M., Subrahmanyam, B. and Giese, B.S., 2017. A Comparison of Sea Surface Salinity in the Equatorial Pacific Ocean during the 1997-1998, 2012-2013, and 2014-2015 ENSO Events. *Climate Dynamics*, 49(9-10), pp. 3513-3526. <https://doi.org/10.1007/s00382-017-3527-y>
14. Li, G., Zhang, Y., Xiao, J., Song, X., Abraham, J., Cheng, L. and Zhu, J., 2019. Examining the Salinity Change in the Upper Pacific Ocean during the Argo Period. *Climate Dynamics*, 53(9-11), pp. 6055-6074. <https://doi.org/10.1007/s00382-019-04912-z>
15. Rostov, I.D., Dmitrieva, E.V. and Rudykh, N.I., 2021. Interannual Variability of Thermal Conditions in the Extratropical Zone of the South Pacific at the Turn of the XX-XXI Centuries. *Physical Oceanography*, 28(6), pp. 612-631. <https://doi.org/10.22449/1573-160X-2021-6-612-631>
16. Qiu, B., Chen, S., Schneider, N., Oka, E. and Sugimoto, S., 2020. On the Reset of the Wind-Forced Decadal Kuroshio Extension Variability in Late 2017. *Journal of Climate*, 33(24), pp. 10813-10828. <https://doi.org/10.1175/JCLI-D-20-0237.1>
17. Kuroda, H., Suyama, S., Miyamoto, H., Setou, T. and Nakanowatari, T., 2021. Interdecadal Variability of the Western Subarctic Gyre in the North Pacific Ocean. *Deep Sea Research Part I: Oceanographic Research Papers*, 169, 103461. <https://doi.org/10.1016/j.dsr.2020.103461>
18. Yasuda, I., 2003. Hydrographic Structure and Variability in the Kuroshio-Oyashio Transition Area. *Journal of Oceanography*, 59(4), pp. 389-402. <https://doi.org/10.1023/A:1025580313836>
19. Rostov, I.D., Dmitrieva, E.V. and Rudykh, N.I., 2023. Interannual Variability of Thermal Characteristics of the Upper 1000-Meter Layer in the Extratropical Zone of the Northwestern Part of the Pacific Ocean at the Turn of the XX-XXI Centuries. *Physical Oceanography*, 30(2), pp. 141-159.
20. Kattsov, V.M., ed., 2022. *[Third Assessment Report on Climate Changes and Their Consequences on the Territory of the Russian Federation]*. Saint Petersburg: Naukoemkie Technologii, 676 p. (in Russian).
21. Kamae, Y., Mei, W., Xie, S.-P., Naoi, M. and Ueda, H., 2017. Atmospheric Rivers over the Northwestern Pacific: Climatology and Interannual Variability. *Journal of Climate*, 30(15), pp. 5605-5619. <https://doi.org/10.1175/jcli-d-16-0875.1>
22. Oey, L.-Y. and Chou, S., 2016. Evidence of Rising and Poleward Shift of Storm Surge in Western North Pacific in Recent Decades. *Journal of Geophysical Research: Oceans*, 121(7), pp. 5181-5192. <https://doi.org/10.1002/2016JC011777>
23. Oka, E., Katsura, S., Inoue, H., Kojima, A., Kitamoto, M., Nakano, T. and Suga, T., 2017. Long-Term Change and Variation of Salinity in the Western North Pacific Subtropical Gyre

- Revealed by 50-Year Long Observations along 137° E. *Journal of Oceanography*, 73(4), pp. 479-490. <https://doi.org/10.1007/s10872-017-0416-2>
24. Yasuda, I., Ito, S.-I., Shimizu, Y., Ichikawa, K., Ueda, K.-I., Honma, T., Uchiyama, M., Watanabe, K., Sunou, N. [et al.], 2000. Cold-Core Anticyclonic Eddies South of the Bussol' Strait in the Northwestern Subarctic Pacific. *Journal of Physical Oceanography*, 30(6), pp. 1137-1157. [https://doi.org/10.1175/1520-0485\(2000\)030<1137:CCAESO>2.0.CO;2](https://doi.org/10.1175/1520-0485(2000)030<1137:CCAESO>2.0.CO;2)
 25. Itoh, S. and Yasuda, I., 2010. Characteristics of Mesoscale Eddies in the Kuroshio–Oyashio Extension Region Detected from the Distribution of the Sea Surface Height Anomaly. *Journal of Physical Oceanography*, 40(5), pp. 1018-1034. <https://doi.org/10.1175/2009JPO4265.1>
 27. Ceballos, L.I., Di Lorenzo, E., Hoyos, C.D., Schneider, N. and Taguchi, B., 2009. North Pacific Gyre Oscillation Synchronizes Climate Fluctuations in the Eastern and Western Boundary Systems. *Journal of Climate*, 22(19), pp. 5163-5174. <https://doi.org/10.1175/2009JCLI2848.1>
 28. Cravatte, S., Delcroix, T., Zhang, D., McPhaden, M. and Leloup, J., 2009. Observed Freshening and Warming of the Western Pacific Warm Pool. *Climate Dynamics*, 33(4), pp. 565-589. <https://doi.org/10.1007/s00382-009-0526-7>
 29. Henley, B.J., Gergis, J., Karoly, D.J., Power, S., Kennedy, J. and Folland, C.K., 2015. A Tripole Index for the Interdecadal Pacific Oscillation. *Climate Dynamics*, 45(11-12), pp. 3077-3090. <https://doi.org/10.1007/s00382-015-2525-1>

Submitted 05.07.2023; approved after review 26.12.2023;
accepted for publication 18.01.2024.

About the authors:

Igor D. Rostov, Head of the Informatics and Ocean Monitoring Laboratory, V.I. Il'ichev Pacific Oceanological Institute, Far Eastern Branch of RAS (3 Baltiyskaya Street, Vladivostok, 690041, Russian Federation), CSc. (Geogr.), **ORCID ID: 0000-0001-5081-7279**, rostov@poi.dvo.ru

Elena V. Dmitrieva, Senior Research Associate, Informatics and Ocean Monitoring Laboratory, V.I. Il'ichev Pacific Oceanological Institute, Far Eastern Branch of RAS (3 Baltiyskaya Street, Vladivostok, 690041, Russian Federation), CSc. (Techn. Sci.), **ORCID ID: 0000-0002-0094-5296**, e_dmitrieva@poi.dvo.ru

Contribution of the authors:

Igor D. Rostov – development of the article structure, processing and analysis of the data, writing the article text

Elena V. Dmitrieva – collection and processing of oceanographic data, calculations, drawing design, text editing

All the authors have read and approved the final manuscript.

The authors declare that they have no conflict of interest.

Original article

Wave Nature and Modulation of Annual Fluctuations in the Level of the Baltic Sea

E.A. Zakharchuk¹, V.N. Sukhachev^{1, 2, ✉}, N.A. Tikhonova^{1, 2}

¹ Saint Petersburg State University, Saint Petersburg, Russian Federation

² N. N. Zubov State Oceanographic Institute, Moscow, Russian Federation

✉ Syhachev@mail.ru

Abstract

Purpose. The study is purposed at estimating the features of spatial-temporal variability of the characteristics of annual fluctuations of the Baltic Sea level based on satellite and contact measurements, their comparing with theoretical dispersion relations of the low-frequency waves of different types, as well as investigating possible mechanisms of the amplitude modulation of annual fluctuations of the Baltic Sea level.

Methods and results. The hypothesis on a wave nature of annual fluctuations of the Baltic Sea level is tested and the reasons for their amplitude modulation are investigated based on the harmonic analysis of satellite altimetry data and the 132-year series of tide gauge sea level measurements in Stockholm. It is shown that the wave-like annual disturbances in the sea level field propagate from the southwest to the northeast at the speed from 0.06 to 0.36 m/s. A comparison of the estimated characteristics of annual waves and theoretical dispersion relations of different types of low-frequency waves has shown that they are identified as internal Kelvin waves over the most of the sea area and their characteristics agree with the theoretical dispersion relations of baroclinic topographic Rossby waves in rare cases only in the southwest of the sea. The perceptible interdecadal changes in the annual wave parameters in the sea level field were noted. As compared to the 1993–2021 period, the 1993–2002 decade is characterized by a decrease of the *Sa* harmonic amplitude by 1.5–3 times, later onset of the maximum of the sea level annual variation (about 1 month later), as well as a noticeable slowdown of the annual wave phase velocity in the southwest of the sea.

Conclusions. The reasons for the amplitude modulation of annual waves in the sea level field are related to the impact of the oscillations with periods 352, 374 and 379 days which are identified in the form of small but significant amplitude maxima in the Fourier series spectra of sea level, wind speed and atmospheric pressure. One more mechanism of the amplitude modulation of annual waves is assumed to be related to the changes in frequency of the Baltic Sea natural baroclinic oscillations due to the interannual variations of its stratification.

Keywords: sea level, seasonal variations, annual rhythm, annual fluctuations, Baltic Sea, Rossby waves, amplitude modulation, Kelvin waves, topographic waves

Acknowledgements: The study was carried out with support of the Russian Science Foundation grant 22-27-00209 “Spatial structure and mechanisms of interannual variability of seasonal fluctuations in the Baltic Sea level”, <https://rscf.ru/en/project/22-27-00209/>.

For citation: Zakharchuk, E.A., Sukhachev, V.N. and Tikhonova, N.A., 2024. Wave Nature and Modulation of Annual Fluctuations in the Level of the Baltic Sea. *Physical Oceanography*, 31(2), pp. 208-230.

© 2024, E.A. Zakharchuk, V.N. Sukhachev, N.A. Tikhonova

© 2024, Physical Oceanography



Introduction

Annual fluctuations are the main component of seasonal sea level variations. They have a pronounced rhythm and the largest amplitude maxima in the spectra of mean monthly sea level values¹ [1, 2]. Theoretical concepts show that seasonal sea level fluctuations are caused by seasonal changes in wind speed and direction, atmospheric pressure, currents, seawater density and water balance components (precipitation, evaporation, continental runoff and water exchange with adjacent sea basins) [3, 4].

The characteristic features of the average annual variation of the Baltic Sea level are its spring minimum, autumn–winter maximum and pronounced asymmetry of level changes manifested in a relatively rapid (4–5 months) decrease in sea level in winter–spring to the minimum value in April – May and a more long-term (7–8 months) level elevation in summer and autumn to the maximum value in November – January [5–10].

The seasonal winter and spring decrease in the Baltic Sea level occurs due to atmospheric pressure increase observed during this period, decrease in the precipitation amount, low continental runoff, sea water density increase, decrease in the speed of southwest winds and change in their direction to the northeast, which contributes to increased water outflow from the Baltic to the North Sea [8]. Mean seasonal increase in the Baltic Sea level from spring to winter takes place as a result of spring increase in river flow, summer increase in precipitation, autumn–winter decrease in atmospheric pressure and sea water density, as well as autumn increase in southwest winds promoting the water inflow from the North Sea into the Baltic one [5, 8].

The observed asymmetry in the annual variation of the Baltic Sea level is due to the fact that hydrometeorological processes causing sea level decrease have spring extremes, while the processes that cause sea level elevation have extreme values separated in time: the maximum river flow is observed in spring and the maximum amount of atmospheric precipitation – in summer, the minimum atmospheric pressure values and the maximum speeds of southwest winds and the inflow of North Sea waters are observed in autumn and winter [5, 8].

The comparative contributions of all the listed hydrometeorological processes to the annual variation of the Baltic Sea level are different. Most scientists believe that the main influence on the mean annual variation of the Baltic Sea level is influenced by seasonal changes in wind speed and, to a lesser extent, atmospheric pressure and water exchange with the North Sea, while the contribution of other hydrometeorological processes is insignificant [8, 9, 11–15].

Annual level fluctuations play an important role in the hydrological regime of the Baltic Sea having a noticeable impact on its shores and coastal infrastructure [16, 17]. They indicate changes in meteorological processes, observed climate warming [7, 18], as well as water exchange with the North Sea [19–21]. Some years also demonstrate a noticeable contribution of seasonal fluctuations of the Baltic Sea to dangerous level elevations in the east of the Gulf of Finland [22]. Numerical hydrodynamic modeling of the Baltic Sea free fluctuations showed that in a stratified sea, rapidly damped baroclinic modes of eigenoscillations are generated with periods

¹ German, V.Kh. and Levikov, S.P., 1988. [*Probabilistic Analysis and Modeling of the Sea Level Oscillations*]. Leningrad: Gidrometeoizdat, 231 p. (in Russian).

of about a year, the magnitude of which is comparable to the average long-term estimates of annual level fluctuations obtained based on the tide gauge and satellite altimetry data analysis [2, 23].

Significant increase of the number of stations for tide gauge level measurements by the end of the 20th century contributed to the studies of regional differences in changes in the characteristics of annual level fluctuations in the coastal Baltic Sea. M. Ekman [24] and I. Medvedev [2] in their works studied the spatial variability of the amplitudes of annual fluctuations in the coastal zone of the Baltic Sea using harmonic analysis of long-term series of mean monthly values of tide gauge sea level measurements. The results indicated an increase in the annual harmonic amplitude from 4–6 cm in the Danish straits to 12–13 cm at the tops of the Gulf of Finland and the Gulf of Bothnia [2, 24]. In addition to amplitude estimates, the article by I. Medvedev also presented the phase values of annual sea level fluctuations at various coasts of the Baltic Sea indicating its increase by 50° when moving from the Danish straits through the Baltic Proper to the top of the Gulf of Bothnia [2].

Long duration of the series of mean monthly sea level values (153–200 years) at some tide gauge stations in the Baltic made it possible to estimate the interannual variability of annual fluctuations in the 19th and 20th centuries [1, 11, 12]. The observed significant positive trend in changes in the annual component of sea level is associated with secular changes in oceanographic conditions in the northeastern part of the North Atlantic due to the movement of the oceanic polar front [1], with the North Atlantic Oscillation on decadal time scales and a general trend towards climate warming [11] and also with secular changes in the Baltic Sea region atmospheric precipitation [12]. However, a study of the interannual variability of the *Sa* harmonic (365.2-day period) in Stockholm for the later period of 1889–2020 already showed the presence of an insignificant positive linear trend, against the background of which multidirectional trends in changes in the *Sa* harmonic amplitude were observed. At the same time, the most significant decrease in the amplitudes of annual sea level fluctuations in various areas of the Baltic Sea has been noted since the early 1980s to the present time and was associated with a decrease in the amplitude of annual fluctuations in wind speed and, to a lesser extent, atmospheric pressure [9].

In [15], S. Barbosa and R. Donner studied annual changes in the Baltic Sea level for 1900–2012 based on its monthly average values at nine coastal stations using discrete wavelet analysis. They did not evaluate the linear trend of changes in the amplitude of the annual component of seasonal level fluctuations identified by other authors [1, 9, 11, 12] but found alternating periods of high and low amplitudes in variations in the annual cycle of seasonal level fluctuations [15]. In [9], E.A. Zakharchuk et al. associated these features of interannual changes in annual fluctuations with their amplitude modulation but the reasons for this modulation were not studied.

New, broader opportunities for studying the variability of seasonal level fluctuations in open areas of oceans and seas have opened up with the advent of continuous satellite altimetry measurements of sea level. In [6], Y. Cheng et al. used the method of cyclostationary empirical orthogonal functions to study the spatial structure patterns and temporal changes in the annual level cycle in the Baltic Sea

based on monthly average satellite altimetry data for 1993–2014. To study the reasons for interannual changes in estimates of the annual variation of the Baltic Sea level, a correlation analysis of the main components of the annual variation of sea level calculated from satellite altimetry data and the main components of various meteorological parameters (zonal wind speed, values of the North Atlantic Oscillation index, atmospheric pressure and air temperature) was carried out. The results showed high correlation coefficients, reaching 0.60–0.80 in all cases [6].

Works [8, 9] proposed to exclude the stationary component of seasonal fluctuations for all hydrometeorological processes from all series before carrying out cross-correlation analysis for a more representative estimate of correlations between interannual changes in seasonal fluctuations in sea level and various hydrometeorological processes. The results showed that a high correlation was observed only between annual anomalies of sea level and annual anomalies of fluctuations in wind speed, atmospheric pressure and air temperature [8]. However, a cross-correlation analysis of annual sea level anomalies in the central part of the open Baltic and annual anomalies of steric changes in the sea level revealed no connection between these processes [9].

Despite the fact that satellite altimetry data make it possible to estimate changes in the amplitudes and phases of seasonal sea level fluctuations in space in sufficient detail, the hypothesis about the wave nature of annual level fluctuations in the Baltic Sea has not yet been studied, although the wave interpretation of annual disturbances in the sea level field has been used repeatedly for other World Ocean regions (for example, in [25–29]). In these works, annual sea level disturbances were identified as baroclinic Kelvin and Rossby waves.

The study is purposed at estimating the features of spatial-temporal variability of the characteristics of annual fluctuations of the Baltic Sea level based on satellite and contact measurements, their comparing with theoretical dispersion relations of the low-frequency waves of different types, as well as investigating possible mechanisms of the amplitude modulation of annual fluctuations of the Baltic Sea level.

Data and methods

An array of combined altimetry data from the following satellites was used to study annual fluctuations in the Baltic Sea level: Jason-3, Sentinel-3A, HY-2A, Saral/AltiKa, Cryosat-2, Jason-2, Jason-1, T/P, ENVISAT, GFO, ERS1/2, including sea level anomaly (SLA) fields with a spatial resolution of $0.25^\circ \times 0.25^\circ$ and a resolution of 1 day (E.U. Copernicus Marine Service Information ²) obtained by the optimal interpolation method for 1993–2021 [30, 31]. When creating the array, corrections for orbital and instrumental errors, correction for the troposphere and ionosphere impact on the delay of the sounding and reflected altimeter pulse were introduced into the initial altimetry data [32]. In addition, fluctuations associated with the static effect of atmospheric pressure, wind waves, as well as ocean and land tides, were excluded from the altimetry data.

² Copernicus. *Copernicus Marine Data Store*. 2024. [online] Available at: <http://marine.copernicus.eu> [Accessed: 05 April 2024].

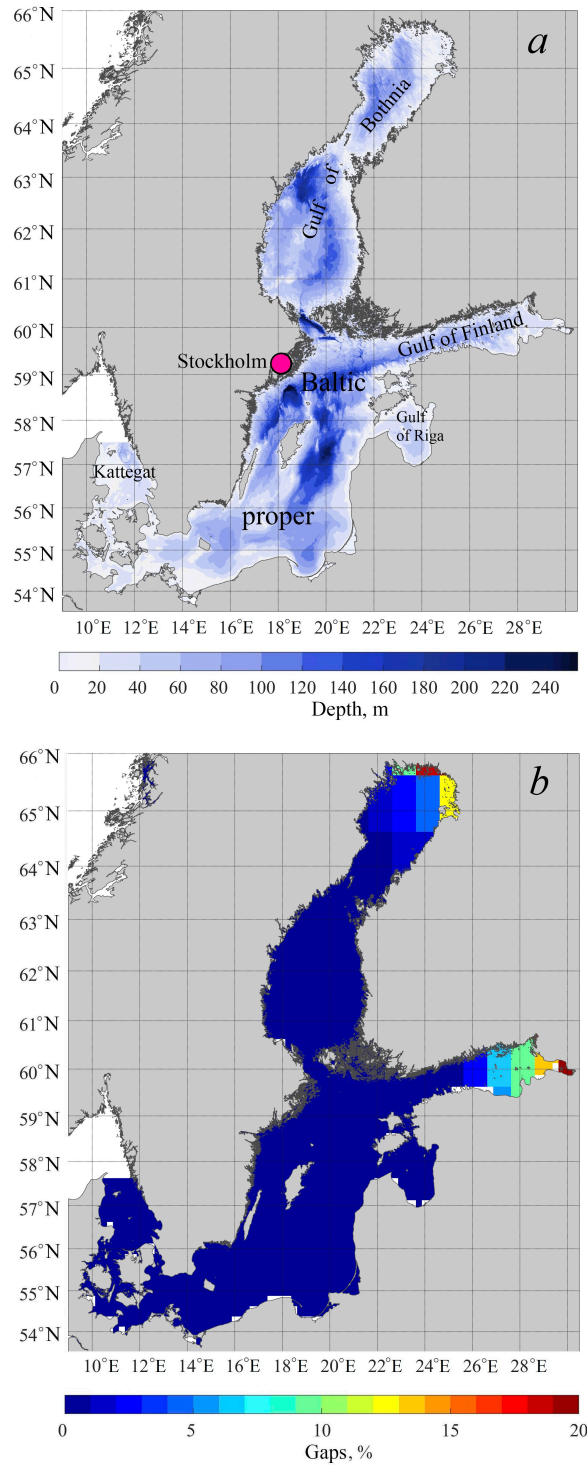


Fig. 1. Bathymetry map of the Baltic Sea and location of the Stockholm tide gauge station (*a*), number of gaps (as a percentage of the total number of series terms) in the nodes of altimetry data grid area (*b*)

Most works devoted to studies of the annual variation of the Baltic Sea level used data from mean monthly level values [1, 2, 11, 12, 24]. However, it was shown in [9] that it is necessary to use series of mean daily sea level values rather than monthly ones for a more accurate estimate of the characteristics of annual sea level fluctuations. Therefore, the present paper uses data from mean daily values of tide gauge and satellite altimetry observations of the Baltic Sea level.

Altimetry data were checked for gaps. The largest number of them varying from 2 to 25% is associated with the presence of fast and drifting ice in winter and occurs in the northern part of the Gulf of Bothnia, as well as in the central and eastern parts of the Gulf of Finland (Fig. 1, *b*).

To study the reasons for the amplitude modulation of annual fluctuations in the Baltic Sea level, we used the longest series of continuous mean daily sea level values at the Stockholm tide gauge station (Fig. 1, *a*) for 1889–2021 obtained from E.U. Copernicus Marine Service².

The amplitude (*A*) and phase (*G*) of annual level fluctuations in a stationary approximation were calculated using harmonic analysis carried out according to the least squares method taking into account the recommendations from the work by G.N. Voinov [33]:

$$A(t) = A_{Sa} \cos(\omega_{Sa} t - G_{Sa}),$$

where A_{Sa} is amplitude; ω_{Sa} is frequency; G_{Sa} is annual harmonic phase from the beginning of the series; t is time.

In areas where altimetry data had gaps due to the presence of ice in winter, the characteristics of annual level fluctuations were estimated as follows. First, gaps in the altimetry data series were filled with the average level value. Then, the Sa harmonic amplitudes and phases were estimated using the aforementioned harmonic analysis procedure. Next, the series of annual sea level fluctuations were pre-calculated based on the estimated amplitudes and phases. The level values were selected from the series of annual sea level fluctuations pre-calculated in this way to fill the gaps in the series of initial altimetry data. Then, the harmonic analysis procedure was repeated and the estimates of the Sa harmonic amplitude and phase a obtained in this way were accepted as the final result.

The accuracy of the amplitudes and phases calculated in the stationary approximation of annual sea level fluctuations was estimated using the method proposed in work³. According to it, correlation coefficient r between the harmonic and the original series of mean daily level values in Stockholm is used to estimate the Sa harmonic significance, which is determined by the Student's test:

$$St = \frac{|r|\sqrt{n-2}}{\sqrt{1-r^2}},$$

where r is correlation coefficient between the original series and Sa harmonic; n is series length. The harmonic is considered significant if $St > St_{cr}$, where St_{cr} is table

³ Malinin, V.N., 2020. [Statistical Methods for Hydrometeorological Data Analysis. Volume 2. Analysis of Time Series and Random Fields]. Saint Petersburg: RGGMU, 196 p. (in Russian).

value of the Student's criterion from work ⁴ depending on the significance level and the number of freedom degrees.

Then, all significant harmonics were excluded from the amplitude spectrum of the Fourier series. The maximum value of the amplitude of the residual series was taken as the root-mean-square error of the Sa harmonic amplitude (σ_A). Root-mean-square error of phase calculation σ_G was calculated using the following formula:

$$\sigma_G = \frac{\sigma_A}{A_{Sa}} \cdot \frac{180}{\pi},$$

where σ_G is root-mean-square error of Sa harmonic phase calculation; σ_A is root-mean-square error of Sa harmonic amplitude calculation; N is number of series members; $\pi = 3,14$; A_{Sa} is Sa harmonic amplitude.

Based on the values of the phase difference between the nodes of the altimetry data grid area, the velocity of movement of annual level fluctuations was estimated:

$$C_x = \frac{\Delta x \cdot 360}{T \Delta F_x}, C_y = \frac{\Delta y \cdot 360}{T \Delta F_y}, C_{Sa} = \sqrt{C_x^2 + C_y^2}, \quad (1)$$

where C_x, C_y are components of the velocity vector projection onto the parallel and meridian; $\Delta x, \Delta y$ is distance between adjacent nodes of the grid area along the parallel and meridian; C_{Sa} is velocity vector module; T is period of fluctuations; $\Delta F_x, \Delta F_y$ is phase difference between grid area nodes along parallel and meridian.

To study the wave nature of annual disturbances in the sea level field, the characteristics of seasonal level fluctuations with a period of 1 year estimated using satellite altimetry data were compared with the known theoretical dispersion relations of various types of low-frequency waves: barotropic and baroclinic topographic Rossby waves belonging to the class of gradient-vorticity waves ⁵ [34] and Kelvin waves belonging to the class of gravitational waves [35, 36].

Theoretical dispersion curves of topographic Rossby waves were calculated using the dispersion relation derived by V.R. Fuks in the linear approximation for closed basin conditions [37, 38]:

$$\omega = \frac{k\beta - kf \frac{\partial \ln H}{\partial y} + n f \frac{\partial \ln H}{\partial x}}{\left(\frac{m\pi}{l_x}\right)^2 + \left(\frac{p\pi}{l_y}\right)^2 + k^2 + n^2 + \left(\frac{2\pi}{R}\right)^2}, \quad (2)$$

where: ω is wave frequency; $\beta = \frac{df}{dy} = \text{const}$ is β -plane approximation, f is Coriolis parameter; $k = \frac{2\pi}{\lambda_x}$, $n = \frac{2\pi}{\lambda_y}$ are wavenumber components; λ_x, λ_y are wavelengths along the x and y axes respectively; H is sea depth; R is Rossby deformation radius.

To estimate the dispersion curves of barotropic topographic Rossby waves, barotropic (external) radius of deformation $R = R_0 = \frac{\sqrt{gH}}{f}$ was used with its values

⁴ Korn, G.A. and Korn, T.M., 1961. *Mathematical Handbook for Scientists and Engineers. Definitions, Theorems, and Formulas for Reference and Review*. New York; Toronto; London: McGraw-Hill Book Company, Inc., 943 p.

⁵ Tareyev, B.A., 1974. [*Dynamics of Baroclinic Disturbances in the Ocean*]. Moscow: MSU, 180 p. (in Russian).

equal to 150, 175 and 200 km [40], where g is free fall acceleration. Dispersion curves of baroclinic topographic Rossby waves were calculated by introducing into equation (2) estimates of baroclinic (inner) Rossby deformation radius $R = R_i = \frac{NH}{f}$,

where $N = \sqrt{\frac{g\Delta\rho}{\rho\Delta z}}$ is Väisälä–Brent frequency; ρ is water density. According to [40–42], the R_i values of the first baroclinic mode were taken to be 2, 5 and 9 km. Specific bottom slopes $\frac{\partial \ln H}{\partial y} = \frac{1}{H} \frac{\partial H}{\partial y}$, $\frac{\partial \ln H}{\partial x} = \frac{1}{H} \frac{\partial H}{\partial x}$ of the Baltic Sea along the x and y axes were $4.2 \cdot 10^{-5}$; $4.6 \cdot 10^{-5}$; $5.0 \cdot 10^{-6}$; l_x , l_y are basin dimensions along the x and y axes taken to be 400 and 1500 km, respectively; m , p is standing wave mode number.

The first term in the numerator of equation (2) describes the wave-forming mechanism for Rossby waves associated with the combined effect of sphericity and rotation of the Earth and the second and third ones are applied for topographic waves generated under the influence of the joint effect of bottom topography variability and the Earth's rotation. In the denominator, the first two terms describe the spatial scale of the basin and the horizontal modes of the standing wave, the third and fourth ones describe the contribution of translational wave motion, and the last term in the denominator describes the environmental conditions (the sea basin depth and its stratification).

The theoretical phase velocities of long barotropic gravitational waves (Kelvin waves) were estimated using the known formula:

$$C = \sqrt{gH}, \quad (3)$$

where H is sea depth; g is acceleration of gravity.

The theoretical phase velocities of long baroclinic gravity waves (internal Kelvin waves) were estimated using the following formula:

$$C_i = \sqrt{g'h'}, \quad (4)$$

where $g' = (\Delta\rho/\rho)g$ is reduced free fall acceleration, g is free fall acceleration, ρ – is average seawater density; $\Delta\rho$ is difference in densities of the upper and lower layers; h' is thickness of the upper quasi-homogeneous layer of the sea [43, 44].

To solve this problem using data on vertical distributions of seawater density obtained from the E.U. Copernicus Marine Service², we estimated average stratification conditions for different Baltic regions for 1993–2018. They made it possible to obtain the following values of the parameters included in formula (4): $h' = 5, \dots, 60$ m; $\Delta\rho/\rho = 0.2, \dots, 75 \cdot 10^{-4}$, $g' = 0.2, \dots, 73 \cdot 10^{-3}$ m/s².

To estimate amplitude modulation features and mechanisms of annual fluctuations in the Baltic Sea level, a 132-year series of average daily sea level values in Stockholm was subjected to moving harmonic analysis [11] without overlap with a period of quasi-stationarity (sliding window) equal to one year. Based on the estimated amplitudes and phases for each period of quasi-stationarity, the series of annual fluctuations were reconstructed. Then, they were combined into the $\zeta_{Sa}(t)$ series describing the interannual changes in the Sa harmonic. Sharp jumps in height were sometimes observed at the junctions of reconstructed series. They were smoothed using the cubic spline method [45] with a smoothing window of 60 days

(the last 30 days of the previous quasi-stationarity period and the first 30 days of the next quasi-stationarity period).

To identify fluctuations with frequencies close to the *Sa* frequency which can cause its amplitude modulation, a harmonic analysis of the 132-year series of average daily sea level values in Stockholm was carried out in a stationary approximation. The amplitudes and phases of fluctuations with periods of 441, 434, 419, *Sa*, 379, 373 and 352 days were estimated. Harmonics with these periods, as well as the sea level series which is a superposition of these harmonics, were reconstructed from the amplitudes and phases. This series was subtracted from the original series of daily average sea level in Stockholm. A series of amplitudes was formed in the range of periods from 90 to 490 days based on the results of harmonic analysis of the residual series. An estimate of 3σ (where σ is standard deviation of the residual series of amplitudes in the range of periods from 90 to 490 days) was taken as a 99% confidence interval [46]. The frequencies of significant amplitude maxima of level fluctuations were identified. The amplitude maxima were then used to describe the amplitude modulation of the *Sa* harmonic.

The Rayleigh criterion was used to separate the signal of the polar tide (a period of about 14 months) and the signal at the *Sa* harmonic frequency:

$$\text{Rel} = \frac{2\pi}{\Delta\omega}, \quad (5)$$

where $\Delta\omega$ is difference between the *Sa* harmonic and polar tide frequencies. This criterion makes it possible to determine the series length required to separate the signals of these processes during harmonic analysis.

A harmonic analysis of series of average daily atmospheric pressure values for 1939–2021 and wind speeds for 1950–2021 in Stockholm obtained from the Swedish Meteorological and Hydrological Institute (SMHI ⁶) portal was carried out to study the causes of amplitude modulation of annual sea level fluctuations.

Results and their interpretation

Figure 2 shows estimates of the amplitudes and phases of the annual *Sa* harmonic obtained at the grid nodes of satellite altimetry data using harmonic analysis of series of average daily sea level values for various periods, root-mean-square errors of their calculation, as well as movement speed of annual fluctuations in the sea level field calculated by formula (1). Estimates of root-mean-square errors prove that the amplitudes of the annual harmonic are reliably identified for all Baltic Sea regions. The minimum amplitude of level fluctuations with a year period is observed in the southwest of the Baltic, where it was 4.5–5 cm in 1993–2021 (Fig. 2, *a*). The amplitude of annual level fluctuations increases to 7–8.5 cm when moving towards the Kattegat Strait and towards the Baltic Proper. The maximum amplitudes of level fluctuations with a period of one year are observed in the north of the Gulf of Bothnia and in the east of the Gulf of Finland, where they reach 9–10 cm (Fig. 2, *a*). These estimates are consistent with the results of the analysis of annual level fluctuations obtained earlier in the works by

⁶ The Swedish Meteorological and Hydrological Institute. *SMHI: Data*. 2024. [online] Available at: <https://www.smhi.se/data> [Accessed: 05 April 2024].

M. Ekman [24] and I. Medvedev [2] based on the results of a harmonic analysis of long-term tide gauge observations of sea level at coastal points of the Baltic, as well as from the results of satellite altimetry data analysis over a shorter period [8].

According to the phase estimates (Fig. 2, *a*), its quasi-monotonic increase when moving from the southwest of the sea to the north and northeast is noted, which indicates the wave nature of annual disturbances in the level field of the Baltic Sea. These spatial phase changes are reliable since they exceed the root-mean-square error of their calculation significantly (Fig. 2, *b*). The phase values indicate that the maximum annual sea level fluctuations in the Kattegat Strait are observed in early and mid October (275–285°) and in the north of the Gulf of Bothnia and east of the Gulf of Finland – in very late November (330°) (Fig. 2, *a*). Propagation velocity of annual waves in the sea level field is 6–36 cm/s (Fig. 2, *c*).

A comparison of the annual fluctuation characteristics for individual decades shows that the same features of their spatial distribution are noted at the qualitative level: the smallest amplitudes of the *Sa* harmonic are in the southwest of the sea and the maximum ones are in the north and northeast, a quasi-monotonic increase in phase is observed from the southwest to north. However, the quantitative differences in the characteristics of annual fluctuations in different decades are very noticeable. Compared to the 1993–2021 period, the southwest of the sea is marked by a several-fold decrease in the amplitude of the *Sa* harmonic (up to 1–2 cm) and its decrease by almost 1.5 times in the north of the Gulf of Bothnia and east of the Gulf of Finland (up to 7–8 cm), later maximum of the annual level variation (by approximately a month), as well as noticeable slowdown in the phase velocity of the annual wave in the southwest of the sea in 1993–2002 (Fig. 2, *f*).

On the contrary, in 2003–2012, throughout the entire sea area, the *Sa* harmonic amplitude increased significantly reaching its maximum values of 5–6 cm in the southwest of the sea and 11–12 cm in the north of the Gulf of Bothnia, the east of the Gulf of Finland and in the Riga Gulf (Fig. 2, *h*); the wave phase velocity increased (Fig. 2, *j*), maximum of the annual level variation was observed approximately 10–15 days earlier (Fig. 2, *h*) compared to the long-term average value estimated for 1993–2021.

In 2012–2021, the annual harmonic amplitude decreased reaching its long-term average values calculated for 1993–2021 in the southern and central parts of the open Baltic while in other sea areas the amplitude exceeded the average values (see Fig. 2, *j*). In this decade, in the southwest of the sea, the phase velocity of the annual wave decreased noticeably again (Fig. 2, *l*) and its amplitude maximum was noted here significantly earlier compared to the long-term average value, although in other areas it corresponded generally to the average value.

Estimates of the probability of phase velocity distribution by gradation indicate that annual waves in the Baltic Sea level field propagated most often at the velocities of 17–36 cm/s (Fig. 3). The phase velocity range of 6–16 cm/s accounts for only 12% of cases (Fig. 3).

Theoretical estimate of phase velocity of barotropic gravity waves calculated using formula (3) for the Baltic Sea average depth of 54 m [3] is 23 m/s, which is two orders of magnitude higher than the values of phase velocities of annual waves estimated from satellite altimetry data (see Figs. 2 and 3). This comparison indicates that annual waves cannot be barotropic gravity ones in the Baltic Sea level field.

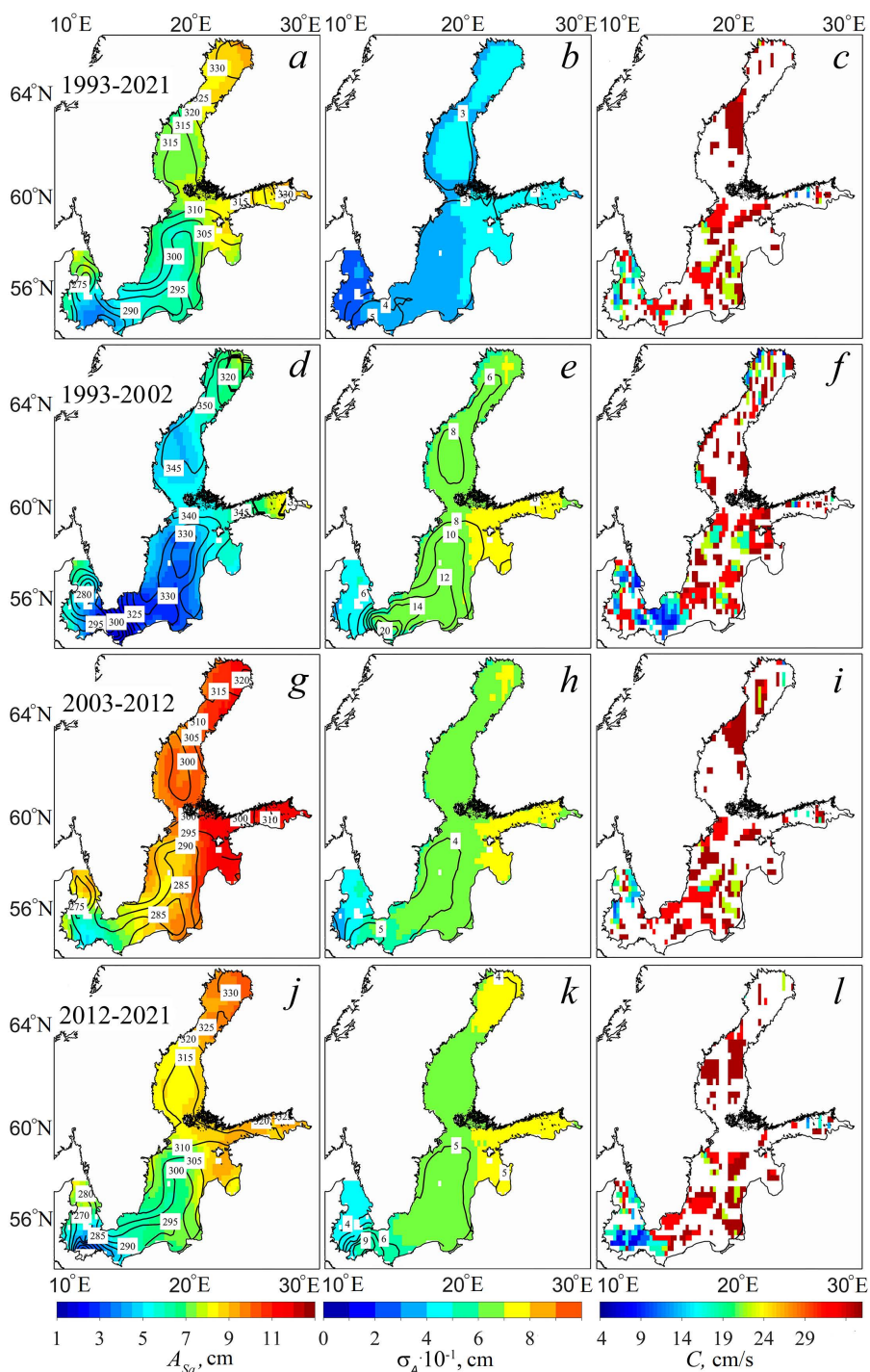


Fig. 2. Amplitude-phase characteristics of the annual Sa harmonic in the Baltic Sea estimated by satellite altimetry data (isolines indicate phases in degrees) (*a, d, g, j*), root-mean-square errors in the estimates of amplitude and phase (isolines) of the annual harmonic (*b, e, h, k*) and estimates of motion velocity of annual sea level fluctuations calculated by formula (1) (*c, f, i, l*) for 1993–2021 (*a – c*), 1993–2022 (*d – f*), 2003–2021 (*g – i*) and 2012–2021 (*j – l*)

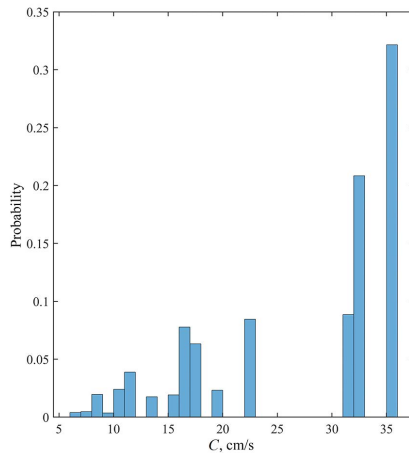


Fig. 3. Probability of the distribution of annual wave phase velocities estimated by satellite altimetry data in the Baltic Sea level field

Estimates of theoretical phase velocities of baroclinic Kelvin waves made using formula (4) for characteristic stratification conditions of the Baltic Sea demonstrate that the velocity values vary from 0.03 to 2.09 m/s. The results presented in Fig. 3 indicate that the propagation velocities of annual sea level disturbances calculated from satellite altimetry data are within the range of theoretical phase velocities of internal gravity waves obtained from formula (4); this makes it possible to identify these waves as baroclinic Kelvin waves.

Figure 4 contains the comparison of empirical characteristics of annual wave-like sea level disturbances estimated from satellite altimetry data with the theoretical dispersion curves of barotropic and baroclinic topographic Rossby waves calculated from relation (2). It is clearly seen that the theoretical dispersion curves of barotropic topographic Rossby waves lie significantly higher than the empirical characteristics of annual sea level fluctuations (Fig. 4, *a*). The empirical values of annual sea level fluctuations do not intersect with the majority of theoretical dispersion curves of baroclinic topographic Rossby waves (Fig. 4, *b*). The exception is theoretical curves describing the propagation of baroclinic topographic Rossby waves under conditions of sharp stratification ($R_i = 9$ km) and relatively small bottom slopes ($4.2 \cdot 10^{-5}$). The southwest of the Baltic Proper is most suitable for such conditions [41, 42]. However, the empirical phase velocities of annual waves intersected by theoretical baroclinic topographic Rossby wave curves correspond to 6–12 cm/s range. This is the range of the slowest annual waves which occur only in 9% of cases (see Fig. 3).

Thus, annual disturbances in the sea level field are identified as baroclinic Kelvin waves most often in much of the Baltic Sea waters and their empirical characteristics correspond to the theoretical dispersion relations of baroclinic topographic Rossby waves in rare cases only in the southwest of the sea.

We propose new wave interpretation of annual level fluctuations for the Baltic Sea. Previously, other hypotheses related to the Ekman mechanism of seasonal increases and decreases in sea level, seasonal changes in water density and water balance components were expressed and studied [5, 10, 12, 13].

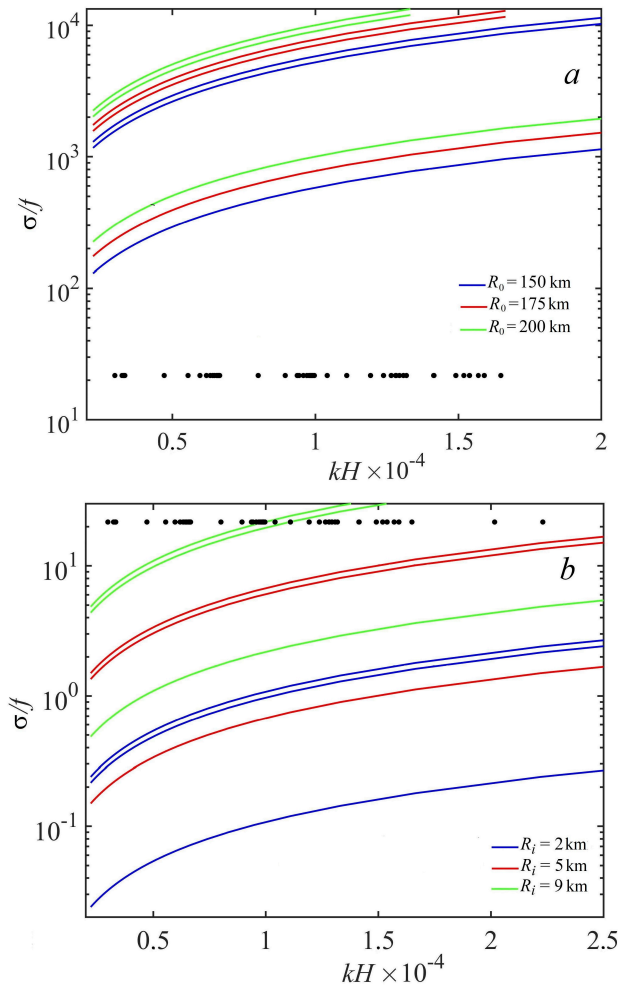


Fig. 4. Comparison of the characteristics of annual fluctuations in the Baltic Sea level calculated using altimetry (black dots) with theoretical dispersion curves of barotropic (a) and baroclinic (b) topographic Rossby waves (lines)

The difference between waves and non-wave oscillations is usually explained by the orbital movements of water particles in the wave, propagation of the waveform in space without mass transfer which is unusual for other types of oscillatory motions, as well as dispersion relation which associates wave frequency with wave number [27, 35, 36]. Wave processes occur in the spectra as narrow-band significant peaks (tidal oscillations serve as a striking example here). Quasi-monotonic propagation of the phase of annual oscillations in the sea level field in space observed in our case (see Fig. 2) and good agreement of their empirical characteristics with theoretical dispersion relations of baroclinic low-frequency waves (see Fig. 4) indicate the wave nature of annual sea level fluctuations.

If quasi-monotonic propagation of Sa harmonic phase were associated, for example, with the observed different times of the high water onset on rivers flowing into the Baltic Sea, then the maximum annual level fluctuations would be observed in spring, when the maximum river runoff is recorded and high relationship between changes in annual

level fluctuations and river runoff would be noted. However, the maximum annual level fluctuations are observed in the autumn–winter period and correlation between changes in annual level fluctuations and river runoff is absent [8, 13]. The lack of correlation is also observed with changes in annual fluctuations of other water balance components [8, 9, 12], as well as with steric vibrations [9], while the relationship with changes in wind speed and atmospheric pressure is high [8, 9].

At the same time, the Ekman mechanism cannot be considered as the main one in generating annual fluctuations in the Baltic Sea level. If this were so, our Fourier analysis results would show two amplitude maxima (in the northeast and southwest of the sea), not one, since in autumn and winter seasonal winds blow from the southwest, and in spring and summer from the north and northeast [8]. Therefore, in this case, the spatial distribution of amplitude-phase characteristics at the *Sa* harmonic frequency would be the same as that of a single-node seiche – with two amplitude maxima at opposite ends of the sea and zero amplitude values at the nodal line which would intersect the open Baltic Sea approximately from the west to the east. In our case (see Fig. 2), no such features are noted: not a maximum but a minimum of annual fluctuations is observed in the southwest of the sea, and the phase and level values increase quasi-monotonically when moving from the southwest to the northeast.

The listed results indicate that annual fluctuations in the sea level field are low-frequency waves identified mainly as baroclinic Kelvin waves. These waves are generated mainly by changes in tangential wind friction and atmospheric pressure. According to estimates [15], the contribution of annual variations in the zonal component of wind speed and atmospheric pressure to the generation of annual sea level fluctuations at different coastal stations for 1979–2012 is 31–62 and 30–47%, respectively.

Thus, the response of the Baltic Sea level surface to the effect of tangential wind friction and atmospheric pressure is not local but wave at the *Sa* harmonic frequency and this response is much greater in magnitude than the one of the level surface to changes in water density and water balance components.

The baroclinic nature of low-frequency waves with one-year period indicates the dependence of their characteristics on stratification which has significant interannual variations in the substantially enclosed and shallow Baltic Sea caused by changes in water exchange with the North Sea, amount of precipitation, continental runoff and evaporation [5, 47–49]. These changes in stratification lead to noticeable variations in the phase velocity (Fig. 2) of baroclinic annual waves in the sea level field from decade to decade.

Figure 5 shows a series of interannual changes in the annual sea level fluctuations in Stockholm obtained using a moving harmonic analysis performed for a quasi-stationarity period of one year. A significant interannual variability in the amplitudes of annual fluctuations is observed. In some years, they reach values of more than 20 cm and decrease to several centimeters in other years. The time course of the *Sa* harmonic demonstrates amplitude modulation with a period from 7–15 to 30–35 years.

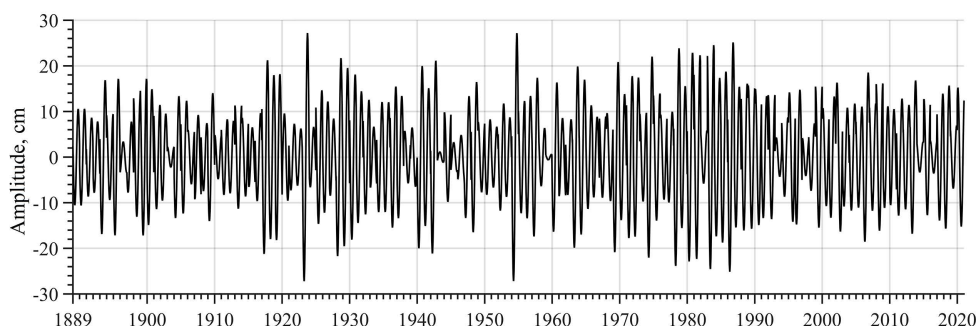


Fig. 5. Reconstructed series of annual sea level fluctuations in Stockholm for the quasi-stationary period equal to one year

A similar feature in changes of the Baltic Sea annual level fluctuations was noted by S. Barbosa and R. Donner [15] from the results of discrete wavelet analysis of series of monthly average values of tide gauge sea level measurements.

To study the causes for the amplitude modulation of annual sea level fluctuations, we will consider the amplitude spectrum of the Fourier series in Stockholm (Fig. 6). The second largest significant amplitude maximum after the peak at the Sa harmonic frequency is observed at a period of 434 days. Next to it, smaller but also significant amplitude maxima are observed at periods of 419 and 441 days. Level fluctuations with such periods are associated with the polar tide, which is caused by free nutation of the Earth's rotation axis [1, 50, 51].

We use Rayleigh criterion (5) in order to separate the polar tide signal ($P = 419$ days) from the Sa harmonic signal. The calculations revealed that the length of the series for separating the signals should be eight years.

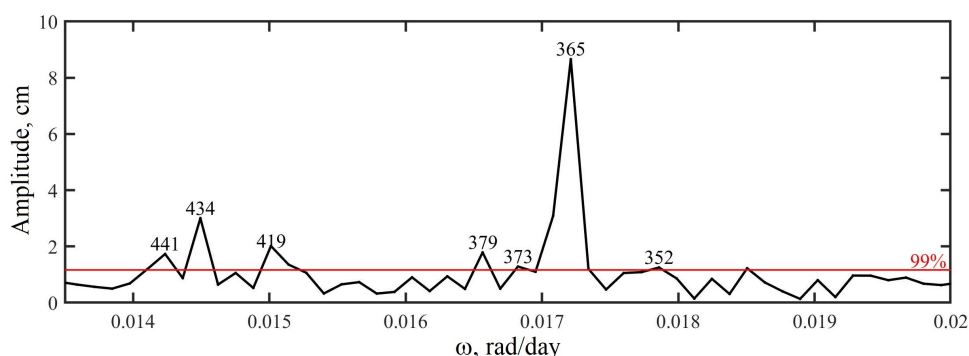


Fig. 6. A part of amplitude spectrum of the Fourier series of the average daily sea level values in Stockholm (numbers above the amplitude maxima are the periods in days) for 1889–2021 which describes the range of seasonal and interannual variability. Red line shows the 99 % confidence interval

Figure 7, *a* shows a reconstructed series of annual sea level fluctuations in Stockholm obtained using a moving harmonic analysis for a quasi-stationary period of eight years and a sliding period of one year. Comparison of this figure with Fig. 5 indicates that the time structure of the modulation of annual fluctuations has been

preserved as a whole, although sharp changes in the Sa harmonic amplitude with periods from one to several years caused by an increase in the quasi-stationarity period have disappeared. Same as in Fig. 5, we observe a decrease in annual fluctuations in the 1900s, 1940s and 1990s, as well as their increase in the 1920s, 1950s, 1970–1980s and 2000s. This result suggests that the pole tide does not affect the amplitude modulation of the annual sea level fluctuations in Stockholm.

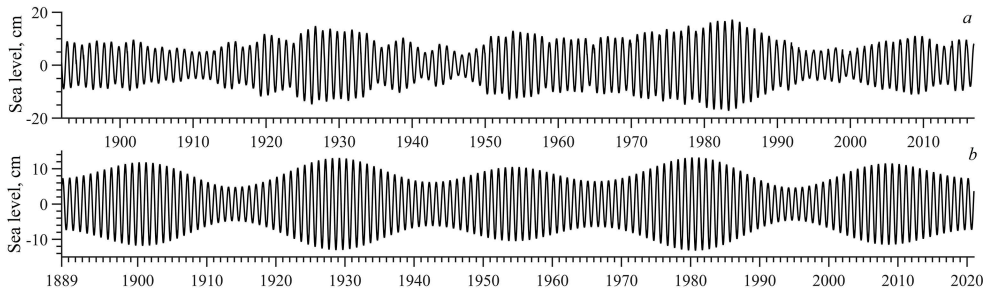


Fig. 7. Pre-calculated series of annual sea level fluctuations in Stockholm for the quasi-stationary period equal to eight years and a one year period of sliding (*a*), as well as a series of level fluctuations obtained by stationary harmonic analysis using equation (6) (*b*)

According to the Rayleigh criterion, a series length of 44 years which exceeds the modulation periods of annual fluctuations is required to separate the Sa harmonic signals from the satellite closest to it with a period of 373 days (see Fig. 6). In this regard, the amplitudes and phases of harmonics that have significant amplitude maxima near the annual cycle were estimated using stationary harmonic analysis:

$$A(t) = A_{Sa} \cos(\omega_{Sa} t - G_{Sa}) + A_{379} \cos(\omega_{379} t - G_{379}) + A_{373} \cos(\omega_{373} t - G_{373}) + A_{352} \cos(\omega_{352} t - G_{352}), \quad (6)$$

where numerical indices indicate the periods of significant amplitude maxima closest to the Sa harmonic.

The series of four harmonics were reconstructed by the estimated amplitudes and phases. Fig. 7, *b* shows a series of superpositions of these four harmonics. It can be seen that the changes in annual sea level fluctuations reconstructed by equation (5) contain the same features of the modulation process as under natural conditions: close variations in the amplitudes of level fluctuations from 5 to 14 cm, coincidence in time of the main maxima and minima, presence of amplitude modulation from 25 to 30 years in the process of periods, alternation of the largest and smallest maxima. This result indicates that small amplitude fluctuations with periods of 352, 373 and 379 days still have a noticeable effect on the amplitude modulation of annual fluctuations in the Baltic Sea level. However, the physical mechanisms for the origin of these fluctuations are unknown. They have not been studied in any scientific publications which is apparently stipulated by their small amplitudes.

Several studies demonstrate that interannual variations in annual fluctuations in the Baltic Sea level are most closely associated with interannual variability of seasonal fluctuations in atmospheric pressure and wind speed [6, 8, 9, 11–15], while we observe their low correlation with steric level fluctuations and water balance components [8, 9]. Therefore, it can be assumed that oscillations with periods of 352,

373 and 379 days are also present in the spectra of atmospheric pressure and wind speed fluctuations affecting the amplitude modulation of these meteorological processes.

In this regard, we are to consider the amplitude spectra of the series of average daily atmospheric pressure values for 1939–2021 and wind speeds for 1950–2021 in Stockholm (Fig. 8). Although the length of the series of these meteorological processes is significantly less than that of the sea level series in Stockholm, it provides fairly well separation of the signals of the *Sa* harmonic and the closest satellite with a period of 373 days which stands out in the sea level spectrum in the form of a significant amplitude maximum (see Fig. 6) according to the Rayleigh criterion. Fig. 8 indicates that the spectra of atmospheric pressure and zonal wind speed component contain small amplitude maxima for oscillations with a period of 379 days as in the sea level spectrum, although this maximum is absent in the spectrum of meridional wind speed component (Fig. 8, *b*). Unlike sea level, the maxima for the period of 373 days is absent in the amplitude spectra of meteorological processes but we observe peaks with periods of 348, 353 days (Fig. 8) which are close to the amplitude maximum of sea level fluctuations of 352 days (see Fig. 6).

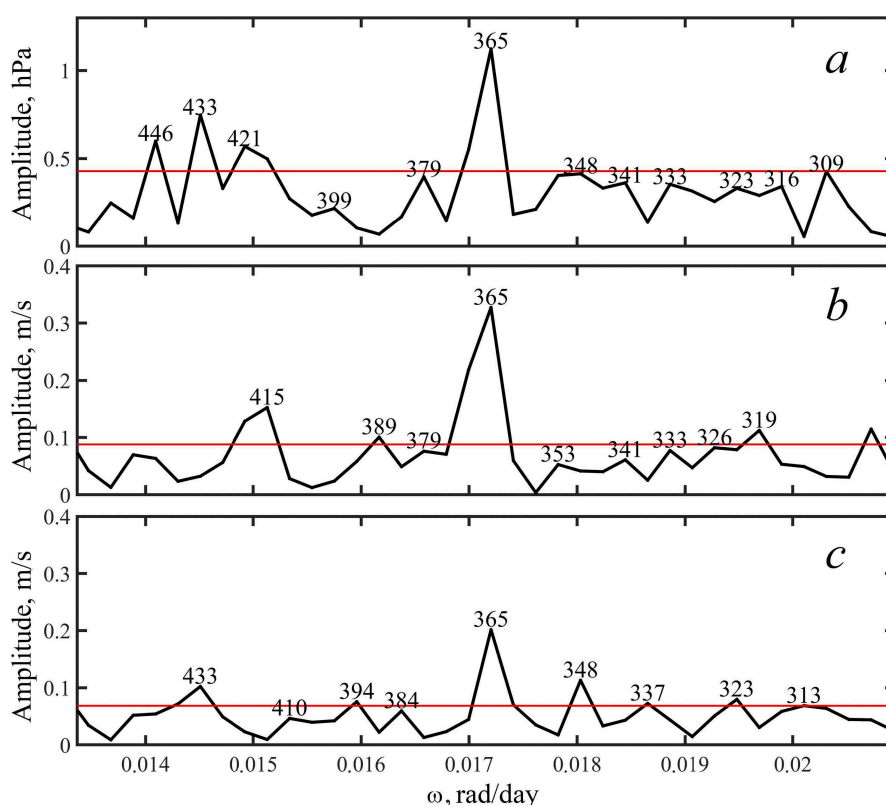


Fig. 8. A part of amplitude spectrum of the Fourier series of the average daily values of atmospheric pressure (*a*), zonal (*b*) and meridional (*c*) wind speed components in Stockholm (numbers above the amplitude maxima are the periods in days) for 1939–2021 which describes the range of seasonal and interannual variability. Red line shows the 99 % confidence interval

Thus, we observe amplitude maxima at the same or similar frequencies as for sea level fluctuations in the spectra of atmospheric pressure and wind speed fluctuations at frequencies located near the *Sa* harmonic frequency, which can lead to a similar modulation of the meteorological processes under consideration.

Another cause for the *Sa* harmonic modulation can be the effect of the Baltic Sea baroclinic eigenoscillations. Numerical experiments with a three-dimensional baroclinic hydrodynamic model of the Baltic Sea revealed that baroclinic modes of eigenoscillations with periods of about one year were generated in a stratified sea in contrast to the barotropic case; their maximum values are observed in the central part of the Baltic Proper and reach 4–5.5 cm [23]. Significant interannual variations in the Baltic Sea stratification which have been observed in recent decades [47] should lead to a shift in the frequency of its baroclinic eigenoscillations relative to the frequency of forced level oscillations generated at the *Sa* harmonic frequency. If the frequency of the baroclinic eigenoscillations coincides with the *Sa* harmonic frequency, a resonance occurs and the amplitude of annual fluctuations increases significantly. When the frequency of baroclinic eigenoscillations deviates from the *Sa* harmonic frequency, the amplitude of annual oscillations decreases and amplitude modulation further appears during the annual sea level variation. Long-term fluctuations in the Baltic Sea stratification are associated mainly with changes in the components of its freshwater balance and water exchange with the North Sea [47]. Our estimates indicated that the *Sa* harmonic modulation periods varied from 7–15 to 30–35 years (see Figs. 5 and 7). Instrumental measurements show that interannual variations in river runoff, precipitation and water exchange through the Danish straits also demonstrate similar cyclicities [5, 47–49]. However, this hypothesis requires additional research using numerical experiments with a three-dimensional baroclinic model.

Conclusion

1. The results of harmonic analysis of satellite altimetry data for the 1993–2021 period indicate that the average *Sa* harmonic amplitude varies from 4.5–5 cm in the southwest of the Baltic Sea to 9–10 cm in the north of the Gulf of Bothnia and the east of the Gulf of Finland. A quasi-monotonic increase in the *Sa* harmonic phase from the southwest to the north and northeast of the sea indicates the wave nature of the annual fluctuations. The propagation velocity of annual fluctuations in the Baltic Sea varies from 0.06 to 0.36 m/s.

2. A comparison of characteristics of annual fluctuations in the Baltic Sea level field with theoretical dispersion relations of various classes of low-frequency waves revealed that annual disturbances in the sea level field are identified as baroclinic Kelvin waves in most cases over most of the Baltic Sea water area and their empirical characteristics correspond to the theoretical dispersion relations of baroclinic topographic Rossby waves in rare cases only in the southwest of the sea.

3. Noticeable changes in the characteristics of annual waves in the sea level field are observed among decades. Compared to the 1993–2021 period, we observe a 1.5–3-fold decrease in the *Sa* harmonic amplitude, later maximum of the annual level

variation (by approximately 1 month), as well as noticeable slowdown of the annual wave phase velocity in the southwest of the sea in the 1993–2002 decade.

On the contrary, the *Sa* harmonic amplitude increased significantly throughout the entire sea area reaching its maximum values of 5–6 cm in the southwest of the sea and 11–12 cm in the north of the Gulf of Bothnia, the east of the Gulf of Finland and the Gulf of Riga in the 2003–2012 decade; wave phase velocity increased and the maximum of the annual level variation was observed approximately 10–15 days earlier compared to the long-term average value estimated for the 1993–2021 period.

In 2012–2021, the annual harmonic amplitude decreased reaching its long-term average values calculated for 1993–2021 in the southern and central parts of the open Baltic Sea, while in other areas of the sea amplitude exceeded average values. In this decade, the annual wave phase velocity decreased noticeably again in the southwest of the sea and its amplitude maximum was noted there significantly earlier compared to the long-term average value, although in other areas it corresponded generally to it.

4. The results of a moving harmonic analysis of a 132-year series of average daily sea level values in Stockholm demonstrate a pronounced amplitude modulation in the temporal variation of the *Sa* harmonic amplitude with a period from approximately 7–15 to 30–35 years. The cause of modulation is shown to be associated with the impact of level fluctuations with periods of 352, 374 and 379 days which stand out in the form of small but significant amplitude maxima in the spectrum of the Fourier series of the sea level in Stockholm. These fluctuations can be caused by atmospheric pressure and wind speed variations. Their spectra contained amplitude maxima at the same or similar frequencies as sea level fluctuations. It is assumed that another mechanism of amplitude modulation of annual waves can be associated with changes in the frequency of the Baltic Sea baroclinic eigenoscillations due to interannual variations in its stratification.

REFERENCES

1. Ekman, M. and Stigebrandt, A., 1990. Secular Change of the Seasonal Variation in Sea Level and of the Pole Tide in the Baltic Sea. *Journal of Geophysical Research: Oceans*, 95(C4), pp. 5379–5383. <https://doi.org/10.1029/jc095ic04p05379>
2. Medvedev, I.P., 2014. Seasonal Fluctuations of the Baltic Sea Level. *Russian Meteorology and Hydrology*, 39(12), pp. 814–822. <https://doi.org/10.3103/S106837391412005X>
3. Gill, A.E. and Niller, P.P., 1973. The Theory of the Seasonal Variability in the Ocean. *Deep-Sea Research and Oceanographic Abstracts*, 20(2), pp. 141–177. [https://doi.org/10.1016/0011-7471\(73\)90049-1](https://doi.org/10.1016/0011-7471(73)90049-1)
4. Leppäranta, M. and Myrberg, K., 2009. *Physical Oceanography of the Baltic Sea*. Berlin; Heidelberg: Springer, 378 p. <https://doi.org/10.1007/978-3-540-79703-6>
5. Terziev, F.S., Rozhkov, V.A. and Smirnova, A.I., eds., 1992. *Hydrometeorology and Hydrochemistry of the Seas of the USSR. Volume 3. Baltic Sea. Issue 1. Hydrometeorological Conditions*. Saint Petersburg: Gidrometeoizdat, 449 p. (in Russian).

6. Cheng, Y., Xu, Q. and Li, X., 2018. Spatio-Temporal Variability of Annual Sea Level Cycle in the Baltic Sea. *Remote Sensing*, 10(4), 528. <https://doi.org/10.3390/rs10040528>
7. Männikus, R., Soomere, T. and Viška, M., 2020. Variations in the Mean, Seasonal and Extreme Water Level on the Latvian Coast, the Eastern Baltic Sea, during 1961-2018. *Estuarine, Coastal and Shelf Science*, 245, 106827. <https://doi.org/10.1016/j.ecss.2020.106827>
8. Zakharchuk, E.A., Sukhachev, V.N., Tikhonova, N.A., Kouraev, A. and Zakharova, E., 2022. Seasonal Fluctuations in Baltic Sea Level Determined from Satellite Altimetry. *Continental Shelf Research*, 249, 104863. <https://doi.org/10.1016/j.csr.2022.104863>
9. Zakharchuk, E.A., Sukhachev, V.N., Tikhonova, N.A. and Litina, E.N., 2022. Stationary and Non-Stationary Description of the Seasonal Sea Level Oscillations in the Baltic Sea Based on the Tide Gauge Data. *Physical Oceanography*, 29(6), pp. 636-658. <https://doi.org/10.22449/1573-160X-2022-6-636-658>
10. Lisitzin, E., 1974. *Sea-Level Changes*. Amsterdam; New York: Elsevier Scientific Pub. Co., 286 p.
11. Plag, H.P. and Tsimplis, M.N., 1999. Temporal Variability of the Seasonal Sea-Level Cycle in the North Sea and Baltic Sea in Relation to Climate Variability. *Global and Planetary Change*, 20(2-3), pp. 173-203. [https://doi.org/10.1016/S0921-8181\(98\)00069-1](https://doi.org/10.1016/S0921-8181(98)00069-1)
12. Hünicke, B. and Zorita, E., 2008. Trends in the Amplitude of Baltic Sea Level Annual Cycle. *Tellus A: Dynamic Meteorology and Oceanography*, 60(1), pp. 154-164. <https://doi.org/10.1111/j.16000870.2007.00277.x>
13. Stramska, M., Kowalewska-Kalkowska, H. and Świrgoń, M., 2013. Seasonal Variability in the Baltic Sea Level. *Oceanologia*, 55(4), pp. 787-807. <https://doi.org/10.5697/oc.55-4.787>
14. Johansson, M.M. and Kahma, K.K., 2016. On the Statistical Relationship between the Geostrophic Wind and Sea Level Variations in the Baltic Sea. *Boreal Environment Research*, 21, pp. 25-43.
15. Barbosa, S.M. and Donner, R.V., 2016. Long-Term Changes in the Seasonality of Baltic Sea Level. *Tellus A: Dynamic Meteorology and Oceanography*, 68(1), 30540. <https://doi.org/10.3402/tellusa.v68.30540>
16. Łabuz, T.A. and Kowalewska-Kalkowska, H., 2011. Coastal Erosion Caused by the Heavy Storm Surge of November 2004 in the Southern Baltic Sea. *Climate Research*, 48(1), pp. 93-101. <https://doi.org/10.3354/cr00927>
17. Weisse, R., Dailidienė, I., Hünicke, B., Kahma, K., Madsen, K., Omstedt, A., Parnell, K., Schöne, T., Soomere, T. [et al.], 2021. Sea Level Dynamics and Coastal Erosion in the Baltic Sea Region. *Earth System Dynamics*, 12(3), pp. 871-898. <https://doi.org/10.5194/esd-12-871-2021>
18. Gordeeva, S.M. and Malinin, V.N., 2014. *Gulf of Finland Sea Level Variability*. Saint Petersburg: RSHU Publishers, 179 p. (in Russian).
19. Samuelsson, M. and Stigebrandt, A., 1996. Main Characteristics of the Long-Term Sea Level Variability in the Baltic Sea. *Tellus A: Dynamic Meteorology and Oceanography*, 48(5), pp. 672-683. <https://doi.org/10.3402/TELLUSA.V48I5.12165>
20. Gustafsson, B.G. and Andersson, H.C., 2001. Modeling the Exchange of the Baltic Sea from the Meridional Atmospheric Pressure Difference across the North Sea. *Journal of Geophysical Research: Oceans*, 106(C9), pp. 19731-19744. <https://doi.org/10.1029/2000JC000593>
21. Ekman, M., 2009. *The Changing Level of the Baltic Sea during 300 Years: A Clue to Understanding the Earth*. Åland Islands: Summer Institute for Historical Geophysics, 155 p.

22. Zakharchuk, E.A. and Tikhonova, N.A., 2011. On the Spatiotemporal Structure and Mechanisms of the Neva River Flood Formation. *Russian Meteorology and Hydrology*, 36(8), pp. 534-541. <https://doi.org/10.3103/S106837391108005X>
23. Zakharchuk, E.A., Tikhonova, N.A., Zakharova, E. and Kouraev, A.V., 2021. Spatiotemporal Structure of Baltic Free Sea Level Oscillations in Barotropic and Baroclinic Conditions from Hydrodynamic Modelling. *Ocean Science*, 17(2), pp. 543-559. <https://doi.org/10.5194/os-17-543-2021>
24. Ekman, M., 1996. A Common Pattern for Interannual and Periodical Sea Level Variations in the Baltic Sea and Adjacent Waters. *Geophysica*, 32(3), pp. 261-272.
25. Chelton, D.B. and Schlax, M.G., 1996. Global Observations of Oceanic Rossby Waves. *Science*, 272(5259), pp. 234-238. <https://doi.org/10.1126/science.272.5259.234>
26. Döös, K., 1999. Influence of the Rossby Waves on the Seasonal Cycle in the Tropical Atlantic. *Journal of Geophysical Research: Oceans*, 104(C12), pp. 29591-29598. <https://doi.org/10.1029/1999jc900126>
27. Belonenko, T.V., Zakharchuk, E.A. and Fuks, V.R., 2004. [*Ocean Gradient-Vorticity Waves*]. Saint Petersburg: SPSU, 215 p. (in Russian).
28. Yuan, D. and Han, W., 2006. Roles of Equatorial Waves and Western Boundary Reflection in the Seasonal Circulation of the Equatorial Indian Ocean. *Journal of Physical Oceanography*, 36(5), pp. 930-944. <https://doi.org/10.1175/JPO2905.1>
29. Calafat, F.M., Wahl, T., Lindsten, F., Williams, J. and Frajka-Williams, E., 2018. Coherent Modulation of the Sea-Level Annual Cycle in the United States by Atlantic Rossby Waves. *Nature Communications*, 9(1), 2571. <https://doi.org/10.1038/s41467-018-04898-y>
30. Bretherton, F.P., Davis, R.E. and Fandry, C.B., 1976. A Technique for Objective Analysis and Design of Oceanographic Experiments Applied to MODE-73. *Deep-Sea Research and Oceanographic Abstracts*, 23(7), pp. 559-582. [https://doi.org/10.1016/0011-7471\(76\)90001-2](https://doi.org/10.1016/0011-7471(76)90001-2)
31. Pujol, M.-I., Faugère, Y., Taburet, G., Dupuy, S., Pelloquin, C., Ablain, M. and Picot, N., 2016. DUACS DT2014: The New Multi-Mission Altimeter Data Set Reprocessed over 20 Years. *Ocean Science*, 12(5), pp. 1067-1090. <https://doi.org/10.5194/os-12-1067-2016>
32. Le Traon, P.-Y., Nadal, F. and Ducet, N., 1998. An Improved Mapping Method of Multisatellite Altimeter Data. *Journal of Atmospheric and Oceanic Technology*, 15(2), pp. 522-534. [https://doi.org/10.1175/1520-0426\(1998\)015<0522:AIMMOM>2.0.CO;2](https://doi.org/10.1175/1520-0426(1998)015<0522:AIMMOM>2.0.CO;2)
33. Voinov, G.N., 2002. Non-Tidal Sea Level Oscillation. In: V. A. Volkov, O. M. Johannessen, V. E. Borodachev, G. N. Voinov, L. H. Pettersson, L. P. Bobylev and A. V. Kouraev, 2002. *Polar Seas Oceanography. An Integrated Case Study of the Kara Sea*. Berlin, Heidelberg: Springer, pp. 61-77.
34. Tareyev, B.A., 1971. Gradient-Vorticity Waves on a Shelf. *Izvestiya of Academy of Sciences, USSR. Atmospheric and Oceanic Physics*, 7(4), pp. 431-436 (in Russian).
35. LeBlond, P.H. and Mysak, L.A., 1978. *Waves in the Ocean*. Amsterdam; Oxford; New York: Elsevier Scientific Publ. Co., 602 p.
36. Pedlosky, J., 1979. *Geophysical Fluid Dynamics*. New York: Springer-Verlag, 626 p.
37. Gusev, A.K., Zakharchuk, E.A., Ivanov, N.E., Klevancyov, U.P., Rogkov, V.A., Tikhonova, N.A. and Fuks, V.R., 2007. [*The Dynamics of the Baltic Sea in the Synoptic Range of Spatial and Temporal Scales*]. Saint Petersburg: Gidrometeoizdat, 354 p. (in Russian).

38. Fuks, V.R., 2005. Gradient-Eddy Waves in the Baltic Sea. *Russian Meteorology and Hydrology*, (9), pp. 47-51.
39. Gill, A.E., 1982. *Atmosphere – Ocean Dynamics*. New York: Academic Press Inc., 662 p.
40. Fennel, W., Seifert, T. and Kayser, B., 1991. Rossby Radii and Phase Speeds in the Baltic Sea. *Continental Shelf Research*, 11(1), pp. 23-36. [https://doi.org/10.1016/0278-4343\(91\)90032-2](https://doi.org/10.1016/0278-4343(91)90032-2)
41. Osiński, R., Rak, D., Walczowski, W. and Piechura, J., 2010. Baroclinic Rossby Radius of Deformation in the Southern Baltic Sea. *Oceanologia*, 52(3), pp. 417-429. <https://doi.org/10.5697/oc.52-3.417>
42. Kurkin, A., Kurkina, O., Rybin, A. and Talipova, T., 2020. Comparative Analysis of the First Baroclinic Rossby Radius in the Baltic, Black, Okhotsk, and Mediterranean Seas. *Russian Journal of Earth Sciences*, 20(4), ES4008. <https://doi.org/10.2205/2020ES000737>
43. Konyaev, K.V. and Sabinin, K.D., 1992. [Waves inside the Ocean]. Saint Petersburg: Gidrometeoizdat, 271 p. (in Russian).
44. Carmack, E.C. and Kulikov, E.A., 1998. Wind-Forced Upwelling and Internal Kelvin Wave Generation in Mackenzie Canyon, Beaufort Sea. *Journal of Geophysical Research: Oceans*, 103(C9), pp. 18447-18458. <https://doi.org/10.1029/98JC00113>
45. De Boor, C., 1978. *A Practical Guide to Splines*. New York: Springer, 348 p.
46. Voinov, G.N., 2012. Techniques for Computations of the Seasonal Variation in the Main Constituents of Tides with the Small Range of Tide (as an Example of the Baltic Sea). *Arctic and Antarctic Research*, (3), pp. 101-109 (in Russian).
47. Liblik, T. and Lips, U., 2019. Stratification Has Strengthened in the Baltic Sea – An Analysis of 35 Years of Observational Data. *Frontiers in Earth Science*, 7, 174. <https://doi.org/10.3389/feart.2019.00174>
48. Litina, E.N., Zakharchuk, E.A. and Tikhonova, N.A., 2020. Dynamics of Hypoxic Zones in the Baltic Sea in the Late XX–Early XXI Century. *Water Resources*, 47(3), pp. 478-485. <https://doi.org/10.1134/S0097807820030082>
49. Lehmann, A., Myrberg, K., Post, P., Chubarenko, I., Dailidienė, I., Hinrichsen, H.-H., Hüseyin, K., Liblik, T., Meier, H.E.M. [et al.], 2022. Salinity Dynamics of the Baltic Sea. *Earth System Dynamics*, 13(1), pp. 373-392. <https://doi.org/10.5194/esd-13-373-2022>
50. Maksimov, I.V. and Karklin, V.P., 1965. “Pole Tide” in the Baltic Sea. *Doklady Akademii Nauk SSSR*, 161(3), pp. 580-582 (in Russian).
51. Medvedev, I.P., Rabinovich, A.B. and Kulikov, E.A., 2014. Pole Tide in the Baltic Sea. *Oceanologia*, 54(2), pp. 121-131. doi:10.1134/S0001437014020179

Submitted 07.08.2023; approved after review 16.10.2023;
accepted for publication 18.01.2024.

About the authors:

Eugeny A. Zakharchuk, Head of Oceanology Department, Institute of Earth Sciences, Saint Petersburg State University (33–35, 10th Line of Vasilievsky Island, 199178, Saint Petersburg, Russian Federation), DSc (Geogr.), **ORCID ID: 0000-0001-6079-5739**, **ResearcherID: N-1644-2013**, **Scopus Author ID: 6603158329**, eazakharchuk@yandex.ru

Natalia A. Tikhonova, Associate Professor of Oceanology Department, Institute of Earth Sciences, Saint Petersburg State University (33–35, 10th Line of Vasilievsky Island, Saint Petersburg, 199178, Russian Federation); Acting Head of Laboratory, Saint Petersburg Branch of N.N. Zubov PHYSICAL OCEANOGRAPHY VOL. 31 ISS. 2 (2024) 229

State Oceanographic Institute (38 Bering Str., Saint Petersburg, 199397, Russian Federation), PhD (Geogr.), **ORCID ID: 0000-0002-4546-4920**, **ResearcherID: I-4647-2015**, **Scopus Author ID: 11239410500**, i@ntikhonova.ru

Vladimir N. Sukhachev, Research Associate, Institute of Earth Sciences, Saint Petersburg State University (33–35, 10th Line of Vasilievsky Island, Saint Petersburg, 199178, Russian Federation); Research Associate, Saint Petersburg Branch of N.N. Zubov State Oceanographic Institute (38 Bering Str., Saint Petersburg, 199397, Russian Federation), PhD, **ORCID ID: 0000-0003-4821-4342**, **ResearcherID: N-7470-2015**, **Scopus Author ID: 55969236600**, syhachev@mail.ru

Contribution of the co-authors:

Eugeny A. Zakharchuk – general supervision of the work, paper writing

Natalia A. Tikhonova – work with series of level, wind and atmospheric pressure in Stockholm; dispersion relations

Vladimir N. Sukhachev – work with altimetry data

The authors have read and approved the final manuscript.

The authors declare that they have no conflict of interest.

Influence of Coastal Upwelling on Chlorophyll a Distribution in the Coastal Zone of the Southeastern Baltic Sea in Summer Periods, 2000–2019

M. V. Kapustina^{1, ✉}, A. V. Zimin^{1, 2}

¹ Shirshov Institute of Oceanology of RAS, Moscow, Russian Federation

² Saint Petersburg State University, Saint Petersburg, Russian Federation

✉ kapustina.mariya@ya.ru

Abstract

Purpose. The study is purposed at obtaining quantitative estimates of coastal upwelling influence on the distribution of chlorophyll a in the coastal zone of the southeastern Baltic Sea during the summer seasons of 2000–2019.

Methods and results. Based on data on the frequency and duration of upwelling events for June–August 2000–2019 and chlorophyll a concentrations from multi-sensor satellite observations in the coastal zone of the southeastern Baltic Sea, long-term and monthly average values of the studied parameters were obtained and the influence of upwelling events on the concentration of chlorophyll a in the surface layer of the sea was assessed. The spatial variability of chlorophyll a in the coastal areas is found to be related to the influence of upwelling events. On average, the chlorophyll a concentration decreases by more than 1 mg/m³ after an upwelling of any duration and in all summer months. The concentration drop is most significant after the upwelling events lasting more than 6 days.

Conclusions. Reduced chlorophyll a concentrations (as compared to the pre-upwelling values) are observed in the course of a week after a coastal upwelling event in the southeastern Baltic Sea.

Keywords: sea surface temperature, coastal upwelling, chlorophyll a concentration, southeastern Baltic Sea, remote sensing data

Acknowledgments: The study was carried out within the framework of the state assignment of IO RAS (theme No. FMWE-2024-0025).

For citation: Kapustina, M.V. and Zimin, A.V., 2024. Influence of Coastal Upwelling on Chlorophyll a Distribution in the Coastal Zone of the Southeastern Baltic Sea in Summer Periods, 2000–2019. *Physical Oceanography*, 31(2), pp. 231-245.

© 2024, M. V. Kapustina, A. V. Zimin

© 2024, Physical Oceanography

Introduction

Upwelling is a common phenomenon which can be observed for ~ 10% of days in the warm period of the year in shallow water areas of the southeastern Baltic Sea (SEB) according to average long-term estimates [1–3]. On average, four upwellings with a total duration of > 20 days are observed in the water area in the summer seasons of 2000–2019 with the mean upwelling area of ~ 620 km². Accordingly, upwelling is undoubtedly an important mechanism for the transport of nutrients into the surface layer [4, 5], which affects bioproductivity of the SEB coastal areas. One



of the indicators of bioproductivity is concentration of the main phytoplankton pigment – chlorophyll *a*. Note that its variability can be studied over a wide range of spatial and temporal scales using satellite observation data.

In the first few days of its development, coastal upwelling in the summer drives surface waters away from the shore. Due to this, a decrease in the content of phytoplankton and its main characteristic, chlorophyll *a* concentration, is observed in the coastal zone [6, 7]. After stabilization of the upwelling, an increase in primary production is observed within several days; it is associated with the development of phytoplankton communities caused by the rise of nutrients into the euphotic zone and temperature increase [8–13]. Further, we noted a primary production decrease associated with the rapid, within one to two weeks, consumption of nutrients raised to the surface [14]. At the same time, the nitrogen-to-phosphorus ratio can vary in the Baltic Sea due to upwelling and it can affect the composition of phytoplankton communities [8, 15]. Sometimes upwelling can lead to the decrease in area productivity, for example, if the raised waters replace the ones coming with the runoff of rivers or lagoons [4, 6], or when upwelling appears persistently and frequently in the same area [16, 17].

The chlorophyll *a* concentration during an upwelling event is also affected by biotic factors and a seasonal variation of the vertical structure of water associated with changes in the gradient and the thermocline and nutricline position [4, 18]. In June, the summer minimum of phytoplankton biomass begins in the SEB after spring algal blooms and massive development of algae due to nutrient depletion of surface waters. In July, the sea surface temperature (SST) becomes higher, a pronounced subsurface thermocline is formed (provoking massive development of nitrogen-fixing cyanobacteria) and the chlorophyll *a* concentration reaches peak values. In August, the chlorophyll *a* concentration decreases in the coastal zone [19].

According to satellite radiometers, the highest chlorophyll *a* concentrations are observed in the coastal zone from Cape Taran to the Curonian Spit coast, where they reach the eutrophic level ($> 4 \text{ mg/m}^3$) [19], which partially overlaps with areas of maximum long-term frequency of upwelling events in the Rybachiy Plateau area and near Cape Taran [2]. At the same time, the works devoted to the issue of assessing the influence of upwelling events on the variability of phytoplankton concentrations in the SEB are based primarily on contact observations that are very rare in space [14] or on consideration of individual cases illustrating the capabilities of satellite research methods [20], although this information (generalized over a long-term period) is important for solving practical problems in the field of recreation and assessing changes in the ecological state of the coastal zone.

The use of remote sensing data enables to conduct large-scale observations of distribution and variability of chlorophyll *a* concentrations [21], including the ones influenced by upwelling [6, 22, 23]. The main advantages of the latter are instantaneous imaging of vast water areas and high spatial resolution. However, it should be noted that the average annual cloud cover in the Baltic Sea is $> 58\%$ [24].

In the presence of clouds, optical satellite data, even those obtained on a regular basis, are very fragmentary. In such conditions, it is advisable to monitor the chlorophyll a concentration not throughout the entire area, but on individual profiles, similar to how it was done in [23, 25].

This study is aimed at obtaining estimates of the coastal upwelling influence on the chlorophyll a distribution in the coastal zone of the southeastern Baltic Sea over the past two decades of the 21st century.

Materials and methods

The initial data for analyzing the relationship between upwelling and chlorophyll a in the SEB were the dates and areas of upwelling events for June – August of 2000–2019 in the SEB coastal zone from [26] and daily data from multisensor satellite observations (combined data from MERIS/ENVISAT, MODIS/AQUA, SeaWiFS/SEASTAR and VIIRS/SUOMI-NPP sensors) of chlorophyll a concentration (mg/m^3) on a regular grid with 1×1 km cell size in the surface layer of the Baltic Sea ¹.

Analysis of spatial and intra-seasonal variability of upwelling frequency and chlorophyll a in the SEB. Averaged monthly maps and summer maps to describe intra-seasonal spatial variability of upwelling events, SST and chlorophyll a in the SEB were constructed for 2000–2019 in the water area shown in Fig. 1. Chlorophyll a concentrations were calculated monthly and for the summer season in those cells where > 25% of the values were observed over the period under consideration. The upwelling frequency was estimated as the number of days with an observed negative temperature anomaly obtained in a given cell using the method from [2] per month or per season.

Influence of upwelling on chlorophyll a concentration in the SEB. Chlorophyll a variability profiles of ~ 20 km in length were constructed for each identified upwelling using Quantum GIS software. Those profiles approximately corresponded to coastal isobaths from 0 to 30–75 m. A total of 9 profiles were constructed along the coast, located normal to the coast at 7–30 km intervals (depending on the coast configuration) (Fig. 1). The position of profiles was selected considering the areas with the highest frequency of upwelling events from [2, 26]. Chlorophyll a values in the profiles were obtained from daily multi-sensor satellite observations. For each upwelling event, one of the profiles that was best provided with the data on chlorophyll a during the period under consideration was selected for analysis by overlaying both parameters under study on a single geographic basis.

¹ Copernicus Marine Service, 2012. *Baltic Sea Reprocessed Surface Chlorophyll Concentration from Multi Satellite Observations*. doi:10.48670/moi-00083

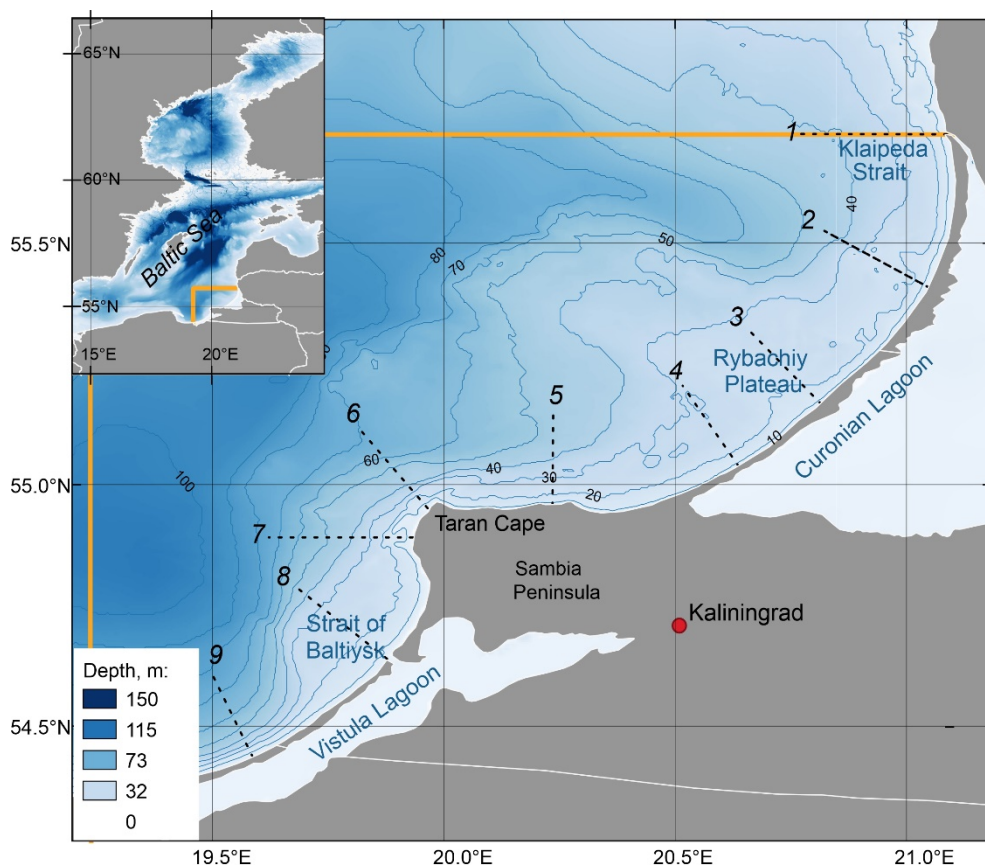


Fig. 1. Study area (yellow box), isobaths in each 10 m (blue curves) ², and profiles used in the analysis of chlorophyll a variability on the sea surface (dashed black lines)

Upwelling zones from [2, 26] were marked on the selected profile, which made it possible to calculate the values of chlorophyll a concentration (mg/m^3) inside this zone and outside of it. Additionally, the mean values of this characteristic throughout the entire profile before, during and after upwelling were estimated. To obtain a satisfactory amount of data on chlorophyll a before and after upwelling, the analysis included the data from a time interval of up to 7 days, except for the cases when the events went beyond the summer season under consideration or when there were no data. A total of 31 upwelling periods with a total duration of 590 days was studied (for cases lasting 1–42 days). The influence of upwelling duration on changes in chlorophyll a concentration, as well as its contribution to intra-seasonal variation and long-term variability, was assessed.

² Weatherall, P., Bringenspar, C., Castro, C.F., Dorschel, B., Drennon, H., Ferrini, V.L., Harper, H.A., Hehemann, L., Jakobsson, M. [et al.], 2022. *The GEBCO_2022 Grid – A Continuous Terrain Model of the Global Oceans and Land*. NERC EDS British Oceanographic Data Centre NOC. doi:10.5285/e0f0bb80-ab44-2739-e053-6c86abc0289c

Results

Analysis of intra-seasonal variability of upwelling frequency and chlorophyll a in the SEB. The areas of the northern coast of the Curonian Spit and the western coast of the Sambia Peninsula are clearly distinguished on the SST map by lower temperatures (lower by 0.5–1 °C) than in the coastal zone as a whole (Fig. 2). Depending on the upwelling frequency in the summer, several areas are distinguished in the coastal waters: the northern coast of the Sambia Peninsula and the western part of the Vistula Spit, where upwelling is observed up to 3 days a month; the area near Cape Taran and the southern part of the Curonian Spit, where upwelling is observed 3–4 days a month; the western coast of the Sambia Peninsula and the northern part of the Curonian Spit, where upwelling is observed more than 4 days a month.

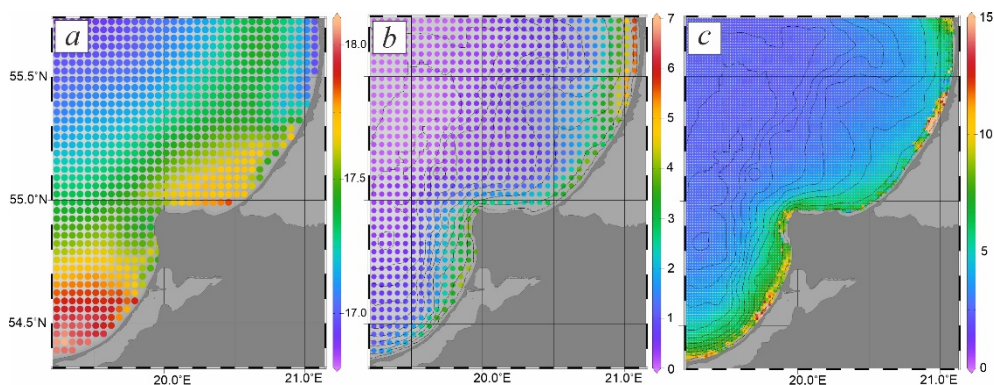


Fig. 2. Summer season mean values of SST (°C) (a), upwelling frequency (multi-year average number of days with negative temperature anomaly per month or season in a given cell) (b), and chlorophyll a concentration (up to 15 mg/m³) (c) in 2000–2019

The mean chlorophyll a concentration in the coastal zone within the 30-meter isobath for the summer seasons of 2000–2019 was 5.3 ± 2.7 mg/m³, which is generally comparable with the mean multi-year concentration values in the Baltic Sea surface layer obtained both from satellite and *in situ*^{3, 4} data [23, 27–30]. However, they have a larger dispersion compared to the estimates obtained from contact observations [31], where the concentration in the 0–10 m layer in the summer seasons of 2003–2007 was $\sim 4.3 \pm 1.6$ mg/m³.

In general, the chlorophyll a concentration in the Baltic Sea varies within a wide range of 0.3–130 mg/m³ [32]. In the area under study, local increases in concentrations are observed due to the runoff of the Vistula River, Vistula and Curonian lagoons. A zone with the depths of < 30 m is clearly distinguished in

³ Wasmund, N., Nausch, G., Postel, L., Witek, Z., Zalewski, M., Gromisz, S., Łysiak-Pastuszek, E., Olenina, I., Kavolyte, R., [et al.], 2000. *Trophic Status of Coastal and Open Areas of the South-Eastern Baltic Sea Based on Nutrient and Phytoplankton Data from 1993–1997*. Warnemünde: Institut für Ostseeforschung, 83 p. (Meereswissenschaftliche Berichte; vol. 38). doi:10.12754/msr-2000-0038

⁴ Bukanova, T., Nizhnikovskaya, O. and Trushevskiy, A., 2016. Assessment of Eutrophication in the Baltic Sea Coastal Waters from Satellite Imagery. In: *2nd Student Workshop on Ecology and Optics of Coastal Zones: Book of Abstracts*. Kaliningrad, Russia, pp. 1–4.

the water area. An increased upwelling frequency (at least 3 days per month) and chlorophyll a concentration ($> 5 \text{ mg/m}^3$) are observed there.

To assess the influence of upwelling intra-seasonal variability on the chlorophyll a concentration, the maps of average monthly values of these parameters were constructed according to the data of 2000–2019, supplemented by SST maps (Fig. 3).

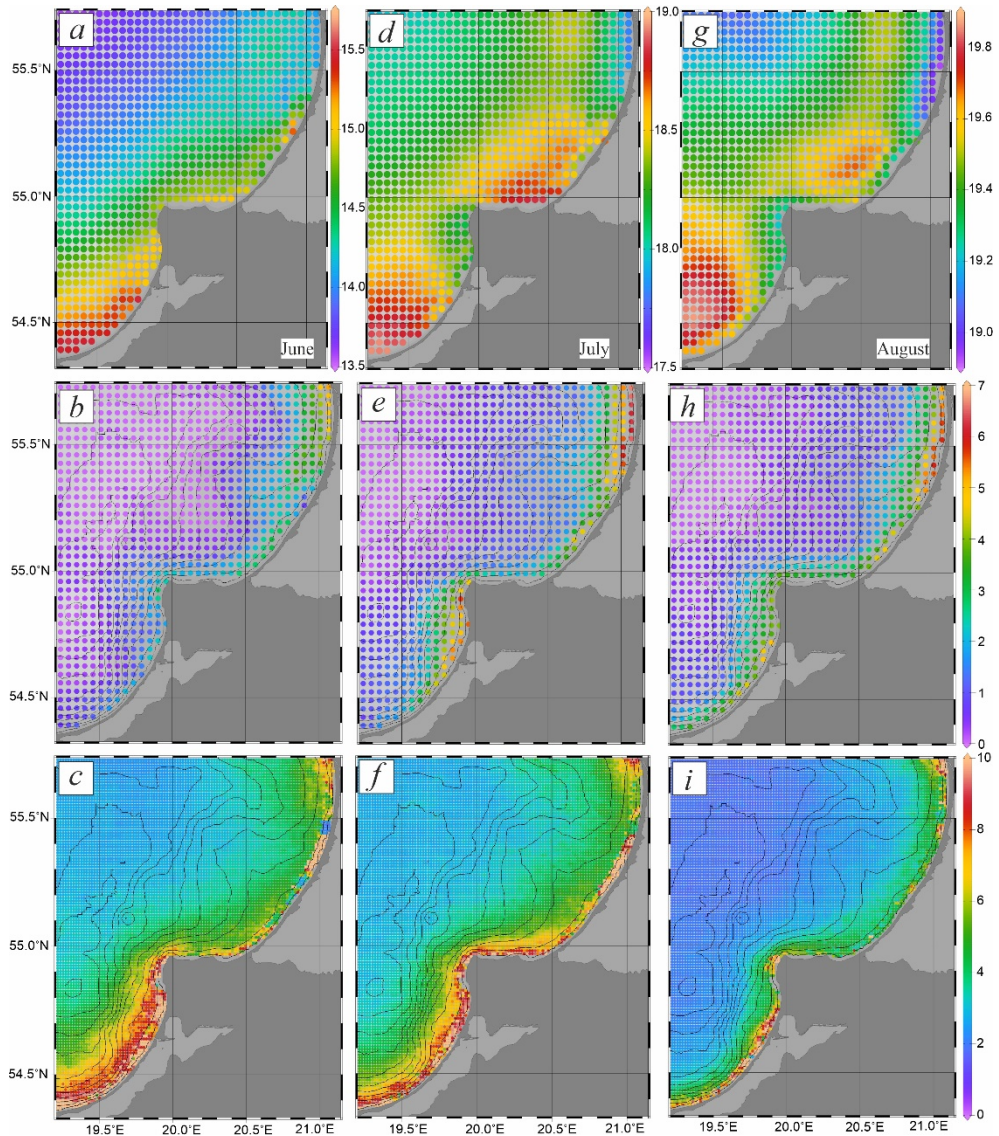


Fig. 3. Intra-seasonal variability of SST (°C) in June (a), July (d) and August (g); upwelling frequency (multi-year average number of the days with negative temperature anomaly per month or season in a given cell) in June (b), July (e) and August (h); chlorophyll a concentration (mg/m^3) in June (c), July (f) and August (i) of 2000–2019

In June, the SST of the coastal zone varied from 13.5°C in the open sea to 15.5 °C in the Vistula Spit western part. Along the northern coast of the region, the temperature was ~ 15 °C. Northwards of the Rybachiy Plateau, a local temperature increase (up to 15.3 °C) was observed, in the Curonian Spit northern part, the temperature was ~ 14.1 °C, which corresponded to the maximum frequency of negative temperature anomalies in this part of the coastal zone (Fig. 3, *a*). In June, upwelling reached its largest area in the Rybachiy Plateau region due to the bottom topography feature – an extensive shallow plateau is observed in this part of the water area. An average upwelling area off the western coast of the Sambia Peninsula in June was significantly less than that off the northern coast, which is associated with a large bottom slope (Fig. 3, *b*). In June, the highest chlorophyll *a* concentrations were observed northwards of the Rybachiy Plateau. The concentrations were higher near the Vistula Spit than along the Sambia Peninsula northern coast and the Curonian Spit southern part, which is probably due to higher SST in this area (Fig. 3, *c*).

Note that in the Baltic Sea the dominant phytoplankton communities in summer are the cyanobacteria *Nodularia spumigena*, *Anabaena* spp. and *Aphanizomenon* sp.⁵ [33]; the first two species are observed at depths of 10 m or less [34], the latter is found at greater depths. Probably, increased chlorophyll *a* concentrations in the southern part of the area under study in June are associated with optimal conditions for the development of cyanobacteria [35]. On average, within a 30-meter isobath the concentration is ~ 6.88 mg/m³, which is comparable with previously obtained estimates^{3, 4} [27, 28].

The SST spatial variability in July is somewhat different from that in June: the highest temperature is observed in the southern part of the region and along its northern coast (up to 19°C). The minimum temperature can be traced in the northern part of the Curonian Spit and is ~ 17.8 °C, in the open part of the sea – up to 18 °C (Fig. 3, *d*). An increase in the number of negative temperature anomalies is observed from June to July. In July, another area of frequent occurrence of negative anomalies appears at the western coast of the Kaliningrad Oblast (Fig. 3, *e*). In the same month, there is a significantly greater number of upwelling events along the western coast of the region compared to other months (~ 6 days per month in July versus 3–4 days in June and August). An algal bloom observed in July, associated with the massive development of cyanobacteria and water temperature rise in the coastal zone, is reflected in the chlorophyll *a* concentration increase along the Sambia Peninsula northern coast (Fig. 3, *f*). At the same time, concentration of the parameter under consideration in the southern part of the region decreases compared to June, which may be related to the depletion of nutrient supply in this area due to an earlier algal bloom. On average, the chlorophyll *a* concentration is ~ 7 mg/m³ in the coastal zone.

⁵ Neumann, T. and Schernewski, G., 2002. Will Algal Blooms in the Baltic Sea Increase in Future? Model Simulations with Different Eutrophication Combat Strategies. In: Deutsches IHP/OHP-Nationalkomitee, 2002. *Low-Lying Coastal Areas – Hydrology and Integrated Coastal Zone Management. International Symposium on Low-Lying Coastal Areas. Hydrology and ICZM*. IHP/OHP-Berichte, Sonderheft 13. Koblenz: Deutsches IHP/OHP-Nationalkomitee, pp. 139-145.

In August, the SST up to isobaths of 20–40 m is slightly lower in the coastal zone than in the areas with greater depths (Fig. 3, *g*). The maximum temperature is also observed in the SEB southern part, in the area of 70-meter isobath (up to 19.9 °C), the minimum is observed in the Curonian Spit northern part (up to 19 °C). In August, a slight decrease in the number of upwelling events compared to July (Fig. 3, *h*) takes place. In August, the area of frequent upwelling manifestation along the Curonian Spit coast and the western coast of the region decreases. This is probably due to the warming in the wide strip of shallow waters and an increase in the seasonal thermocline depth. The largest number of upwelling events in August, as well as in June – July, is observed at the exit from the Curonian Lagoon, which is also noted in [20]. In August, the mean values of chlorophyll a concentration are slightly lower than in June and July ($< 5 \text{ mg/m}^3$), which is also noted in [36, 37]. The highest values are observed westwards of Cape Taran and at the exits from the lagoons (Fig. 3, *i*).

The increased values of chlorophyll a concentration are naturally observed at the exits from the lagoons. In the area close to the Klaipeda Strait, the zone with increased concentrations in June and July is smaller than in the Strait of Baltiysk area. The increased concentration values in the southern part may be associated with the effect of the Vistula River runoff; in the northern part – with the propagation of the Curonian Lagoon waters to the north. This can probably be explained by the fact that, in general, the Curonian Lagoon is characterized by a higher level of phytoplankton productivity compared to the Vistula Lagoon [38].

The described spatial variability of chlorophyll a in the SEB coastal zone indicates the presence of not only intra-seasonal fluctuations, but also regional distribution features, possibly caused by the influence of mesoscale processes (such as upwelling) developing in the coastal zone.

To quantify the impact of upwelling events on the chlorophyll a concentration in the coastal zone, an analysis of the upwelling events provided by the satellite data was carried out.

Quantitative assessment of upwelling influence on chlorophyll a concentration in the SEB. Table 1 provides the mean values of chlorophyll a concentration on the profile before, during and after the upwelling in 2000–2019. The dashes correspond to the periods with no available data.

It follows from Table 1 that lower chlorophyll a concentrations in the coastal zone after upwelling, compared to the concentration values before it, appear regardless of its duration. Over the entire study period, chlorophyll a drops by 0.4 mg/m^3 after the start of upwelling and by 1.42 mg/m^3 (27%) after its finish. The greatest decrease in concentration ($\sim 4.5 \text{ mg/m}^3$ or 67%) after upwelling was observed in June 2016. Moreover, in 9 out of 31 cases, the decrease in concentration after upwelling was $> 3 \text{ mg/m}^3$ (a drop of 37–67%), in 11 cases – $> 1 \text{ mg/m}^3$. The chlorophyll a concentration during upwelling, on average, was often lower on the profile than in the upwelling zone. This is probably due to generally increased concentration values in the coastal zone (see Fig. 2, *c*).

Table 1

Chlorophyll a concentration before, during and after upwelling

Upwelling dates on profile	Profile number	Upwelling duration, days	Mean concentration of chlorophyll <i>a</i> , mg/m ³		
			before upwelling	during upwelling	after upwelling
04–10.07.2001	3	7	6.26	5.22	2.57
23–31.07.2001	3	9	2.72	3.27	5.70
23–26.08.2001	3	4	3.22	4.33	3.03
17–19.07.2002	4	3	6.12	5.67	2.84
04–31.08.2002	4	27	5.19	4.51	–
02–05.06.2003	6	4	1.22	1.98	1.67
16.07–14.08.2003	1	30	4.34	7.31	4.52
07–15.08.2004	4	9	4.55	3.59	3.83
09–13.07.2005	9	5	8.95	7.56	5.66
03–09.07.2006	4	7	6.36	3.92	3.35
12.07–22.08.2006	4	42	3.35	3.78	1.52
07–12.06.2007	6	6	9.59	7.27	–
15–16.06.2007	6	1	–	7.66	6.96
01–10.06.2008	7	10	–	3.78	5.31
13–15.07.2008	8	3	7.62	8.50	7.57
27.07–03.08.2008	8	8	7.50	6.88	3.54
30.06–05.07.2009	8	6	–	5.76	6.72
30.06–08.07.2009	2	9	5.13	4.52	4.85
08–11.08.2009	8	4	6.18	8.68	2.05
15–20.07.2010	8	6	9.66	8.92	8.79
04–06.08.2011	4	3	3.79	5.36	3.07
23–27.07.2014	2	5	6.63	3.46	2.57
23–29.07.2014	4	7	5.39	3.78	2.74
09.08.2014	2	1	2.54	2.76	2.53
15–25.08.2015	9	11	5.78	4.70	2.69
05–09.06.2016	5	5	6.70	4.57	2.21
01–05.07.2018	6	5	3.33	5.26	3.86
16–21.07.2018	6	6	4.45	2.76	5.27
25–29.07.2018	6	5	5.27	3.12	–
31.07.2018	6	1	–	2.67	2.72
01–08.08.2019	4	8	3.32	2.46	2.51
Mean value for 2000–2009			5.52	5.48	4.22
Mean value for 2010–2019			5.17	4.15	3.54
Mean value for 2000–2019			5.38	4.97	3.95

Within the period of 2000–2009, the chlorophyll *a* increase after upwelling was noted three times: at the end of July 2001, beginning of June 2003 and in mid-July – August 2003 (see Table 1); within the period of 2010–2019, the increase after upwelling was observed only in July 2018.

The average decrease in chlorophyll *a* concentration after upwelling in the second decade is slightly greater than in the first one. This may be due both to the changes in characteristics of the studied upwelling events (changes in their duration and frequency by month) and to the influence of seasonal variation in

the chlorophyll *a* concentration: in the second half of July – August a natural decrease takes place, which may be due to the depletion of nutrient supply in this area; in the second decade, the largest share of all considered upwelling events were the upwellings of July and August.

Most of the studied (see Table 1) upwelling events lasted up to 5 days (14 out of 31). Moreover, in the first decade the duration of upwelling events included in the analysis is ~ 10 days; in the second decade – slightly more than 5. After short upwelling events (5 days or less), the chlorophyll *a* concentration drops by an average of 1.24 mg/m^3 , after longer ones – by 1.89 mg/m^3 .

To illustrate the upwelling effect on the chlorophyll *a* concentration in the coastal zone, the maps of its changes in June 2007 are demonstrated in Fig. 4.

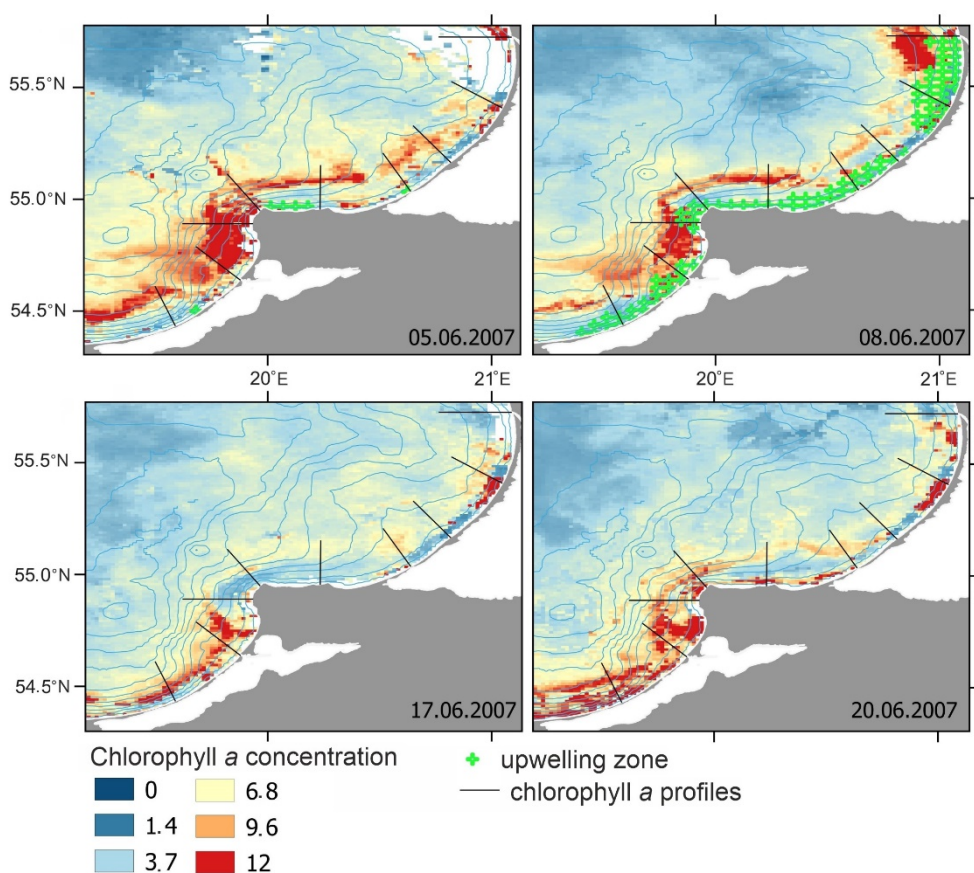


Fig. 4. Changes in chlorophyll *a* concentration during and after the upwelling event on June 4–16, 2007

The upwelling observed on 4–16 June 2007 led to the following change in the chlorophyll *a* concentration: on the first day (June 5), its mean value in the upwelling zone decreased to $\sim 3 \text{ mg/m}^3$, while outside the upwelling zones it was $\sim 10 \text{ mg/m}^3$ (Fig. 4). A chlorophyll *a* front, characterized by a two-fold drop in concentration (from 7–8 to 4 mg/m^3), was noted on profile 6 (Fig. 1, Cape Taran area)

on 8 June at the upwelling boundary at ~ 9 km from the coast. A concentration drop of 40–50% was demonstrated in [25]. After the end of the upwelling (June 17), the concentration in the coastal zone of ~ 7 km wide was still reduced; its increase in the coastal zone was noted only since June 20, on the fourth day after the end of the upwelling.

Previously, it was shown for the Baltic Sea that in coastal areas there is a time delay between phytoplankton growth and the nutrient supply to the surface layer as a result of upwelling [8, 23, 39]. For example, in the Gulf of Finland and off the island of Gotland, the increase in phytoplankton biomass occurred with a 2–3-week delay after the upwelling. In [11], no growth of phytoplankton was noted after the upwelling; the authors attribute this to the fact that 10 days after the end of one upwelling, the next one began. In this case, the time interval between nutrient supply and phytoplankton growth depends not only on the upwelling characteristics, but also on the species composition of phytoplankton in its upwelling area, as well as on the ratio of nutrients and the temperature of the water raised to the surface layer. An important factor is also the length of an adaptation period of phytoplankton communities raised to the surface layer to temperature, light, and nutrient concentrations [7].

In addition, due to the presence of a seasonal variation in the chlorophyll *a* concentration, associated with abiotic factors and succession of the phytoplankton community, it is also important to know the quantitative contribution of upwelling events to the variability of its concentration during the summer season on the profiles under study (see Fig. 1). The changes in concentration are presented in Table 2.

Table 2

Changes in mean chlorophyll *a* concentration in summer months due to upwelling

Month	Mean concentration of chlorophyll <i>a</i> , mg/m ³	Upwelling mean duration, days	Mean concentration of chlorophyll <i>a</i> , mg/m ³	
			before upwelling	after upwelling
June	5.27	5.20	5.84	4.04
July	5.33	7.18	5.98	4.58
August	3.78	12.11	4.21	2.65

Chlorophyll *a* mean values on the profiles are approximately equal in June and July with the highest weighted mean concentration observed in June. This difference probably reflects intra-seasonal variation of the upwelling influence on concentrations. Moreover, their average duration amounted to 5.2–7.18 days in June–July and increased significantly by August. Within the week after the upwelling, the chlorophyll *a* concentration demonstrates reduced values in all months and amounts to ~ 1.4–1.8 mg/m³. Compared to the long-term average data, its greatest decrease is observed in June. Moreover, July had the greatest number of significant concentration decreases after the upwelling (6 times out of 9 within the entire study period – by more than 3 mg/m³ and 8 times out of 11 – by more than 1 mg/m³).

A joint analysis of chlorophyll a and SST satellite data shows that a decrease in its concentration caused by upwelling leads to a positive effect on water quality in the coastal zone [39]. It is worth noting that in the works studying algal blooms, it is indicated that in most cases blooms are observed already at a distance from the coast and it is comparable to the upwelling width [40].

The performed analysis confirms the need to take into account the intra-seasonal variation of chlorophyll a concentration when considering the influence of upwelling events, which is important for correct assessments of changes in the ecological state of the coastal zone.

Conclusion

According to the data on the frequency and duration of upwelling events in June – August 2000–2019 and multisensor satellite observations of chlorophyll a concentration in the coastal zone of the southeastern Baltic Sea, long-term and monthly average values of the studied parameters were obtained. High concentrations were observed in the area of exits from the Vistula and the Curonian lagoons, the highest concentrations were found northwards of the Rybachiy Plateau. Moreover, in the Curonian Spit northern part, in the area of the highest frequency of upwelling events, the zone with increased chlorophyll a concentrations had a smaller area than in the Strait of Baltiysk. In June, the upwelling zone had the largest area in the Rybachiy Plateau region, while the chlorophyll a concentration there was lower than northwards and southwards of the plateau. This indicated a possible relationship between the chlorophyll a spatial variability and the frequency of upwelling events.

In the study area, nine 20-kilometer profiles from the coast towards the sea were analyzed, on which the chlorophyll a concentrations were calculated for a week before, during and after the upwelling. This provided the assessment of their influence on concentration. It was demonstrated that a decrease in concentration was observed after an upwelling event of any duration and in all months; on average, after an upwelling event the concentration dropped by more than 1 mg/m³ (27%). After short upwelling events (lasting less than 5 days), the chlorophyll a concentration decreased, on average, by 1.24 mg/m³, after longer ones – by 1.89 mg/m³. On average, in June–August, the concentration dropped by approximately 1.4–1.8 mg/m³ after upwelling; in July, a significant decrease was observed most often. The noted difference reflects the presence of an intra-seasonal variation in the upwelling influence on the chlorophyll a concentration in the considered water area associated with both abiotic factors and succession of the phytoplankton community.

The analysis of temporal variability of chlorophyll a concentration revealed that a few days after the upwelling its growth begins, which is probably associated with the development of phytoplankton communities caused by nutrient supply to the photic layer and is often stimulated by the water temperature increase.

The decrease in chlorophyll a concentration after upwelling in the second decade of the current century is slightly greater than in the first one, which is likely due to the changes in the characteristics of the events included in the analysis. In the second decade, a decrease in the duration of upwelling was observed, most significant – in July and August. On average, in 2000–2009, upwelling throughout the SEB lasted about a week (7.1 days), in 2010–2019 – 4.66 days. Most of those

studied occurred during upwelling events lasting less than 5 days (14 out of 31, 7 in each decade) and 6–10 days (13 upwellings). Moreover, in the first decade of the 21st century the duration of upwelling events is ~ 10 days, in the second – ~ 5.

In the future, some targeted observations are required in upwelling zones and beyond them in order to analyze the species composition of phytoplankton communities. This will enable us to identify the influence of upwelling on the ecological state of the Baltic Sea waters, including algal blooms with a massive development of potentially toxic cyanobacteria.

REFERENCES

1. Lehmann, A., Myrberg, K. and Höfllich, K., 2012. A Statistical Approach to Coastal Upwelling in the Baltic Sea Based on the Analysis of Satellite Data for 1990–2009. *Oceanologia*, 54(3), pp. 369-393. <https://doi.org/10.5697/oc.54-3.369>
2. Kapustina, M.V. and Zimin, A.V., 2021. Upwelling Spatiotemporal Characteristics in the Southeastern Baltic Sea in 2010–2019. *Fundamentalnaya i Prikladnaya Gidrofizika*, 14(4), pp. 52-63. <https://doi.org/10.7868/S2073667321040055> (in Russian).
3. Bednorz, E., Półrolniczak, M. and Tomczyk, A.M., 2021. Regional Circulation Patterns Inducing Coastal Upwelling in the Baltic Sea. *Theoretical and Applied Climatology*, 144, pp. 905-916. <https://doi.org/10.1007/s00704-021-03539-7>
4. Kowalewski, M., 2005. The Influence of the Hel Upwelling (Baltic Sea) on Nutrient Concentrations and Primary Production – the Results of an Ecohydrodynamic Model. *Oceanologia*, 47(4), pp. 567-590.
5. Lips, I., Lips, U. and Liblik, T., 2009. Consequences of Coastal Upwelling Events on Physical and Chemical Patterns in the Central Gulf of Finland (Baltic Sea). *Continental Shelf Research*, 29(15), pp. 1836-1847. <https://doi.org/10.1016/j.csr.2009.06.010>
6. Krężel, A., Szymanek, L., Kozłowski, Ł. and Szymelfenig, M., 2005. Influence of Coastal Upwelling on Chlorophyll a Concentration in the Surface Water along the Polish Coast of the Baltic Sea. *Oceanologia*, 47(4), pp. 433-452.
7. Zalewski, M., Ameryk, A. and Szymelfenig, M., 2005. Primary Production and Chlorophyll a Concentration during Upwelling Events along the Hel Peninsula [the Baltic Sea]. *Oceanological and Hydrobiological Studies*, 34(Suppl. 2), pp. 97-113.
8. Vahtera, E., Laanemets, J., Pavelson, J., Huttunen, M. and Kononen, K., 2005. Effect of Upwelling on the Pelagic Environment and Bloom-Forming Cyanobacteria in the Western Gulf of Finland, Baltic Sea. *Journal of Marine Systems*, 58(1-2), pp. 67-82. <https://doi.org/10.1016/j.jmarsys.2005.07.001>
9. Nausch, M., Nausch, G., Lass, H.U., Mohrholz, V., Nagel, K., Siegel, H. and Wasmund, N., 2009. Phosphorus Input by Upwelling in the Eastern Gotland Basin (Baltic Sea) in Summer and Its Effects on Filamentous Cyanobacteria. *Estuarine, Coastal and Shelf Science*, 83(4), pp. 434-442. <https://doi.org/10.1016/j.ecss.2009.04.031>
10. Lips, I. and Lips, U., 2010. Phytoplankton Dynamics Affected by the Coastal Upwelling Events in the Gulf of Finland in July–August 2006. *Journal of Plankton Research*, 32(9), pp. 1269-1282. <https://doi.org/10.1093/plankt/fbq049>
11. Kuvaldina, N., Lips, I., Lips, U. and Liblik, T., 2010. The Influence of a Coastal Upwelling Event on Chlorophyll a and Nutrient Dynamics in the Surface Layer of the Gulf of Finland, Baltic Sea. *Hydrobiologia*, 639(1), pp. 221-230. <https://doi.org/10.1007/s10750-009-0022-4>
12. Wasmund, N., Tuimala, J., Suikkanen, S., Vandepitte, L. and Kraberg, A., 2011. Long-Term Trends in Phytoplankton Composition in the Western and Central Baltic Sea. *Journal of Marine Systems*, 87(2), pp. 145-159. <https://doi.org/10.1016/j.jmarsys.2011.03.010>
13. Kudryavtseva, E.A. and Aleksandrov, S.V., 2019. Hydrological and Hydrochemical Underpinnings of Primary Production and Division of the Russian Sector in the Gdansk Basin of the Baltic Sea. *Oceanology*, 59(1), pp. 49-65. <https://doi.org/10.1134/S0001437019010077>

14. Krek, A.V., Krek, E.V., Danchenkov, A.R., Krechik, V.A. and Kapustina, M.V., 2021. The Role of Upwellings in the Coastal Ecosystem of the Southeastern Baltic Sea. *Regional Studies in Marine Science*, 44(1), 101707. <https://doi.org/10.1016/j.rsma.2021.101707>
15. Zhurbas, V., Laanemets, J. and Vahtera, E., 2008. Modeling of the Mesoscale Structure of Coupled Upwelling/Downwelling Events and the Related Input of Nutrients to the Upper Mixed Layer in the Gulf of Finland, Baltic Sea. *Journal of Geophysical Research: Oceans*, 113(C5), C05004. <https://doi.org/10.1029/2007JC004280>
16. Huntsman, S.A. and Barber, R.T., 1977. Primary Production off Northwest Africa: the Relationship to Wind and Nutrient Conditions. *Deep Sea Research*, 24(1), pp. 25-33. [https://doi.org/10.1016/0146-6291\(77\)90538-0](https://doi.org/10.1016/0146-6291(77)90538-0)
17. Siegel, H., Gerth, M., Neumann, T. and Doerffer, R., 1999. Case Studies on Phytoplankton Blooms in Coastal and Open Waters of the Baltic Sea Using Coastal Zone Color Scanner Data. *International Journal of Remote Sensing*, 20(7), pp. 1249-1264. <https://doi.org/10.1080/014311699212713>
18. Janssen, F., Neumann, T. and Schmidt, M., 2004. Inter-Annual Variability in Cyanobacteria Blooms in the Baltic Sea Controlled by Wintertime Hydrographic Conditions. *Marine Ecology Progress Series*, 275, pp. 59-68. <https://doi.org/10.3354/meps275059>
19. Gogolev, D.G., Bukanova, T.V. and Kudryavtseva, E.A., 2020. Chlorophyll «a» Concentration in the South-Eastern Baltic Sea in Summer 2018 (on Satellite Data). *Vestnik of Immanuel Kant Baltic Federal University. Series: Natural and Medical Sciences*, (4), pp. 83-91 (in Russian).
20. Dabuleviciene, T., Kozlov, I.E., Vaiciute, D. and Dailidienė, I., 2018. Remote Sensing of Coastal Upwelling in the South-Eastern Baltic Sea: Statistical Properties and Implications for the Coastal Environment. *Remote Sensing*, 10(11), 1752. <https://doi.org/10.3390/rs10111752>
21. Pitarch, J., Volpe, G., Colella, S., Krasemann, H. and Santoleri, R., 2016. Remote Sensing of Chlorophyll in the Baltic Sea at Basin Scale from 1997 to 2012 Using Merged Multi-Sensor Data. *Ocean Science*, 12(2), pp. 379-389. <https://doi.org/10.5194/os-12-379-2016>
22. Kratzer, S., Brockmann, C. and Moore, G., 2008. Using MERIS Full Resolution Data to Monitor Coastal Waters – A Case Study from Himmerfjärden, a Fjord-Like Bay in the Northwestern Baltic Sea. *Remote Sensing of Environment*, 112(5), pp. 2284-2300. <https://doi.org/10.1016/j.rse.2007.10.006>
23. Uiboupin, R., Laanemets, J., Sipelgas, L., Raag, L., Lips, I. and Buhhalko, N., 2012. Monitoring the Effect of Upwelling on the Chlorophyll a Distribution in the Gulf of Finland (Baltic Sea) Using Remote Sensing and in Situ Data. *Oceanologia*, 54(3), pp. 395-419. <https://doi.org/10.5697/oc.54-3.395>
24. Paszkuta, M., Zapadka, T. and Krężel, A., 2019. Assessment of Cloudiness for Use in Environmental Marine Research. *International Journal of Remote Sensing*, 40(24), pp. 9439-9459. <https://doi.org/10.1080/01431161.2019.1633697>
25. Dabuleviciene, T., Vaiciute, D. and Kozlov, I.E., 2020. Chlorophyll-a Variability during Upwelling Events in the South-Eastern Baltic Sea and in the Curonian Lagoon from Satellite Observations. *Remote Sensing*, 12(21), 3661. <https://doi.org/10.3390/rs12213661>
26. Kapustina, M.V. and Zimin A.V., 2021. Upwelling Frequencies in the South-Eastern Baltic Sea in 2000-2019. In: MSU, 2021. *X International Conference “Marine Research and Education” (MARESEDU-2021): Conference Proceedings*. Tver: PoliPRESS. Vol. 1(3), pp. 152-156 (in Russian).
27. Nakonieczny, J., Renk, H. and Wiktor, J., 1991. Chlorophyll a Concentration and Distribution in the Southern Baltic in the Years 1979-1983. *Oceanologia*, 30, pp. 77-91.
28. Kudryavtseva, E., Aleksandrov, S., Bukanova, T., Dmitrieva, O. and Rusanov, I., 2019. Relationship between Seasonal Variations of Primary Production, Abiotic Factors and Phytoplankton Composition in the Coastal Zone of the South-Eastern Part of the Baltic Sea. *Regional Studies in Marine Science*, 32, 100862. <https://doi.org/10.1016/j.rsma.2019.100862>
29. Kopelevich, O.V. and Sahling, I.V., 2020. Interannual Changes of the Bio-Optical Characteristics in the Surface Layer of the Seas Surrounding the Western Part of Russia from Data of Satellite

- Ocean Color Scanners. *Fundamental and Applied Hydrophysics*, 13(2), pp. 16-24. <https://doi.org/10.7868/S2073667320020021>
30. Stramska, M., Konik, M., Aniskiewicz, P., Jakacki, J. and Darecki, M., 2021. Comparisons of Satellite and Modeled Surface Temperature and Chlorophyll Concentrations in the Baltic Sea with in Situ Data. *Remote Sensing*, 13(15), 3049. <https://doi.org/10.3390/rs13153049>
 31. Aleksandrov, S.V. and Kudryavtseva, E.A., 2012. Chlorophyll “a” and Primary Production of Phytoplankton. In: V. V. Sivkov, ed., 2012. *Oil and Environment of the Kaliningrad Region. Vol. II: Sea*. Kaliningrad: Terra Baltica, 576 p. (in Russian).
 32. Kratzer, S. and Moore, G., 2018. Inherent Optical Properties of the Baltic Sea in Comparison to Other Seas and Oceans. *Remote Sensing*, 10(3), 418. <https://doi.org/10.3390/rs10030418>
 33. Kahru, M., Horstmann, U. and Rud, O., 1994. Satellite Detection of Increased Cyanobacteria Blooms in the Baltic Sea: Natural Fluctuation or Ecosystem Change? *AMBIO: A Journal of the Human Environment*, 23, pp. 469-472.
 34. Hajdu, S., Högländer, H. and Larsson, U., 2007. Phytoplankton Vertical Distributions and Composition in Baltic Sea Cyanobacterial Blooms. *Harmful Algae*, 6(2), pp. 189-205. <https://doi.org/10.1016/j.hal.2006.07.006>
 35. Ennet, P., Kuosa, H. and Tamsalu, R., 2000. The Influence of Upwelling and Entrainment on the Algal Bloom in the Baltic Sea. *Journal of Marine Systems*, 25(3-4), pp. 359-367. [https://doi.org/10.1016/S0924-7963\(00\)00027-0](https://doi.org/10.1016/S0924-7963(00)00027-0)
 36. Evtushenko, N.V. and Sheberstov, S.V., 2016. Study of the Cycles of Phytoplankton Blooms in the Baltic Sea from Aqua MODIS Data. *Sovremennye Problemy Distantionnogo Zondirovaniya Zemli iz Kosmosa*, 13(3), pp. 114-124. <https://doi.org/10.21046/2070-7401-2016-13-3-114-124> (in Russian).
 37. Bukanova, T.V., Bubnova, E.S. and Aleksandrov, S.V., 2022. Remote Monitoring of the Offshore Site of the Rosyanka Carbon Polygon (the Baltic Sea): First Results. *Sovremennye Problemy Distantionnogo Zondirovaniya Zemli iz Kosmosa*, 19(6), pp. 234-247. <https://doi.org/10.21046/2070-7401-2022-19-6-234-247> (in Russian).
 38. Aleksandrov, S.V. and Gorbunova, Yu.A., 2012. Phytoplankton Production and Chlorophyll Content in Different Types of Estuaries. *Vestnik of Immanuel Kant Baltic Federal University. Series: Natural and Medical Sciences*, (1), pp. 90-98 (in Russian).
 39. Wasmund, N., Nausch, G. and Voss, M., 2012. Upwelling Events May Cause Cyanobacteria Blooms in the Baltic Sea. *Journal of Marine Systems*, 90(1), pp. 67-76. <https://doi.org/10.1016/j.jmarsys.2011.09.001>
 40. Löptien, U. and Dietze, H., 2022. Retracing Cyanobacteria Blooms in the Baltic Sea. *Scientific Reports*, 12(1), 10873. <https://doi.org/10.1038/s41598-022-14880-w>

Submitted 10.04.2023; approved after review 12.01.2024;
accepted for publication 18.01.2024.

About the authors:

Mariya V. Kapustina, Junior Research Associate, Shirshov Institute of Oceanology of RAS (36 Nakhimovskiy Ave., Moscow, 117997, Russian Federation), **ORCID ID: 0000-0002-7507-3170**, **ResearcherID: L-2625-2016**, **Scopus AuthorID: 57201388973**, kapustina.mariya@ya.ru

Aleksei V. Zimin, Chief Research Associate, Shirshov Institute of Oceanology of RAS (36 Nakhimovskiy Ave., Moscow, 117997, Russian Federation), DSc (Geogr.), Associate Professor, **ORCID ID: 0000-0003-1662-6385**, **ResearcherID: C-5885-2014**, **Scopus AuthorID: 55032301400**, zimin2@mail.ru

Contribution of the co-authors:

Mariya V. Kapustina – methodology, data collection and processing, obtained data interpretation, visualization, original draft preparation

Aleksei V. Zimin – methodology, scientific supervision, article review and editing

The authors have read and approved the final manuscript.

The authors declare that they have no conflict of interest.

Temporal Variability of the Beryllium-7 (^7Be) Scavenging Ratio in the Sevastopol Region

D. A. Kremenchutskii

Marine Hydrophysical Institute of RAS, Sevastopol, Russian Federation
✉ d.kremenchutskii@mhi-ras.ru

Abstract

Purpose. The study is purposed at identifying the features of temporal variability in the relation of ^7Be scavenging ratio at the seasonal and interannual time intervals depending on the amount and frequency of precipitation.

Methods and Results. The scavenging ratio was assessed based on the field data on the ^7Be concentration values in the atmosphere and precipitation in 2012–2020. Application of ANOVA made it possible to examine the relationship between the scavenging ratio and the variations in ^7Be concentrations in the atmosphere and precipitation. The relationship between the scavenging ratio and the precipitation amount and frequency was studied by the correlation method of analysis.

Conclusions. The scavenging ratio values averaged over a season and a year varied within the ranges 423–1286 and 508–919, respectively. The geometric mean value of the scavenging ratio was 719^{+227}_{-173} .

The intraannual variability of the scavenging ratio is absent at the 95% confidence level. The variability in average annual values of the scavenging ratio demonstrates a decrease in 2013 (as compared to 2012) from 664 to 508, an increase to 919 in 2016 and again a decrease to 516 in 2020. The ANOVA results indicate that variability of the scavenging ratio values averaged over a season and a year is due to the variation in ^7Be concentration in precipitation by 90 and 74%, respectively. In its turn, the long-term seasonal variability of ^7Be concentration in precipitation is conditioned by the variations in ^7Be concentration in the atmosphere ($r = 0.64$) and in the precipitation amount ($r = -0.50$). The relationship between the annual values of ^7Be concentration in precipitation and its concentration in the atmosphere or with the precipitation parameters has not been revealed. The correlation analysis results indicate that the variability of precipitation parameters (amount and frequency) produces no statistically significant effect at the 95% confidence level upon the variability of scavenging ratio values at seasonal and annual time intervals.

Keywords: Beryllium-7 (^7Be), precipitation, atmospheric aerosol, scavenging ratio

Acknowledgements: The author is grateful to G. F. Batrakov, A. P. Arbuzova and T. M. Ivanova for their assistance in obtaining the data. The data for the study were obtained within the framework of state task of the Ministry of Science and Higher Education of Russian Federation (FNNN-2024-0001). Data analysis was carried out under the Russian Science Foundation grant (No. 22-77-10056).

For citation: Kremenchutskii, D.A., 2024. Temporal Variability of the Beryllium-7 (^7Be) Scavenging Ratio in the Sevastopol Region. *Physical Oceanography*, 31(2), pp. 246-257.

© 2024, D. A. Kremenchutskii

© 2024, Physical Oceanography

Introduction

Beryllium-7 (^7Be) is a radionuclide of cosmogenic origin characterized by a relatively short half-life (~ 53 days). It is formed in the atmosphere: approximately 2/3 in the stratosphere and the remaining 1/3 in the troposphere [1]. ^7Be enters the marine environment mainly (80–90%) with precipitation [2].



The remaining 10–20% accrue to the dry deposition flux. Works discussing the possibility of using [3–6] or using [7–9] this radionuclide as a tracer to obtain quantitative estimates of the entry of other substances (primarily so-called geotracers) from the atmosphere into the marine environment have been issued since the last decade. For this purpose, the parameters for removing substances from the atmosphere based on data on the ^7Be concentration in the atmosphere and precipitation (or marine environment) are first calculated and then their flux is estimated. Such parameters can be deposition velocity and scavenging ratio according to [5, 10–12]. The deposition velocity relates the substance flux to its concentration in the atmosphere while the scavenging ratio relates the substance concentration in precipitation to its concentration in the atmosphere. Although each of these two parameters can be used to obtain quantitative estimates of both substance flux from the atmosphere with precipitation and its concentration in precipitation, the first parameter (deposition velocity) receives objectively more attention than the second one (scavenging ratio). In particular, the available literature contains information on the monthly, seasonal and annual average values of the ^7Be deposition velocity, their temporal variability and factors determining it [11, 13–15]. At the same time, the depth of research into the scavenging ratio is limited by calculating this parameter value [11, 16–18].

The study is purposed at identifying the features of temporal variability in the relation of ^7Be scavenging ratio in rainfall to its concentration in the atmosphere at the seasonal and interannual time intervals depending on the amount and frequency of precipitation.

Materials and methods

Determination of ^7Be concentration in the surface atmosphere and in atmospheric precipitation. The methods used for collecting and processing samples of atmospheric precipitation and aerosols with the subsequent determination of ^7Be activity in them are described in detail in [15, 19, 20]. A summary of these methods is given below.

Atmospheric aerosol and precipitation samples were taken from the roof of the building of Marine Hydrophysical Institute of RAS. A Petryanov filter (FPP-15-1.5) was used to concentrate the aerosol. The average speed of air pumping through the filter was $\sim 525 \text{ m}^3 \cdot \text{h}^{-1}$. As a rule, four daily samples (Monday – Friday) and one three-day sample (Friday – Monday) were taken during the week. The filter was compressed into a tablet with a diameter of 5.2 cm and a height of 0.5 cm after the completion of air filtration. Moist atmospheric precipitation samples were collected using a 0.64 m^2 cuvette connected to a 50 L plastic barrel. The precipitation in the barrel, if any, was collected immediately after sampling the atmospheric aerosol. Radionuclide concentration from wet atmospheric precipitation samples was carried out using Dowex HCR-S/S cation exchange resin. The resin was packaged in a Petri dish with a diameter of 5.2 cm and a height of 1.4 cm or in a test tube with a diameter of 2.8 cm and a height of 7 cm.

In all cases, ^7Be activity measurements in the samples were carried out on a gamma spectrometer with one of two detectors: a NaI(Tl) crystal with a diameter and a height of 6.3 cm or a NaI(Tl) crystal with a diameter and a height of 10 cm with a well with a diameter of 3 cm and a height of 6 cm. Both crystals had a resolution of 7% for the ^{137}Cs peak and were located in a low-background multilayer protection. The single sample activity was recorded for 5–24 hours. The total error in measuring ^7Be activity in samples usually did not exceed 15%.

The total number of 2,056 samples of atmospheric aerosols and 405 samples of rainfall was collected and processed in 2012–2020. The obtained atmospheric and precipitation ^7Be concentrations were averaged for each individual season and year under this study. As a result, two series of average seasonal and average annual values lasting 36 seasons and 9 years were obtained for each parameter.

Meteorological parameters. Precipitation amount data was obtained by normalizing the precipitation sample volume to the sampler area. Precipitation frequency data represents the number of days with precipitation in a particular season or year.

Scavenging ratio of ^7Be was calculated as follows:

$$W = \kappa \frac{C_w}{C_a}, \quad (1)$$

where W is scavenging ratio; κ is correction taking into account the difference in density of water and air, equal to $1.2 \cdot 10^{-3}$; C_w and C_a are seasonally averaged ^7Be concentrations in moist atmospheric precipitation and on atmospheric aerosols, respectively, $\text{Bq} \cdot \text{m}^{-3}$.

Knowing the scavenging ratio, it is possible to estimate the ^7Be flux from the atmosphere with precipitation using the following equation:

$$F = \frac{WC_a Pr}{k}, \quad (2)$$

where F is flux, $\text{Bq} \cdot \text{m}^{-2} \cdot \text{season}^{-1}$; Pr is precipitation amount, $\text{mm} \cdot \text{season}^{-1}$.

Results and discussion

Basic statistics. Figure 1 shows the obtained series of observations of ^7Be concentrations in the atmosphere and precipitation, as well as the scavenging ratio estimates. Seasonally and annually averaged values of ^7Be concentration in precipitation varied in the ranges of 1.2–5.4 and 1.5–3.0 $\text{Bq} \cdot \text{L}^{-1}$, respectively, in 2012–2020 (Fig. 2, *a*). The majority (80%) of the seasonally averaged concentration values were in the range of 1.4–3.6 $\text{Bq} \cdot \text{L}^{-1}$. The 10th and 90th percentiles for average annual values coincide with the minimum and maximum of this series due to its relatively short duration for this series and the remaining two series shown in Fig. 2. Variation coefficients were 38.5 and 22.8% for seasonal and annual values. The arithmetic mean and median values of seasonally averaged ^7Be concentrations were 2.4 and 2.2 $\text{Bq} \cdot \text{L}^{-1}$, respectively. This indicates that the distribution of seasonal concentration values may be different from normal.

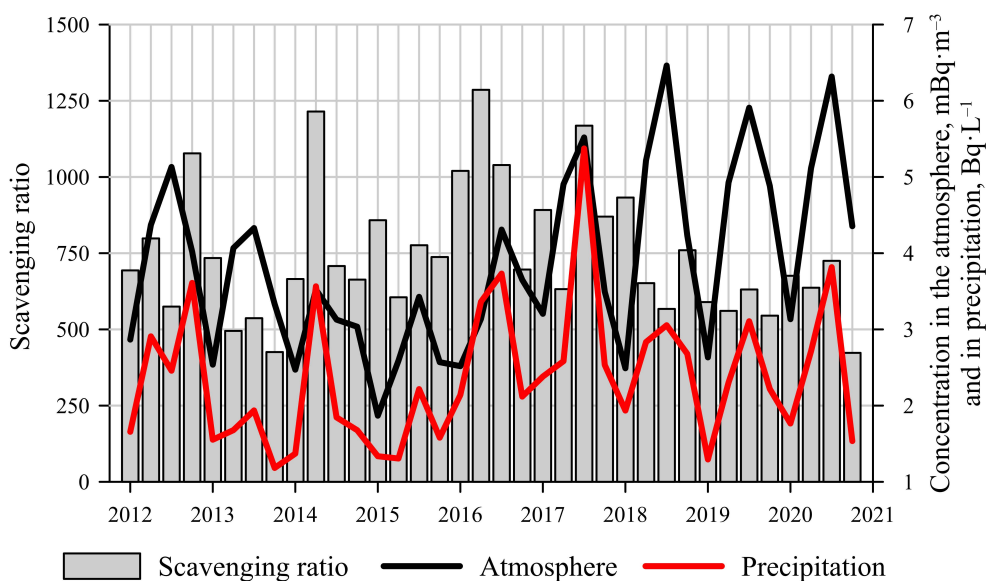


Fig. 1. Seasonal variability of ^7Be concentrations in the atmosphere and precipitation, as well as their scavenging ratio

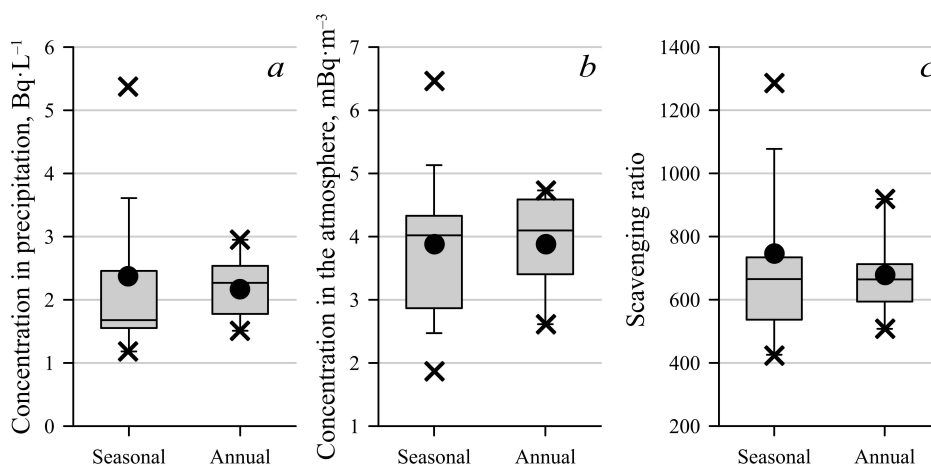


Fig. 2. Frequency distribution of the data on seasonal and annual values of ^7Be concentrations: *a* – in precipitation, *b* – in the atmosphere; *c* – scavenging ratio

Seasonally and annually averaged values of ^7Be concentrations in the atmosphere varied within the range of 1.9–6.5 and 2.6–4.7 $\text{mBq}\cdot\text{m}^{-3}$, respectively (Fig. 2, *b*). The main variability (80%) of the seasonally averaged values occurred in the range of 2.5–5.5 $\text{mBq}\cdot\text{m}^{-3}$. As in the case of ^7Be concentration in atmospheric precipitation, the 10th and 90th percentile values for the average annual concentration of this radionuclide in the atmosphere coincide with the minimum and maximum, respectively. Variation coefficients were 30.7 and 19.5% for seasonal and annual values. The arithmetic mean and median values of seasonally averaged ^7Be

concentrations in the atmosphere were 3.9 and $3.6 \text{ mBq}\cdot\text{m}^{-3}$. They are close, but not equal to each other, which can indicate that their distribution is different from normal.

The seasonally and annually averaged values of the scavenging ratio varied in the ranges of 423 – 1286 and 508 – 919 , respectively (Fig. 2, c), according to the estimates obtained using equation (1). The 10th and 90th percentile values were 537 and 1078 for the seasonal mean scavenging ratios. Variation coefficients were 28.8 and 19.8% for seasonal and annual values. The arithmetic mean (746) and median (695) values of seasonal ratios are close, but not equal to each other.

Analysis of the results of the Shapiro–Wilk tests for normality shows that the distributions of data on the ^7Be concentration in precipitation and on scavenging ratio are statistically significantly different from normal at the 95% confidence level. On the contrary, the distribution of data on the ^7Be concentration in the atmosphere is not statistically significantly different from normal at the 95% confidence level.

The obtained mean ^7Be concentrations in precipitation (geometric mean – $2.2^{+1.0}_{-0.7} \text{ Bq}\cdot\text{L}^{-1}$) and in the atmosphere (arithmetic mean $3.9 \pm 1.2 \text{ mBq}\cdot\text{m}^{-3}$), and scavenging ratio (geometric mean – 719^{+227}_{-173}) coincide well with the literature data. The available literature shows the following values concerning ^7Be concentration in precipitation ($\text{Bq}\cdot\text{L}^{-1}$): 2.9 – for Detroit, Michigan, USA [16]; 2.5 – for Huelva, Spain [11]; 2.6 – for Malaga, Spain [17]; $1.1^{+1.8}_{-0.7}$ – for Mangalore, India [18]. The following values are given concerning ^7Be concentration in the atmosphere ($\text{mBq}\cdot\text{m}^{-3}$): 4.8 – for Detroit, Michigan, USA [16]; 4.9 – for Huelva, Spain [11]; 4.0 – for Lisbon, Portugal [21]; 4.2 – for Malaga, Spain [17]; $6.9^{+2.1}_{-1.6}$ – for Mangalore, India [18]. The following estimates have been published regarding the scavenging ratios: 948 – for Detroit, Michigan, USA [16]; 496 ± 180 – for Huelva, Spain [11]; 840 – for Malaga, Spain [17]; 553^{+719}_{-312} – for Mangalore, India [18].

Seasonal variability of the scavenging ratio averaged over the entire observation period is shown in Fig. 3, a. No pronounced seasonal variability can be seen in the series under consideration. An ANOVA was carried out in order to confirm that the difference in seasonal mean scavenging ratios was not statistically significant. Its results show that the seasonal average values differ from each other statistically insignificantly at the 95% confidence level. Thus, it can be concluded that the period under study revealed no seasonal variability in the scavenging ratio.

The ANOVA was carried out in order to obtain quantitative estimates of the influence of variations in ^7Be concentration in the atmosphere and in precipitation on the seasonal variability of the scavenging ratio. Its results show that the temporal variability of the scavenging ratio is determined by variations in ^7Be concentration in precipitation and in the atmosphere by 90 and 10% , respectively. The correlation analysis results indicate a strong, statistically significant correlation at the 99% confidence level ($r = 0.62$) between the scavenging ratio and ^7Be concentration values in precipitation (Fig. 4, a). No statistically significant correlation between the scavenging ratio variability and ^7Be concentration in the atmosphere can be observed even at the 90% confidence level

($r = -0.20$) (Fig. 4, *b*). No relationship between the long-term variability of seasonal average scavenging ratio and the precipitation amount and frequency was confirmed as the correlation coefficients were -0.25 ($p = 0.14$) and 0.004 ($p = 0.98$), respectively.

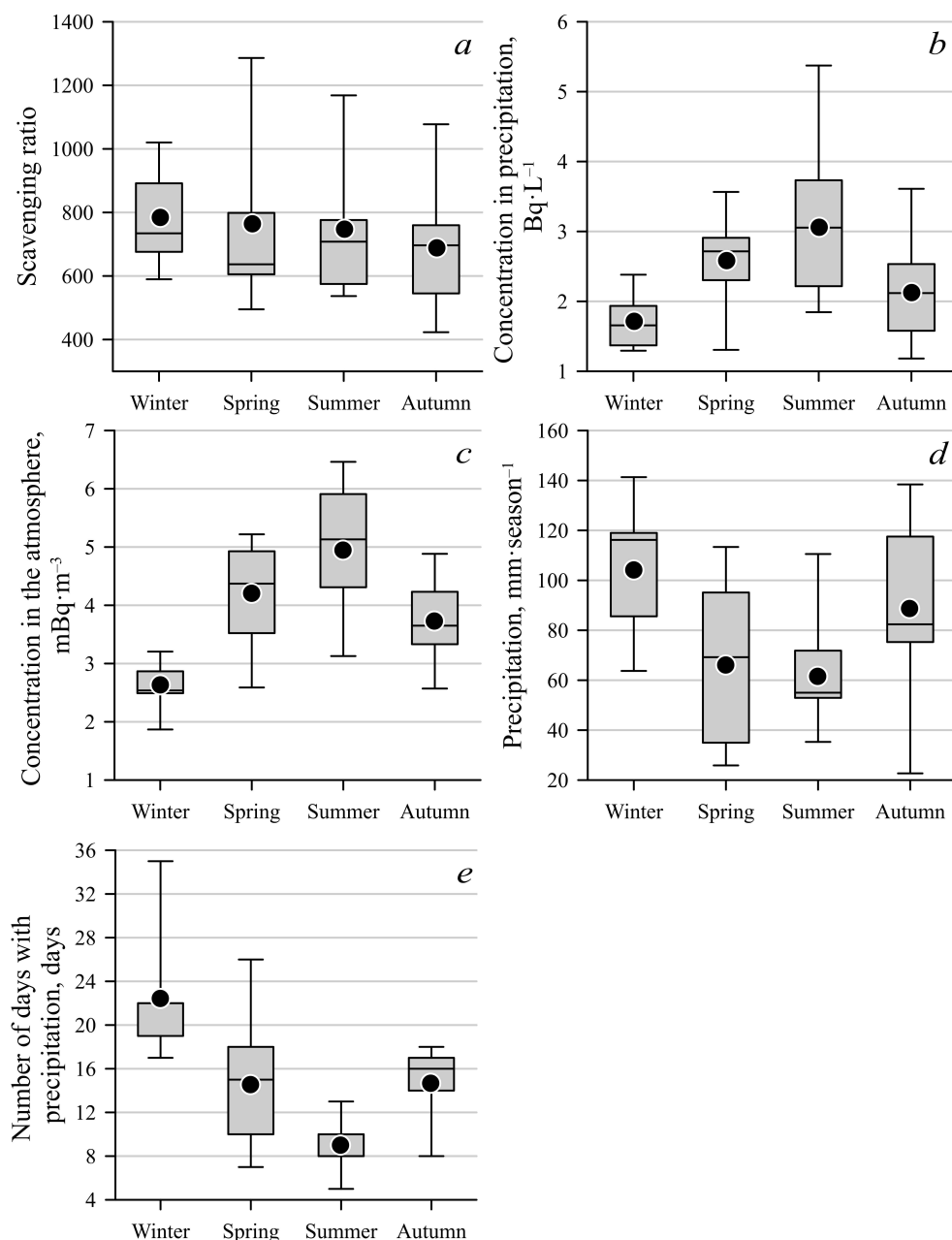


Fig. 3. Averaged over the observation period data on seasonal variability of: scavenging ratio (*a*), ^7Be concentration in precipitation (*b*), ^7Be concentration in the atmosphere (*c*), precipitation amount (*d*) and precipitation frequency (*e*)

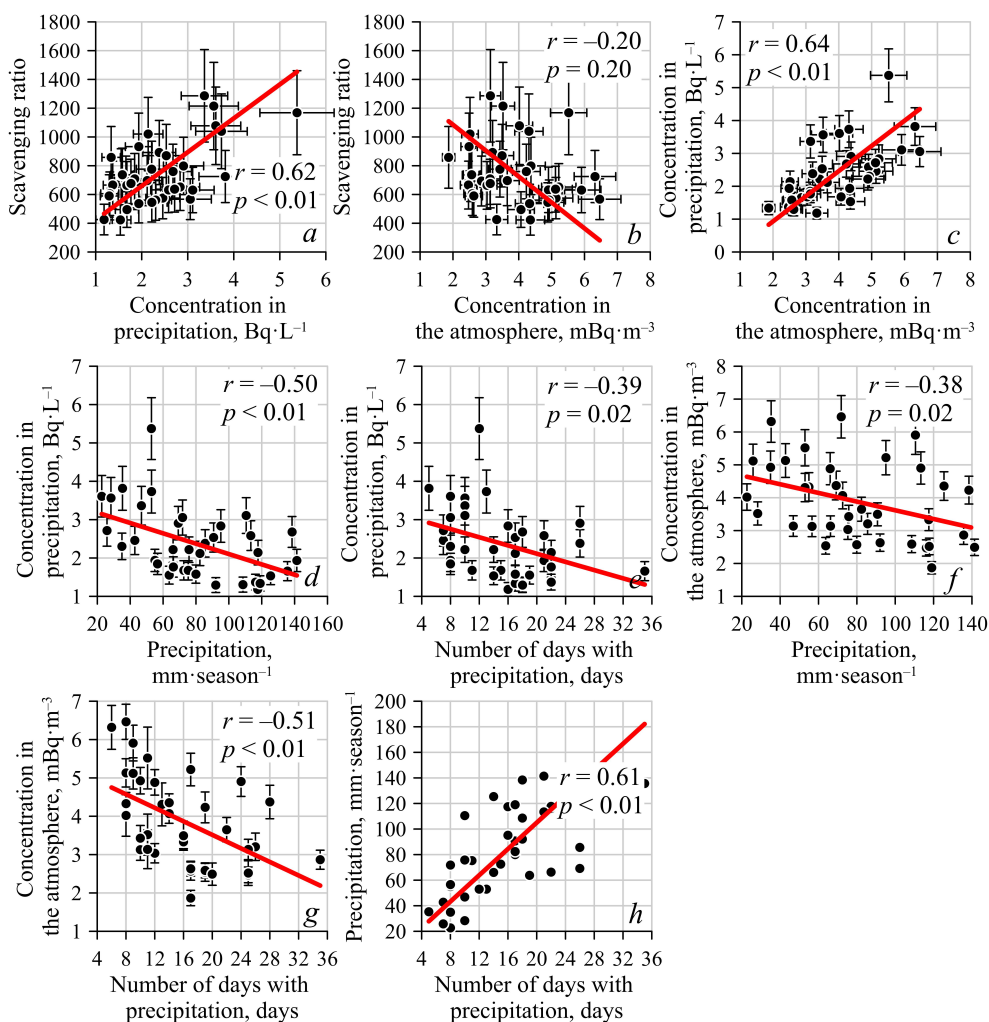


Fig. 4. Relationship between the seasonal values of various parameters: *a* – scavenging ratio and ^7Be concentration in precipitation; *b* – scavenging ratio and ^7Be concentration in the atmosphere; *c* – ^7Be concentrations in precipitation and atmosphere; *d* – ^7Be concentration in precipitation and precipitation amount; *e* – ^7Be concentration in precipitation and a number of days with precipitation, *f* – ^7Be concentration in the atmosphere and precipitation amount; *g* – ^7Be concentration in the atmosphere and precipitation frequency; and *h* – precipitation amount and precipitation frequency

Fig. 3, *b* shows the intraannual variability of ^7Be concentration in precipitation averaged over the entire observation period. The ANOVA results confirm a statistically significant seasonal variability of ^7Be concentration in precipitation with a maximum in the summer season ($2.9 \text{ Bq}\cdot\text{L}^{-1}$) and a minimum in the winter season ($1.7 \text{ Bq}\cdot\text{L}^{-1}$) at the 95% confidence level. The correlation analysis results show that the temporal variability of the seasonally averaged ^7Be concentration in precipitation is statistically significantly associated at the 95% confidence level with the temporal variability of ^7Be concentration in the atmosphere ($r = 0.64$), as well as with the amount ($r = -0.50$) and frequency ($r = -0.39$) of precipitation

(Fig. 4, *c – e*). Note that the strongest connection is observed precisely with ^7Be concentration in the atmosphere. Thus, an increase in the ^7Be concentration in the atmosphere and a decrease in the precipitation amount and frequency are accompanied by an increase in the radionuclide concentration in precipitation. ^7Be concentration in the atmosphere takes on a maximum value in the summer season (Fig. 3, *c*) and the precipitation amount and frequency is minimal (Fig. 3, *d, e*), which explains the observed maximum concentration of this radionuclide in precipitation in this season (Fig. 3, *b*). ^7Be concentration in the atmosphere takes a minimum value in winter and the precipitation amount and frequency is maximum, which determines the minimum ^7Be concentration in precipitation observed at this time. The authors of [17] noted the presence of a similar seasonal variation in ^7Be concentration in precipitation for a station located in Malaga, Spain. They indicated that such seasonal variability is most likely due to the intraannual distribution of precipitation and ^7Be concentrations in the atmosphere, which were similar to those noted in the present study.

Temporal variability of seasonally averaged values of ^7Be concentration in the atmosphere is statistically significantly associated with the precipitation amount ($r = -0.38$) and frequency ($r = -0.51$) at the 95% confidence level (Fig. 4, *f, g*). Thus, a decrease in the precipitation amount and frequency increases ^7Be content in the atmosphere. In turn, the considered precipitation parameters (amount and frequency) are also interrelated. Thus, an increase in the frequency of precipitation is accompanied by an increase in its quantity with a correlation coefficient of 0.61 (Fig. 4, *h*). This relationship between the seasonal variability of ^7Be concentration in the atmosphere and precipitation parameters, as well as the relationship between the parameters under consideration, has already been noted in recent studies [15, 22].

Interannual variability of the scavenging ratio. Figure 5 shows the resulting series of observations of interannual variability of the studied parameters.

A decrease in the scavenging ratio values from 664 to 508 was observed in 2012–2013, then followed by a long period of their growth to 919 in 2016, which then was followed by a long period of decrease to 516 in 2020. Thus, the average annual scavenging ratio values changed by 1.8 times during the period under study. Interannual variability of ^7Be concentration in precipitation shows similar dynamics: a decrease from 2.3 to 1.5 $\text{Bq}\cdot\text{L}^{-1}$ was observed in 2012–2013, then followed by a short period of relatively small fluctuations (1.8 and 1.6 $\text{Bq}\cdot\text{L}^{-1}$ in 2014 and 2015), an increase in concentration to 3.0 $\text{Bq}\cdot\text{L}^{-1}$ in 2017 and then its decrease to 2.0 $\text{Bq}\cdot\text{L}^{-1}$ in 2020. Thus, the average annual values of ^7Be concentration in precipitation changed by a factor of 2 in 2012–2020.

The ANOVA results show that the temporal variability of the average annual scavenging ratio values is determined by 74% by ^7Be concentration variations in precipitation and by 26% in the atmosphere. Thus, the contribution of variability in ^7Be concentration in the atmosphere to the variation in average annual scavenging ratios increased by 2.6 times compared to the same for seasonal values.

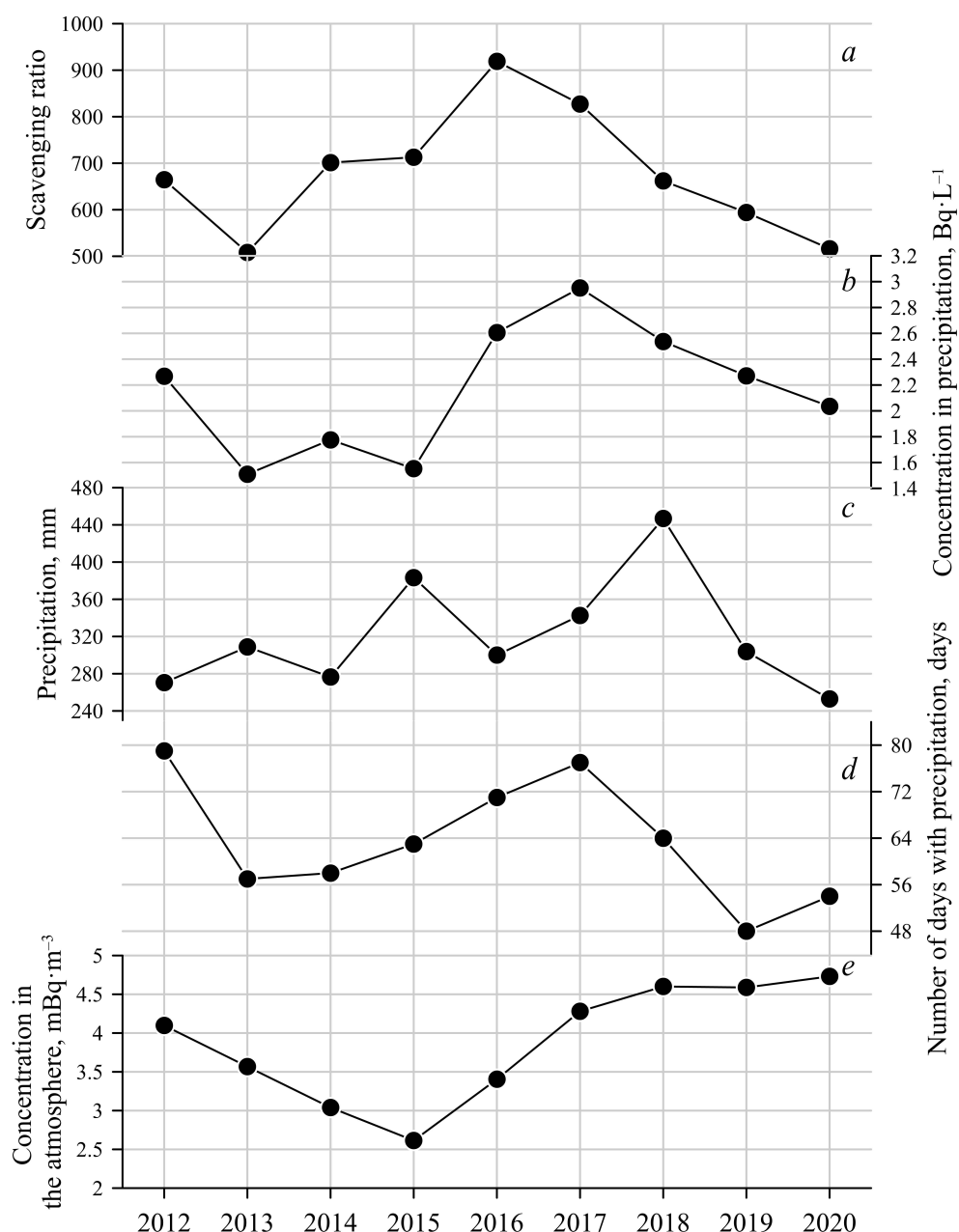


Fig. 5. Temporal variability of annual values of: scavenging ratio (a), ^7Be concentration in precipitation (b), precipitation amount (c), precipitation frequency (d) and ^7Be concentration in the atmosphere (e)

The correlation analysis results show no statistically significant relationships at the 95% confidence level between the variability of annual concentration ratios and the amount ($r = 0.19$, $p = 0.63$) or frequency ($r = 0.66$, $p = 0.06$) of precipitation. A strong, statistically significant correlation at the 90% confidence level between the scavenging ratio and the number of days with precipitation (the more rainy days in a year, the higher the average annual value of the scavenging ratio) is a rather

unexpected result. Formula (1) shows that the scavenging ratio value is directly proportional to ^7Be concentration in precipitation and inversely proportional to its concentration in the atmosphere. On a synoptic time scale, an increase in the precipitation frequency can lead to a decrease in the ^7Be concentration in the atmosphere due to the fact that it takes time for its concentration to recover after precipitation (1–2 days) [23]. As a result of a decrease in ^7Be concentration in the atmosphere, its concentration in precipitation decreases proportionally (all other precipitation parameters being equal). Thus, no relationship between precipitation frequency and scavenging ratios is to be expected (the lack of such a relationship for temporal variability in seasonal values is reported above). Physical processes that cause such a relationship between annual values are not obvious.

No statistically significant correlations at the 90% confidence level between ^7Be concentration in the atmosphere and the studied precipitation parameters were indicated. Thus, the obtained values of the correlation coefficients between ^7Be concentration in the atmosphere and the precipitation amount and frequency were 0.18 ($p = 0.64$) and 0.53 ($p = 0.14$), respectively.

Conclusions

This paper presents field data on the temporal variability of ^7Be concentrations in the atmosphere and precipitation in 2012–2020. Seasonally averaged concentrations of this radionuclide in the atmosphere and precipitation varied in the ranges of 1.9–6.5 $\text{mBq}\cdot\text{m}^{-3}$ and 1.2–5.4 $\text{mBq}\cdot\text{L}^{-1}$. These data made it possible to obtain quantitative estimates of the seasonal and annual scavenging ratio values, which were 423–1286 and 508–919, respectively, with a geometric mean of 719^{+227}_{-173} . The ANOVA results show that temporal fluctuations in seasonal and annual scavenging ratio values are determined to a greater extent by variations in ^7Be concentration in precipitation (90 and 74%, respectively) than by variations in its concentration in the atmosphere. The correlation analysis results indicate that fluctuations in seasonal values of ^7Be concentration in precipitation are associated with variations in its concentration in the atmosphere ($r = 0.64$, $p < 0.01$) and with variability in precipitation amount ($r = -0.50$, $p < 0.01$). The variability of annual values of ^7Be concentration in precipitation is statistically significant at the 95% confidence level and is not associated with variations in the considered precipitation parameters (amount and frequency). The analysis results indicate that there is no relation between time series of concentration ratios and precipitation parameters at seasonal and annual time intervals. In other words, it is not possible to estimate the seasonal or annual average scavenging ratio using precipitation amount and frequency data only.

REFERENCES

1. Lal, D. and Peters, B., 1967. Cosmic Ray Produced Radioactivity on the Earth. In: K. Sitte, ed., 1967. *Kosmische Strahlung II / Cosmic Rays II*. Handbuch der Physik / Encyclopedia of Physics, vol. 9/46/2. Berlin; Heidelberg: Springer, pp. 551–612. https://doi.org/10.1007/978-3-642-46079-1_7
2. Zhang, F., Wang, J., Baskaran, M., Zhong, Q., Wang, Y., Paatero, J. and Du, J., 2021. A Global Dataset of Atmospheric ^7Be and ^{210}Pb Measurements: Annual Air Concentration and

- Depositional Flux. *Earth System Science Data*, 13(6), pp. 2963-2994. <https://doi.org/10.5194/essd-13-2963-2021>
3. Ioannidou, A., 2021. Activity Size Distribution of ^7Be in Association with Trace Metals in the Urban Area of the City of Thessaloniki, Greece. *Atmospheric Environment*, 45(6), pp. 1286-1290. <https://doi.org/10.1016/j.atmosenv.2010.12.006>
4. Kadko, D., Landing, W.M. and Shelley, R.U., 2015. A Novel Tracer Technique to Quantify the Atmospheric Flux of Trace Elements to Remote Ocean Regions. *Journal of Geophysical Research: Oceans*, 120(2), pp. 848-858. <https://doi.org/10.1002/2014JC010314>
5. Anderson, R.F., Cheng, H., Edwards, R.L., Fleisher, M.Q., Hayes, C.T., Huang, K.-F., Kadko, D., Lam, P.J., Landing, W.M. [et al.], 2016. How Well Can We Quantify Dust Deposition to the Ocean? *Philosophical Transactions of the Royal Society A: Mathematical, Physical and Engineering Sciences*, 374(2081), 20150285. <https://doi.org/10.1098/rsta.2015.0285>
6. Kadko, D., Landing, W.M. and Buck, C.S., 2020. Quantifying Atmospheric Trace Element Deposition over the Ocean on a Global Scale with Satellite Rainfall Products. *Geophysical Research Letters*, 47(7), e2019GL086357. <https://doi.org/10.1029/2019GL086357>
7. Kadko, D., Aguilar-Islas, A., Bolt, C., Buck, C.S., Fitzsimmons, J.N., Jensen, L.T., Landing, W.M., Marsay, C.M., Rember, R. [et al.], 2019. The Residence Times of Trace Elements Determined in the Surface Arctic Ocean during the 2015 US Arctic GEOTRACES Expedition. *Marine Chemistry*, 208, pp. 56-69. <https://doi.org/10.1016/j.marchem.2018.10.011>
8. Kadko, D., Aguilar-Islas, A., Buck, C.S., Fitzsimmons, J.N., Landing, W.M., Shiller, A., Till, C.P., Bruland, K.W., Boyle, E.A. [et al.], 2020. Sources, Fluxes and Residence Times of Trace Elements Measured during the U.S. GEOTRACES East Pacific Zonal Transect. *Marine Chemistry*, 222, 103781. <https://doi.org/10.1016/j.marchem.2020.103781>
9. Marsay, C.M., Kadko, D., Landing, W.M. and Buck, C.S., 2022. Bulk Aerosol Trace Element Concentrations and Deposition Fluxes during the U.S. GEOTRACES GP15 Pacific Meridional Transect. *Global Biogeochemical Cycles*, 36(2), e2021GB007122. <https://doi.org/10.1029/2021GB007122>
10. Papastefanou, C., 2006. Radioactive Nuclides as Tracers of Environmental Processes. *Journal of Radioanalytical and Nuclear Chemistry*, 267(2), pp. 315-320. <https://doi.org/10.1007/s10967-006-0050-8>
11. Lozano, R.L., San Miguel, E.G., Bolívar, J.P. and Baskaran, M., 2011. Depositional Fluxes and Concentrations of ^7Be and ^{210}Pb in Bulk Precipitation and Aerosols at the Interface of Atlantic and Mediterranean Coasts in Spain. *Journal of Geophysical Research: Atmospheres*, 116(D18), D18213. <https://doi.org/10.1029/2011JD015675>
12. Kremenchutskii, D.A., 2022. Precipitation Scavenging of Beryllium-7 (^7Be): Observation Results and Parameterization. *Chemosphere*, 307(2), 135908. <https://doi.org/10.1016/j.chemosphere.2022.135908>
13. Chae, J.-S. and Kim, G., 2019. Large Seasonal Variations in Fine Aerosol Precipitation Rates Revealed Using Cosmogenic ^7Be as a Tracer. *Science of The Total Environment*, 673, pp. 1-6. <https://doi.org/10.1016/j.scitotenv.2019.03.482>
14. Liu, G., Wu, J., Li, Y., Su, L. and Ding, M., 2020. Temporal Variations of ^7Be and ^{210}Pb Activity Concentrations in the Atmosphere and Aerosol Deposition Velocity in Shenzhen, South China. *Aerosol and Air Quality Research*, 20(7), pp. 1607-1617. <https://doi.org/10.4209/aaqr.2019.11.0560>
15. Kremenchutskii, D.A., 2022. Temporal Variability of Aerosol Wet Deposition Velocity in the Sevastopol Region: Observational Data. *Physical Oceanography*, 29(4), pp. 321-333.
16. McNeary, D. and Baskaran, M., 2003. Depositional Characteristics of ^7Be and ^{210}Pb in Southeastern Michigan. *Journal of Geophysical Research: Atmospheres*, 108(D7), 4210. <https://doi.org/10.1029/2002JD003021>

17. Dueñas, C., Gordo, E., Liger, E., Cabello, M., Cañete, S., Pérez, M. and De La Torre-Luque, P., 2017. ^7Be , ^{210}Pb and ^{40}K Depositions over 11 Years in Málaga. *Journal of Environmental Radioactivity*, 178–179, pp. 325–334. <https://doi.org/10.1016/j.jenvrad.2017.09.010>
18. Mohan, M.P., D'Souza, R.S., Nayak, S.R., Kamath, S.S., Shetty, T., Kumara, K.S., Mayya, Y.S. and Karunakara, N., 2019. Influence of Rainfall on Atmospheric Deposition Fluxes of ^7Be and ^{210}Pb in Mangaluru (Mangalore) at the Southwest Coast of India. *Atmospheric Environment*, 202, pp. 281–295. <https://doi.org/10.1016/j.atmosenv.2019.01.034>
19. Kremenchutskii, D.A. and Kononov, S.K., 2022. Beryllium-7 (^7Be) and Its Variability in the Near-Surface Atmosphere of Crimea, the Black Sea Region. *Atmospheric Pollution Research*, 13(5), 101406. <https://doi.org/10.1016/J.APR.2022.101406>
20. Kremenchutskii, D.A. and Batrakov, G.F., 2023. Seasonal Variations in Total Deposition Velocity and Washout Ratio of Fine Aerosols Revealed from Beryllium-7 (^7Be) Measurements in Sevastopol, the Black Sea Region. *Atmospheric Pollution Research*, 14(3), 101698. <https://doi.org/10.1016/J.APR.2023.101698>
21. Carvalho, A.C., Reis, M., Silva, L. and Madruga, M.J., 2013. A Decade of ^7Be and ^{210}Pb Activity in Surface Aerosols Measured over the Western Iberian Peninsula. *Atmospheric Environment*, 67, pp. 193–202. <https://doi.org/10.1016/j.atmosenv.2012.10.060>
22. Efimov, V.V., Volodin, E.M., Anisimov, A.E. and Barabanov, V.S., 2015. Regional Projections of Climate Change for the Black Sea – Caspian Sea Area in Late XXI Century. *Physical Oceanography*, (5), pp. 49–66. <https://doi.org/10.22449/1573-160X-2015-5-49-66>
23. Kremenchutskii, D.A., 2021. Influence of Precipitation on the Daily Beryllium-7 (^7Be) Activity Concentration in the Atmospheric Surface Layer. *Journal of Environmental Radioactivity*, 237, 106722. <https://doi.org/10.1016/J.JENVRAD.2021.106722>

Submitted 15.05.2023; approved after review 12.01.2024;
accepted for publication 18.01.2024.

About the author:

Dmitrii A. Kremenchutskii, Senior Researcher, Marine Hydrophysical Institute of RAS (2 Kapitanskaya Str., Sevastopol, 299011, Russian Federation), CSc (Geogr.), **ORCID ID: 0000-0002-8747-6612**, **ResearchID: AAC-1673-2020**, d.kremenchutskii@mhi-ras.ru

The author has read and approved the final manuscript.

The author declares that he has no conflict of interest.

Original article

Vertical Distribution of Oxygen and Hydrogen Sulfide in the Deep Part of the Black Sea Based on the 2017–2019 Expedition Data**S. I. Kondratev** ✉, **A. V. Masevich***Marine Hydrophysical Institute of RAS, Sevastopol, Russian Federation*

✉ skondratt@mail.ru

Abstract

Purpose. The purpose of the work is to analyze the features of vertical distribution of the dissolved oxygen and hydrogen sulfide in the deep part of the Black Sea in the modern period.

Methods and results. The data obtained in 11 expeditions of Marine Hydrophysical Institute (MHI) of RAS in the Black Sea within the economic zone of Russia in 2017–2019 were used. These surveys included more than 200 deep-sea stations at which the hydrochemical samples were taken at specific isopycnal surfaces by means of a cassette of 12 bathometers of the Sea-Bird 911 plus CTD Seabird-Electronics INC device; as a rule, it was a series of σ_t values equal to 16.30; 16.20; 16.10; 16.00; 15.95; 15.90; 15.80; 15.60; 15.40; 15.20; 15.00 and 14.60 kg/m³. Such a scheme made it possible to determine both general vertical distribution of oxygen in the oxycline and depth of hydrogen sulfide occurrence with an accuracy of up to 0.05 kg/m³ in the conventional density scale.

Conclusions. All surveys showed a decrease in oxygen content with depth (and occurrence of oxycline, respectively) starting below isopycnal surface $\sigma_t = 14.5$ kg/m³. The position of sub-oxygen zone upper boundary defined by the isooxygen 10 μ M was not strictly isopycnal, but fell on the range of isopycnals $\sigma_t = 15.7$ –15.85 kg/m³. However, it was not possible to identify a relation between the change in the position of the upper boundary and a certain hydrological season. For example, the deepest occurrence of the upper boundary below $\sigma_t = 15.8$ kg/m³ was observed both in November and December 2017 and August 2018. The lowering of isooxygen 10 μ M to $\sigma_t = 15.9$ kg/m³ in the Kerch shelf area is related to a more voluminous and colder intermediate layer above the shelf in December 2017. Only one of 11 surveys showed the position of hydrogen sulfide upper boundary determined by isosulfide 3 μ M raised almost to $\sigma_t = 16.0$ kg/m³ in April 2017. In all other cases (including the one in August 2017, i.e. six months after its rising), it was invariably found within range $\sigma_t = 16.10$ –16.15 kg/m³. The concentration of hydrogen sulfide at the depths of 1750–2000 m has remained unchanged at level 383 ± 2 μ M over the past 25 years.

Keywords: Black Sea, vertical distribution of oxygen and hydrogen sulfide, sub-oxygen zone, field data

Acknowledgements: The study was carried out within the framework of the theme of state assignment FNNN-2024-0001 "Fundamental research into the processes that determine the flow of matter and energy in the marine environment and at its boundaries, the state and evolution of the physical and biogeochemical structure of marine systems in modern conditions".

For citation: Kondratev, S.I. and Masevich, A.V., 2024. Vertical Distribution of Oxygen and Hydrogen Sulfide in the Deep Part of the Black Sea Based on the 2017–2019 Expedition Data. *Physical Oceanography*, 31(2), pp. 258-270.

© 2024, S. I. Kondratev, A. V. Masevich

© 2024, Physical Oceanography

Introduction

The Black Sea is the largest euxinic basin in the world where hydrogen sulfide occurs at a depth of 90–150 m depending on the area (the greatest contrast in the depths of its occurrence is represented by the centers of cyclonic and anticyclonic



gyres, shelf edge and continental slope) [1, 2]. The main cause for hydrogen sulfide formation is weakened vertical exchange when oxygen-containing surface water can penetrate downward only to a certain depth.

The vertical exchange weakening is due to the constant Black Sea stratification by salinity and density at which a constant halocline among isohalines of 18.5–21.5 [3, 4] and a pycnocline among isopycnals of 14.5–16.5 kg/m³ take place, as well as a cold intermediate layer (CIL) with a temperature of < 8 °C and a core located at isopycnal surface depth $\sigma_t = 14.5$ kg/m³ [4]. This structure makes it possible for oxygenated surface waters to sink only to a certain depth during winter aeration. As a rule, winter aeration reached isopycnal surface depths within the range of 14.2–14.5 kg/m³ in the last decades of the past century [5, 6]. Recent years showed the gradual decrease of the penetration depth to $\sigma_t = 14.2$ –14.3 kg/m³ due to warm winters [7, 8].

In such a situation, below the isopycn $\sigma_t = 14.5$ kg/m³, only CIL waters become the source of oxygen required for the oxidation of the particular organic matter (POM) descending from the overlying waters. This results in the oxygen content gradual decrease with the depth and occurrence of the oxycline which gradually moves to the so-called sub-oxygen zone. Its upper boundary is defined by the isooxygen 10 µM (or 20 µM according to some researchers) [9] and its lower boundary is the isopycnal surface at which oxygen disappears (i.e. its content becomes less than a defined minimum of 3 µM). In fact, the lower boundary is the upper one of the hydrogen sulfide occurrence, below which sulfates become the POM oxidizer instead of dissolved oxygen. The reduction of sulfates results in the hydrogen sulfide formation.

One of the most important tasks of the Black Sea expeditionary research in the modern period is monitoring the position of the upper boundary of hydrogen sulfide zone where the oxidizer for the POM decomposition process changes when the sulfate anion becomes an acceptor of electrons instead of dissolved oxygen. The presence of oxygen in the Black Sea surface waters provides the usual trophic chain typical for any ocean: phytoplankton formed during the photosynthesis from inorganic (and also organic) forms of nutrients serves as food for zooplankton which in turn provides food for larger marine organisms. Only certain types of bacteria can exist in the hydrogen sulfide zone with no oxygen. A shift in the boundary of the hydrogen sulfide zone, namely its rise to the surface, threatens the life of surface water organisms.

Since November 2015, MHI has carried out systematic comprehensive expeditionary studies of the Black Sea within the economic zone of the Russian Federation, in particular, monitoring the lower boundary of the sub-oxygen zone. The results obtained made it possible to compare these data with the results of individual short-term MHI expeditions of past years [10] and start a detailed analysis of the state of this zone. The features of its upper and lower boundaries in 2015–2016 [11], as well as the causes for the rise of the hydrogen sulfide zone in certain areas of the Black Sea northwestern shelf (NWS) [12], were considered.

This work, which continues the research of [10–12], is purposed at studying the features of oxygen and hydrogen sulfide vertical distribution in the water column of the Black Sea based on the data from 11 expeditions of R/V *Professor Vodyanitsky* in 2017–2019.

Materials and methods

Fig. 1 shows the location of all hydrochemical stations in 11 cruises in 2017–2019 during which samples for oxygen and hydrogen sulfide content were taken. Deep-sea hydrochemical samples were taken at specific isopycnal surfaces by means of a cassette of 12 bathometers of the Sea-Bird 911 plus CTD Seabird-Electronics INC device. As a rule, it was a series of σ_t values equal to 16.30; 16.20; 16.10; 16.00; 15.95; 15.90; 15.80; 15.60; 15.40; 15.20; 15.00 and 14.60 kg/m³. At 8 stations, sampling for hydrogen sulfide and oxygen was carried out by three probings at 37 horizons: in the first two probings, the samples were taken by depth, from a maximum immersion of 2000 m (for technical reasons the probe was not immersed deeper), then through each 50 m to 1800 m depth and further – through each 100 m. In the third probing, samples were taken by the series of isopycnals given above and from the surface with a plastic jar.

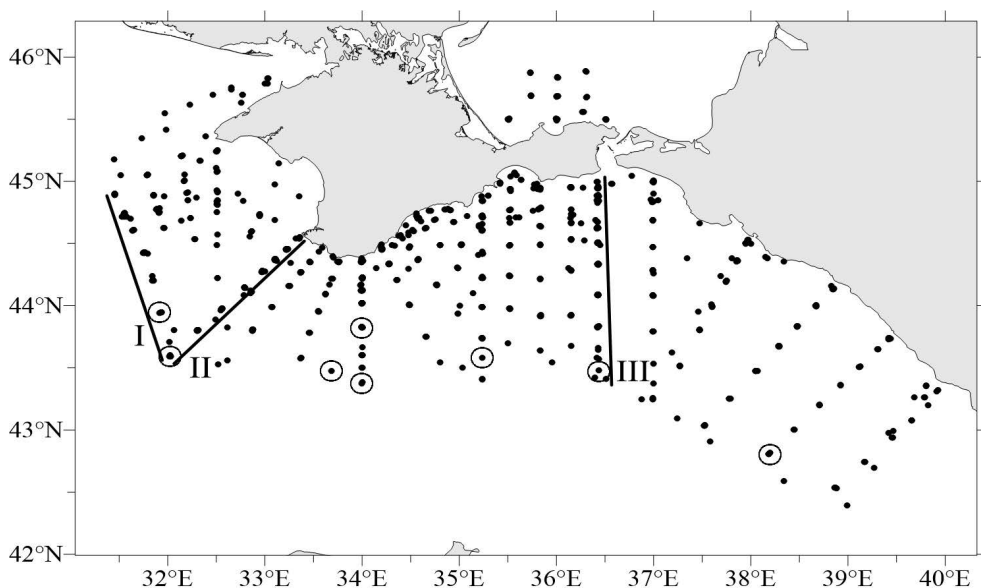


Fig. 1. Map of the deep-sea stations at which the samples for oxygen and hydrogen sulfide were taken in 2017–2019. Solid lines indicate sections I–III which were carried out in each cruise if possible. Circles indicate the stations where samples were taken at 37 horizons.

After constructing averaged vertical oxygen profiles obtained using the Surfer or Grafer programs, such a sampling scheme made it possible to determine the upper boundaries of the sub-oxygen layer and the hydrogen sulfide zone, as well as

the thickness of the sub-oxygen zone located between them, with a resolution of up to $0.05 \text{ kg/m}^3 \sigma_t$ which corresponds to an accuracy of $\sim 5 \text{ m}$ in the depth scale.

We applied an oxygen sensor in addition to sampling in order to obtain vertical oxygen profiles in six expeditions (given below). The readings of the sensor for each station were calibrated using three samples taken at the surface, in the middle of the oxycline ($\sigma_t = 15.0 \text{ kg/m}^3$) and in the beginning of the sub-oxygen zone ($\sigma_t = 15.8 \text{ kg/m}^3$).

The hydrogen sulfide content was found by the iodometric method according to the technique ¹ with iodine consumption at isopycn $\sigma_t = 15.8 \text{ kg/m}^3$ taken as zero. The error in determining hydrogen sulfide is estimated at $\pm 3 \text{ } \mu\text{M}$. Oxygen concentration was found by the Winkler method modified in terms of sampling with low oxygen content in accordance with the method [13] which provides the results with an accuracy of $\pm 0.01 \text{ ml/L}$ [14]. In both cases, 200 ml volumetric flasks and narrow-necked oxygen bottles were purged with argon 15 min before sampling.

Further, the average vertical profiles of distribution of oxygen and hydrogen sulfide concentrations relative to the conventional density scale were calculated with a discreteness of 0.1 kg/m^3 in conventional density range $\sigma_t = 13.0 - 17.3 \text{ kg/m}^3$ for each expedition. Averaging was carried out using the inverse distance method followed by additional smoothing using the low pass filtering method ².

Discussion of results

Vertical profiles of oxygen and hydrogen sulfide. Based on the vertical oxygen profiles obtained by averaging field data from six expeditions (dashed lines in Fig. 2), one can get the impression that in all cases the subsurface maximum of oxygen was observed and the beginning of oxycline (i.e. a noticeable decrease in oxygen concentration with depth) rose to the occurrence depth of isopycnal surface $\sigma_t = 14.0 \text{ kg/m}^3$. However, when analyzing the oxygen sensor data (solid lines in Fig. 2), it becomes clear that the subsurface maximum of oxygen was observed only in April 2017 and the beginning of oxycline was still located near isopycnal surface $\sigma_t = 14.5 \text{ kg/m}^3$ and was not subject to any seasonal changes since all four surveys in 2017 (April, June, November, December) showed that it remained at the same level.

It should also be noted that all profiles coincide below isopycn $\sigma_t = 15.0 \text{ kg/m}^3$, when the oxygen content becomes $< 150 \text{ } \mu\text{M}$. Its concentration below the indicated isopycn was higher than in other surveys by a value exceeding the determination error, which is estimated at approximately 1% [13] within the range of 30–150 μM , only in November 2017.

¹ Bordovsky, O.K. and Ivanenkov, V.N., eds., 1978. *Methods for Hydrochemical Studies in the Ocean*. Moscow: Nauka, 271 p. (in Russian).

² Masevich, A.V., 2022. *Dynamics of Oxygen in the Main Pycnocline of the Black Sea*. Thesis Cand. Geogr. Sci. Sevastopol, 151 p. (in Russian).

Here, we should take into account that the conditions for the 2009–2019 CIL maximum formation were observed in 2017 [15]. Therefore, the relative decrease in temperature and increase in oxygen concentration in the CIL are observed in 2017 compared to previous and subsequent years [16]. This increase could cause a short-term oxygen concentration rise below isopycn $\sigma_t = 15.0 \text{ kg/m}^3$ in November 2017 (in December it disappeared).

Fig. 3 shows the density scales of oxygen and hydrogen sulfide vertical profiles averaged over field data recorded in 11 MHI expeditions.

Practical merging of vertical oxygen profiles (Fig. 3, *a*) with a more detailed analysis (Fig. 3, *b*) shows that the sub-oxygen zone upper boundary determined by an oxygen concentration of $10 \text{ }\mu\text{M}$ varies over time from 15.7 kg/m^3 to 15.9 kg/m^3 , which corresponds to an interval of 40 m in the depth scale. The impossibility to identify any dependence of the upper boundary position on the season is not surprising since the time for updating the characteristics in this water layer exceeds the season significantly [17, 18]. The latter is indirectly confirmed by the fact that two out of three cases when the upper boundary of the sub-oxygen zone was located below $\sigma_t = 15.8 \text{ kg/m}^3$ occurred in winter months (November and December 2017), but a similar deepening was also observed in August 2018.

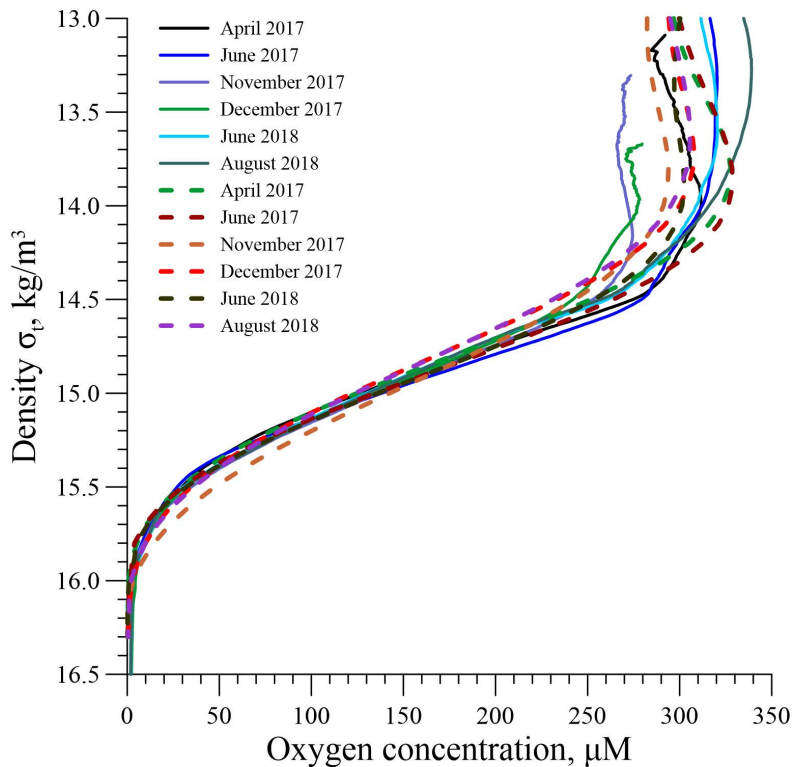


Fig. 2. Vertical profiles of oxygen in the density scale for six surveys obtained by the averaged Winkler method (dashed lines) and oxygen sensor data (solid lines)

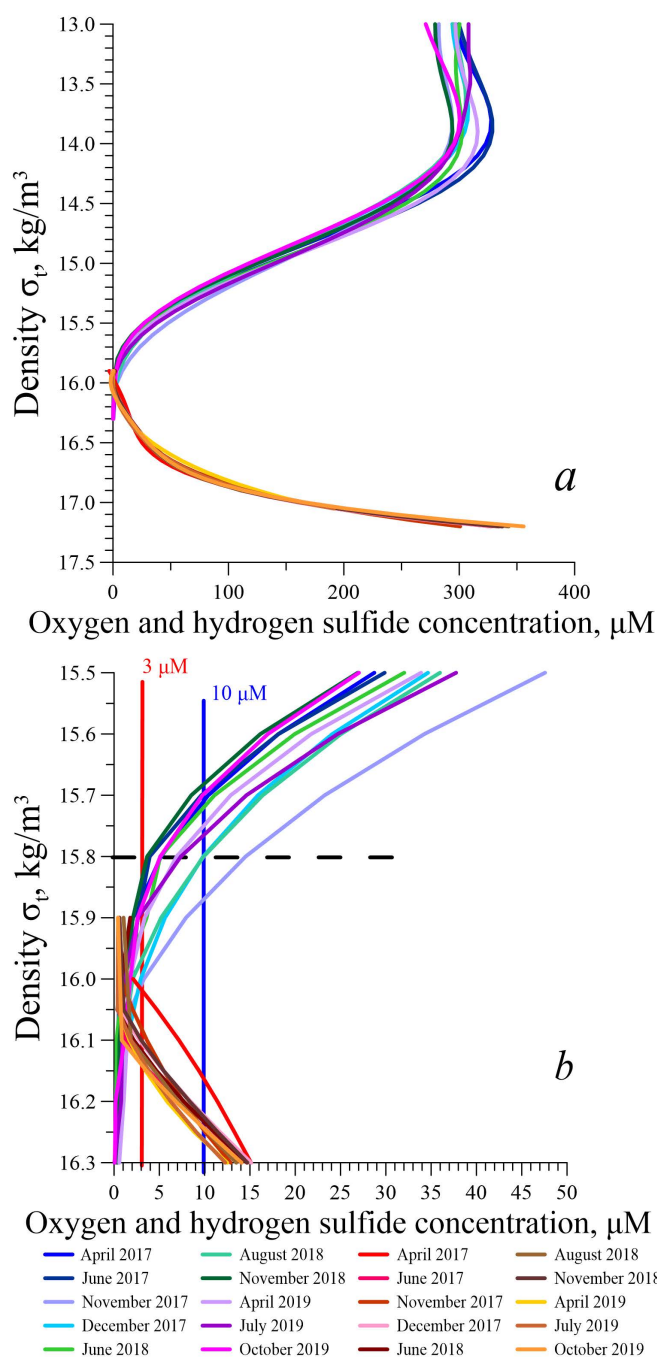


Fig. 3. Vertical profiles of oxygen and hydrogen sulfide in the density scale over the entire thickness (a) and in interval $\sigma_t = 15.5$ – 16.3 kg/m^3 (b) in the Black Sea in 2017–2019

The lowest position of the sub-oxygen zone upper boundary at $\sigma_t = 15.87 \text{ kg/m}^3$ (Fig. 3, b) was observed in November 2017, the year of the maximum CIL formation over the past 10 years [13].

The vertical distribution of hydrogen sulfide turned out to be more isopycnal as isosulfide $3 \mu\text{M}$ was located in the isopycnal range of $16.10\text{--}16.15 \text{ kg/m}^3$ during 10 expeditions and only the survey performed in April 2017 showed its noticeable rise to almost $\sigma_t = 16.0 \text{ kg/m}^3$.

Position of the sub-oxygen zone at the sections. As a rule, all surveys conducted in 2017–2019 (except for August 2018) included “century” section II (Fig. 1) along the Cape Chersonesos – the Bosphorus Strait line since it was historically regularly studied, even in 1995–2015, when expeditionary research of the Black Sea deep parts was performed extremely rarely [10].

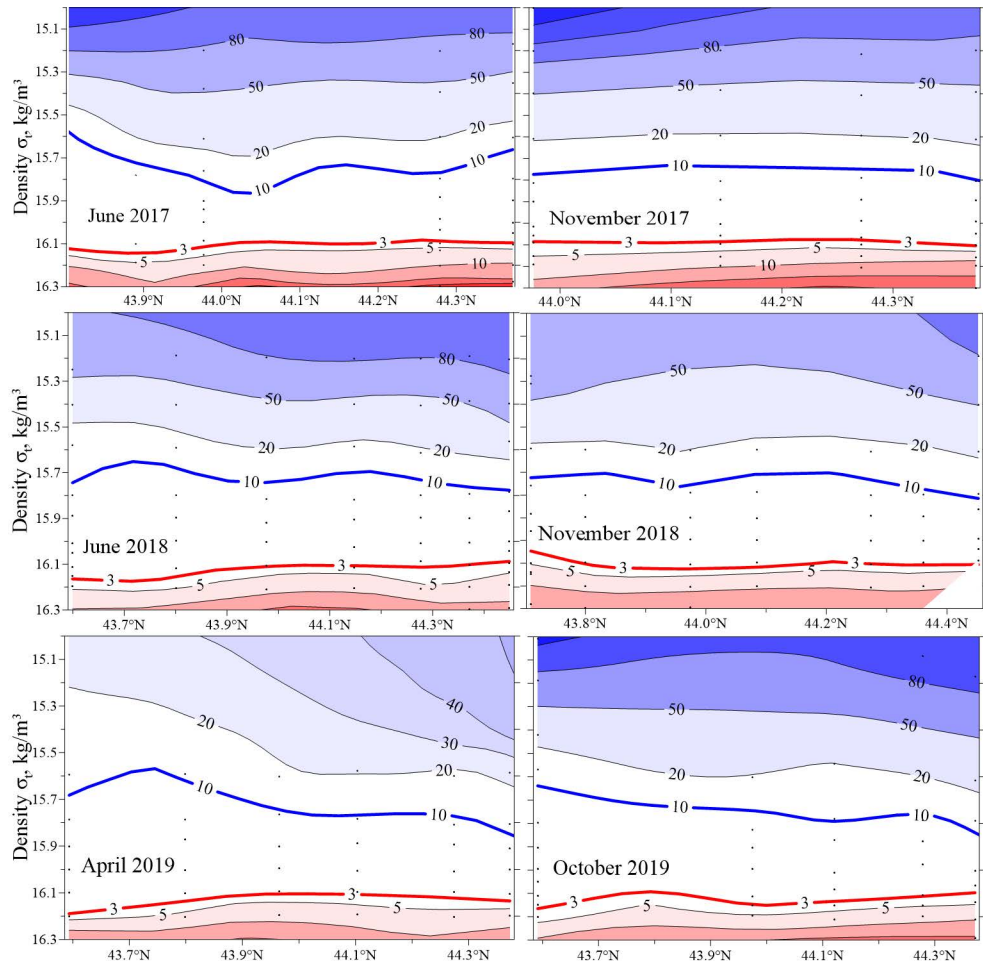


Fig. 4. Position of sub-oxygen zone at "century" section II Cape Chersonesos – the Bosphorus Strait in 2017–2019

Fig. 4 shows that isosulfide $3 \mu\text{M}$ was constantly located in the isopycnal range of $16.10\text{--}16.15 \text{ kg/m}^3$. Against the background of this homogeneity, isooxygen $10 \mu\text{M}$ changed its position in a larger range of the conventional density scale ($15.6\text{--}15.85 \text{ kg/m}^3$) while separate surveys revealed that the sub-oxygen zone upper

boundary could either be located isopycnally (April, November 2017) or move noticeably on the density scale (June 2017, April 2019).

In addition to the “century” section, the 2017–2019 survey included “diagonal” section I (Fig. 1), which was periodically carried out perpendicular to the NWS edge, since previously a rise in the hydrogen sulfide zone was regularly discovered near it, in some cases up to depths of 85–90 m [12]. Fig. 5 shows that isooxygen 10 μM in all surveys was located almost isopycnally, but changed its position within range $\sigma_t = 15.6\text{--}15.8\text{ kg/m}^3$, and isosulfide 3 μM was invariably located near isopycnal surface $\sigma_t = 16.1\text{ kg/m}^3$.

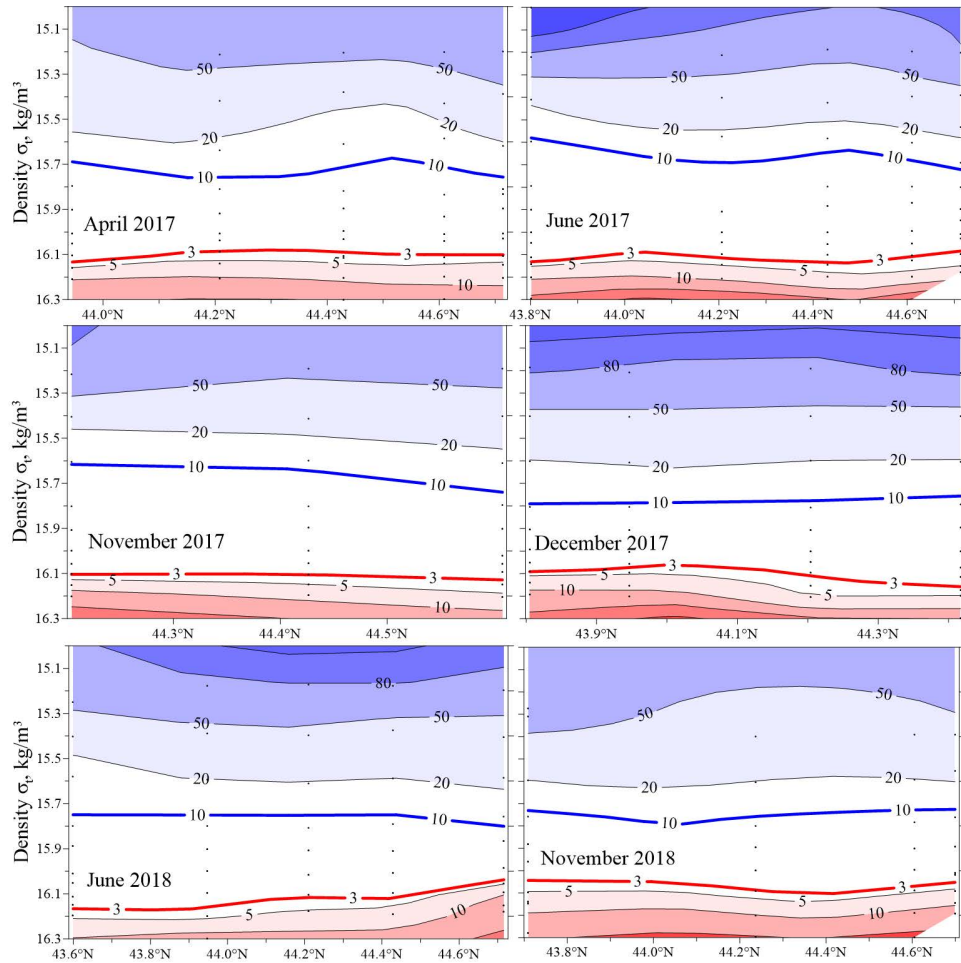


Fig. 5. Position of sub-oxygen zone at section I in 2017–2019

Meridional section III (Fig. 1) southwards of the Kerch Strait is of particular interest when assessing the possible rise of hydrogen sulfide zone near the shelf edge [12]. Fig. 6 shows the position of the sub-oxygen zone at this section in 2017–2019. A relatively stable position of the sub-oxygen zone upper boundary within the range of $15.65\text{--}15.8\text{ kg/m}^3$ and of the hydrogen sulfide upper boundary within the range of $16.15\text{--}16.20\text{ kg/m}^3$ was observed in almost all surveys in this section.

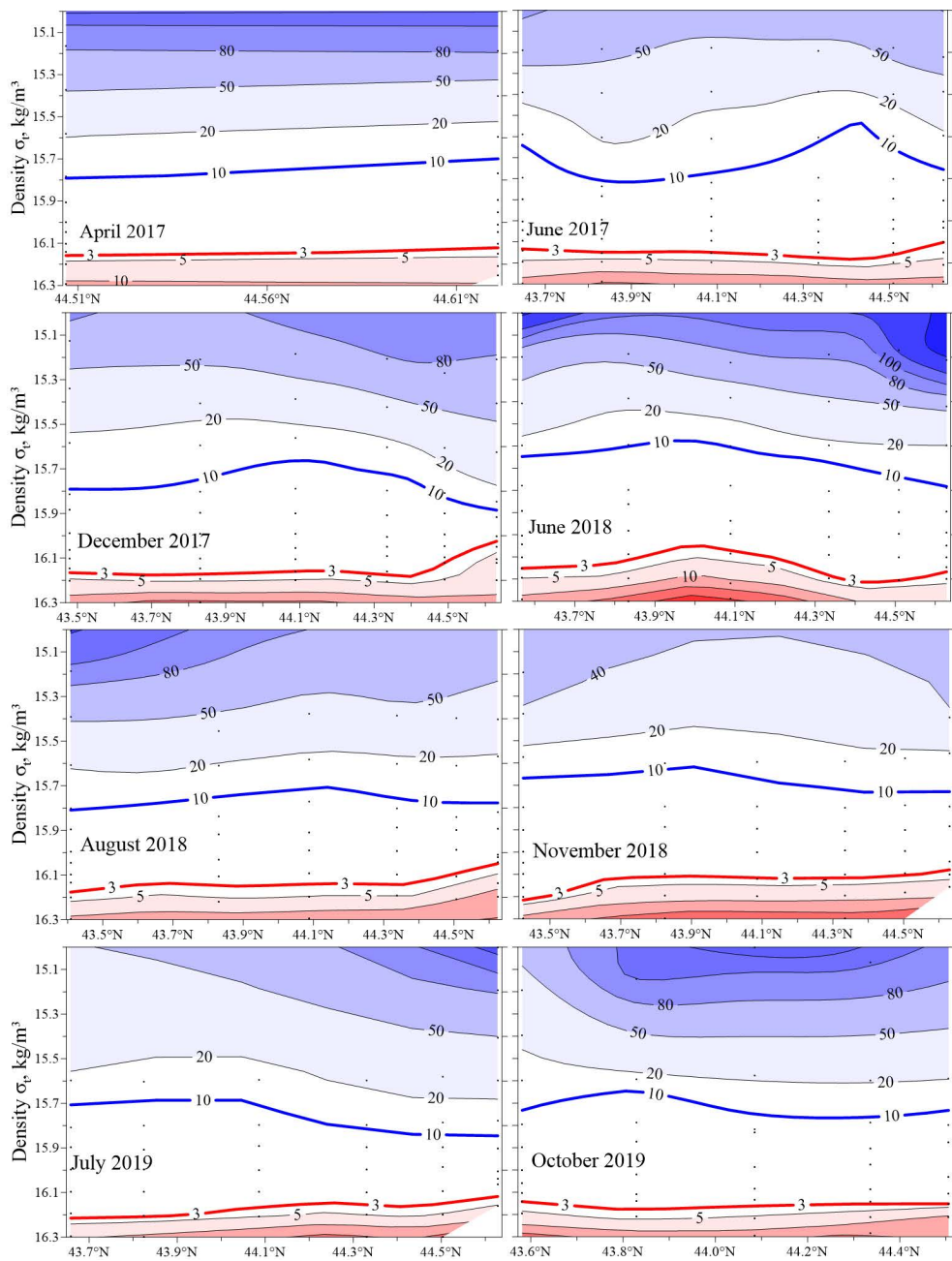


Fig. 6. Position of sub-oxygen zone at section III in 2017–2019

Against this background of relative stability, when the upper boundary of the indicated zone did not drop below $\sigma_t = 15.8 \text{ kg/m}^3$ and the lower one was located in a small interval near isopycn $\sigma_t = 16.1 \text{ kg/m}^3$, the survey in December 2017 is outlined. In this case, clear narrowing of the sub-oxygen zone was observed at two stations closest to the shelf both due to the lowering of isooxygen $10 \mu\text{M}$

from $\sigma_t = 15.7\text{--}15.8 \text{ kg/m}^3$ to $\sigma_t = 15.9 \text{ kg/m}^3$ and due to the rise of isosulfide $3 \text{ }\mu\text{M}$ from $\sigma_t = 16.15 \text{ kg/m}^3$ to $\sigma_t = 16.05 \text{ kg/m}^3$. Thus, the sub-oxygen zone thickness was ~ 0.15 units σ_t on the density scale.

The lowering of isooxygen $10 \text{ }\mu\text{M}$ can be explained by the fact that the CIL can be the only oxygen source for the sub-oxygen zone and it becomes clear when considering the temperature vertical distribution in the Kerch section in December 2017 (Fig. 7) that the CIL defined by a temperature of 8°C was both thicker and colder than the surrounding waters in $44.4^\circ\text{--}44.6^\circ\text{N}$ region. This was the very source of the additional amount of oxygen which was enough not only to oxidize the POM, but also to lower isooxygen $10 \text{ }\mu\text{M}$ to $\sigma_t = 15.9 \text{ kg/m}^3$.

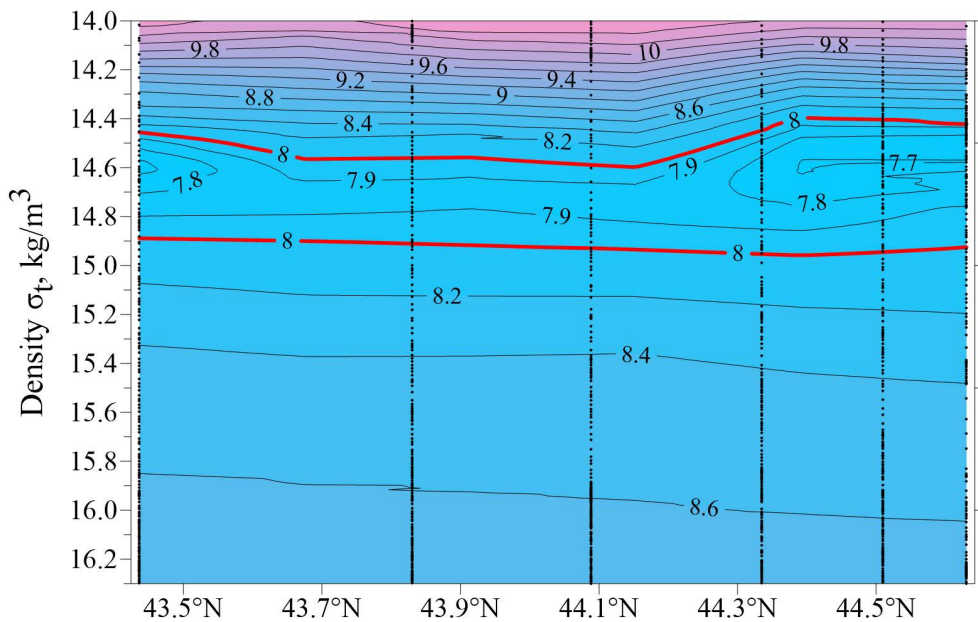


Fig. 7. Temperature at section III by an STD sensor in December 2017

We explained a similar rise of hydrogen sulfide upper boundary in the NWS by the features of the bottom topography [12] which can also occur in this case.

Hydrogen sulfide maximum concentrations in the Black Sea. The hydrogen sulfide content was determined in the depth range of 1750–2000 m with a discreteness of 50 m at 8 stations depicted in Fig. 1. As is known, a uniform distribution of hydrological and hydrochemical characteristics is observed in the bottom waters of the Black Sea deep part below 1750 m due to convective mixing as a result of heat coming from the bottom surface [19]. The maximum content of hydrogen sulfide, as well as trends towards its change, are of great interest among such characteristics. Thus, a significant increase in the hydrogen sulfide bottom concentrations was observed in the past century, after which its content stabilized at level $378\text{--}387 \text{ }\mu\text{M}$ [11]. As can be seen from the Table which presents the hydrogen sulfide concentrations at 8 deep-sea stations below 1750 m, almost all these values

fall into the interval presented above. After combining the values for all stations into one array after statistical testing ³, we find that the hydrogen sulfide content at depths > 1750 m in the Black Sea is $383 \pm 2 \mu\text{M}$.

Hydrogen sulfide content (μM) in the Black Sea at the 1750–2000 m depths in 2017–2019

Period	Quantity of measurements	Minimum	Maximum	Average	σ
April 2017	9	378.5	383.4	381.3	1.66
June 2017	14	379.1	388.3	383.6	2.80
November 2017	3	381.7	386.1	383.5	2.27
December 2017	8	381.1	387.9	384.7	2.39
June 2018	7	379.0	386.0	382.2	2.42
August 2018	4	382.4	384.8	383.8	1.03
November 2018	4	377.8	385.6	380.5	3.48
October 2019	6	379.8	382.7	381.3	1.31

Conclusions

Based on the results of 11 expeditions of Marine Hydrophysical Institute of RAS in the Black Sea in 2017–2019, the following was revealed:

1. The decrease in oxygen content with depth (and, accordingly, the oxycline occurrence) began below the isopycnal surface $\sigma_t = 14.5 \text{ kg/m}^3$ in all surveys.

2. The position of the sub-oxygen zone upper boundary determined by isooxygen $10 \mu\text{M}$ was not strictly isopycnal, but within isopycnal interval $\sigma_t = 15.7\text{--}15.85 \text{ kg/m}^3$. The deepest location of the upper boundary below $\sigma_t = 15.8 \text{ kg/m}^3$ was observed in November and December 2017, as well as in August 2018.

3. We assume that the decrease in isooxygen $10 \mu\text{M}$ to $\sigma_t = 15.9 \text{ kg/m}^3$ in the Kerch shelf area is associated with the presence of a more voluminous and colder intermediate layer above the shelf in December 2017.

4. The position of hydrogen sulfide upper boundary determined by isosulfide $3 \mu\text{M}$ was raised almost to $\sigma_t = 16.0 \text{ kg/m}^3$ in only one of 11 surveys in April 2017. It was invariably within range $\sigma_t = 16.10\text{--}16.15 \text{ kg/m}^3$ in all other cases (including one in August 2017, i.e. six months after its rising).

5. Hydrogen sulfide concentration has remained unchanged at 1750–2000 m depths over the past 25 years and is located at level $383 \pm 2 \mu\text{M}$.

REFERENCES

1. Murray, J.W. and Izdar, E., 1989. The 1988 Black Sea Oceanographic Expedition: Overview and New Discoveries. *Oceanography*, 2(1), pp. 15-21. <https://doi.org/10.5670/oceanog.1989.25>
2. Murray, J.W., 1991. The 1988 Black Sea Oceanographic Expedition: Introduction and Summary. *Deep Sea Research Part A, Oceanographic Research Papers*, 38(suppl. 2), pp. S655-S661. [https://doi.org/10.1016/S0198-0149\(10\)80002-0](https://doi.org/10.1016/S0198-0149(10)80002-0)

³ Sevastyanov, B.A., 1982. *A Course in Probability Theory and Mathematical Statistics*. Moscow: Nauka, 256 p. (in Russian).

3. Konovalov, S.K. and Murray, J.W., 2001. Variations in the Chemistry of the Black Sea on a Time Scale of Decades (1960–1995). *Journal of Marine Systems*, 31(1-3), pp. 217-243. [https://doi.org/10.1016/S0924-7963\(01\)00054-9](https://doi.org/10.1016/S0924-7963(01)00054-9)
4. Konovalov, S.K. and Eremeev, V.N., 2012. Regional Features, Stability and Evolution of Biochemical Structure of the Black Sea Waters. In: S. K. Konovalov, V. N. Eremeev, eds., 2012. *Stability and Evolution of the Oceanological Characteristics of the Black Sea Ecosystem*. Sevastopol: ECOSI-Gidrofizika, pp. 273-299 (in Russian).
5. Akpinar, A., Fach, B.A. and Oguz, T., 2017. Observing the Subsurface Thermal Signature of the Black Sea Cold Intermediate Layer with Argo Profiling Floats. *Deep Sea Research Part I: Oceanographic Research Papers*, 124, pp. 140-152. <https://doi.org/10.1016/j.dsr.2017.04.002>
6. Miladinova, S., Stips, A., Garcia-Goriz, E. and Macias Moy, D., 2017. Black Sea Thermohaline Properties: Long-Term Trends and Variations. *Journal of Geophysical Research: Oceans*, 122(7), pp. 5624-5644. <https://doi.org/10.1002/2016JC012644>
7. Miladinova, S., Stips, A., Garcia-Goriz, E. and Macias Moy, D., 2018. Formation and Changes of the Black Sea Cold Intermediate Layer. *Progress in Oceanography*, 167, pp. 11-23. <https://doi.org/10.1016/j.pocean.2018.07.002>
8. Titov, V.B., 2003. Interannual Renewal of the Cold Intermediate Layer in the Black Sea over the Last 130 Years. *Russian Meteorology and Hydrology*, (10), pp. 51-56.
9. Tuğrul, S., Murray, J.W., Friederich, G.E. and Salihoğlu, İ., 2014. Spatial and Temporal Variability in the Chemical Properties of the Oxic and Suboxic Layers of the Black Sea. *Journal of Marine Systems*, 135, pp. 29-43. <https://doi.org/10.1016/j.jmarsys.2013.09.008>
10. Kondratev, S.I. and Vidnichuk, A.V., 2018. Features of the Oxygen and Hydrogen Sulfide Vertical Distribution in the Black Sea Based on the Expedition Data Obtained by Marine Hydrophysical Institute in 1995–2015. *Physical Oceanography*, 25(5), pp. 390-400. <https://doi.org/10.22449/0233-7584-2018-5-390-400>
11. Kondratev, S.I. and Vidnichuk, A.V., 2020. Vertical Distribution of Oxygen and Hydrogen Sulphide in the Black Sea in 2016. *Vestnik Moskovskogo Universiteta, Seriya 5, Geografiya*, 2020(3), pp. 91-99 (in Russian).
12. Kondratev, S.I., Masevich, A.V. and Belokopytov, V.N., 2022. Position of the Top Boundary of the Hydrogen Sulfide Zone over the Shelf Edge of the Crimea. *Vestnik Moskovskogo Universiteta. Seriya 5, Geografiya*, 2022(3), pp. 97-107 (in Russian).
13. Carpenter, J.H., 1965. The Accuracy of the Winkler Method for Dissolved Oxygen Analysis. *Limnology and Oceanography*, 10(1), pp. 135-140. <https://doi.org/10.4319/lo.1965.10.1.0135>
14. Carpenter, J.H., 1965. The Chesapeake Bay Institute Technique for the Winkler Dissolved Oxygen Method. *Limnology and Oceanography*, 10(1), pp. 141-143. <https://doi.org/10.4319/lo.1965.10.1.0141>
15. Capet, A., Vandenbulcke, L. and Grégoire, M., 2020. A New Intermittent Regime of Convective Ventilation Threatens the Black Sea Oxygenation Status. *Biogeosciences*, 17(24), pp. 6507-6525. <https://doi.org/10.5194/bg-17-6507-2020>
16. Vidnichuk, A.V. and Konovalov, S.K., 2021. Changes in the Oxygen Regime in the Deep Part of the Black Sea in 1980–2019. *Physical Oceanography*, 28(2), pp. 180-190. <https://doi.org/10.22449/1573-160X-2021-2-180-190>
17. Krivosheya, V.G., Ovchinnikov, I.M. and Skirta, A.Yu., 2002. Interannual Variations of the Renewal of Cold Intermediate Layer in the Black Sea. In: A. G. Zatsepin, M. V. Flint, eds., 2002. *Multidisciplinary Investigations of the Northeastern Part of the Black Sea*. Moscow: Nauka, pp. 27-39 (in Russian).
18. Belokopytov, V.N., 2011. Interannual Variations of the Renewal of Waters of the Cold Intermediate Layer in the Black Sea for the Last Decades. *Physical Oceanography*, 20(5), pp. 347-355. <https://doi.org/10.1007/s11110-011-9090-x>
19. Ivanov, V.A. and Belokopytov, V.N., 2013. *Oceanography of the Black Sea*. Sevastopol: MHI, 210 p.

Submitted 23.05.2023; approved after review 12.01.2024;
accepted for publication 18.01.2024.

About the authors:

Sergey I. Kondratev, Senior Research Associate, Marine Biogeochemistry Department, Marine Hydrophysical Institute of RAS (2 Kapitanskaya Str., Sevastopol, 299011, Russian Federation), CSc (Chem.), **ORCID ID: 0000-0002-2049-7750**, **ResearcherID: F-8972-2019**, **Scopus Author ID: 35784380700**, skondratt@mail.ru

Anna V. Masevich, Junior Research Associate, Marine Biogeochemistry Department, Marine Hydrophysical Institute of RAS (2 Kapitanskaya Str., Sevastopol, 299011, Russian Federation), CSc (Geogr.), **ORCID ID: 0000-0002-0889-020X**, **ResearcherID: AAO-2592-2020**, **Scopus Author ID: 58544083700**, anna_vidnichuk@mhi-ras.ru

Contribution of the co-authors:

Sergey I. Kondratev – formulation of goals and objectives of the study, analysis of literature data, analysis of results and their interpretation, discussion of work results, preparation of paper text

Anna V. Masevich – analysis of literature on the research problem, collection and systematization of data, construction of drawings and graphs, discussion of work results

The authors have read and approved the final manuscript.

The authors declare that they have no conflict of interest.

Underwater Ridge Impact on the Motion of Anticyclonic Eddies over a Sloping Bottom as a Result of the Topographic Beta-Effect: Laboratory Experiment

A. G. Zatsepin^{1, 2}, D. N. Elkin^{1, 2}, ✉

¹ Shirshov Institute of Oceanology of RAS, Moscow, Russian Federation

² Marine Hydrophysical Institute of RAS, Sevastopol, Russian Federation

✉ dmelkin@mail.ru

Abstract

Purpose. The work is purposed at investigating the underwater ridge impact on the motion of anticyclonic eddies over a sloping bottom as result of the topographic beta-effect in the laboratory conditions.

Methods and Results. The experiments are carried out in a cylindrical tank located on a rotating platform. A cone is placed into the tank so that its base coincides with the cylinder lower base. The cone height is less than the base radius. Before the start of each experiment, the tank is filled with fresh or salt water of certain salinity. The fluid layer height exceeds that of the cone in the tank. The anticyclonic eddies are generated using a local constant source of a blue-colored fresh water flow. The source is located directly below the water layer surface at a distance equal to a half of the tank's radius from its center. Having achieved the critical diameter, the generated eddies drift along the isobaths in the “western” direction (“north” is at the cone top in the tank center) due to the topographic beta-effect. The experiments were carried out over the cone with a smooth surface, and over the cone with a ridge on its side whose height was significantly smaller than that of the cone located on the path of the eddy drift. In the experimental runs with the ridge, the drift both of barotropic (fresh water in the tank) and baroclinic (salt water in the tank) eddies slowed down as compared to the eddy drift velocities in the absence of the ridge. After crossing the ridge, the orbital velocity of the eddies also decreased significantly.

Conclusions. Field observations and numerical modeling of the Sevastopol anticyclonic eddy in the Black Sea moving over the continental slope along the isobaths in the southwestern direction showed that the eddy motion slowed down in the area of the underwater ridge formed by a local rise in the bottom relief between two canyons – the Danube and the Western Dnieper paleochannels. The results of the laboratory experiment have confirmed the data of field observations and numerical modeling on a slowdown of the Sevastopol eddy motion and a decrease in its orbital velocity while crossing the underwater ridge due to the topographic beta-effect.

Keywords: rotating fluid, sloping bottom, numerical modeling, fluid motion, eddy motion, bathymetry

Acknowledgments: The work was carried out with financial support of the RSF grant No. 21-77-10052 and within the framework of the theme of state assignment FMWE-2021-0002 (IO RAS). The authors are grateful to Arseniy Aleksandrovich Kubryakov for his proposal to perform the laboratory experiment on studying the impact of an underwater ridge on the motion of mesoscale eddies over a sloping bottom in a rotating fluid.

For citation: Zatsepin, A.G. and Elkin, D.N., 2024. Underwater Ridge Impact on the Motion of Anticyclonic Eddies over a Sloping Bottom as a Result of the Topographic Beta-Effect: Laboratory Experiment. *Physical Oceanography*, 31(2), pp. 271-283.

© 2024, A. G. Zatsepin, D. N. Elkin

© 2024, Physical Oceanography



Introduction

Mesoscale eddies formed in the Black Sea mainly due to the instability and meandering of the Rim Current ¹ move, as a rule, in the direction of this current but at a significantly lower velocity [1]. In several areas of the sea, the continental slope (the Rim Current core is located above the lower part of it) is quite wide and, apparently, has a significant impact on the dynamics of this current and the associated eddies [2]. Such areas include the western part of the sea, where the so-called Sevastopol anticyclonic eddy is often observed. This mesoscale anticyclone is presumably formed due to the Rim Current flowing around the Crimean Peninsula [3] during its weakening phase [4]. After its formation, the eddy moves southwest above the continental slope and then, at a distance of about 100 km from the Crimean Peninsula, sometimes stops moving and becomes quasi-stationary [5].

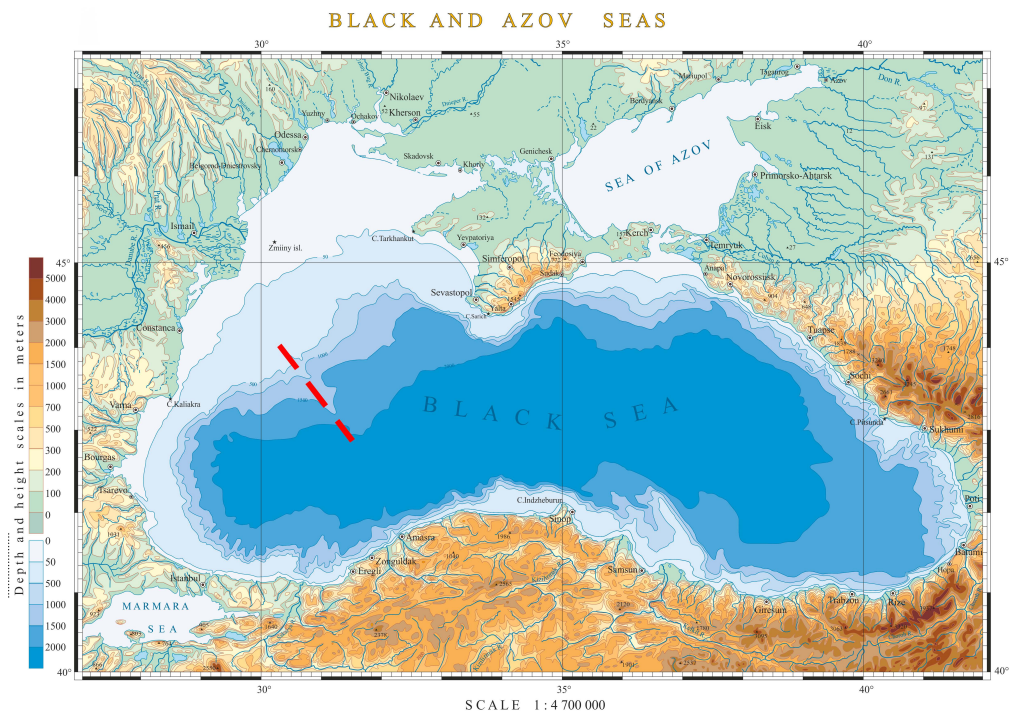


Fig. 1. Topography of the Azov-Black Sea basin (map was compiled by R.R. Stanichnaya). Red dotted line shows the along-slope ridge location in the western part of the Black Sea continental slope

The “hovering” of the Sevastopol eddy over the continental slope leads to a strong and long-term eddy impact on the cross-shelf exchange. The studies

¹ Blatov, A.S., Bulgakov, N.P., Ivanov, V.A., Kosarev, A.N. and Tuljulkun, V.S., 1984. *Variability of the Black Sea Hydrophysical Fields*. Leningrad: Gidrometeoizdat, 240 p. (in Russian).

revealed that this process can significantly affect the lateral flow of nutrients and the functioning of the western Black Sea ecosystem [6–9]. After a few weeks, the Sevastopol eddy ceases to be motionless, continues to move southwestward and finally dissipates when approaching the southern part of the Black Sea basin [1, 10].

One of the possible causes (discussed in the literature) for the slowdown and temporary stop of the Sevastopol eddy is the impact of bottom topography features, namely the along-slope ridge, which is located on the path of the eddy movement in this part of the Black Sea [11]. It is believed that this underwater ridge (see Fig. 1) was formed by a local rise of the seabed between two canyons – the Danube and the Western Dnieper paleochannels [10].

In connection with the foregoing, the goal was set to study the impact of the underwater ridge on the movement of anticyclonic eddies over a sloping bottom under the topographic beta-effect in rotating fluid in laboratory conditions. The article continues the research begun in the works ^{2, 3}.

Experimental setup and experimental methodology

The experimental setup is represented in Fig. 2. The experiments were carried out in a cylindrical tank 60 cm in diameter and 28 cm in height (2) placed in the center of a one-meter platform rotating counterclockwise (1). A cone was placed at the tank bottom so that its base coincided with the cylinder lower base (3). The angle between the cone generatrix and the horizontal was 15°. The cone height was 8 cm.

The experiment was prepared as follows. Before its start, the tank was filled with uniform density water, fresh or with a certain salinity S (from 1 to 4‰). The fluid layer height in the tank was 19 cm, so that the top of the cone was below the water surface. Then the cyclonic (counterclockwise) rotation of the platform with a period of $T = 5$ s ($f = 4\pi/T = 1.25$ c⁻¹ – Coriolis parameter) was switched on. After about 10 minutes, the water in the tank spun up to a condition of a solid-state rotation. After this, video cameras were turned on and a local source of water flow was launched, through which blue-colored fresh water with a flow rate close to constant laminarly entered the near-surface layer in the tank. The source (5) was a vertical tube 1.0 cm in diameter, the end of which was located just below the water layer surface at a distance equal to a half of the tank radius from its center. The source was supplied with water at an almost constant flow rate from a volumetric burette (8) fixed to the platform stand; it was filled with fresh water colored with an intense blue dye. An anticyclonic eddy (6) was formed under the operating source in a short time. Moreover, if the water in the tank was fresh,

² Zatsepin, A.G. and Elkin, D.N., 2023. [Laboratory Study of Underwater Ridge Influence on Movement of Anticyclonic Eddies over Inclined Bottom in Rotating Fluid Influenced by Topographic Beta Effect]. *Multiphase Systems*, 18(4), pp. 382–384 (in Russian).

³ Zatsepin, A.G. and Elkin, D.N., 2024. Underwater Ridge Influence on Anticyclonic Eddies Motion over a Sloping Bottom in a Rotating Fluid. In: *Marine Research Education, 2024. XII International Conference “Marine Research and Education” MARESEDU-2023: Proceedings*. Tver: PoliPress. Vol. II(IV), pp. 119–126 (in Russian).

barotropic anticyclonic eddies (eddy columns) were generated. If the water in the tank was saline, baroclinic eddies (surface eddy lenses) were generated under the source. This method of generating eddies in rotating fluid was frequently used before in laboratory experiments [12].

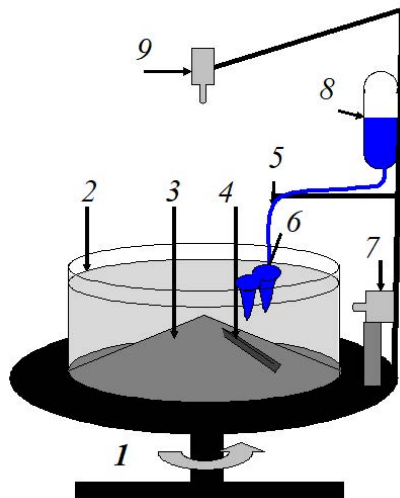


Fig. 2. Diagram of the laboratory set-up: 1 – cyclonically rotating platform; 2 – organic glass cylindrical tank; 3 – cone; 4 – ridge; 5 – tube; 6 – colored water flowing from the source and anticyclonic eddies formed under it; 7 – side-view video camera; 8 – volumetric burette with tap; 9 – top-view video camera (Adapted from sources ^{2,3})

A barotropic eddy column reaching the bottom is directly affected by the bottom topography. Although a baroclinic eddy (a surface eddy lens) ends at a certain depth, it is also affected by the bottom topography. Due to the law of potential eddy conservation, an anticyclonic eddy column reaching the bottom is formed under it. Along with this eddy column in the lower water layer, the surface eddy lens generates an interconnected eddy structure. Owing to the topographic beta-effect (its brief description is given below), barotropic and baroclinic eddies formed under the source move above the cone in the “westward” – anticyclonic direction. To visualize their orbital rotation, small paper pellets are scattered over the surface of the water layer. Video recording of their movement makes it possible to quantify the orbital velocity of eddies.

The experiments were carried out at constant values of the platform rotation angular velocity and the fluid level in the tank, the source flow rate $Q \approx 1.7 \text{ cm}^3/\text{s}$. Only water salinity in the tank varied from experiment to experiment. One set of experiments was carried out over a cone with a smooth surface, another set was carried out with the same parameter values and over the surface of a cone with an along-slope ledge in the form of a ridge (4). The ridge was located on the path of the eddy drift at a distance of 20 cm from the source in the anticyclonic direction (clockwise). The ratio of the ridge height to the total depth of the water layer in

the eddy propagation area was 0.1–0.2. Thus, the ridge in the experiment was a relatively small obstacle approximately similar to its Black Sea counterpart. For video recording of the experiment, a top-view video camera (9) was located on top of the platform, and a side-view video camera (7) was located on the side.

In the course of each experiment, anticyclonic eddies were periodically generated under the source during its operation. Upon reaching a certain diameter, they left and drifted along isobaths in the “western” direction (“north” is the cone top in the tank center) due to the topographic beta-effect. A periodic escape of eddies from under the source was found and described in [13, 14].

The essence of this process, most clear in the barotropic case, is as follows. The law of mass conservation of fluid flowing from a source states that the axisymmetric expansion rate of an anticyclonic barotropic eddy column is $U = Q/(\pi D H_0)$, where Q is source flow rate; D is increasing diameter of the eddy column; H_0 is fluid layer thickness in the tank under the source. Due to the topographic beta-effect caused by bottom sloping in the radial direction, the eddy column drifts in the azimuthal anticyclonic direction at the velocity $V = (\beta_t D^2)/4$ [15, 16], i.e., the drift grows quadratically with a column diameter increase. Here $\beta_t = f \operatorname{tg} \alpha / H_0$ is topographic beta-effect parameter, where $f = 2\Omega$ is Coriolis parameter, $\Omega = 2\pi/T$ is angular velocity of the platform rotation; α is angle of the cone generatrix inclination to the horizontal. At some point, the condition $V > U$ is met and an eddy column leaves from under the source. It follows from this inequality that $D > (4Q/\pi f \operatorname{tg} \alpha)^{1/3}$.

Taking $D_t = (4Q/\pi f \operatorname{tg} \alpha)^{1/3}$ as a critical scale of the eddy column, we estimate its drift velocity scale:

$$V_t = \beta_t D_t^2 / 4 = (1/4\pi)^{1/3} (Q^2 f \operatorname{tg} \alpha)^{1/3} / H_0.$$

These relationships have been experimentally tested and, except for numerical coefficients, have received convincing confirmation [13, 14]. It was found that the value of measured beta-drift velocity V_b is approximately five times greater than V_t : $V_b \approx 5V_t$, and the real diameter $D_b \approx 4.5D_t$. When the source operates for a long time, a chain of anticyclonic eddy columns (barotropic case) or eddy lenses (baroclinic case), following each other along the isobaths, is formed. In this experiment, the impact of an along-slope ridge on the eddy motion velocity in a chain, both barotropic and baroclinic, was studied. In this case, special attention was paid to observing the dynamics and structure of the first eddy in the chain.

Results of experiments and their discussion

After each experiment, the following parameters of the eddy current were determined based on the video data processing: translational velocity of eddy propagation from the source in the anticyclonic direction; maximum orbital velocity of water rotation in eddies; eddy diameter (based on the distance from the eddy center to the orbit of maximum velocity); ridge impact on the parameters of eddy current.

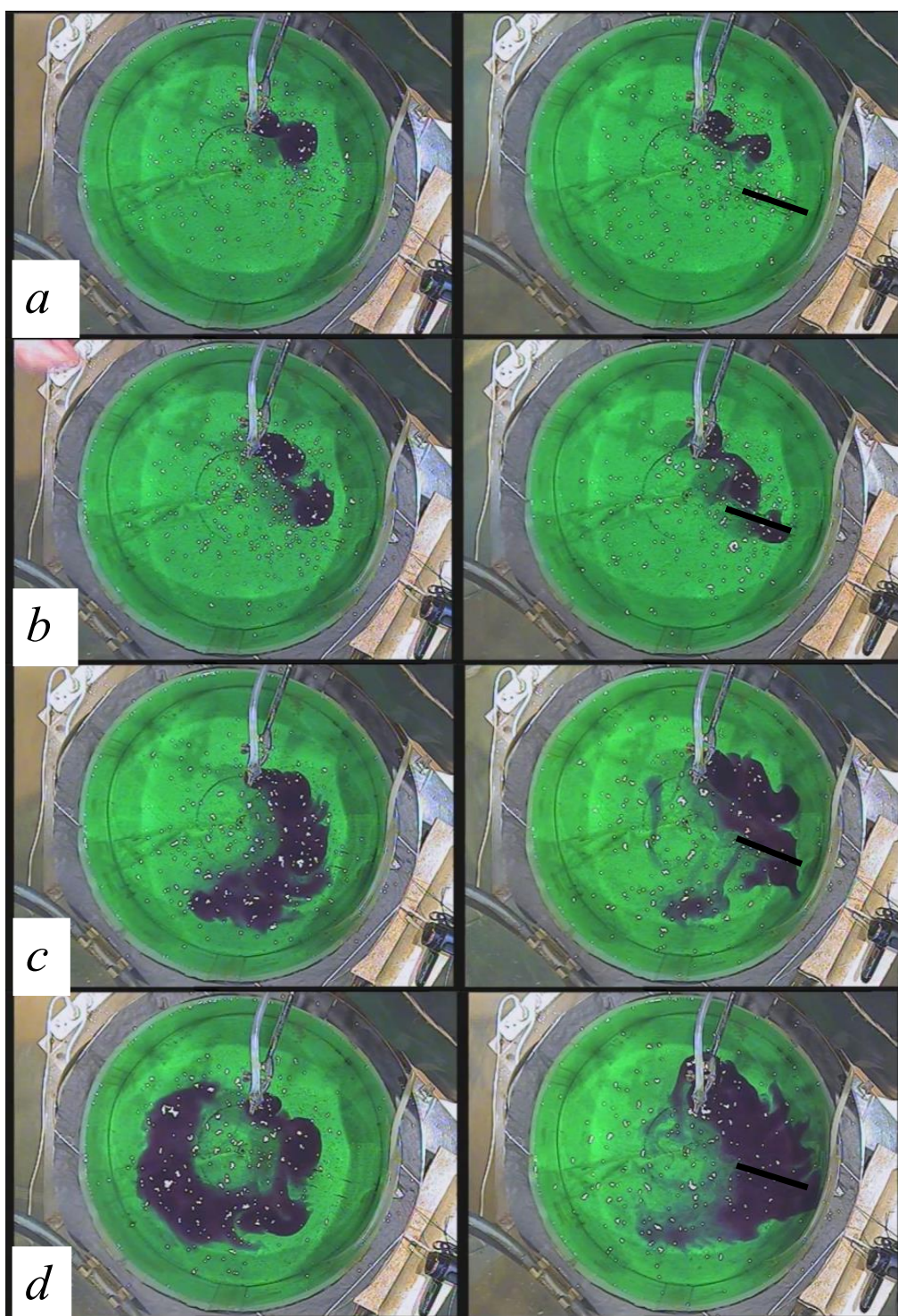


Fig. 3. Experiment with a smooth cone (*left*) and a ridge on the cone surface (*right*) (top view) at relation t/T equal to 12 (*a*); 18 (*b*); 42 (*c*) and 66 (*d*). Salinity of water in the tank $S = 1\text{‰}$ (Sources ^{2,3})

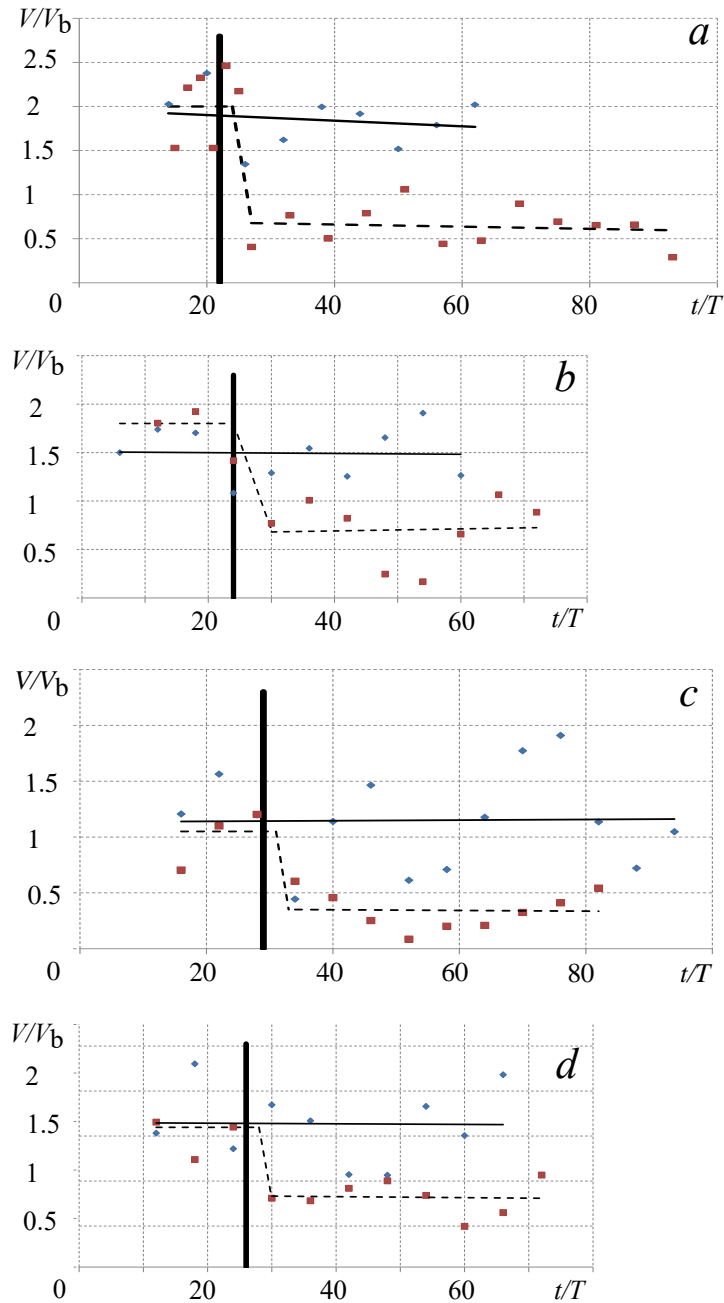


Fig. 4. Dependence of V/V_b on t/T in the experiment with: homogeneous fresh liquid (*a*) and liquid with salinity S equal to 1 (*b*), 2 (*c*) and 4 ‰ (*d*). Blue diamonds denote the experiment over the cone with a smooth surface, red squares – the experiment over the cone with a ridge, thick black line shows the moment when the current front crosses the ridge, thin solid line – the trend line for the experiments over the cone with a smooth surface, thin dashed line – the trend line for the experiments over the cone with a ridge (Source ³)

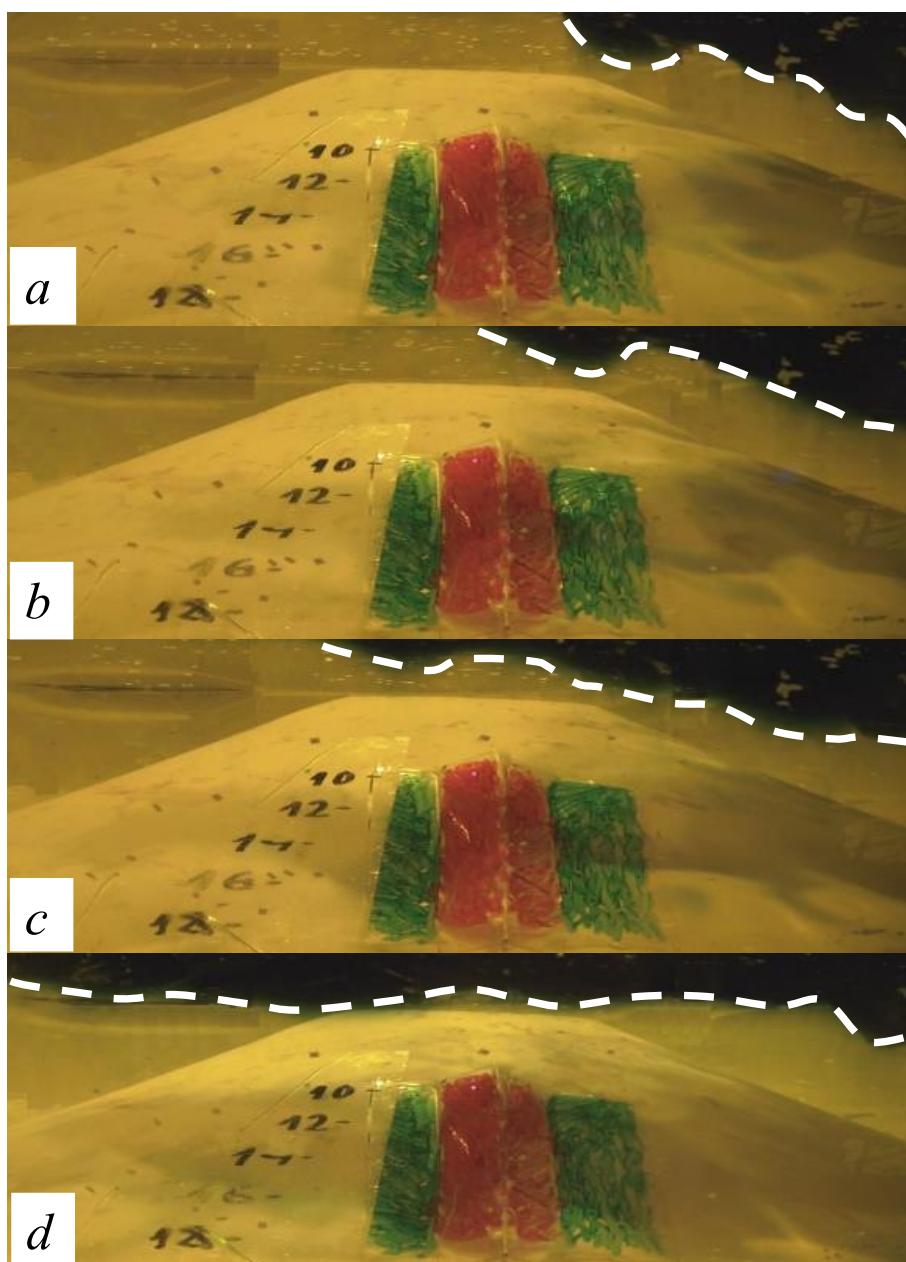


Fig. 5. Baroclinic eddy current (side view) colored blue and moving from right to left over the cone with a ridge (colored red) at t/T equal to 52 (a), 54 (b), 66 (c) and 90 (d). Salinity of water in the tank $S = 1\%$. White dotted line shows the boundary between the upper layer of fresh water and the lower layer of salt water (Sources ³)

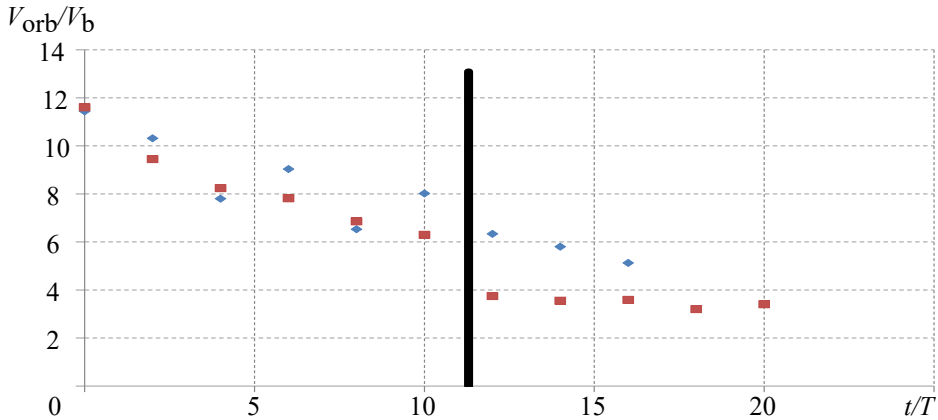


Fig. 6. Dependence of V_{orb}/V_b on t/T . Blue diamonds denote the experiment over the cone with a smooth surface, red squares – the experiment over the cone with a ridge. Thick black line shows the moment when the current front passes over the ridge. Salinity of water in the tank $S = 2\text{‰}$ (Source ³)

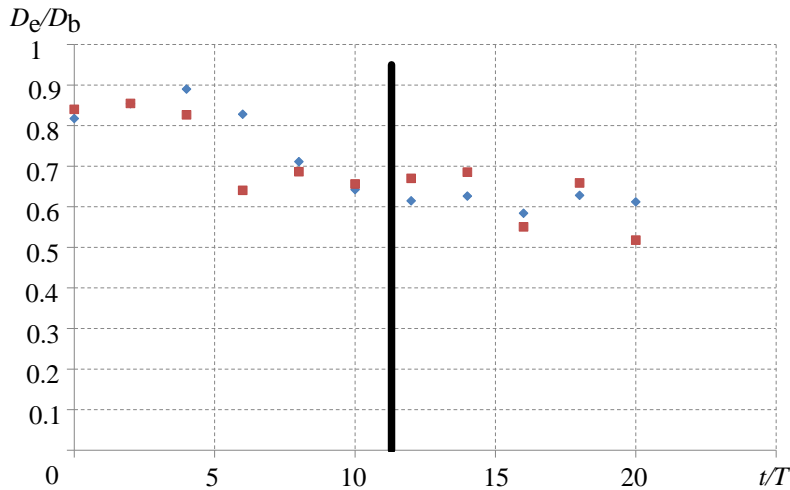


Fig. 7. Dependence of D_e/D_b on t/T . Blue diamonds denote the experiment over the cone with a smooth surface, red squares – the experiment over the cone with a ridge. Thick black line shows the moment when the current front passes over the ridge. Salinity of water in the tank $S = 2\text{‰}$ (Source ³)

Figure 3 demonstrates a video footage of eddy current propagation in the anticyclonic direction over a cone without a ridge-shaped ledge and with it.

Since the images in both figures were taken at approximately the same moments in time, it follows from their comparison that the ridge greatly slows down the eddy current propagation and contributes to the destruction of individual eddies. Indeed, the calculations have shown that when crossing a ridge, the azimuthal velocity of the eddy current decreases by a factor of two or more (see Fig. 4). The strongest flow slowdown occurs, as one would expect, in the case of barotropic eddy columns (Fig. 4, *a*). The density stratification weakens the topographic beta-effect, but does not suppress it completely. The ridge reduces the penetration depth of the baroclinic

eddy current (Fig. 5) and the orbital velocity of eddies (Fig. 6). It is curious that the ridge does not have a significant effect on the diameter of eddies D_e (Fig. 7).

An important question is this: are source-generated anticyclonic eddies baroclinically stable or unstable? In all experiments, the disintegration of one eddy into two or more smaller ones was not observed. At the same time, it is of interest to estimate the Burger number $Bu = (Rd/R_e)^2$, where $Rd = (g'H_0)^{1/2}/f$ is baroclinic radius of deformation; $R_e = D_e/2$ is eddy radius ($g' = g\beta S$, here g is gravitational acceleration; β is salinity compression coefficient; S is water salinity in the tank), the Burger number variation over time and compare the calculated values of Bu with the critical value characterizing the eddy transition from a baroclinically stable to an unstable state.

The dependence of Bu on dimensionless time t/T for $S = 2\text{‰}$ is shown in Fig. 8. It can be seen that Bu values increase with time from 0.35–0.40 to 0.62–0.72 (due to a decrease in the eddy diameter). This means that if a baroclinic eddy was stable under the source, it will continue to remain stable, since to achieve baroclinic instability the Bu parameter must be significantly less than one [17]. In addition, as was demonstrated in [2, 17], the bottom slope additionally stabilizes baroclinic flows and eddies, i.e., makes them more stable. Based on this, we can conclude that in this series of experiments baroclinic instability did not manifest itself and did not have a significant effect on the evolution of baroclinic anticyclonic eddies [18].

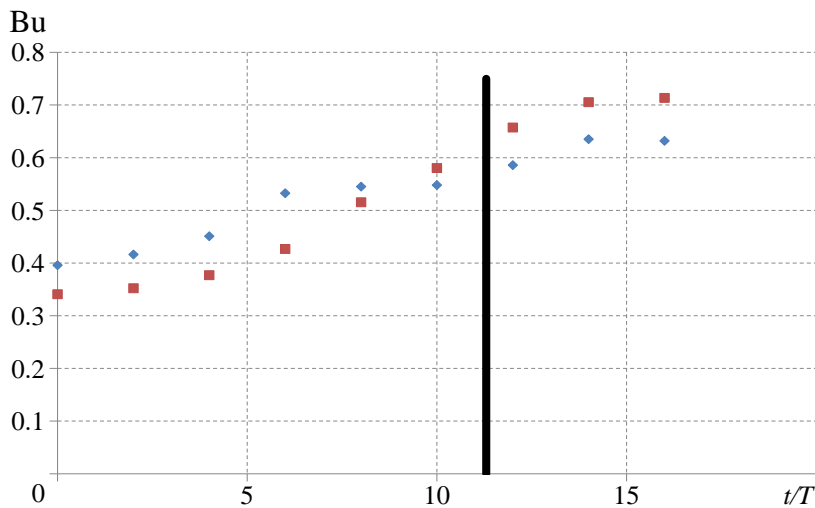


Fig. 8. Dependence of Bu number on dimensionless time for $S = 2\text{‰}$

Figure 9 shows a diagram of anticyclonic eddy passage over the ridge. The moment in time when eddy (A) comes close to the ridge is demonstrated in Fig. 9, *a*. The anticyclonic eddy moves down the slope creeping onto the ridge and trying to move along the isobath. In this case, cyclonic eddy (C) of smaller diameter is formed above it (Fig. 9, *b*). This eddy pair tends to move in the cyclonic direction, so the anticyclone motion in the anticyclonic direction slows down. Since an anticyclone is a larger and more powerful eddy compared to a cyclone, it “spins” the latter around

itself (Fig. 9, *c*). Eventually both eddies cross the ridge (Fig. 9, *d*). Soon after this, the cyclone dissipates and the weakened anticyclone continues to move in the anticyclonic direction due to the topographic beta-effect.

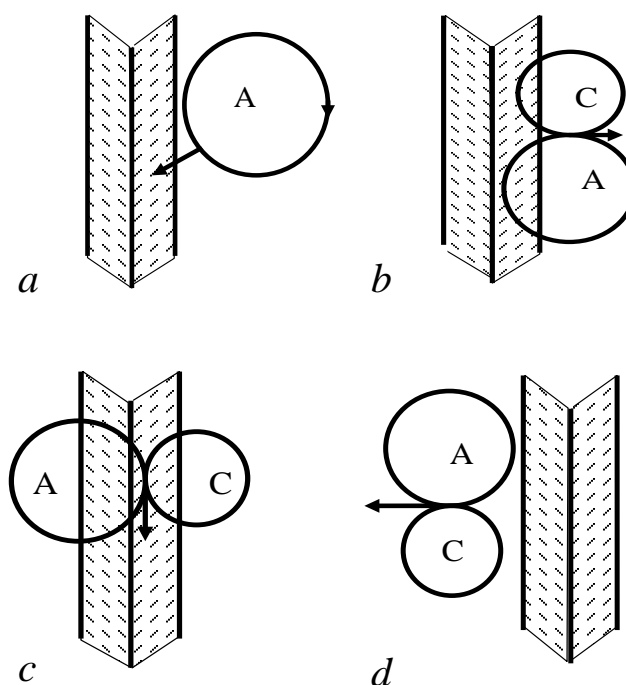


Fig. 9. Diagram of passage of an anticyclonic vortex over the ridge (A is an anticyclonic eddy, C is a cyclonic eddy) (Sources ^{2,3})

Conclusion

The laboratory experiments were carried out to study the impact of an underwater ridge located on an inclined bottom and directed along its slope on barotropic and baroclinic anticyclonic eddies moving along the isobaths in the anticyclonic direction (to the “west”) due to the topographic beta-effect.

In the experiments with a ridge, the “western” drift of anticyclonic barotropic and baroclinic eddies slows down significantly. After crossing the ridge, the orbital velocity of water rotation in the eddies decreases significantly and a trend towards decrease in the penetration depth of baroclinic eddies is observed, i.e., towards reduction of their potential energy and more rapid dissipation.

The results of the experiment confirmed field observations, as well as numerical modeling in terms of noticeable impact of a low along-slope underwater ridge located in the Black Sea western part on the propagation of the Sevastopol anticyclonic eddy and its orbital velocity. At the same time, “stationarity” of eddies in front of the ridge was not noted in the experiments: although they slowed down their motion along the isobaths, they did not stop and “hover” in one place for a long time. The most likely cause for this is a generation of a chain of eddies in the experiments, rather than individual ones. The dynamics of eddies in a chain differs from the dynamics of a single one, since subsequent eddies push the previous

ones and contribute to their passage over the ridge and further movement. Subsequently, it is planned to perform experiments with a single anticyclonic eddy in rotating fluid above a sloping bottom with and without a ridge. Perhaps these experiments will provide a closer correspondence of the results with the data of field observations and numerical hydrodynamic modeling.

REFERENCES

1. Kubryakov, A.A. and Stanichny, S.V., 2015. Seasonal and Interannual Variability of the Black Sea Eddies and Its Dependence on Characteristics of the Large-Scale Circulation. *Deep Sea Research Part I: Oceanographic Research Papers*, 97, pp. 80-91. <https://doi.org/10.1016/j.dsr.2014.12.002>
2. Zatsepin, A.G., Emel'yanov, S.V., Denisov E.S., Kremenetskiy, V.V., Poyarkov, S.G., Stroganov, O.Yu., Denisov, E.S., Stanichnaya, R.R. and Stanichny, S.V., 2005. Effect of Bottom Slope and Wind on the Near-Shore Current in a Rotating Stratified Fluid: Laboratory Modeling for the Black Sea. *Oceanology*, 45(Suppl. 1), pp. S13-S26.
3. Ivanov, V.A. and Belokopytov, V.N., 2013. *Oceanography of Black Sea*. Sevastopol: ECOSI-Gidrofizika, 210 p.
4. Kubryakov, A.A. and Stanichny, S.V., 2015. Mesoscale Eddies in the Black Sea from Satellite Altimetry Data. *Oceanology*, 55(1), pp. 56-67. <https://doi.org/10.1134/S0001437015010105>
5. Ginzburg, A.I., Kostyanoy, A.G., Nezlin, N.P., Solov'yev, D.M., Stanichnaya, R.R. and Stanichny, S.V., 2001. Anticyclonic Eddies over the Northwestern Continental Slope in the Black Sea and Transport of Chlorophyll-Rich Waters into Its Abyssal Basin. *Mapping Sciences and Remote Sensing*, 38(2), pp. 130-143. <https://doi.org/10.1080/07493878.2001.10642171>
6. Ginzburg, A.I., Kostianoy, A.G., Soloviev, D.M. and Stanichny, S.V., 2000. Remotely Sensed Coastal/Deep-Basin Water Exchange Processes in the Black Sea Surface Layer. In: D. Halpern, ed., 2000. *Satellites, Oceanography and Society*. Elsevier Oceanography Series, vol. 63. Chapter 15. New York: Elsevier Science, pp. 273-287. [https://doi.org/10.1016/S0422-9894\(00\)80016-1](https://doi.org/10.1016/S0422-9894(00)80016-1)
7. Oguz, T., 2002. Role of Physical Processes Controlling Oxycline and Suboxic Layer Structures in the Black Sea. *Global Biogeochemical Cycles*, 16(2), 1019. <https://doi.org/10.1029/2001GB001465>
8. Shapiro, G.I., Stanichny, S.V. and Stanychna, R.R., 2010. Anatomy of Shelf-Deep Sea Exchanges by a Mesoscale Eddy in the North West Black Sea as Derived from Remotely Sensed Data. *Remote Sensing of Environment*, 114(4), pp. 867-875. <https://doi.org/10.1016/j.rse.2009.11.020>
9. Kubryakov, A.A., Stanichny, S.V., Zatsepin, A.G. and Kremenetskiy, V.V., 2016. Long-Term Variations of the Black Sea Dynamics and Their Impact on the Marine Ecosystem. *Journal of Marine Systems*, 163, pp. 80-94. <https://doi.org/10.1016/j.jmarsys.2016.06.006>
10. Ginzburg, A.I., Kostianoy, A.G., Nezlin N.P., Soloviev, D.M. and Stanichny, S.V., 2002. Anticyclonic Eddies in the Northwestern Black Sea. *Journal of Marine Systems*, 32(1-3), pp. 91-106. [https://doi.org/10.1016/S0924-7963\(02\)00035-0](https://doi.org/10.1016/S0924-7963(02)00035-0)
11. Staneva, J.V., Dietrich, D.E., Stanev, E.V. and Bowman, M.J., 2001. Rim Current and Coastal Eddy Mechanisms in an Eddy-Resolving Black Sea General Circulation Model. *Journal of Marine Systems*, 31(1-3), pp. 137-157. [https://doi.org/10.1016/S0924-7963\(01\)00050-1](https://doi.org/10.1016/S0924-7963(01)00050-1)
12. Kostianoy, A.G. and Zatsepin, A.G., 1989. Laboratory Experiments with Baroclinic Vortices in a Rotating Fluid. *Elsevier Oceanography Series*, 50(C), pp. 691-700. [https://doi.org/10.1016/S0422-9894\(08\)70215-0](https://doi.org/10.1016/S0422-9894(08)70215-0)
13. Zatsepin, A.G. and Didkovskii, V.L. On one Mechanism for the Formation of Mesoscale Eddy Structures in the Ocean Slope Zone. *Doklady Akademii Nauk*, 347(1), pp. 109-112 (in Russian).

14. Zatsepin, A.G., Didkovski, V.L. and Semenov, A.V., 1998. Self-Oscillatory Mechanism of Inducing a Vortex Structure by a Stationary Local Source over a Sloping Bottom in a Rotating Fluid. *Oceanology*, 38(1), pp. 43-50.
15. Kamenkovich, V.M., Koshlyakov, M.N. and Monin, A.S., eds., 1986. *Synoptic Eddies in the Ocean*. Environmental Fluid Mechanics, vol. 5. Dordrecht: Springer, 444 p. <https://doi.org/10.1007/978-94-009-4502-9>
16. Shapiro, G.I., 1984. Structure of the Mesoscale Vortex Lens in the Ocean Thermocline. *Doklady Akademii Nauk SSSR*, 276(6), pp. 1477-1479 (in Russian).
17. Zatsepin, A.G., Elkin, D.N. and Shvartsman, D.R., 2023. Preliminary Results of Laboratory Investigations of the Evolution of Non-Frontal Eddies in a Two-Layered Rotating Fluid. *Journal of Oceanological Research*, 51(1), pp. 5-35. [https://doi.org/10.29006/1564-2291.JOR-2023.51\(1\).1](https://doi.org/10.29006/1564-2291.JOR-2023.51(1).1) (in Russian).
18. Kubryakov, A.A., Mizyuk, A.I. and Stanichny, S.V., 2024. Stationarity and Separation of the Sevastopol Eddies in the Black Sea: The Role of Eddy-Topographic Interaction and Submesoscale Dynamics. *Journal of Marine Systems*, 241, 103911. <https://doi.org/10.1016/j.jmarsys.2023.103911>

Submitted 11.10.2023; approved after review 01.11.2023;
accepted for publication 18.01.2024.

About the authors:

Dmitry N. Elkin, Research Associate, Shirshov Institute of Oceanology of RAS (36 Nakhimovskiy Ave., Moscow, 117997, Russian Federation), CSc (Phys.-Math.), **ORCID ID: 0000-0002-9232-9852**, dmelkin@mail.ru

Andrey G. Zatsepin, Head of Experimental Ocean Physics Laboratory, Shirshov Institute of Oceanology of RAS (36 Nakhimovskiy Ave., Moscow, 117997, Russian Federation), DSc (Phys.-Math.), **ORCID ID: 0000-0002-5527-5234**, zatsepin@ocean.ru

Contribution of the co-authors:

Dmitry N. Elkin – assembling laboratory set-up, conducting experimental studies, data processing, building of dependencies, preparation of drawings, writing and revision of the original text

Andrey G. Zatsepin – formulation of the research problem, data analysis, formulation of results and conclusions, writing and revision of the original text

The authors have read and approved the final manuscript.

The authors declare that they have no conflict of interest.

Evaluation of Sea Ice Drift in the Arctic Marginal Ice Zone based on Sentinel-1A/B Satellite Radar Measurements

E. V. Plotnikov^{1, ✉}, I. E. Kozlov¹, E. V. Zhuk¹, A. V. Marchenko²

¹ Marine Hydrophysical Institute of RAS, Sevastopol, Russian Federation

² University Centre in Svalbard, Longyearbyen, Norway

✉ ev.plotnikov@ya.ru

Abstract

Purpose. The object of the work is to construct an automated system for calculating sea ice drift velocity fields using Sentinel-1A/B radar measurements based on the normalized maximum cross-correlation approach. The conditions and results of a numerical experiment aimed at evaluating the effectiveness of this technique for 63 pairs of radar images of the Fram Strait region for the summer-autumn periods in 2017 and 2018 are presented. Both the calculation algorithm and the qualitative and quantitative characteristics of the results are described in details. The effectiveness of the approach being applied to regular monitoring of ice drift is considered.

Methods and Results. The maximum cross-correlation (MCC) approach was used for calculations. It is based on automated finding of photographically similar fragments in the pairs of images with a known sensing time interval. The Pearson correlation coefficient was applied as a proximity metric. As a result, 63 sea ice drift velocity fields were constructed in the Fram Strait region, each with a spatial scale of approximately several hundred thousand square kilometers. The method for filtering false correlations is proposed.

Conclusions. The approach applied in the study makes it possible to obtain automatically the sea ice drift velocity fields from the satellite data with high spatial resolution (40 m). The reconstructed velocity fields cover significant areas of the ocean surface. The method proposed for filtering false correlations permits to extract effectively the fragments with distortions resulting from the MCC algorithm limitations, from the calculation results.

Keywords: sea ice drift dynamics, sea ice, optical flow, maximum cross-correlation approach, Sentinel-1A/B images, Fram Strait, Arctic Ocean

Acknowledgements: The study was carried out with financial support of the Russian Science Foundation grant No. 21–17–00278 (analysis, validation and development of a web-service to store sea ice drift fields) and within the framework of the theme of state assignment № FNNN-2024-0017 (development of the method for calculating sea ice drift velocity based on satellite radar data).

For citation: Plotnikov, E.V., Kozlov, I.E., Zhuk, E.V. and Marchenko, A.V., 2024. Evaluation of Sea Ice Drift in the Arctic Marginal Ice Zone Based on Sentinel-1A/B Satellite Radar Measurements. *Physical Oceanography*, 31(2), pp. 284-294.

© 2024, E. V. Plotnikov, I. E. Kozlov, E. V. Zhuk, A. V. Marchenko

© 2024, Physical Oceanography

Introduction

Sea ice drift monitoring is an important component of the Arctic geophysical process research. The data obtained can be used to solve a wide range of theoretical and practical problems. Nowadays, one of the most promising approaches to solve this problem is the analysis of satellite images in visible, infrared and microwave ranges. Sequences of satellite images related to the same fragment of the sea surface and a narrow time interval can be used to simulate sea surface dynamics, in particular, sea ice drift velocity and direction. At the same time, approaches for calculating optical flow are often used to solve the problem described. Extensive



literature on this approach describes both algorithms and features of their use in practice depending on the source data specifics [1–9]. The calculation automation problem is relevant due to the volume of satellite image archives available today. Its successful solution opens up the possibility of obtaining regular and long-term observations of sea ice drift dynamics.

This direction has received widespread development in the last decade; the research results are presented, e.g., in [10–14]. In this case, various tracking algorithms are used in relation to the data from MODIS, Sentinel-1, Sentinel-2, Landsat-8 and a number of others, mainly in the optical range. Important factors are source image resolution, ability to effectively optimize calculations for processing large amounts of data and automation of calculations. The present paper describes an automated approach making it possible to estimate sea ice dynamics from radar images with a resolution of 40 m covering an area of approximately several hundred thousand square kilometers. According to the authors, practical results on the use of an automatic data processing system with such parameters are published for the first time.

After the launch of Sentinel-1A/B synthetic aperture radar (SAR) satellites, obtaining pairs of radar images of the Arctic Region with a short time delay became possible, which offered an opportunity to evaluate the kinematic characteristics of various meso- and submesoscale processes in the upper layer of the Arctic seas [15–19]. In the application to the evaluation of ice drift velocity fields in [16], the authors demonstrated the possibility of effective calculation of such fields in the areas of intense eddy dynamics in the marginal ice zone (MIZ) with a spatial resolution $O(100\text{ m})$ based on the maximum cross-correlation approach. In [20, 21], the authors applied machine-learning methods to identify the MIZ eddies in satellite SAR data in order to show further development of this direction.

The present paper aims at describing general methodology and demonstrating effectiveness of the computational scheme for automatic Sentinel-1A/B satellite data processing to simulate sea ice drift fields in the MIZ. The proposed methodology was applied to a three-month data set related to the Fram Strait region. The approach used made it possible to automatically process a statistically significant amount of data and obtain high-quality results that confirm the approach effectiveness for quick monitoring of ice field drift dynamics in the marginal ice zone of the Arctic.

Data and methods

Sentinel-1A/B radar images obtained for the Fram Strait region in 2017 and 2018 represented initial data. Specifically, L1 Ground Range Detected products with a $40 \times 40\text{ m}$ pixel and a spatial resolution of $93 \times 87\text{ m}$ in Extra Wide Swath shooting mode were used. Satellite radar images were obtained from the archives of the Copernicus Open Access Hub service (<https://scihub.copernicus.eu>).

A total of 63 pairs of images obtained in September 2017, as well as in July and September 2018, were selected. The time range between successive measurements was from 48 to 52 minutes for each pair of radar images, which were chosen based on considerations of information content determined by the manifestation of surface structures in the drifting ice field. The data were interpolated onto a regular grid with $40 \times 40\text{ m}$ resolution and then the intersections of the scanned areas were identified

on each radar image. Additionally, the images were smoothed using a median filter with a sliding window of 20×20 pixels. Fig. 1 shows a pair of Sentinel-1A/B radar images for 26 July 2018 obtained in this way.

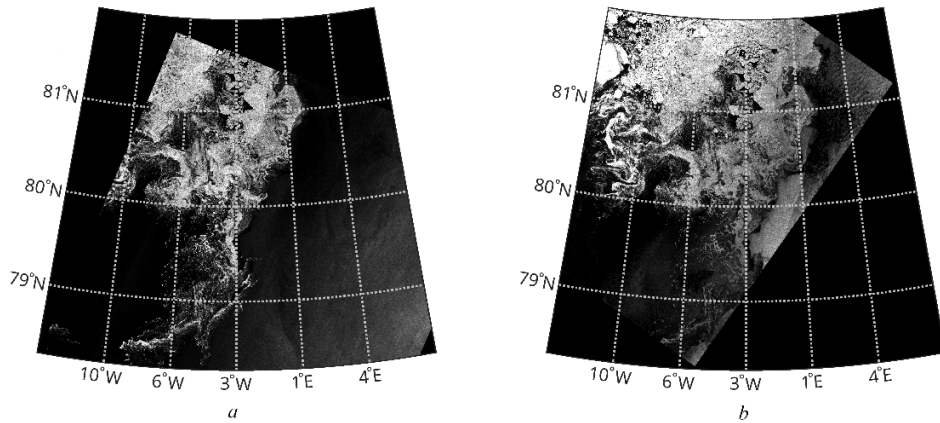


Fig. 1. A pair of Sentinel-1A (a) and Sentinel-1B (b) radar images for 15 September 2018 with the drifting ice present in the marginal ice zone of the Fram Strait

The main algorithm used in data processing is provided by the normalized maximum cross-correlation (MCC) approach [1, 3, 4, 6, 7, 9] based on obtaining the most correlated fragments in the analyzed images, the displacement of which from each other does not exceed the theoretically possible one. The neighborhoods of each pixel in both images are selected and then a normalized cross-correlation function is constructed for them. The deviation of this function maximum position from the central point is taken as the desired shift, i.e., the displacement of a texture fragment from image to image. Formally, the approach can be described as follows: the image matrices are denoted as I_1 and I_2 . Let us consider a pixel with i and j indices. Let the neighborhood have a square shape and size $N \times N$, where N is odd;

$$k = \left\{ i - (N-1)/2, \quad l = \left\{ j - (N-1)/2 \right\} \right\},$$

$$M_1 = \frac{1}{N^2} \sum_{k,l} I_1(k,l) \text{ and } M_2(u,v) = \frac{1}{N^2} \sum_{k,l} I_2(k+u, l+v).$$

Then the normalized cross-correlation function will have the following form:

$$F(u,v,i,j) = \frac{\sum_{i,k} (I_1(k,l) - M_1)(I_2(k+u, l+v) - M_2(u,v))}{\sqrt{\left(\sum_{l,k} (I_1(k,l) - M_1)^2 \right) \left(\sum_{l,k} (I_2(k+u, l+v) - M_2)^2 \right)}}.$$

Here $-u_{\max} \leq u \leq u_{\max}$, $-v_{\max} \leq v \leq v_{\max}$, where u_{\max} and v_{\max} are specified maximum possible shifts in both coordinates. The required values u_0 and v_0 for the pixel with i and j indices are such that $F((u_0, v_0, i, j) = \max(F(u, v, i, j))$, where u and v take values from the interval above. After finding the described values for all $(N-1)/2 < i < S_1 - (N-1)/2 + 1$ and $(N-1)/2 < j < -(N-1)/2 + 1$, where (S_1, S_2) is size of the images, we obtain U and V matrices of size $(S_1 - N - u_{\max} + l, S_2 - N - v_{\max} + l)$.

Figure 2 shows both components (u_0 and v_0) of the vector field constructed in this way with parameters $N = 80$ $u_{\max} = v_{\max} = 50$ according to the data shown in Fig. 1.

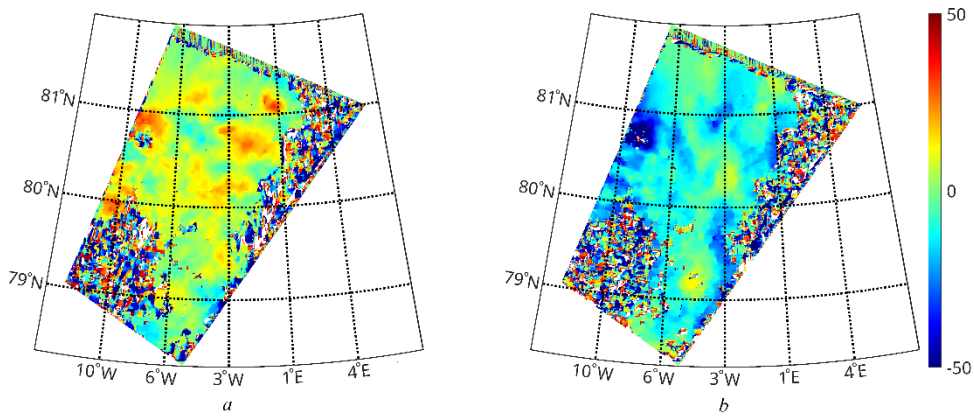


Fig. 2. Pixel shifts corresponding to the velocity field components u_0 (a) and v_0 (b) and obtained on 26 July 2018 using the MCC algorithm for the Sentinel-1A/B radar images

The correspondence of the fragments containing useful data to the fragments where the presence of ice accumulations in the original images is clearly visible is noteworthy here. The rest of the image is either uninformative or contains noise, which is a manifestation of an effect called “spurious correlations.” The principal generally accepted approach for filtering corresponding fragments is a lower limit for the minimum value of the cross-correlation function and cutting off pixels that do not satisfy this condition. Obviously, a morphological analysis of the resulting field could be an effective approach here. However, the authors decided to take a different path taking into account that operator $(I_1, I_2) \rightarrow (U, V)$ is not symmetric.

Let us denote the indices of its neighborhood as $k = \left\{ i - (N-1)/2 + (N-1)/2 \right\}$, $l = \left\{ j - (N-1)/2 + (N-1)/2 \right\}$. Suppose (u_0, v_0) is the calculated shift and for any displacements fragment $I_1(k, l)$ is maximally correlated with fragment $I_2(k + u_0, l + v_0)$. Then correlation of $I_1(k - u_0, l + v_0)$ and $I_2(k, l)$ should also be high. Therefore, if the described

calculation is carried out taking I_2 as the first image and I_1 as the second one, the results should be close when the signs of both components change. Let us name this as an inverse calculation. The cosine of the angle between the vectors of two such fields can be used to estimate proximity. Figure 3, *a* shows the values of this quantity. Here, the correspondence of fragments with high cosine values to fragments with informative data is clearly visible, which confirms the effectiveness of the approach described. It is possible to obtain a mask for which the calculated velocity fields are relevant by setting the optimal threshold value. A threshold of 0.92 was used for calculations. In addition, a gradient filter can be used to highlight high spatial heterogeneity areas in order to remove residual noise. The maximum value of the variation of the u and v components in a neighborhood of 3×3 pixels (Fig. 3, *b*) is chosen for each pixel. All fragments exceeding a threshold value of 2.51 are cut off.

After implementing the described filtering procedure, a number of small individual fragments with doubtful information content remain in the resulting mask. To remove them, the mask is divided into connected components and the number of pixels contained is calculated for each of them. The component is cut if this number is less than the specified threshold. The component area ratio to the area of the entire scene was chosen as the evaluation value and the value of 0.25% was chosen as the threshold.

To summarize all the aforesaid, we can briefly describe the algorithm for processing a pair of radar images as follows:

- unpacking and reprojection of source data onto a regular grid;
- direct and inverse calculations using the normalized maximum cross-correlation approach;
- filtering of irrelevant fragments;
- compression of the scene taking into account the boundaries of the mask obtained at the previous step;
- removal of small individual mask components;
- transformation of shifts into a velocity (m/s) field.

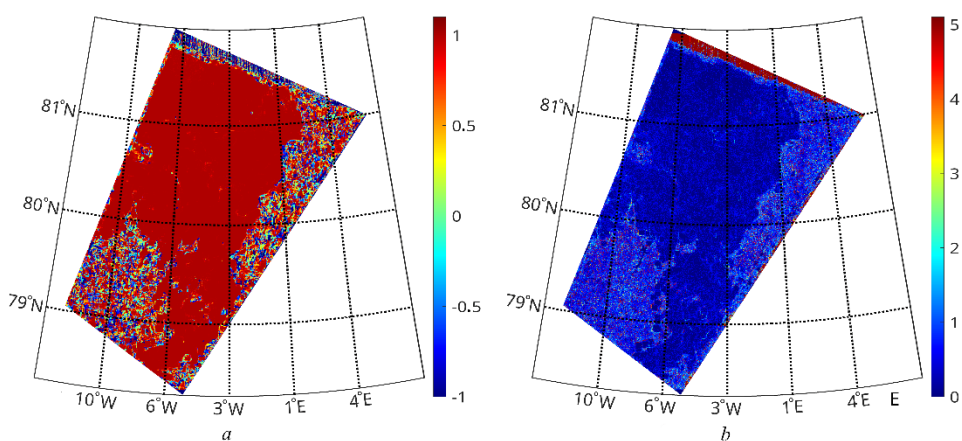


Fig. 3. Spatial distribution of the cosine of angle between the vectors of calculated shifts resulted from direct and inverse calculations (*a*); assessment of the homogeneity of the shift components over the 3×3 pixel window (*b*)

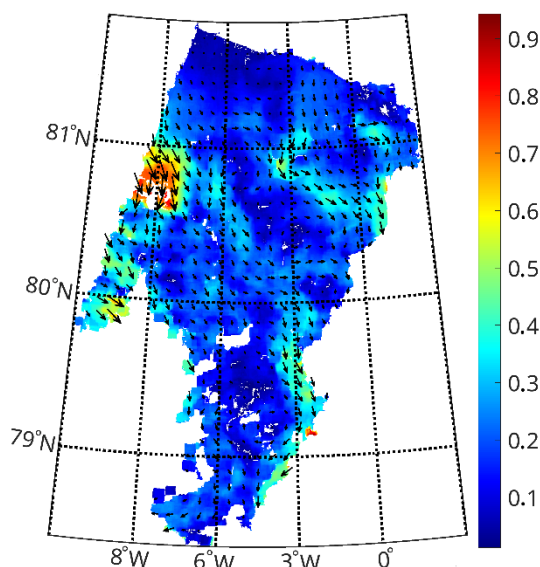


Fig. 4. Final result of calculation of the ice drift velocity (m/s) field in the Fram Strait for 26 July 2018

The entire data processing result is shown in Fig. 4. It can be seen that the range of observed ice drift velocities is 0.1–0.8 m/s, the average speed is ~ 0.2 –0.3 m/s, the dominant direction of ice drift is southern/southeastern. Maximum drift speeds are observed in the northwestern sector, as well as on the southeastern periphery of the area shown.

Results

The results of calculations are 63 vector fields of ice drift velocity describing the horizontal movement of sea ice accumulations in the Fram Strait MIZ. For a pair of images ($10,000 \times 10,000$ pixels), the running time of the used implementation of the MCC algorithm with a sliding window size of 80×80 and maximum shifts $u_{\max} = 50, v_{\max} = 50$ is about two hours, when calculated in two threads on a computer with Intel i5 12500H processor running Debian GNU/Linux 12 operating system.

An objective evaluation of the described approach effectiveness is difficult due to the lack of reference data on surface sea dynamics. The most promising approach in the present case seems to be a comparison of the velocity fields modelled from satellite data with field data on the direction and speed of the ice drift obtained based on the stationary geolocation sensors (GPS trackers) installed on ice floes. Figure 5 shows the drift trajectory of such a sensor against the velocity field background calculated from satellite data.

Unfortunately, the authors do not have a statistically significant array of field data for a more detailed comparison. However, Fig. 5 shows that measurements from two independent sources agree well in direction and absolute value. In addition, a certain idea of the approach relevance can be obtained based on the expert evaluation of the structure of the modelled fields and the correspondence of the visible displacements of contrast structures in image textures to the calculated

shifts. From this viewpoint, the calculation results demonstrate high quality. Fragments with clearly visible inconsistencies are effectively eliminated using an automatic filtering procedure while the number of discarded pixels is negligible compared to their total number in areas with well-defined contrasts. This algorithm demonstrated no significant redundancy or insufficiency. Mesoscale and submesoscale dynamic structures (such as individual eddies, eddy dipoles or ice filaments) visible in the images are also clearly seen in the velocity fields obtained.

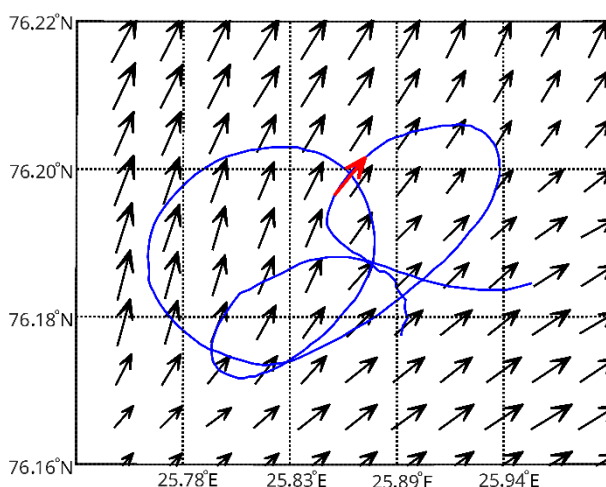


Fig. 5. Comparison of the ice drift velocity vectors derived from satellite data with the field measurements obtained from the data of GPS trackers installed on ice. Blue curve shows the trajectory of ice floes based on the field data. Red arrow highlights a fragment of field measurements coinciding in time with satellite imagery. Time of Sentinel-1 acquisitions: at 5:02 UTC and at 5:51 UTC on 26.04.2019. GPS tracker is traced from 26.04.2019 (00:10) to 27.04.2019 (11:30)

Visualization of satellite products with ice drift fields

At the next stage, the products with sea ice drift velocity fields simulated from quasisynchronous satellite data are posted on the webpage of Laboratory of Marine Polar Research (LMPR) of Marine Hydrophysical Institute of RAS at http://polar-space.ru/arctic_currents. To do this, the calculated fields are first interpolated onto a grid with a 40 m step and recorded as netCDF files. A data visualization system based on client-server architecture was developed for the Web. Figure 6 shows the general structure of the visualization system for this satellite product.

This system stores netCDF format data with ice drift fields as a file archive on the server. A special software module was developed in Python to display ice drift velocities on a geographic map. It converts the source data into images with a single speed scale for all files. The name of each picture file contains a date in order to establish a one-to-one correspondence between a user request and a displayed ice drift field.

The user interface (UI) for selecting and displaying the product of interest was developed using jQuery javascript libraries. The map service functions are implemented using the mapBox GL library. The UI makes it possible to select the ice drift field for the date of interest by scrolling through an array of dates or selecting the desired date from the list. Figure 7 shows an example of the UI at [http://polar-space.ru/arctic currents](http://polar-space.ru/arctic_currents) for the selected date 26 July 2018.

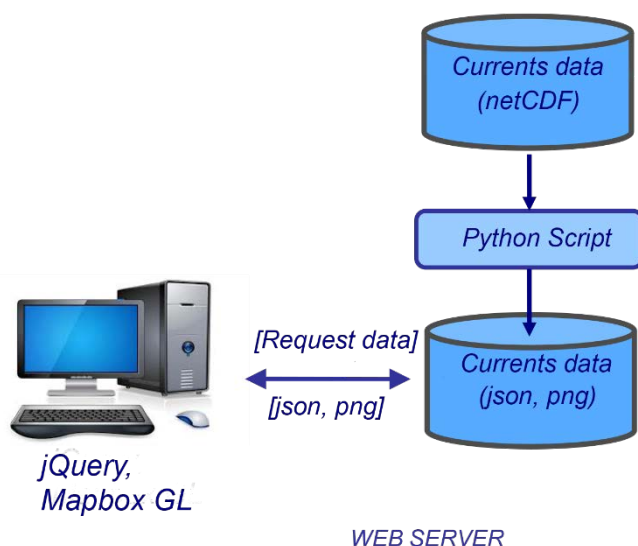


Fig. 6. General structure of the system for visualizing the products with ice drift fields (available at http://polar-space.ru/arctic_currents)

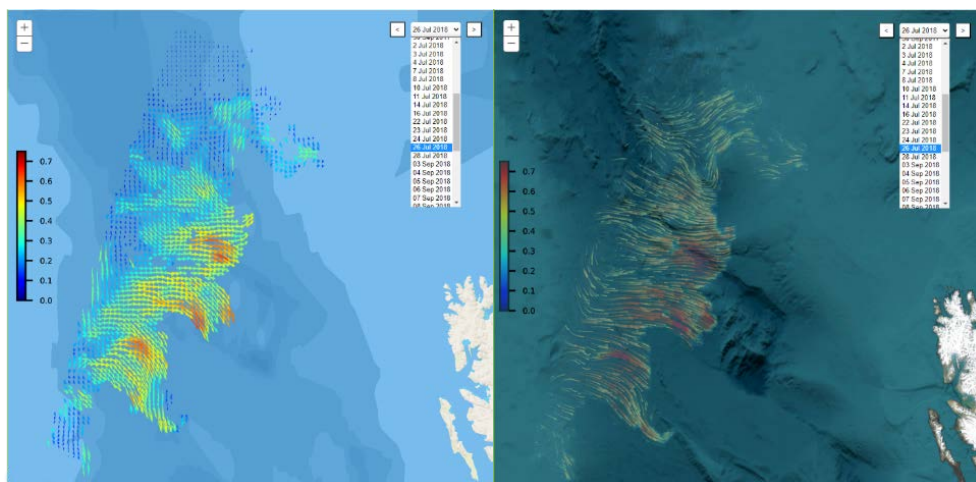


Fig. 7. User interface of the system for visualizing the products with ice drift fields in the marginal ice zone of the Fram Strait for 26 July 2018. *On the left* is an example of a static display of ice drift fields, *on the right* – a dynamic field using the Wind-JS library

The developed UI contains a choice of displaying data with ice drift fields in the form of not only a static picture (Fig. 7, left), but also a dynamic field (Fig. 7, right). This task is implemented with the Wind-JS library (<https://github.com/Esri/wind-js>) adapted to display ice drift vectors. The input data are json files containing the values of the ice drift zonal and meridional components. A special software module was developed in Python to generate these files automatically. To date, all processed data for 2017 and 2018 have been posted on the LMPR MHI website. In addition, the existing interface is supplemented with the ability to download ice drift fields of interest in netCDF format.

Conclusion

The paper describes the general methodology for processing quasisynchronous measurements of Sentinel–1A/B satellite SARs operating in tandem for 5 years (2016–2021) to obtain time-regular ice drift velocity fields in the Arctic marginal ice zone. As a rule, temporal resolution of the resulting products with ice drift velocity fields is 1 day in the European sector of the Arctic and from 1 to 5 days in other Arctic regions.

Limited to the initial data set, validation of the resulting velocity fields with *in situ* measurements showed good agreement between them. Nevertheless, the research will be continued in this direction to determine objective statistics of the quality of calculated ice drift velocity fields.

Compared to the existing products concerning ice drift in the Arctic, the presented approach and the simulated velocity fields are distinguished by a significantly higher spatial resolution (40 m), relative simplicity of the methods used and low requirements for computing resources.

The resulting products with ice drift velocity fields in the marginal ice zone of the Arctic are available at <http://polar-space.ru/arctic> currents and can be used by specialists to solve a number of practical problems including evaluation of the MIZ dynamics and evolution and processes in it, as well as for comparison with other satellite products and validation of ocean general circulation models with lower resolution.

Sentinel–1A/B data were obtained from the archives of the Copernicus Open Access Hub service (available at: <https://scihub.copernicus.eu>).

REFERENCES

1. Alexanin, A.I., Alexanina, M.G. and Karnatsky, A.Y., 2013. Automatic Computation of Sea Surface Velocities on a Sequence of Satellite Images. *Current Problems in Remote Sensing of the Earth from Space*, 10(2), pp. 131-142 (in Russian).
2. Beauchemin, S.S. and Barron, J.L., 1995. The Computation of Optical Flow. *ACM Computing Surveys (CSUR)*, 27(3), pp. 433-466. <https://doi.org/10.1145/212094.212141>
3. Barron, J.L. and Thacker, N.A., 2005. *Tutorial: Computing 2D and 3D Optical Flow*. Imaging Science and Biomedical Engineering Division, Medical School, University of Manchester. Vol. 1. https://faculty.runi.ac.il/toky/old_courses/videoproc-07/handouts/2004-012.pdf [Accessed: 10 April 2024].
4. Emery, W.J., Thomas, A.C., Collins, M.J., Crawford, W.R. and Mackas, D.L., 1986. An Objective Method for Computing Advective Surface Velocities from Sequential Infrared Satellite Images. *Journal of Geophysical Research: Oceans*, 91(C11), pp. 12865-12878. <https://doi.org/10.1029/JC091iC11p12865>
5. Fortun, D., Bouthemy, P. and Kervrann, C., 2015. Optical Flow Modeling and Computation: A Survey. *Computer Vision and Image Understanding*, 134, pp. 1-21. <https://doi.org/10.1016/j.cviu.2015.02.008>
6. Luo, J. and Konofagou, E., 2010. A Fast Normalized Cross-Correlation Calculation Method for Motion Estimation. *IEEE Transactions on Ultrasonics, Ferroelectrics, and Frequency Control*, 57(6), pp. 1347-1357. <https://doi.org/10.1109/TUFFC.2010.1554>
7. Lawrence, P., 2016. The Derivation of Sea Surface Velocities from Satellite Imagery Using Maximum Cross Correlation (MCC). *The Plymouth Student Scientist*, 9(1), pp. 145-161. <http://hdl.handle.net/10026.1/14119>
8. Stark, M., 2013. *Optical Flow PIV: Improving the Accuracy and Applicability of Particle Image Velocimetry*. MS Thesis. ETH. Department of Mechanical and Process Engineering. <https://doi.org/10.3929/ethz-a-009767070>

9. Sun, D., Roth, S., Lewis, J.P. and Black, M.J., 2008. Learning Optical Flow. In: D. Forsyth, P. Torr, A. Zisserman, eds., 2008. *Computer Vision—ECCV 2008. ECCV 2008. Lecture Notes in Computer Science*, vol. 5304. Springer, Berlin, Heidelberg, pp. 83-97. https://doi.org/10.1007/978-3-540-88690-7_7
10. Kwok, R., Schweiger, A., Rothrock, D.A., Pang, S. and Kottmeier, C., 1998. Sea Ice Motion from Satellite Passive Microwave Imagery Assessed with ERS SAR and Buoy Motions. *Journal of Geophysical Research: Oceans*, 103(C4), pp. 8191-8214. <https://doi.org/10.1029/97JC03334>
11. Samardžija, I., 2018. Two Applications of a Cross-Correlation Based Ice Drift Tracking Algorithm; Ship-Based Marine Radar Images and Camera Images from a Fixed Structure. In: FEDU, 2018. *Proceedings of the 24th IAHR International Symposium on Ice*. Vladivostok: Far Eastern Federal University, pp. 141-151.
12. Lopez-Acosta, R., Schodlok, M.P. and Wilhelmus, M.M., 2019. Ice Floe Tracker: An Algorithm to Automatically Retrieve Lagrangian Trajectories via Feature Matching from Moderate-Resolution Visual Imagery. *Remote Sensing of Environment*, 234, 111406. <https://doi.org/10.1016/j.rse.2019.111406>
13. Wang, M., König, M. and Oppelt, N., 2021. Partial Shape Recognition for Sea Ice Motion Retrieval in the Marginal Ice Zone from Sentinel-1 and Sentinel-2. *Remote Sensing*, 13(21), 4473. <https://doi.org/10.3390/rs13214473>
14. Howell, S.E.L., Brady, M. and Komarov, A.S., 2022. Generating Large-Scale Sea Ice Motion from Sentinel-1 and the RADARSAT Constellation Mission Using the Environment and Climate Change Canada Automated Sea Ice Tracking System. *The Cryosphere*, 16(3), pp. 1125-1139. <https://doi.org/10.5194/tc-16-1125-2022>
15. Kozlov, I.E. and Mikhaylichenko, T.V., 2021. Estimation of Internal Wave Phase Speed in the Arctic Ocean from Sequential Spaceborne SAR Observations. *Current Problems in Remote Sensing of the Earth from Space*, 18(5), pp. 181-192. <https://doi.org/10.21046/2070-7401-2021-18-5-181-192> (in Russian).
16. Kozlov, I.E., Plotnikov, E.V. and Manucharyan, G.E., 2020. Brief Communication: Mesoscale and Submesoscale Dynamics in the Marginal Ice Zone from Sequential Synthetic Aperture Radar Observations. *The Cryosphere*, 14(9), pp. 2941-2947. <https://doi.org/10.5194/tc-14-2941-2020>
17. Kozlov, I.E. and Atadzhanova, O.A., 2021. Eddies in the Marginal Ice Zone of Fram Strait and Svalbard from Spaceborne SAR Observations in Winter. *Remote Sensing*, 14(1), 134. <https://doi.org/10.3390/rs14010134>
18. Artamonova, A.V. and Kozlov, I.E., 2023. Eddies in the Norwegian and Greenland Seas from the Spaceborne SAR Observations in Summer, 2007. *Physical Oceanography*, 30(1), pp. 112-123. <https://doi.org/10.29039/1573-160X-2023-1-112-123>
19. Marchenko, A.V., Morozov, E.G., Kozlov, I.E. and Frey, D.I., 2021. High-Amplitude Internal Waves Southeast of Spitsbergen. *Continental Shelf Research*, 227, 104523. <https://doi.org/10.1016/j.csr.2021.104523>
20. Khachatryan, E. and Sandalyuk, N., 2022. On the Exploitation of Multimodal Remote Sensing Data Combination for Mesoscale/Submesoscale Eddy Detection in the Marginal Ice Zone. *IEEE Geoscience and Remote Sensing Letters*, 19, pp. 1-5. <https://doi.org/10.1109/LGRS.2022.3215202>
21. Khachatryan, E., Sandalyuk, N. and Loizou, P., 2023. Eddy Detection in the Marginal Ice Zone with Sentinel-1 Data Using YOLOv5. *Remote Sensing*, 15(9), 2244. <https://doi.org/10.3390/rs15092244>

Submitted 06.09.2023; approved after review 29.12.2023;
accepted for publication 18.01.2024.

About the authors:

Evgeniy V. Plotnikov, Junior Researcher, Marine Hydrophysical Institute of RAS (2 Kapitanskaya Str., Sevastopol, 299011, Russian Federation), **ORCID ID: 0000-0003-4365-9369**, **Scopus Author ID: 57190382092**, **SciProfiles: 2325823**, ev.plotnikov@ya.ru

Igor E. Kozlov, Leading Researcher, Head of Marine Polar Research Laboratory, Marine Hydrophysical Institute of RAS (2 Kapitanskaya Str., Sevastopol, 299011, Russian Federation), CSc. (Phys.-Math.), **ORCID ID: 0000-0001-6378-8956**, **ResearcherID: G-1103-2014**, **Scopus Author ID: 49963767500**, ik@mhi-ras.ru

Elena V. Zhuk, Junior Researcher, Marine Hydrophysical Institute of RAS (2 Kapitanskaya Str., Sevastopol, 299011, Russian Federation), **ORCID ID: 0000-0002-4263-7734**, **Scopus Author ID: 57191412660**, alenixx@gmail.com

Aleksey V. Marchenko, Department of Arctic Technologies, University Centre in Svalbard (P.O. Box 156 N-9171 Longyearbyen, Norway), CSc. (Phys.-Math.), Professor, **ORCID ID: 0000-0003-4169-0063**, **Scopus Author ID: 7101880290**, **ResearcherID: GSD-3516-2022**, aleksey.marchenko@unis.no

Contribution of the co-authors:

Evgeniy V. Plotnikov – methodology and software development, carrying out numerical experiments, preparation of the article text

Igor E. Kozlov – problem statement, data and article text preparation

Elena V. Zhuk – development of the data access web resource, web database formation, preparation of the article text

Aleksey V. Marchenko – preparation of GPS tracker data

The authors have read and approved the final manuscript.

The authors declare that they have no conflict of interest.

Extreme Black Sea Storm in November, 2023

V. A. Dulov, M. V. Yurovskaya ✉, V. V. Fomin, M. V. Shokurov,
Yu. Yu. Yurovsky, V. S. Barabanov, A. V. Garmashov

Marine Hydrophysical Institute of RAS, Sevastopol, Russian Federation

✉ mvkosnik@gmail.com

Abstract

Purpose. The purpose of the study is to describe comprehensively the extreme storm in the Black Sea in November 2023 in terms of wind and wave field characteristics, based on model calculations, satellite data and field measurements.

Methods and results. The atmospheric fields are calculated using the WRF model, and the wave fields – using the SWAN model. The wind and wave fields, as well as their development during the storm are described in detail. The phenomenon of wave shadowing by the Crimean Peninsula is studied. Using the data available for the storm period, the calculation results are compared to the data from satellite altimeters, the CFOSAT SWIM wave scatterometer and synthetic aperture radars. The data of *in situ* measurements carried out during the storm with the standard equipment of the oceanographic platform in the coastal zone of the Southern Coast of Crimea are presented. The wave characteristics near the oceanographic platform are calculated using the nested grid method.

Conclusions. It was found that during the storm in the Black Sea in November 2023, the maximum wave heights and the maximum wave periods exceeded 9 m and 13 s, respectively. A large amount of satellite data confirmed the calculation results. The results of wave modelling near the oceanographic platform are consistent with *in situ* measurements. Since the applied configuration of models permitted calculation of the fields of wave physical characteristics with a high degree of reliability, they can be used for an authentic forecast of extreme storms in the Black Sea. The shadowing of waves by the Crimean Peninsula has led to a decrease by a factor of ~ 2 or more in the heights of extreme waves in the coastal waters from the southern tip of the peninsula to Cape Chauda (35.8°E).

Keywords: natural disasters, extreme storm, Black Sea, wind waves, WRF atmospheric model, SWAN wave model, marine *in situ* data, satellite wave altimeters, CFOSAT SWIM wave scatterometer, oceanographic platform

Acknowledgments: The work was carried out within the framework themes of state assignments of FSBSI FRC MHI FNNN-2024-0001, FNNN-2022-0002, FNNN-2024-0012, FNNN-2024-0014, FNNN-2024-0016 and grant No. 169-15-2023-002 of Federal Service for Hydrometeorology and Environmental Monitoring, dated 03.01.2023. The authors are thankful to E.M. Lemesenko, the head of the Black Sea hydrophysical subsatellite polygon of Marine Hydrophysical Institute of RAS for providing the video records of storm waves.

For citation: Dulov, V.A., Yurovskaya, M.V., Fomin, V.V., Shokurov, M.V., Yurovsky, Yu.Yu., Barabanov, V.S. and Garmashov, A.V., 2024. Extreme Black Sea Storm in November, 2023. *Physical Oceanography*, 31(2), pp. 295-316.

© 2024, V. A. Dulov, M. V. Yurovskaya, V. V. Fomin, M. V. Shokurov, Yu. Yu. Yurovsky,
V. S. Barabanov, A. V. Garmashov

© 2024, Physical Oceanography

Introduction

On 25–27 November 2023, there was a storm with extremely strong wind waves in the Black Sea, causing significant destruction of embankments, piers and coastal structures. In particular, the building of the Institute of Biology of the Southern Seas of the Russian Academy of Sciences was damaged in Sevastopol Bay, which led to



the death of about 500 rare marine animals. Several concrete piers were destroyed in the Sevastopol area, the village of Lyubimovka and the surrounding area of the Chersonesus Lighthouse were flooded. Serious destruction took place on the Southern Coast of Crimea (SCC) and on the Caucasian coast of the Black Sea. The media called this natural disaster the “storm of the century.” Such a high-profile incident requires discussion from the viewpoint of oceanology and a detailed description in terms of physical quantity fields.

Information about the evolution of wave characteristic fields at the sea scale follows from wave modelling based on wind speed data from atmospheric models. Modern satellite methods of ocean sounding, as well as contact measurement data, make it possible to verify modelling results and confirm their reliability. A case study of the November “storm of the century” in the Black Sea, combining catastrophic event modelling and available measurement data, has obvious practical significance.

Extreme Black Sea storms were described in a number of works as part of the study of the Black Sea wind-wave regime using the data from wavegauge measurements at weather stations [1, 2], numerical modelling of wave fields [3–7] and estimates of the wave energy potential in the Black Sea [8, 9]. Some examples of model calculations for specific extreme storms are given in [7, 10, 11]. The current level of research into both wind-wave climate and extreme storms involves a combined analysis of the results of numerical modelling, satellite and contact measurements [12, 13]. A comparison of the results of wave modelling in the Black Sea with contact measurements was carried out in [5, 14–16] and with satellite altimeter data in [16–18]. For extreme storms in the listed studies, the maximum values of significant wave heights were 10–12 m. The comparisons of model calculations with satellite and contact data cover large time intervals, as a result, the contribution of extreme storms in this type of research is relatively small. Therefore, confirming the adequacy of modelling the events of extreme storms remains a critical problem.

The present paper gives a case study of the Black Sea catastrophic storm of 25–27 November 2023. Its in-depth development is presented below based on simulations using the WRF atmospheric model and the SWAN wave model. The attention to the wind field is due to the critical importance of its features for the wave field formation. A detailed description of the model configurations with a list of the used parameterizations of physical processes is given to reproduce the results discussed below. The calculations were verified using a large amount of available satellite measurement data. If altimetry estimates of wave heights have previously been repeatedly used in studies of waves in the Black Sea, the SWIM radar data from the CFOSAT satellite is apparently used for the first time to estimate directions and wavelengths in the Black Sea. The paper presents field wave measurement data from the oceanographic platform of the Black Sea hydrophysical subsatellite polygon of Marine Hydrophysical Institute (MHI) of RAS, covering the entire storm period. The purpose of the work is to provide a detailed description of the wave field evolution during the event and to carry out the most accurate verification of the results using satellite and *in situ* data.

Data and models

Regional WRF atmospheric model. The MHI operational atmospheric forecast system based on the WRF model operates in MHI to provide data (heat, moisture and momentum flows on the sea surface) for the Black Sea circulation model in the MHI Marine Forecast Center, as well as for other scientific research in the field of atmospheric interaction and seas in the region. To reproduce such mesoscale phenomena correctly as, for example, breezes, local winds such as boras and local eddies, a spatial resolution of 5–10 km is required because publicly available forecast arrays do not have the necessary detail. The technology of calculating meteorological parameters based on numerical data solving basic equations of thermo- and hydrodynamics for a limited area within the framework of the WRF-ARW mesoscale model is used. The results of the NCEP/NCAR operational global atmospheric forecast in the USA, carried out every 6 hours for 16 days in advance, were used as input data. These data, abbreviated as GFS and publicly available at <https://www.nco.ncep.noaa.gov>, have a spatial resolution of 0.25°, a 6-hour time resolution and 44 vertical levels. The WRF-ARW model (version 4.5) deployed at the MHI cluster was used. The modelling domain with a horizontal grid step of 9 km included the waters of the Black and Azov seas and the Crimean Peninsula, as well as the waters of the Caspian, Marmara, Aegean and partly Mediterranean seas. The domain grid was 368 × 203 nodes and 45 vertical levels. To parameterize the atmospheric planetary boundary layer, the Mellor-Yamada-Janjic scheme was chosen, the Tiedke scheme – to parameterize cumulus convection, the RRTMG scheme – to calculate radiative transfer in the atmosphere and the Thompson scheme – to calculate phase transitions of water and ice and the transport of hydrometeors in clouds. A four-layer NOAH soil model was used to determine heat and moisture fluxes on the land surface. Documentation for the model with a detailed description of parameterizations is available at <https://www2.mmm.ucar.edu/wrf>. The fields of meteorological parameters were calculated for the period from 24 November 2023 (00:00) to 28 November 2023 (00:00) (UTC time is given here and below).

SWAN wave model. In this study, the Simulating WAVes Nearshore Model Cycle III version 41.45 (SWAN) [19, 20] was used to calculate characteristics of extreme waves. It has already been used in MHI to study extreme storm situations in the Azov-Black Sea basin [3, 6, 21, 22]. The SWAN model belongs to the third-generation spectral models and considers wind input, non-linear quadruplet wave-wave interactions, dissipation of energy due to whitecapping and bottom friction, as well as wave breaking¹ at critical depths. For the wave model input, wind speed U_{10} at a height of 10 m was specified from the WRF atmospheric model. Friction speed at the wave generation source was determined by the aerodynamic formula

¹ SWAN. *Scientific and Technical Documentation. SWAN Cycle III Version 41.45AB*. 2023. [online] Available at: swanmodel.sourceforge.io/online_doc/swantech/swantech.html [Accessed: 10 April 2024].

$u_* = \sqrt{C_d} U_{10}$, where drag coefficient C_d was approximated by a polynomial of the second degree with respect to U_{10} [23]. The process of whitecapping was described by the model in the formulation [24], bottom friction was determined based on the relations from [25]. The angular resolution of the model was 10° . The frequency coordinate used 36 nodes. Minimum frequency was $f_0 = 0.033$ Hz. Other frequencies were determined using the formula $f_n = 1.1 f_{n-1}$ ($n \geq 1$). Integration over time was carried out using an implicit difference scheme with a step of 30 minutes in the parallel computing mode on the MHI cluster.

The frequency-angular spectra of waves $S(f, \vartheta)$ were calculated from 24 November (00:00) to 28 November (00:00). The fields of significant wave height $H_S = 4\sqrt{\iint S(f, \vartheta) df d\vartheta}$, the direction of waves ϑ_p at the frequency of spectral peak f_p and the period of the spectral peak waves $T = 2\pi/f_p$ were used for analysis. Below, the H_S , ϑ_p and T characteristics will be called the height, direction and wave period for brevity.

Field measurements were carried out from a stationary oceanographic platform of the Black Sea hydrophysical subsatellite polygon of MHI located approximately 500 m away from the coast, where the sea depth is about 28 m. In Fig. 1, *a*, the platform position is marked by a red asterisk on the satellite optical image from <https://www.arcgis.com/apps/View/index.html?appid=504e3ff67457481e839bb941a709350f>. The image is also overlaid with ETOPO1 1 Arc-Minute Global Relief Model bathymetry from <https://www.ncei.noaa.gov/products/etopo-global-relief-model>. Meteorological and wavegauge measurements were carried out in the background mode using a Davis Vantage Pro 2 weather station and a string wave gauge with data transmitted to the shore via a radio channel [14, 26]. Based on successive 20-minute fragments of wave records in the standard way [27], the frequency spectra of waves $S(f)$, the height of significant waves $H_S = 4\sqrt{\int S(f) df}$ and the frequency of spectral peak waves f_p were estimated.

Figure 1, *b* shows a video capture made in the automatic mode on 26 November during a storm at 14:00–14:20. Three vertical structural elements, highlighted in color, were used as an array of “optical wave gauges.” The water level on the corresponding vertical lines was converted into vertical displacements of the sea surface at three points using the known exact position of the video camera and its optical parameters. The triangle in the figure shows a virtual plane connecting these points, which gives large-scale wave slopes in two orthogonal directions. Thus, these data are similar to the data of a standard wave buoy², and their processing by the triplet analysis method [28] enables us to estimate the frequency-angular spectrum of waves for the video recording time period (a more detailed description of the estimation method is given in [29, 30]).

² Earle, M., 1996. *Nondirectional and Directional Wave Data Analysis Procedures*. NDBC Technical Document 96-01. Slidell, USA : Stennis Space Center, 43 p.

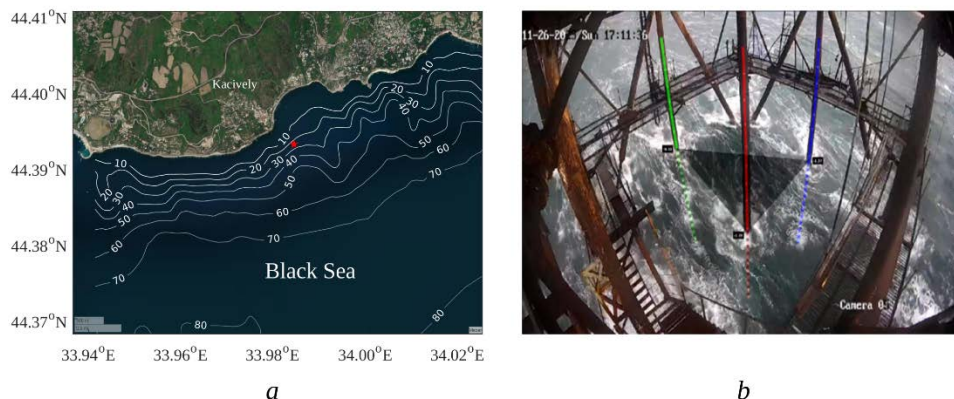


Fig. 1. Location of the oceanographic platform (marked with a red asterisk) (a) and the platform piles (highlighted in color) as wave gauges (b)

Satellite measurements. The work uses the data from altimeters, the CFOSAT SWIM wave scatterometer and synthetic aperture radar (SAR) during the storm. Altimeters are traditionally used to measure wave heights [12]. The altimetry data were taken from the open archives of the Copernicus Marine Environment Monitoring Service (CMEMS) available at https://data.marine.copernicus.eu/product/WAVE_GLO_PHY_SWH_L3_NRT_014_001/description. Capabilities of the SWIM cone-scanning radar [31] installed on the Chinese-French CFOSAT satellite are currently the subject of intensive research [32, 33]. The SWIM instrument is designed to obtain estimates of the spatial spectrum of waves, which, however, turned out to be very noisy [31]. Therefore, only the directions and wavelengths of the spectral peak were used in this study – the CFOSAT SWIM Level-2 data from <https://data-cersat.ifremer.fr/projects/iwwoc/>. SAR images traditionally used in marine research make it possible to monitor the fields of surface wind speed at a qualitative and quantitative level [34]. Besides, they contain images of dominant wind waves [35]. C-band SAR images are not affected by clouds, which is especially important in extreme weather conditions when the sea is covered by heavy clouds. The three C-band SAR images used were obtained from <https://browser.dataspace.copernicus.eu>. The information on all satellite data is summarized in Table 1. Altimeter and CFOSAT SWIM radar tracks are shown in Fig. 2.

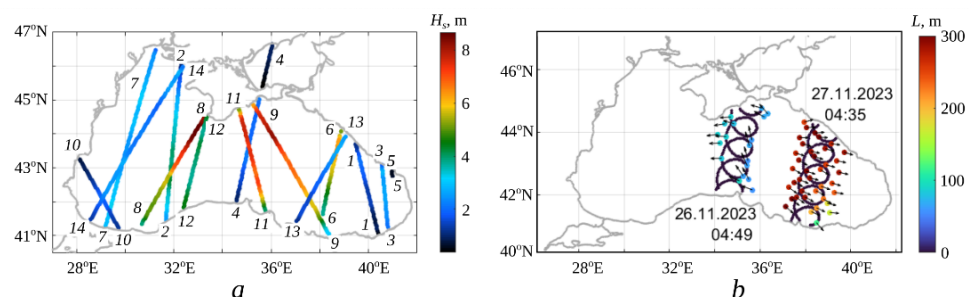


Fig. 2. Measurement data: a – satellite altimeter tracks indicating wave heights H_s ; b – tracks of the SWIM sensor (CFOSAT) with indicated direction (arrows) and wavelengths L (color)

Table 1

Satellite data			
Physical characteristic, sensor	Satellite	Track number	Time of flight
Wave height, altimeter	<i>SARAL-AltiKa</i>	1	02:41 (26.11)
	<i>CryoSat-2</i>	2	09:05 (26.11)
	<i>CryoSat-2</i>	3	20:14 (26.11)
Wave direction and wavelength, SWIM, wave height, altimeter	<i>CFOSAT</i>	4	04:49 (26.11)
	<i>CFOSAT</i>	5	15:30 (26.11)
	<i>CFOSAT</i>	6	04:35 (27.11)
Wave height, altimeter	<i>HaiYang-2B</i>	7	04:41 (27.11)
	<i>HaiYang-2C</i>	8	20:23 (26.11)
	<i>JASON-3</i>	9	21:46 (26.11)
	<i>JASON-3</i>	10	22:08 (27.11)
	<i>Sentinel-3A</i>	11	19:06 (26.11)
	<i>Sentinel-3B</i>	12	08:21 (27.11)
	<i>Sentinel-6A</i>	13	12:59 (26.11)
	<i>Sentinel-6A</i>	14	13:21 (27.11)
Normalized radar cross-section, SAR	<i>Sentinel-1A</i>	–	04:06 (26.11)
	<i>Sentinel-1A</i>	–	15:20 (26.11)
	<i>Sentinel-1A</i>	–	03:17 (27.11)

Overall picture of the storm in the Black Sea

Wind field. The weather in the Black Sea region on 25–26 November 2023 was determined by a powerful extratropical cyclone with the center moving from the Balkan Peninsula through the Black Sea to Crimea and further to the north. Analysis of archived fields of sea level pressure, geopotential and the temperature on 25–27 November 2023 gives the following scenario for cyclone formation. The cyclone originated on the southeastern boundary of a deep, meridionally elongated trough in an area of strong horizontal temperature gradient. An intense and fairly compact cyclone is formed to the southeast of the trough, manifesting in the pressure field at sea level. Fig. 3, a shows its trajectory and pressure at sea level at its center (in hPa) according to the calculations using the WRF model. The time intervals between the graph points are 6 hours, the starting point (in the southwest) corresponds to 25 November 2023 (00:00). Cyclones with a similar trajectory are typical for the Black Sea region; traditionally they are called “southern” cyclones. They form over the Mediterranean Sea, move northeast, pass over the western part of the Black Sea and then move north across the territory of Russia. This type of Black Sea cyclone includes the well-known storm of 10–11 November 2007, which led to catastrophic consequences. It had almost the same trajectory and the maximum wind speed reached 30 m/s [36].

Figures 3, *b – e* show the wind fields over the Black Sea according to the calculations using the WRF model. Fig. 3, *b* demonstrates a very complex wind field: the hurricane enters the southwestern sector of the Black Sea against the background of a south-southeast storm wind with an area of maximum values above 20 m/s, occupying the central and eastern parts of the sea. In Fig. 3, *c* the hurricane is moving over the Black Sea to the north-northeast while maintaining

a south-southeast wind in the eastern Black Sea. In Fig. 3, *d*, the “eye” of the hurricane reaches the western tip of Crimea; over the Black Sea to the west of 37°E, the wind field acquires a clearly defined cyclonic “centrally symmetric” structure, typical for tropical cyclones. Fig. 3, *e* corresponds to the moment of time after the hurricane makes landfall – the cyclonic wind field covers the Black Sea almost completely. Then, over time, the wind speed decreases as the hurricane moves away from the sea.

In Fig. 3, *f*, model calculations are confirmed by available satellite radar images. Against the light background of the images, corresponding to land backscatter and sea surface scattering at high wind speeds, dark areas of the absence of storm winds are distinguished. At 04:14 on 26 November (left photo), a dark area elongated between 43° and 44°N coincides with the line of change in wind speed direction (occlusion front), emanating from the “eye” of the hurricane and is clearly seen in Fig. 3, *b*. At 15:20 (right photo), a cold front is visible between the stormy and moderate wind zones, shown in the model field for 15:00 in Fig. 3, *d*.

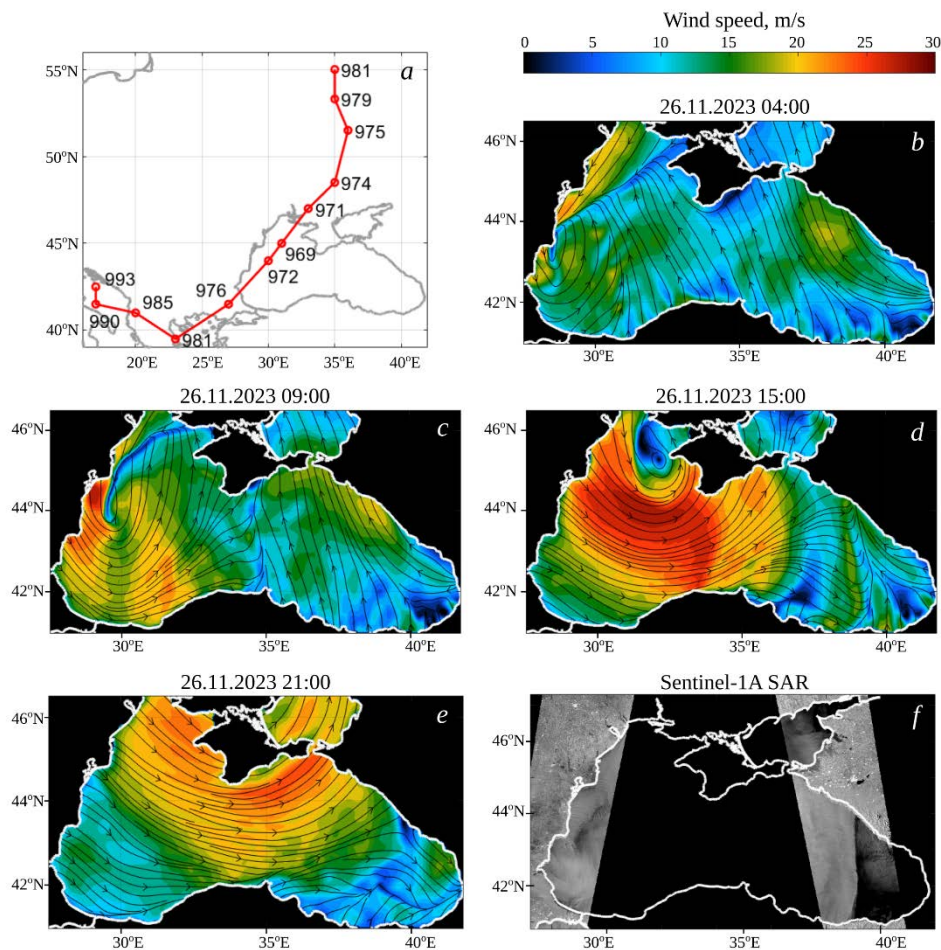


Fig. 3. Atmospheric characteristics: hurricane track and sea level pressure in its center (*a*); streamlines and wind speed on 26 November at 04:00 (*b*), 09:00 (*c*), 15:00 (*d*), 21:00 (*e*). Satellite radar images obtained on 26 November at 04:14 (left) and 15:20 (right) (*f*)

Field of wind waves. Figures 4 and 5 show wave field development on 26 November 2023 according to the calculations using the SWAN model for the entire Black Sea on a grid with a resolution of 4.5×4.5 km (246×160 nodes). Fig. 4, *a* – *d* shows spatial distributions of wave height (color) and direction (arrows) for four moments in time: 13:00, 16:00, 19:00 and 21:00. Figure 5 shows time dependences of wave height and period at six different points of the sea. The positions of the points are shown in Fig. 4, *e*, their coordinates are in the headings of the tabs in Fig. 5. Point 1 was selected in the central part of the sea, points 2 – 6 – several kilometers seaward of Sevastopol, Kaciveli, the Kerch Strait, Novorossiysk and Sochi, respectively.

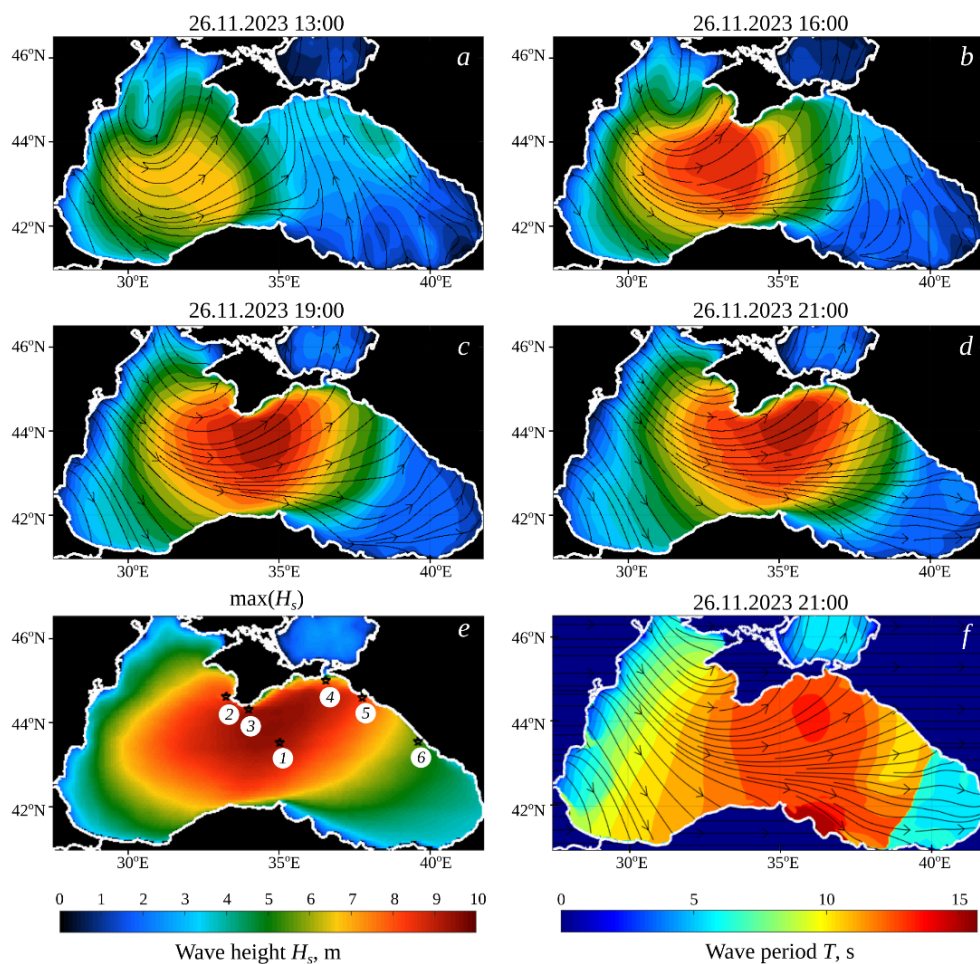


Fig. 4. Field of wind waves: height and direction of waves on 26 November at 13:00 (*a*), 16:00 (*b*), 19:00 (*c*), 21:00 (*d*); distribution of maximum wave heights during the storm period (*e*); periods and directions of waves on 26 November at 21:00 (*f*)

By 10:00, as a result of the hurricane passage through the western part of the sea (Fig. 3, *b*, *c*), an area of storm waves with heights of up to 3 m and periods of up to 8 s, spreading to the east and northeast, is formed. Its boundary has not yet reached the sea center (point 1 in Fig. 5), but near the coast of Crimea (points 2 and 3 in

Fig. 5) the beginning of a monotonous increase in wave height can be seen. At this moment, there are already storm waves generated by a local strong wind near the Caucasian coast of the Black Sea. This area is seen in Fig. 3, *b, c*. Accordingly, wave heights are 3–4 m and higher at points 4–6 in Fig. 5.

Further, the storm area boundary moves eastward with increasing height and period of storm waves. By 13:00, wave heights reach 4–5 m (Fig. 4, *a*), a distinct increase in waves begins in the sea center (point 1) and near Kaciveli (point 3), and the waves continue to increase near Sevastopol (point 2). By 16:00, the area of the most intense storm waves covers the entire sea center, wave heights reach 7 m (Fig. 4, *b*). At 19:00, the storm area continues to spread to the east, the wave heights already exceed 9 m (Fig. 4, *c*). Around this time, maximum wave heights are reached in the sea center (point 1) and Kaciveli (point 3). The moments of reaching maximum wave heights are highlighted in Fig. 5 by vertical lines. By 21:00, intense storm waves reach the Caucasian coast of the Black Sea (points 4, 5). Fig. 4, *d, f* shows the fields of wave heights and periods along with wave directions at 21:00. Throughout the entire Black Sea water area, except its western and eastern extremities, a field of developing wind waves is established with propagation directions close to the wind direction shown in Fig. 3, *e*. Wave periods in the sea center reach 11 s or more (Fig. 4, *f*; point 1 in Fig. 5). A storm wave front (Fig. 4, *f*), spreading to the east, is clearly seen in the eastern part of the sea. Around 00:00 on 27 November, the waves reach their maximum heights and maximum periods near Novorossiysk (points 2 and 5 in Fig. 5); near Sochi, storm waves begin to grow (point 6 in Fig. 5). At approximately 04:00 on 27 November, the waves reach their maximum near Sochi (point 6 in Fig. 5). Then, with a gradual decrease in wind speed, the wave height decreases.

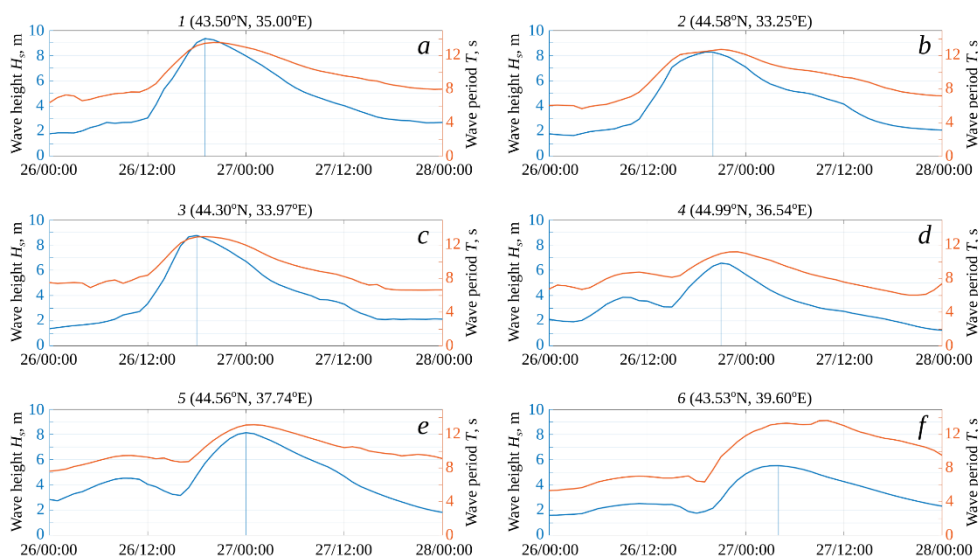


Fig. 5. Dependences of wave heights and periods on time for the points in the sea shown in Fig. 4, *e*: center of the sea (1), regions of Sevastopol (2), Kaciveli (3), Kerch Strait (4), Novorossiysk (5), Sochi (6)

Figure 4, *e* shows the distribution of maximum wave heights over the Black Sea during the storm period. In the sea center, covering almost half of its area, the wave heights exceeded 8 m. The area of waves with heights of 8 m or more covered areas near Sevastopol, Yalta and Novorossiysk, wave heights near Sochi reached 5–6 m. The maximum wave periods exceeded 13 s, and at point 6 in the Sochi region they approached 14 s (Fig. 4, *f*; point 6 in Fig. 5).

Comparison of wave characteristic calculations and satellite data. Figure 6 characterizes the correspondence between model calculations and satellite measurements. Fig. 6, *a*, *c*, *e* shows examples of altimetry data comparison and wave height calculation at the moments of satellite passage. The figures show a certain agreement both in wave height values and in its variability along the track. For example, in the southern parts of all tracks there is a transition from high storm waves in the sea center to moderate height waves on the southern periphery of the storm in accordance with model calculations. In Fig. 6, *a*, both in the model and in the altimetry data, an area of reduced wave height is observed near the coast of Crimea.

In Fig. 6, *b*, *d*, the SWIM radar data from the CFOSAT satellite are superimposed on the fields of wave periods and directions calculated for the moments of satellite passage. The calculation of wave periods T from satellite-measured wavelengths L was carried out using the dispersion relation for linear waves at finite sea depth $T = 2\pi/\sqrt{gk \tanh(kh)}$, where $k = 2\pi/L$; g is gravity; h is sea depth at the point under consideration [37]. In Fig. 6, *b*, *d*, the wave periods calculated from satellite measurements are shown in the form of circles, the color of which corresponds to the color scale, and the measured wave directions are shown by arrows. The time of the first satellite scene (Fig. 6, *b*) corresponds to the pre-storm state of the sea – propagation of waves generated by the wind field that existed there before the storm (see Fig. 3, *b*). The time of the second flight of the satellite corresponds to the active phase of the storm (Fig. 6, *d*), but the wind speed in the area of the southern part of the track at this moment had already dropped to 15 m/s and lower. For the wave periods calculated by the model (13–14 s, see Fig. 6, *d*), the inverse wave age $\alpha = 2\pi U_{10}/(gT)$ does not exceed 0.74, which is lower than the value of 0.83, characterizing the fully developed waves with the Pierson–Moskowitz spectrum [38]. Thus, the waves in the southern part of the track are also swell.

Figure 6, *b* shows correspondence of wave periods with some discrepancy between the calculated and measured wave directions. It is understandable in a situation of mixed waves, when there are simultaneously developing waves from an incipient storm in the eastern part of the sea and a swell coming from the west. Figure 6, *d* demonstrates reasonable agreement between the measurement and simulation results for both the period and the direction of the waves. However, in the southern part of the track, the model calculation overestimates the swell period compared to the measured one. Figure 6, *f* shows a fragment of a satellite SAR image for a point in the eastern part of the sea with coordinates 41.1°E and 42.4°N (27 November 2023, 03:17), where the dominant waves are clearly observed. A 1 km long segment is superimposed on the image. The segment length fits

4 wavelengths, which corresponds to the wavelengths of 250 m and thus to a wave period of 12.7 s. This estimate is consistent with the CFOSAT SWIM measurements, although it is lower than the value obtained from the model ($T = 13.95$ s). For the considered point, the wind speed according to the WRF model was $U_{10} = 9.6$ m/s, which gives the inverse wave age $\alpha = 0.24$, i.e., the waves are definitely a swell. This satellite image confirms the overestimation of the swell wave period by the model calculation.

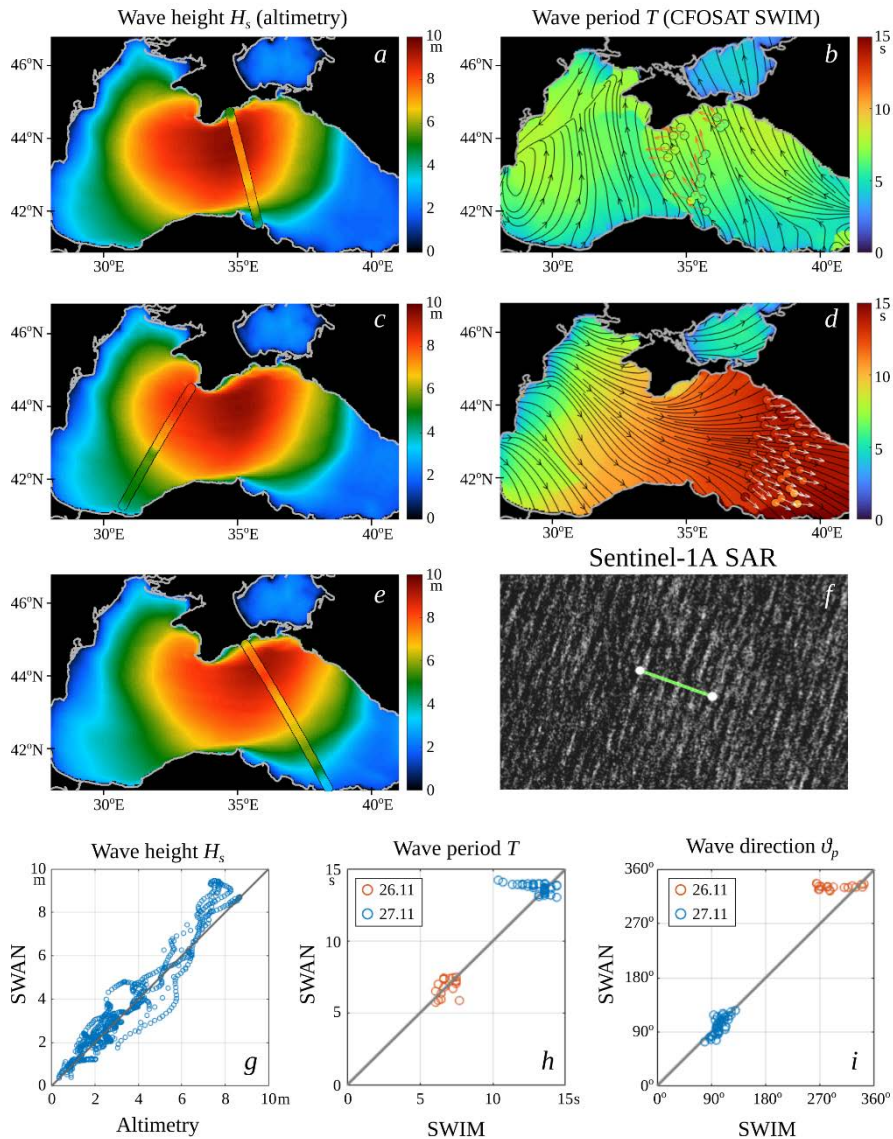


Fig. 6. Comparison of model calculations and satellite data: simulated wave height fields with the superimposed altimeter data from 26 November at 19:06 (a), 20:23 (c), 21:46 (e); simulated fields of wave periods and directions with the superimposed SWIM data from 26 November at 04:49 (b) and 27 November at 04:35 (d); fragment of SAR image with the superimposed line of 1 km long (f). Comparison of simulations and satellite data in terms of wave heights (g), periods (h) and directions (i)

Physical mechanisms of swell dissipation and evolution are not completely understood nowadays [39–41] and parameterizations of swell evolution mechanisms in wave models continue to be improved [42–45]. However, in the SWAN model, the methods for calculating swell and wind waves do not differ [41]. This is probably responsible for the discrepancies in the direction of the swell waves in the first satellite pass and the obvious overestimation by the model of the periods of swell waves in the southern part of the track during the second flight.

Figure 6, *g – i* summarizes the considerations of this subsection. Figure 6, *g* shows a comparison with calculations for all altimeter tracks data shown in Fig. 2 and Table 1. Figure 6, *h, i*, presents the comparison for all CFOSAT SWIM data by periods and wave directions, respectively, with points for the first and second satellite shown in red and blue. Table 2 shows data correlation coefficients, bias and root-mean-square error calculated from the point clouds in Fig. 6, *g – i*. Note that the error in measuring wave heights with an altimeter for the open ocean is 16 cm [46], but in coastal areas it can increase up to 1.6 m [47]. Recent work [46] validated CFOSAT SWIM data on an extensive array of field measurements, resulting in standard errors (RMSE) for wavelengths and directions over 38 m and 9.1 degrees. At the same time, the residuals for individual measurements can be over 70 m and 20 degrees when observing waves with a length of 225 m (Fig. 5 in [46]). As follows from the dispersion relation for linear waves in deep water, errors in the wavelength δL are related to errors in the wave period by the relation $\delta T = \pi \delta L / (gT)$. That is, an error of 38 m for wave periods of 10–3 s corresponds to errors in period estimation $\delta T \approx 1.2 - 0.9$ s. Thus, we can conclude that our comparison of model calculations with individual satellite measurements shows very reasonable agreement. For the purposes of the present study, it is important that there is a correspondence between the heights and periods of the highest developing waves ($H_s = 4 - 9$ m) and the directions of waves in the active phase of the storm.

Table 2

Degree of consistency between the satellite and calculated data			
Characteristics of waves	Bias	RMS	Correlation coefficient
Height	0.21 m	0.66 m	0.97
Period	0.48 s	1.4 s	0.92
Direction	9 degrees	26 degrees	0.98

Storm off the Southern Coast of Crimea

The phenomenon of wave shadowing by the Crimean Peninsula. *The* above model calculations highlight an area of decreased wave height in the water area adjacent to the coast from the southern tip of Crimea to Cape Meganom (35.08°E) and further from the Feodosiya Gulf to Cape Chauda (35.8°E) (Fig. 4, *c – e*). In this area, the wave height does not exceed 4–5 m, while more seaward it reaches 8–9 m. The altimetry data confirm the presence of this area (Fig. 6, *a*). According to

the contact measurements from an oceanographic platform located in the western part of the area, the wave height did not exceed 4 m.

The presence of the area is associated with the shadowing of developing wind waves coming from the west by the Crimean Peninsula. The wave field formation in this area involves waves coming from the southwest, as well as young waves generated by local wind, and, possibly, the effects of nonlinear processes and refraction of waves coming from the west and reaching the south of Crimea. However, the shadowing effect in this case plays a major role, since the calculated wave spectra do not contain energetically significant (i.e., significantly affecting the H_S value) wave harmonics propagating to the east.

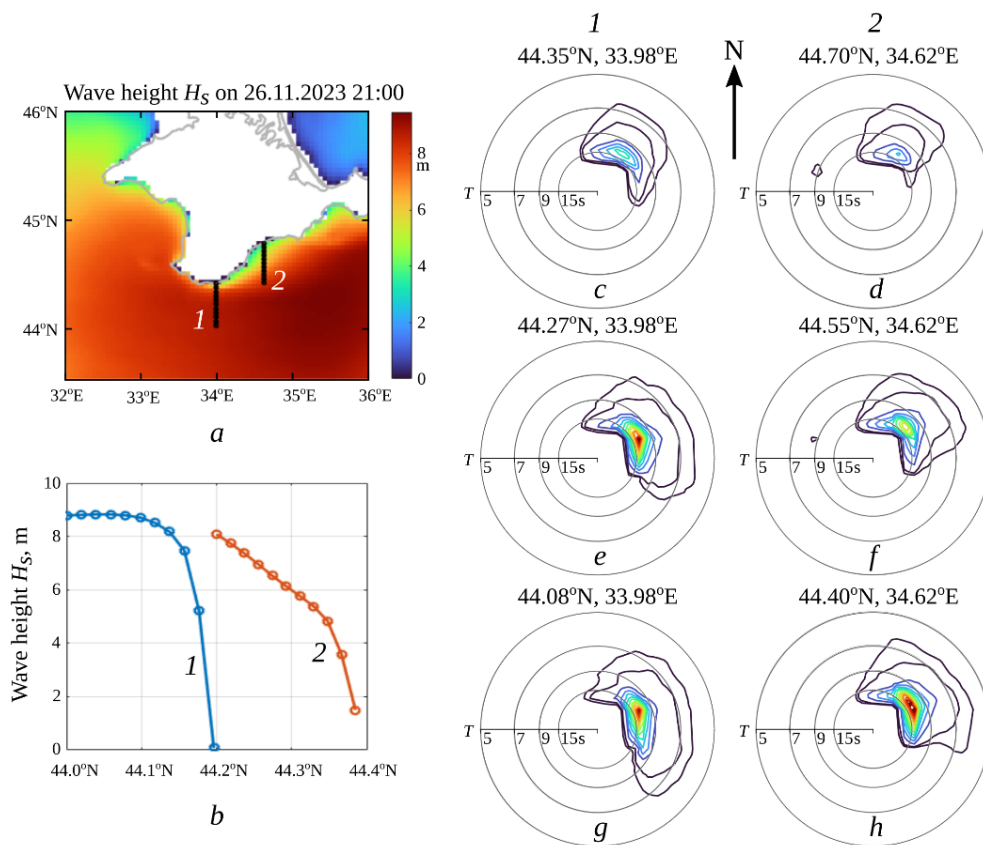


Fig. 7. Shadowing of waves by the Crimean Peninsula: *a* – transects 1 and 2 superimposed on the simulated field of wave heights; *b* – wave height along transects 1 and 2; frequency-angular spectra of waves along transects 1 (*c*, *e*, *g*) and 2 (*d*, *f*, *h*), where the circles (from larger radius to smaller one) correspond to wave periods 5, 7, 9, 15 s

In Fig. 7, this phenomenon is illustrated by latitudinal sections of the wave field, covering spatial regions of the shadowing absence and presence (Fig. 7, *a*, section 1 corresponds to the oceanographic platform longitude). Figure 7, *b* shows variation of wave heights along latitude. Figure 7, *c* – *h* shows changes in the calculated frequency-angular spectra along the transect. In these figures, presented in polar coordinates,

the frequency is plotted along the radius, the geographic azimuth is measured from the direction to the north (in the figure – vertically upward) and shows where the wave harmonic propagates. Spectral density is indicated in arbitrary units.

Domains of the transects are approached by waves developed from the western extremity of the sea, which have a relatively wide angular spectrum. The Crimean Peninsula obscures some of the wave propagation directions, which leads to the vanishing of the corresponding wave harmonics from the spectrum. In the southern part of the transects (Fig. 7, *e, g*), the spectra include waves propagating both to the northeast and southeast. In the northern part of the transects (Fig. 7, *c, d*), the waves propagating to the southeast are absent due to shadowing. Figure 7, *e, f* shows the transition between these states. As a result of “cutting off” the southeastern direction waves from the spectrum, the total wave energy decreases significantly and the wave height decreases from 9 m to ~ 4 m (Fig. 7, *a, b*).

Thanks to the shadowing, the damage caused by the storm in the central and eastern parts of the SCC turned out to be significantly lower than it would have been in the absence of this effect.

Wave modelling near the oceanographic platform. The wave measurements taken not far enough from the coast, for example, at Cape Chersonesus or at the oceanographic platform in Kaciveli, strictly speaking, cannot be compared with model calculations on a large grid. Comparison requires calculations on a sufficiently fine grid and the model must adequately take into account the influence of shallow water effects on wave evolution. In [14], a comparison of wave characteristics calculated using the WAM Cycle 4 wave model [48] on a coarse grid with measurements from an oceanographic platform was carried out. Only waves coming from the open sea were considered and as a result a good correspondence was obtained. In this study, in contrast to [14], extreme waves with wavelengths reaching 200 m or more in deep water and significantly exceeding the sea depth of 28 m are considered. In this case, it is fundamentally important to consider the influence of bathymetry details on wave characteristics.

To simulate storm waves in the area of the MHI oceanographic platform on 24–28 November 2023, as before, the SWAN Cycle III model (version 41.45) ¹ was used, but to increase the spatial resolution, a four-step nested grid method was applied. At the first step, wave fields were simulated for the entire Black Sea on a grid with a resolution of 4.5×4.5 km (246×160 nodes). At the second step, waves for the water area including the South Coast on a grid of 0.8×1.13 km (234×122 knots) were calculated. At the third step, waves were modeled in the coastal zone of the SCC from the village of Ponizovka to Simeiz with a resolution of 200×200 m (171×198 knots). At the fourth step, with a resolution of 15×20 m (118×91 knots), the wave fields in the coastal waters of Kaciveli, including the oceanographic platform, were modeled. During calculations at the second, third and fourth steps, the wave parameters at the liquid boundaries of computational domains were determined by interpolating model data from the previous steps. As before, surface wind fields from the WRF mesoscale atmospheric model were used as forcing.

The SWAN model operates in the approximation of geometric optics: the dimensions of inhomogeneities in the medium should significantly exceed the wavelengths. Strictly speaking, the calculation at the fourth modelling step is not completely correct, since the grid step turns out to be smaller than the wavelength. However, the coastline and bottom topography in the water area surrounding the platform experience significant changes at scales of 30–50 m. The fourth calculation step was carried out to consider this variability to some extent in the model. At the same time, the use of a four-step approach ensures the solution continuity when approaching the platform from the open sea.

Field measurement and modelling results. Fig. 8 shows measurement data from the oceanographic platform in comparison with the calculation. Fig. 8, *a* shows wind speed and direction; Fig. 8, *b* – wave height and period; Fig. 8, *c, e* – instantaneous frequency spectrum according to the measurements of the string wave recorder and calculations, respectively; Fig. 8, *d, f* – frequency-angular spectra according to the measurements of the “optical” wave recorder and calculations, respectively. The frequency-angular spectra are presented in polar coordinates, where the azimuth the waves come from is indicated.

As follows from these data, on 26 November, from 06:00 to 16:00, the wind direction changes to ~255 degrees with a simultaneous increase in its speed (Fig. 8, *a*). In the time period 16:00–18:00, the wind speed is close to the maximum value of 28 m/s and on 27 November from 18:00 to ~02:00 it drops to 13 m/s with a constant wind direction. These wind characteristics persist on 27 November until 14:00, after which the wind speed gradually decreases. Fig. 8, *a* shows the correspondence of the calculated wind speed and its direction to the measured values.

The wave height on 26 November (Fig. 8, *b*) in the time interval 06:00–15:00 increases to 3–4 m and then remains approximately at this level until 19:00. In the time interval 19:00–24:00, the wave height decreases to 1 m. Fig. 8, *b* shows that the model qualitatively correctly describes the temporal variability of wave height and period, although it overestimates these characteristics.

Figure 8, *c* shows changes in the spectral shape of the wave over time, in particular, the evolution of spectral peak frequency. As follows from the figure, the strongest transformation of the spectrum occurred from 10:00 to 14:00. Then, until 22:00, the period of the spectral peak waves was 11.7–12.8 s, corresponding to wavelengths of 167–187 m when recalculated using the dispersion relation for surface waves [37] at a final sea depth of 28 m at the platform location. If we assume that the wave frequency remained the same when approaching the shore, then in deep water these waves had a length of 214–256 m. Comparison of Fig. 7, *c, e* demonstrates the correspondence of waves frequency spectra and their temporal variability.

The frequency-angular spectrum assessment (Fig. 8, *d*) shows that the main system waves come from the west (240 degrees), from a direction close to the wind direction indicated by the arrow. At the same time, a system of lower intensity swell waves, which come from the east (~90 degrees), is observed. They were generated by the wind field that existed in the central and eastern parts of the sea at the time of the cyclone arrival (Fig. 3, *b* and its discussion) and generated a wave system that

was observed by CFOSAT during its first flight (Fig. 6, *d*). Fig. 8, *d*, *f* shows the agreement of the spatial spectra: the calculation conveys the frequency and direction of the dominant wave system well. The system of swell waves coming from the east, although with some distortions, is also reproduced by the model.

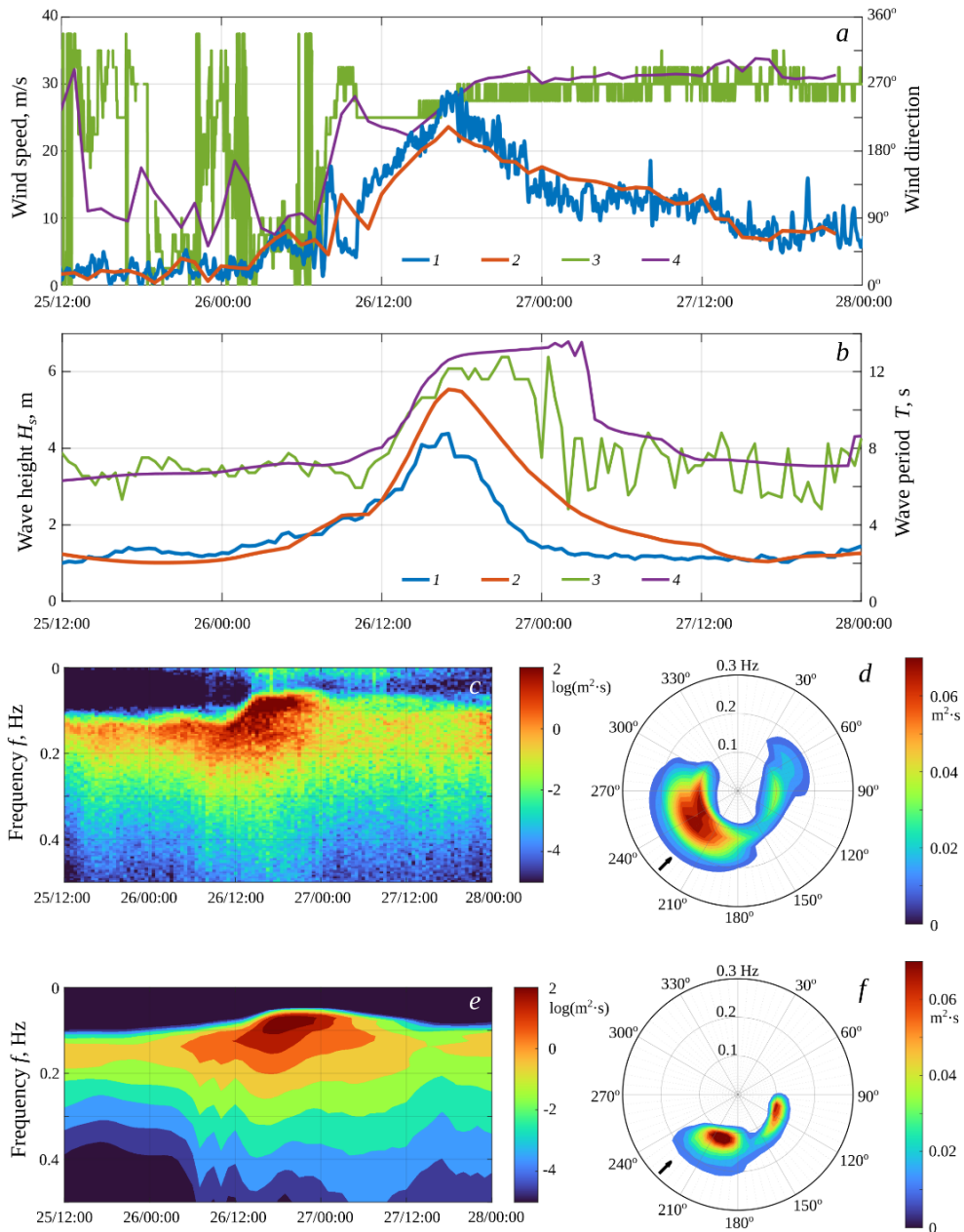


Fig. 8. Shadowing of waves by the Crimean Peninsula: *a* – transects 1 and 2 superimposed on the simulated field of wave heights; *b* – wave height along transects 1 and 2; frequency-angular spectra of waves along transects 1 (*c*, *e*, *g*) and 2 (*d*, *f*, *h*), where the circles (from larger radius to smaller one) correspond to wave periods 5, 7, 9, 15 s

Proper operation of the string wave gauge can be confirmed by the presence in its signal of fluctuations of infragravitational frequencies ranging from 0.02 Hz and below (Fig. 8, *c*). These fluctuations are most intense during the period of an “active storm” with the highest wave heights (from 14:00 on 26 November to 09:00 on 27 November) in accordance with generally accepted ideas [49, 50]. The recorded infragravity response of the sea to the storm can be the subject of a special study [51].

Correspondence of the model calculations to the *in situ* measurements from the oceanographic platform can be considered as another confirmation of the model calculation correctness when describing an extreme storm in the Black Sea.

Conclusion

A case study of the November 2023 extreme storm in the Black Sea provided a detailed picture of the storm evolution in terms of physical wave characteristic fields—significant wave heights, directions, and spectral peak wave periods. The atmospheric fields were calculated using the WRF model and the wave fields were calculated using the SWAN model. To verify the modelling results, available data from satellite altimeters, the CFOSAT SWIM wave scatterometer and synthetic aperture radars were used, and SWIM data were used to analyze the Black Sea storm, apparently, for the first time. The data from *in situ* measurements carried out during the storm by standard equipment from the oceanographic platform of the Black Sea hydrophysical subsatellite polygon of Marine Hydrophysical Institute of RAS provided detailed information about the storm at the point of the Crimea coastal zone, where the platform is located. A four-step nested grid method was used to calculate waves near the oceanographic platform using the SWAN model. Thus, a comprehensive study of a specific catastrophic event with extreme wave characteristics was carried out.

A joint analysis of the results obtained prompts the following statements:

- the results of model calculations are confirmed by a large amount of satellite data. The calculation of wave characteristics near the oceanographic platform is consistent with the *in situ* measurements from the platform;
- during the November 2023 storm in the Black Sea, the maximum wave heights and maximum wave periods exceeded 9 m and 13 s, respectively;
- since the used model configurations permitted to obtain the fields of physical characteristics of waves with a high degree of reliability without involving additional sources of information, they can be used for reliable forecasting of extreme storms in the Black Sea;
- shadowing of waves by the Crimean Peninsula led to a decrease in the height of extreme waves by two or more times in the extended coastal waters from the southern tip of the peninsula to Cape Chauda, significantly reducing the dangers and risks associated with the extreme storms there.

REFERENCES

1. Repetin, L.N., Belokopytov, V.N. and Lipchenko M.M., 2003. Winds and Wave Perturbations in the Southwest Crimean Coast. In: MHI, 2003. *Ecological Safety of Coastal and Shelf Zones and*

- Comprehensive Use of Shelf Resources*. Sevastopol: ECOSI-Gidrofizika. Iss. 9, pp. 13-28 (in Russian).
2. Goryachkin, Yu.N. and Repetin, L.N., 2009. Storm Wind and Wave Regime near the Black Sea Coast of Crimea. In: MHI, 2009. *Ecological Safety of Coastal and Shelf Zones and Comprehensive Use of Shelf Resources*. Sevastopol: ECOSI-Gidrofizika. Iss. 19, pp. 56-69 (in Russian).
 3. Divinsky, B.V., Fomin, V.V., Kosyan, R.D. and Ratner, Y.D., 2020. Extreme Wind Waves in the Black Sea. *Oceanologia*, 62(1), pp. 23-30. <https://doi.org/10.1016/j.oceano.2019.06.003>
 4. Divinsky, B.V. and Kosyan, R.D., 2018. Wave Climate of the Coastal Zone of the Crimean Peninsula. *Physical Oceanography*, 25(2), pp. 93-101. <https://doi.org/10.22449/1573-160X-2018-2-93-101>
 5. Akpinar, A. and Bingölbalı, B., 2016. Long-Term Variations of Wind and Wave Conditions in the Coastal Regions of the Black Sea. *Natural Hazards*, 84(1), pp. 69-92. <https://doi.org/10.1007/s11069-016-2407-9>
 6. Polonsky, A.B., Fomin, V.V. and Garmashov, A.V., 2011. Characteristics of Wind Waves of the Black Sea. *Reports of the National Academy of Sciences of Ukraine*, (8), pp. 108-112 (in Russian).
 7. Efimov, V.V. and Komarovskaya, O.I., 2009. [Atlas of Extreme Wind Waves of the Black Sea]. Sevastopol: ECOSI-Gidrofizika, 59 p. (in Russian).
 8. Divinsky, B.V. and Kuklev, S.B., 2022. Climate Variations of Certain Wave Parameters at the Inlet of Novorossiysk Bay. *Oceanology*, 62(2), pp. 155-161. <https://doi.org/10.1134/S0001437022020035>
 9. Rusu, L., 2015. Assessment of the Wave Energy in the Black Sea Based on a 15-Year Hindcast with Data Assimilation. *Energies*, 8(9), pp. 10370-10388. <https://doi.org/10.3390/en80910370>
 10. Ivanov, V.A., Dulov, V.A., Kuznetsov, S.Yu., Dotsenko, S.F., Shokurov, M.V., Saprykina, Y.V., Malinovsky, V.V. and Polnikov, V.G., 2012. Risk Assessment of Encountering Killer Waves in the Black Sea. *Geography, Environment, Sustainability*, 5(1), pp. 84-111. <https://doi.org/10.24057/2071-9388-2012-5-1-84-111>
 11. Ivanov, V.A., Shokurov, M.V., Dulov, V.A., Kudryavtsev, V.N. and Soukissian, T., 2013. Atmospheric Modeling for Advance Warning of Weather Disasters in the Black Sea Region. *Geography, Environment, Sustainability*, 6(4), pp. 31-47. <https://doi.org/10.24057/2071-9388-2013-6-4-31-47>
 12. Ardhuin, F., Stopa, J.E., Chapron, B., Collard, F., Husson, R., Jensen, R.E., Johannessen, J., Mouche, A., Passaro, M., [et al.], 2019. Observing Sea States. *Frontiers in Marine Science*, 6, 124. <https://doi.org/10.3389/fmars.2019.00124>
 13. Rusu, E., 2016. Reliability and Applications of the Numerical Wave Predictions in the Black Sea. *Frontiers in Marine Science*, 3, 95. <https://doi.org/10.3389/fmars.2016.00095>
 14. Shokurov, M.V., Dulov, V.A., Skiba, E.V. and Smolov, V.E., 2016. Wind Waves in the Coastal Zone of the Southern Crimea: Assessment of Simulation Quality Based on in Situ Measurements. *Oceanology*, 56(2), pp. 214-225. <https://doi.org/10.1134/S0001437016020181>
 15. Divinsky, B.V. and Kosyan, R.D., 2017. Spatiotemporal Variability of the Black Sea Wave Climate in the Last 37 Years. *Continental Shelf Research*, 136, pp. 1-19. <https://doi.org/10.1016/j.csr.2017.01.008>
 16. Myslenkov, S. and Chernyshova, A., 2016. Comparing Wave Heights Simulated in the Black sea by the SWAN Model with Satellite Data and Direct Wave Measurements. *Russian Journal of Earth Sciences*, 16(5), pp. 1-12. <https://doi.org/10.2205/2016ES000579>

17. Gippius, F.N. and Myslenkov, S.A., 2020. Black Sea Wind Wave Climate with a Focus on Coastal Regions. *Ocean Engineering*, 218, 108199. <https://doi.org/10.1016/j.oceaneng.2020.108199>
18. Myslenkov, S., Zelenko, A., Resnyanskii, Y., Arkhipkin, V. and Silvestrova, K., 2021. Quality of the Wind Wave Forecast in the Black Sea Including Storm Wave Analysis. *Sustainability*, 13(23), 13099. <https://doi.org/10.3390/su132313099>
19. Booij, N., Ris, R.C. and Holthuijsen, L.H., 1999. A Third-Generation Wave Model for Coastal Regions. 1. Model Description and Validation. *Journal of Geophysical Research: Oceans*, 104(C4), pp. 7649-7666. <https://doi.org/10.1029/98JC02622>
20. Zijlema, M. and Van der Westhuysen, A.J., 2005. On Convergence Behaviour and Numerical Accuracy in Stationary SWAN Simulations of Nearshore Wind Wave Spectra. *Coastal Engineering*, 52(3), pp. 237-256. <https://doi.org/10.1016/j.coastaleng.2004.12.006>
21. Ratner, Yu.B., Fomin, V.V., Kholod, A.L. and Ivanchik, A.M., 2021. Updated System for the Sea Wave Operational Forecast of the Black Sea Marine Forecasting Center. *Physical Oceanography*, 28(5), pp. 579-595. <https://doi.org/10.22449/1573-160X-2021-5-579-595>
22. Fomin, V.V. and Polozok, A.A., 2021. Wind Waves in the Balaklava Bay under Extreme Wind Conditions. *Ecological Safety of Coastal and Shelf Zones of Sea*, (1), pp. 5-22. <https://doi.org/10.22449/2413-5577-2021-1-5-22> (in Russian).
23. Zijlema, M., van Vledder, G.Ph. and Holthuijsen, L.H., 2012. Bottom Friction and Wind Drag for Wave Models. *Coastal Engineering*, 65, pp. 19-26. <https://doi.org/10.1016/j.coastaleng.2012.03.002>
24. Komen, G.J., Hasselmann, S. and Hasselmann, K., 1984. On the Existence of a Fully Developed Wind-Sea Spectrum. *Journal of Physical Oceanography*, 14(8), pp. 1271-1285. [https://doi.org/10.1175/1520-0485\(1984\)014<1271:OTEOAF>2.0.CO;2](https://doi.org/10.1175/1520-0485(1984)014<1271:OTEOAF>2.0.CO;2)
25. Madsen, O.S., Poon, Y.-K. and Graber, H.C., 1988. Spectral Wave Attenuation by Bottom Friction: Theory. *Coastal Engineering Proceedings*, 1(21), 34. <https://doi.org/10.9753/icce.v21.34>
26. Smolov, V.E. and Rozvadovskiy, A.F., 2020. Application of the Arduino Platform for Recording Wind Waves. *Physical Oceanography*, 27(4), pp. 430-441. <https://doi.org/10.22449/1573-160X-2020-4-430-441>
27. Yefimov, V.V., 1981. [*Dynamics of Wave Processes in the Boundary Layers of the Atmosphere and Ocean*]. Kiev: Naukova Dumka, 256 p. (in Russian).
28. Krogstad, H.E., 2005. Conventional Analysis of Wave Measurement Arrays. In: D. Hauser, K. Kahma, H.E. Krogstad, S. Lehner, J.A.J. Monbaliu and L.R. Wyatt, eds., 2005. *Measuring and Analysing the Directional Spectra of Ocean Waves*. Luxembourg: Office for Official Publications of the European Communities, pp. 56-71. <https://doi.org/10.25607/OBP-811>
29. Dulov, V., Kudryavtsev, V. and Skiba, E., 2020. On Fetch- and Duration-Limited Wind Wave Growth: Data and Parametric Model. *Ocean Modelling*, 153, 101676. <https://doi.org/10.1016/j.ocemod.2020.101676>
30. Yurovsky, Yu.Yu. and Dulov, V.A., 2020. MEMS-Based Wave Buoy: Towards Short Wind-Wave Sensing. *Ocean Engineering*, 217, 108043. <https://doi.org/10.1016/j.oceaneng.2020.108043>
31. Hauser, D., Tourain, C., Hermozo, L., Alraddawi, D., Aouf, L., Chapron, B., Dalphinnet, A., Delaye, L., Dalila, M. [et al.], 2021. New Observations from the SWIM Radar On-Board CFOSAT: Instrument Validation and Ocean Wave Measurement Assessment. *IEEE Transactions on Geoscience and Remote Sensing*, 59(1), pp. 5-26. <https://doi.org/10.1109/TGRS.2020.2994372>

32. Hermozo, L., Rodriguez Suquet, R., Tourain, C., Hauser, D., Schippers, P., Aouf, L., Dalphiné, A., Sutherland, P., Marié, L., Gounou, A. [et al.], 2022. CFOSAT: Latest Improvements in the Swim Products and Contributions in Oceanography. In: GRSS, 2022. *IGARSS 2022 - 2022 IEEE International Geoscience and Remote Sensing Symposium*. IEEE, pp. 6768-6771. <https://doi.org/10.1109/IGARSS46834.2022.9883958>
33. Jiang, H., Mironov, A., Ren, L., Babanin, A.V., Wang, J. and Mu, L., 2022. Validation of Wave Spectral Partitions from SWIM Instrument On-Board CFOSAT against in Situ Data. *IEEE Transactions on Geoscience and Remote Sensing*, 60, 4204013. <https://doi.org/10.1109/TGRS.2021.3110952>
34. Mouche, A.A., Chapron, B., Zhang, B. and Husson, R., 2017. Combined Co- and Cross-Polarized SAR Measurements under Extreme Wind Conditions. *IEEE Transactions on Geoscience and Remote Sensing*, 55(12), pp. 6746-6755. <https://doi.org/10.1109/TGRS.2017.2732508>
35. Collard, F., Ardhuin, F. and Chapron, B., 2009. Monitoring and Analysis of Ocean Swell Fields from Space: New Methods for Routine Observations. *Journal of Geophysical Research: Oceans*, 114(C7), C07023. <https://doi.org/10.1029/2008JC005215>
36. Ovsienko, S.N., Fashchuk, D.J., Zatsepa, S.I., Ivchenko, A.A. and Petrenko, O.A., 2008. Storm of 11 November, 2007, in Strait of Kerch: Chronology of Events, Mathematical Modeling and Geographic/Ecological Analysis of Oil Spill. In: SOI, 2008. *Proceedings of SOI*. Moscow: SOI. Iss. 211, pp. 307-339 (in Russian).
37. Phillips, O.M., 1977. *The Dynamics of the Upper Ocean*. Cambridge, New York: Cambridge University Press, 336 p.
38. Hasselmann, K., Barnett, T.P., Bouws, E., Carlson, H., Cartwright, D.E., Enke, K., Ewing, J.A., Gienapp, H., Hasselmann, D.E. [et al.], 1973. Measurements of Wind-Wave Growth and Swell Decay during the Joint North Sea Wave Project (JONSWAP). *Ergänzungsheft zur Deutschen Hydrographischen Zeitschrift, Reihe A*, A8(12), pp. 1-95. <https://doi.org/citeulike-article-id:2710264>
39. Ardhuin, F., Chapron, B. and Collard, F., 2009. Observation of Swell Dissipation across Oceans. *Geophysical Research Letters*, 36(6), L06607. <https://doi.org/10.1029/2008GL037030>
40. Babanin, A.V. and Jiang, H., 2017. Ocean Swell: How Much Do We Know. In: ASME, 2017. *Proceedings of the ASME 2017 36th International Conference on Ocean, Offshore and Arctic Engineering*. Vol. 3A: Structures, Safety and Reliability, V03AT02A010. <https://doi.org/10.1115/OMAE2017-61692>
41. Babanin, A.V., Rogers, W.E., de Camargo, R., Doble, M., Durrant, T., Filchuk, K., Ewans, K., Hemer, M., Janssen, T. [et al.], 2019. Waves and Swells in High Wind and Extreme Fetches, Measurements in the Southern Ocean. *Frontiers in Marine Science*, 6, 361. <https://doi.org/10.3389/fmars.2019.00361>
42. Ardhuin, F., Rogers, E., Babanin, A.V., Filipot, J.-F., Magne, R., Roland, A., van der Westhuysen, A., Queffelec, P., Lefevre, J.-M. [et al.], 2010. Semiempirical Dissipation Source Functions for Ocean Waves. Part I: Definition, Calibration, and Validation. *Journal of Physical Oceanography*, 40(9), pp. 1917-1941. <https://doi.org/10.1175/2010JPO4324.1>
43. Badulin, S.I. and Zakharov, V.E., 2017. Ocean Swell within the Kinetic Equation for Water Waves. *Nonlinear Processes in Geophysics*, 24(2), pp. 237-253. <https://doi.org/10.5194/npg-24-237-2017>
44. Kudryavtsev, V., Yurovskaya, M. and Chapron, B., 2021. 2D Parametric Model for Surface Wave Development under Varying Wind Field in Space and Time. *Journal of Geophysical Research: Oceans*, 126(4), e2020JC016915. <https://doi.org/10.1029/2020JC016915>
45. Yurovskaya, M., Kudryavtsev, V. and Chapron, B., 2023. A Self-Similar Description of the Wave Fields Generated by Tropical Cyclones. *Ocean Modelling*, 183, 102184. <https://doi.org/10.1016/j.ocemod.2023.102184>

46. Hay, A., Watson, C., Legresy, B., King, M. and Beardsley, J., 2023. In Situ Validation of Altimetry and CFOSAT SWIM Measurements in a High Wave Environment. *Journal of Atmospheric and Oceanic Technology*, 40(10), pp. 1137-1152. <https://doi.org/10.1175/JTECH-D-23-0031.1>
47. Woo, H.-J. and Park, K.-A., 2022. Validation of Significant Wave Height from Jason-3 and Sentinel-3A/B and Relation to Tidal Currents in Coastal Regions of the Korean Peninsula. *International Journal of Remote Sensing*, 43(3), pp. 961-996. <https://doi.org/10.1080/01431161.2022.2026520>
48. WAMDI Group, 1988. The WAM Model – A Third Generation Ocean Wave Prediction Model. *Journal of Physical Oceanography*, 18(12), pp. 1775-1810. [https://doi.org/10.1175/1520-0485\(1988\)018<1775:TWMTGO>2.0.CO;2](https://doi.org/10.1175/1520-0485(1988)018<1775:TWMTGO>2.0.CO;2)
49. Bertin, X., de Bakker, A., van Dongeren, A., Coco, G., André, G., Ardhuin, F., Bonneton, P., Bouchette, F., Castelle, B. [et al.], 2018. Infragravity Waves: From Driving Mechanisms to Impacts. *Earth-Science Reviews*, 177, pp. 774-799. <https://doi.org/10.1016/j.earscirev.2018.01.002>
50. Dolgikh, G.I. and Plotnikov, A.A., 2018. Peculiarities of Generation of Infragravity Waves. *Russian Meteorology and Hydrology*, 43(8), pp. 516-519. <https://doi.org/10.3103/S1068373918080034>
51. Nose, T., Babanin, A. and Ewans, K., 2024. Directional Characteristics of Infragravity Waves during Storms in the Nearshore Coastal Region. *Journal of Coastal Research*, 40(2), pp. 353-363. <https://doi.org/10.2112/JCOASTRES-D-23-00015.1>

Submitted 27.03.2024; approved after review 02.04.2024;

accepted for publication 11.04.2024.

About the authors:

Vladimir A. Dulov, Chief Researcher, Marine Hydrophysical Institute of RAS (2 Kapitanskaya Str., Sevastopol, 299011, Russian Federation), DSc (Phys.-Math.), **ORCID ID: 0000-0002-0038-7255**, **ResearcherID: F-8868-2014**, dulov1952@gmail.com

Maria V. Yurovskaya, Senior Researcher, Head of the Applied Marine Physics Laboratory, Marine Hydrophysical Institute of RAS (2 Kapitanskaya Str., Sevastopol, 299011, Russian Federation), CSc (Phys.-Math.), **ORCID ID: 0000-0001-6607-4641**, **ResearcherID: F-8957-2014**, mvkosnik@gmail.com

Vladimir V. Fomin, Chief Researcher, Marine Hydrophysical Institute of RAS (2 Kapitanskaya Str., Sevastopol, 299011, Russian Federation), DSc (Phys.-Math.), **ORCID ID: 0000-0002-9070-4460**, **ResearcherID: H-8185-2015**, v.fomin@mhi-ras.ru

Mikhail V. Shokurov, Leading Researcher, Marine Hydrophysical Institute of RAS (2 Kapitanskaya Str., Sevastopol, 299011, Russian Federation), DSc (Phys.-Math.), **ORCID ID: 0000-0003-1595-8281**, **ResearcherID: M-7160-2017**, shokurov.m@gmail.com

Yury Yu. Yurovsky, Leading Researcher, Head of the Applied Marine Physics Laboratory, Marine Hydrophysical Institute of RAS (2 Kapitanskaya Str., Sevastopol, 299011, Russian Federation), CSc (Phys.-Math.), **Scopus Author ID: 24377122700**, **ORCID ID: 0000-0002-9995-3965**, **ResearcherID: F-8907-2014**, y.yurovsky@mhi-ras.ru

Vladislav S. Barabanov, Senior Researcher, Head of the Applied Marine Physics Laboratory, Marine Hydrophysical Institute of RAS (2 Kapitanskaya Str., Sevastopol, 299011, Russian Federation), CSc (Phys.-Math.), **ORCID ID: 0000-0002-2689-161X**, **ResearcherID: C-6007-2013**, wbarbs@gmail.com

Anton V. Garmashov, Senior Researcher, Head of the Applied Marine Physics Laboratory, Marine Hydrophysical Institute of RAS (2 Kapitanskaya Str., Sevastopol, 299011, Russian Federation), CSc (Geogr.), **ORCID ID: 0000-0003-4412-2483**, **ResearcherID: P-4155-2017**, ant.gar@mail.ru

Contribution of the co-authors:

Vladimir A. Dulov – general scientific supervision of the research; formulation of the goals and objectives; writing an article text; analysis of results and their interpretation; description and discussion of the research results; formulation of conclusions; critical text analysis

Maria V. Yurovskaya – collection of available materials on the research topic; analysis of results and their interpretation; data systematization, visualization and presentation; participation in the discussion of article materials and editing the article text; critical text analysis

Vladimir V. Fomin – participation in the discussion of article materials; software debugging; data processing; text editing

Mikhail V. Shokurov – participation in the discussion of article materials; text editing; software debugging; data processing

Yury Yu. Yurovsky – methodology, data processing; data visualization and presentation; participation in the discussion of article materials

Vladislav S. Barabanov – software debugging; data processing; participation in the discussion of article materials

Anton V. Garmashov – review of literature on the research problem; participation in the discussion of article materials and text editing

The authors have read and approved the final manuscript.

The authors declare that they have no conflict of interest.